PICOSECOND DYNAMICS OF FREE CARRIER POPULATIONS, SPACE-CHARGE FIELDS, AND PHOTOREFRACTIVE NONLINEARITIES IN ZINCBLENDE SEMICONDUCTORS

Thomas S. Stark, B. S., M. S.

Dissertation Prepared for the Degree of

DOCTOR OF PHILOSOPHY

UNIVERSITY OF NORTH TEXAS

August 1999

APPROVED:

Donald R. Ponikvar, Major Professor
Chris Little, Minor Professor
Duncan Weathers, Committee Member
Jose Perez, Committee Member
Samuel E. Matteson, Chair of the Department of Physics
C. Neal Tate, Dean of the Robert B. Toulouse School of Graduate Studies

Stark, Thomas S., Picosecond Dynamics of Free-Carrier Populations, Space-Charge Fields, and Photorefractive Nonlinearities in Zincblende Semiconductors. Doctor of Philosophy (Physics), August, 1999, 274 pp., 3 tables, 58 illustrations, references, 110 titles.

Generally, nonlinear optics studies investigate optically-induced changes in refraction or absorption, and their application to spectroscopy or device fabrication. The photorefractive effect is a nonlinear optical effect that occurs in solids, where transport of an optically-induced free-carrier population results in an internal space-charge field, which produces an index change via the linear electrooptic effect. The photorefractive effect has been widely studied for a variety of materials and device applications, mainly because it allows large index changes to be generated with laser beams having only a few milliwatts of average power.

Compound semiconductors are important photorefractive materials because they offer a near-infrared optical response, and because their carrier transport properties allow the index change to be generated quickly and efficiently. While many researchers have attempted to measure the fundamental temporal dynamics of the photorefractive effect in semiconductors using continuous-wave, nanosecond- and picosecond-pulsed laser beams, these investigations have been unsuccessful. However, studies with this goal are of clear relevance because they provide information about the fundamental physical processes that produce this effect, as well as the material's speed and efficiency limitations for device applications.

In this dissertation, for the first time, we time-resolve the temporal dynamics of the photorefractive nonlinearities in two zincblende semiconductors, semi-insulating GaAs and undoped CdTe. While CdTe offers a lattice-match to the infrared material $Hg_xCd_{1-x}Te$, semi-insulating GaAs has been widely used in optoelectronic and high-speed electronic applications. We use a novel transient-grating experimental method that allows picosecond temporal resolution and high sensitivity. Our results provide a clear and detailed picture of the picosecond photorefractive response of both materials, showing nonlinearities due to hot-carrier transport and the Dember space-charge field, and a long-lived nonlinearity that is due to the EL2 midgap species in GaAs. We numerically model our experimental results using a general set of equations that describe nonlinear diffraction and carrier transport, and obtain excellent agreement with the experimental results in both materials, for a wide variety of experimental conditions.

ACKNOWLEDGEMENTS

The author would like to acknowledge the generous and loving support of his family, especially his mother, father, wife and son. The author would also like to acknowledge the encouragement and nurturing influence of Dr. G. Bruce Taggart and Dr. Charles T. Butler, two undergraduate professors. Finally, the author would like to acknowledge the generosity of Richard and Martha Schultz of Marengo, IA, and the Cundall family of Denton, TX.

TABLE OF CONTENTS

LIST OF TABLES

LIST OF ILLUSTRATIONS

CHAPTER I

INTRODUCTION

1.1 Dissertation Objective

Semiconductors are a uniquely important class of materials. The electronic and optical properties of these materials form the basis for electronic computing machines and optoelectronic devices such as diode lasers, light emitting diodes and detectors. In recent years, spectroscopic techniques based on nonlinear optics have provided both a sensitive and non-invasive means of studying the electronic and optical properties of semiconductors (P.N. Butcher et al., 1990 and A. Miller et al., 1981). Moreover, these studies have the potential for providing information relevant to the design of optical switching or processing devices based on these nonlinear optical properties.

Zincblende semiconductors such as the III-V material Gallium Arsenide (GaAs) and the II-VI material Cadmium Telluride (CdTe) are excellent materials in which to study nonlinear optical phenomena. Several properties of GaAs have made it the material of choice for electronic and optoelectronic applications. For example, the high electronic mobility in GaAs has led to its use in the construction of high-speed integrated circuits (L.F. Eastman, 1986). Furthermore, unlike Silicon, GaAs is a direct band-gap material. This property, together with the fact that GaAs can be lattice matched to ternary compounds such as Aluminum Gallium Arsenide ($Al_xGa_{1-x}As$), has led to

extensive use of GaAs in diode lasers (T. Li, 1985). As a consequence of its use in these areas, the crystal growth, device processing and materials properties of GaAs have been thoroughly studied. Therefore, not only is GaAs available in high quality crystalline form, but the important physical constants of the material are readily available in the current literature. In addition, use of GaAs-based nonlinear optical devices offers the appealing prospect of integrating diode laser, nonlinear-optical, and electronic computing technologies into a single optoelectronic micro-circuit. Though less studied than GaAs, CdTe has been touted as a sensitive photorefractive material (A. M. Glass and J. Strait, 1988). In addition, while CdTe has been used in liquid crystal imaging and solar energy conversion (K. Zanio, 1978), it offers a lattice match to the important infrared detection material $Hg_xCd_{1-x}Te$.

One of the most widely studied optical nonlinearities is what has come to be known as the photorefractive effect. The photorefractive effect occurs in solids, and arises when transport of an optically-induced free-carrier population results in an internal space-charge field. If the material lacks inversion symmetry, the internal space-charge field produces a change in the index of refraction via the linear electrooptic effect. When the photorefractive effect was first observed by Ashkin et al. in 1966, it was thought to be optical damage. However, as it was further studied, the photorefractive effect was found to offer some unique and useful properties, while allowing large effective nonlinearities to be generated with average laser powers of a few milliwatts. Indeed, as we will see when we discuss the photorefractive effect in greater detail in the next section, for these

reasons the photorefractive nonlinearity has been studied in a wide variety of materials and for a wide variety of applications.

As we will see in the next section, compound semiconductors such as semi-insulating GaAs and undoped CdTe are important photorefractive materials because their material properties allow this optical nonlinearity to be generated both quickly and efficiently (A.M. Glass et al., 1984 and A.L. Smirl et al., 1988). However, while the photorefractive effect has been extensively studied in semiconductors for this reason, no study has yet detailed the fundamental limits of these materials in these areas. Therefore, in this dissertation, we seek to time resolve the fundamental dynamics of the photorefractive nonlinearities in semi-insulating GaAs and undoped CdTe for the first time. This study is of clear relevance, since it has the potential for providing information on the fundamental formation mechanisms for this optical nonlinearity, as well as the information useful in the design of improved photorefractive devices.

1.2 The Photorefractive Effect – A More Detailed Discussion

As we stated in the previous section, the goal of this dissertation is to study the picosecond photorefractive effects that occur in semi-insulating GaAs and undoped CdTe. As a result, before proceeding, it is necessary to discuss the photorefractive effect in greater detail. While this provides insight into the organization of this dissertation, it also provides occasion to review the literature in this area.

The photorefractive effect is a change in the index of refraction that results from a photogenerated space-charge field. Typically, the space-charge field is produced by a charge separation that results from the drift or diffusion of photogenerated charge

carriers. Since the photorefractive effect follows from the electrooptic properties of the material, the induced index change depends on the symmetry of the crystal (through the electrooptic tensor) and the orientation of the space-charge field relative to the crystallographic axes. The photorefractive index change, Δn, can be expressed by the following equation:

$$\Delta n = \frac{1}{2} n_b^3 r_{eo} E_{sc} . \qquad (1.1)$$

Here n_b is the background index of refraction and r_{eo} is the effective linear electrooptic coefficient. The quantity E_{sc} is the space-charge field, and is related through Poisson's equation,

$$\nabla \cdot E_{sc} = \frac{e}{\varepsilon_0 \varepsilon_r} \sum_i n_i(x) \qquad (1.2)$$

to the material dielectric constant, $\varepsilon_0 \varepsilon_r$ and the spatially varying densities of photogenerated charge carriers, $n(x)$.

The photorefractive effect was first attributed to charge migration, the generation of a space-charge field, and the material's linear electrooptic response, by Chen (1969). While Chen considered the drift of photogenerated electrons in the material's internal field, later theories for space-charge field formation built on this, considering drift and diffusion of carriers, the effect of the space-charge field on carrier transport (J. J Amodei, 1971) and the bulk photovoltaic effect (A. M. Glass et al., 1974). Kukhtarev later considered all of these processes, along with a sinusoidal illumination pattern and the

effects of applied electric fields, to produce the most comprehensive steady-state theory to date (1979).

Initially, the photorefractive effect was studied because it allows long-lived nonlinearities to be generated on micron (10^{-6} m) spatial scales, and is therefore useful for holographic data storage (Chen et al., 1968). Since that time, the photorefractive effect has been used to demonstrate a wide variety of applications, ranging from holographic interferometry, to real-time image processing, to phase locking of multiple lasers (J.P. Huignard and A. Marrakchi, 1981, J.O. White and A. Yariv, 1980, H. Rajbenbach et al., 1989, Y.H. Ja, 1985, and J. Feinberg and G.D. Bacher, 1982).

Photorefraction has been studied in three main material types: the ferroelectric cubic oxides, the sillenites, and the compound semiconductors. In order to review the work that has been done in studying photorefractive materials, we consider figures of merit that have been used to shed light on the suitability of these materials for device applications (G.C. Valley et al., 1988). These figures of merit also serve to illustrate the important properties of the compound semiconductors that we wish to study in the remainder of this thesis. Here it is important to note that, for device applications, a material is considered optimum when it allows a large space-charge field to be generated quickly and efficiently, and by virtue of a large linear electrooptic coefficient, produces a large change in the index of refraction. The four figures of merit that are considered are summarized in table 1.1 for each of the material types listed above.

Material	$\Delta n/E_{sc}$ $(n_b^3 r_{eo})$	Sensitivity $(n_b^3 r_{eo}/\varepsilon_r)$	Efficiency $(\mu\tau)$	Speed (μ)
Ferroelectrics				
$LiNbO_3$ (a)	320 [pm/V]	11 [pm/V]	$6.0x10^{-13}$ [cm^2/V]	0.8 [cm^2/V-s]
$KNbO_3$ (b)	690	14	$5x10^{-12} – 2x10^{-8}$	0.5
$BaTiO_3$ (c)	11300	5	$1x10^{-9} – 1x10^{-11}$	0.5
$LiTaO_3$ (d)	342	8	$2.6x10^{-12}$	–
Sillenites				
$Bi_{12}SiO_{20}$	82	1.8	$1.0x10^{-7}$	0.03
$Bi_{12}GeO_{20}$(e)	55.7	1.4	$1.98x10^{-6}$	0.09
Compound Semiconductors				
GaAs	43	3.3	$5.0x10^{-5}$	5000
InP	52	4.1	$1.5x10^{-5}$	1500
CdTe	126	12	$1.0x10^{-5}$	1000

(a) H. Kurz et al., 1977, considers r_{33}
(b) E. Kratzig and R. Orlowski, 1978 considers r_{33}
(c) P. Günther and F. Micheron, 1978 considers r_{51}
(d) E. Kratzig et al., 1980
(e) electron mobility and recombination data from G. Pauliat and G. Roosen, 1990, electrooptic coefficient and index of refraction from P. Yeh, 1993
Data for $Bi_{12}SiO_{20}$ are from P. Günther and J.P. Huignard, 1988
Data for the Compound Semiconductors are from A.M. Glass and J. Strait, 1988 and G.C. Valley et al., Opt. Lett., 1989

Table 1.1 – Comparison of figures of merit for the three commonly studied photorefractive material types. Data for the semiconductors assume a carrier recombination constant of 10ns.

The first figure of merit to consider is the photorefractive index change that can be generated per unit space charge field ($\Delta n/E_{sc}$). This quantity is determined from equation (1.1) and is, not surprisingly, proportional to the material's linear electrooptic coefficient ($n_b^3 r_{eo}$). As can be seen from the table, the photorefractive index change per space charge field is largest in Ferroelectric cubic oxide materials such as $BaTiO_3$, $LiNbO_3$ and $KnbO_3$. With the exception of $BaTiO_3$ and the compound semiconductor CdTe, the index change per unit space-charge field in these materials is roughly one order of magnitude larger than in the other material types. This is due mainly to the relatively large electrooptic coefficients of these materials. It is for this reason that the Ferroelectric cubic oxide materials have received the most attention in photorefractive studies. Unfortunately, though they have large electrooptic coefficients, these materials have important draw-backs.

The index change per space charge field takes into account only the electrooptic response of the material and consequently does not consider the relative ease or difficulty in generating a space-charge field. It is therefore important to discuss those figures of merit which consider this aspect of the photorefractive effect. The first of these, the photorefractive sensitivity, is defined as the index change that is generated by a unit charge density separated by a given distance. As can be seen from equations (1.1) and (1.2), this figure of merit is given by $n_b^3 r_{eo}/\varepsilon_r$ and considers both the material dielectric constant, and electrooptic response. From Table 1.1, it is immediately obvious that the photorefractive sensitivity is nearly constant for all the materials listed. This is due to the fact that, in these materials and on these time scales, the electrooptic response is tied to

the ionic polarizability, so that the same material properties that give rise to a large electrooptic response also give rise to a large permittivity constant (S. M. Silence et al., 1995). Thus, approximately the same index change can be generated in all of the material types for a given carrier density and charge separation. This illustrates an important point about the Ferroelectric materials: though these materials have a large electrooptic response, their high dielectric response limits the magnitude of the space-charge field that can be generated for a given carrier density and charge separation.

The nearly-constant photorefractive sensitivity of the ferroelectrics, sillenites and compound semiconductors has prompted the study of photorefractive effects in organic crystals (K. Sutter and P. Günter, 1990) and polymers (S. Ducharme et al., 1991), where the electrooptic response is not tied to the ionic polarizability (S. M. Silence et al., 1995). However, since photogeneration and charge transport in organic materials does not follow the model that has been developed for inorganic crystals, these materials can not be compared with the inorganic materials using the figures of merit shown in Table 1.1. Moreover, though organic crystals and polymers have shown promise as photorefractive materials, they have some important limitations. For example, these materials offer a slow response, and they are most easily generated in thin optical films, which leads to a small overall effect.

While the photorefractive sensitivity considers the dielectric and electrooptic responses, the photorefractive efficiency, which is the product of the carrier mobility, μ and lifetime, τ, considers the efficiency of the material in producing a space-charge field. That is, the photorefractive efficiency considers the charge separation that can be

generated on a per-carrier basis. This is one of the important aspects of the material that we wish to consider. When the $\mu\tau$ product is large, the photogenerated carriers travel a large distance before recombining and thus generate a large space-charge field.

As the table indicates, although large index changes can be generated in the ferroelectric materials, these materials typically have small mobility-lifetime products and thus are inefficient at producing a space-charge field. Because they offer improved efficiency, photorefractive effects have been extensively studied in sillenite materials such as $Bi_{12}SiO_{20}$. From the table, these materials can be seen to have mobility-lifetime products that are an order of magnitude larger than the most efficient ferroelectrics. It must be noted that in reviewing the literature on the sillenite materials, the reader will find these materials touted as "sensitive" photorefractive materials, which would appear to be in disagreement with the results summarized in Table 1.1 and described above. However, the sensitivity that is spoken of in the literature is the *photographic sensitivity*, which is related to the photorefractive efficiency (J. P. Huignard, et al., 1980). While the sillenites offer improved efficiency over the ferroelectrics, these materials have some important draw-backs. For example, while these materials are optically-active, they have low carrier mobilities and are therefore slow in producing a space charge field.

Table 1.1 shows that the optimum materials for speed and sensitivity are the compound semiconductors. As shown in the table, GaAs, as well as CdTe and InP have carrier mobilities on the order of 10^3 $cm^2/V\text{-}s$, allowing space-charge field formation to occur quickly (on picosecond or faster time scales (A.M. Glass et al., 1988 and A.L. Smirl et al., 1988)). In addition, high quality semiconducting materials can have carrier

lifetimes as long as 10ns. This, with the high mobilities shown in Table 1.1 make their efficiencies roughly two orders of magnitude larger than those of the sillenite materials.

Photorefraction was first studied in semiconductors by Glass et al. (1984). Using a CW laser operating in the near infrared wavelength range, these authors showed that GaAs:Cr and InP:Fe offered a greater "speed" and efficiency than the more widely studied Ferroelectric materials. Later, experiments with CW laser beams in semi-insulating GaAs (M. B. Klein, 1984) and CdTe:V (R.B. Blysma et al., 1987) produced similar conclusions. However, while these experiments showed that semiconductors have increased "speed" and efficiency over the other material types, they failed to detail the fundamental dynamics of space-charge field formation in these materials. This is because the photorefractive "speed" that is observed in experiments with CW and nanosecond pulsed laser beams is the time for the photorefractive nonlinearity to rise to steady-state. This is not the fundamental formation time of the space-charge field, which is the time required for a single charge carrier to reach its equilibrium separation in the absence of recombination.

In addition to the studies described above, "photorefractive" effects have also been studied at excitation energies slightly lower than the bandgap energy in bulk semiconducting materials (A. Partovi et al., 1990), as well as in semiconductor quantum well structures (A. M. Glass, et al., 1990). These studies relied on an applied electric field, as well as the transport of photogenerated charge carriers to produce a space-charge field. However, these studies are not summarized in table 1.1 because they rely on the Franz-Keldysh (V. W. Franz, 1958, L.V. Keldysh, 1958) and Quantum Confined Stark

effects (D.A.B. Miller et al., 1985), instead of the linear electrooptic effect. The Franz-Keldysh and Quantum Confined Stark effects are quadratic in the electric field strength, and are field-induced changes in the absorption and refraction near the band edge.

In an effort to understand the fundamental speed and efficiency limitations of semiconducting materials, as well as the fundamental mechanisms responsible for the formation of the photorefractive nonlinearity, a collaborative research effort between the University of Iowa and Hughes Research Laboratories was established. The objective of this research effort has been to use ultrashort optical pulses to temporally resolve the formation and decay of the photorefractive nonlinearity, and to investigate carrier dynamics and space-charge field formation on small spatial dimensions. This work began in 1986, with the first demonstration of a picosecond photorefractive effect in semiconductors (G.C. Valley, et al., 1986). Using GaAs, this group showed that photorefractive beam coupling could be observed with 43ps duration pulses at a wavelength of 1.06μm. Since that time, this research has identified new sources for the photorefractive nonlinearity in GaAs and demonstrated the complexity of measuring photorefractive effects on picosecond time scales (A.L. Smirl et al., 1988 and G.C. Valley and A.L. Smirl, 1988). Furthermore, as part of this effort, picosecond photorefractive effects have been demonstrated in CdTe:V and InP:Fe (G.C. Valley, et al., 1989) and used to demonstrate fast, sensitive switching in GaAs (A.L. Smirl et al., 1989). However, these initial studies had notable limitations. Most importantly, the measurement techniques that were employed throughout their work did not allow the photorefractive nonlinearity to be time-resolved.

1.3 Organization

In this dissertation, a transient-grating measurement technique will be presented that allows the free-carrier and photorefractive nonlinearities in GaAs and CdTe to be separated and time-resolved for the first time. This technique was conceived and developed by Prof. A.L. Smirl and Dr. W.A. Schroeder (W.A. Schroeder et al., 1991, A.L. Smirl et al., 1990). The use of this measurement technique allows the Dember contribution to the photorefractive response to be unambiguously observed for the first time. The Dember space-charge field is only observable on picosecond time scales, and is responsible for producing ambipolar diffusion of electrons and holes. In addition, the data presented in this thesis show for the first time an ultrafast contribution to the photorefractive response in both materials that is an order of magnitude larger than the photorefractive response on picosecond (10^{-12} s) time scales. This contribution is postulated to arise from the diffusion of "hot carriers", which are free carriers whose characteristic temperature is larger than that of the lattice.

As part of this dissertation we present a numerical model that describes the picosecond dynamics of the free carrier populations and space-charge fields in these materials. Whereas other models of the photorefractive process consider as initial conditions a weakly modulated optical intensity pattern, our model is unique in that it considers the picosecond evolution of the carriers and field resulting from a strongly modulated optical intensity pattern. In producing predictions that are in excellent agreement with the experimental results for a wide range of conditions, our model and the experimental results together illustrate some interesting effects that are characteristic

of the photorefractive nonlinearity. Moreover, in providing simultaneous pictures of the evolution of the free carrier populations (through the free-carrier nonlinearity) and space-charge fields (through the photorefractive nonlinearities), our experimental and numerical results provide a comprehensive picture of the picosecond carrier transport processes in these materials.

This dissertation contains a total of nine chapters. Chapter II considers carrier generation, recombination and the related optical nonlinearities in GaAs and CdTe for our experimental conditions. Chapter III considers carrier transport, space-charge field formation and the photorefractive nonlinearities in these materials. The use of picosecond optical pulses introduces some important differences between our experiments and the more traditional experiments conducted with CW laser beams, and we point out these differences in Chapters II and III where they are relevant. In order to review the "traditional" method for measuring picosecond photorefractive effects in semiconductors, but also to introduce the reader to the complexities involved in making measurements of this type, we discuss two-beam coupling and transient-energy transfer in Chapter IV. The most important result of Chapter IV is that the goals of this thesis can not be met with the two-beam coupling measurement technique. The measurement method that is used in these experiments, the Photorefractive Polarization-Rotation Transient-Grating (PPRTG) measurement technique, is discussed in Chapter V. This is followed in Chapter VI by a discussion of our numerical modeling method. Chapters VII and VIII present the experimental results obtained for undoped CdTe and semi-insulating GaAs. Finally, the important conclusions of this thesis are summarized in Chapter IX.

This thesis also contains three appendices. In Appendix A, we discuss photorefractive polarization rotation in our undoped CdTe crystal. In Appendix B, we give a source listing of the computer codes that are used in modeling our experimental results. In Appendix C, we derive the equations that are used in Chapter III, which describe the carrier and field dynamics in the low modulation limit.

CHAPTER II

OPTICAL CARRIER GENERATION, RECOMBINATION AND ASSOCIATED NONLINEAR ABSORPTION AND REFRACTION IN GaAs AND CdTe AT WAVELENGTHS NEAR 1.0μm

2.1 Introduction

In Chapter I we described the photorefractive effect and noted that the initial step in generating this optical nonlinearity is the photogeneration of free carriers. It is therefore fitting, as we investigate picosecond photorefractive effects in semi-insulating GaAs and undoped CdTe, to begin by discussing optical carrier generation in these materials. We begin by considering optical carrier generation and carrier recombination in semi-insulating GaAs, and then extend the discussion to consider these processes in undoped CdTe. As we will see along the way, excitation with our 1ps duration 960nm optical pulses results in a variety of absorptive and refractive optical nonlinearities, apart from the photorefractive effect. In later parts of this thesis, we will show that the measurement of picosecond photorefractive effects is complicated by the presence of these and other competing optical nonlinearities. Unless otherwise stated, throughout this and the other chapters, the GaAs and undoped CdTe crystals should be assumed to be at

room temperature.

2.2 Semi-insulating Gallium Arsenide (GaAs)

2.2.1 Single-Photon Transitions at 960nm

Light absorption in semi-insulating GaAs, and the subsequent generation of free carriers, is dictated by the material band structure, which is shown in figure 2.1 for values of k near 0 (J.S. Blakemore, 1982). Included in the figure are the light hole (*LH*), heavy-hole (*HH*) and split-off (*SO*) valence bands, and the G, *L* and *X* conduction band valleys.

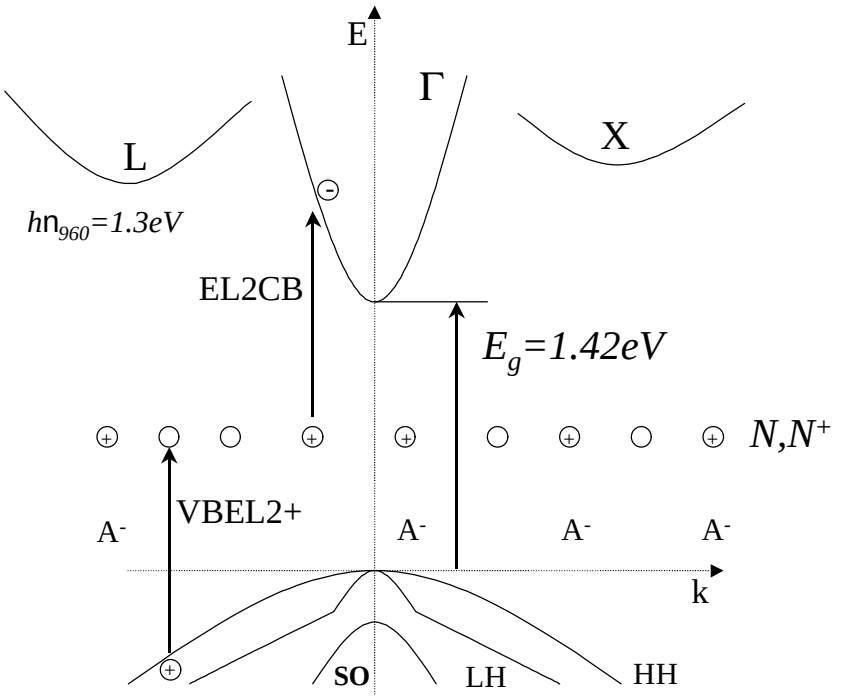

Figure 2.1 – Schematic diagram of the band structure of semi-insulating GaAs near k=0 illustrating the EL2 light absorption and carrier generation processes. Included in the figure are negatively-charged acceptors (A^-), the Γ, L and X conduction band valleys and the heavy-hole (HH), light hole (LH) and split off (SO) valence bands. Transitions between the split-off and light-hole valence bands and ionized EL2 are possible, although not shown for clarity of presentation.

It is clear from this figure that semi-insulating GaAs is a direct-gap semiconductor; that is, both the valence band maximum and the conduction band minimum are at k=0. Since the valence-to-conduction band energy difference of 1.42eV is greater than the 1.3eV photon energy of the 960nm radiation, single-photon band-to-band transitions are not allowed in these experiments.

However, semi-insulating GaAs also possesses EL2 antisite defects (G. M. Martin and S. Makram-Ebeid, 1986). Shown in figure 2.1, these species act as donors, and are present in both neutral and ionized form (A. Mircea et al., 1976). Since the EL2 defect centers are optically active and have been shown to lie 0.8eV below the conduction band edge, single photon transitions between the valence band and ionized EL2, and between the neutral EL2 and conduction band are energetically possible with the 960nm radiation used in these experiments.

Also shown in figure 2.1, the material also contains a population density of negatively charged acceptors (A^-). The “dark” (before illumination) density of ionized EL2 is exactly equal to the density of acceptors, so that the material is semi-insulating. Since the photon energy of the 960nm radiation is not sufficient to cause transitions from the negatively charged acceptors to the conduction band, optically-induced transitions involving these species will not be considered in this thesis.

The transitions from the neutral EL2 to the conduction band (EL2CB), and from the valence band to the ionized EL2 (VBEL2+) are shown in figure 2.1. In the EL2CB transition, electrons are promoted to the conduction band by photoionization of the neutral EL2. In the VBEL2+ transition, electrons are excited from the valence band to

neutralize the ionized EL2, a process that produces free holes in the valence band. The change in the electron, hole and ionized EL2 populations due to these processes is expressed by the following set of rate equations:

$$\frac{\partial n}{\partial t} = \frac{\sigma_e \left(N - N^+\right) I}{h\nu} \ , \qquad (2.1)$$

$$\frac{\partial p}{\partial t} = \frac{\sigma_h N^+ I}{h\nu} \ , \qquad (2.2)$$

and

$$\frac{\partial N^+}{\partial t} = \frac{\sigma_e (N - N^+) I}{h\nu} - \frac{\sigma_h N^+ I}{h\nu} . \qquad (2.3)$$

where I is the intensity of the incident radiation, hν is the excitation photon energy, N, N^+ and (N-N^+) are the total, ionized and neutral EL2 densities, and σ_e and σ_h are the wavelength-dependent EL2CB and VBEL2+ transition cross-sections. (Note: in this thesis, indirect transitions involving the neutral EL2 and X and L conduction band valleys will not be considered. This is because these transitions are indirect and, therefore less probable than transitions involving the Γ conduction band valley.)

Absorption at the EL2 sites also attenuates the incident light. The depletion of the incident beam intensity due to the processes discussed above can be described by the phenomenological beam propagation equation:

$$\frac{dI}{dz} = -\sigma_e (N - N^+) I - \sigma_h N^+ I \ . \qquad (2.4)$$

At low beam intensities, where photoexcitation does not change the ionized EL2 density from its dark value (N^+_o), an effective EL2 linear absorption coefficient,

$$\alpha_{eff} = \sigma_e (N - N_0^+) + \sigma_h N_0^+, \qquad (2.5)$$

can be defined.

EL2 absorption has been well characterized in the crystal used in our experiments. The dark concentration of ionized EL2 (N^+_o) has been measured by conductivity as a function of temperature to be 1.4×10^{15} cm^{-3} (M. B. Klein, 1984). In addition, CW photorefractive measurements have been used to determine the effective trap density in our crystal (M. B. Klein, 1984), which together with the dark density of ionized EL2, implies a dark density of 1.2×10^{16} cm^{-3} neutral EL2 (N-N^+_o) (G.C. Valley et al., 1989). The ratio of the VBEL2+ and EL2CB cross-sections (σ_h/σ_e) has been determined by differential transmission to be 0.76 at a wavelength of 1.06 μm (G.C. Valley et al., 1989).

The value of the EL2CB and VBEL2+ cross sections are determined by measuring the small signal absorption for our crystal, and then using the values given above for N-N^+_o, N^+_o, and σ_h/σ_e to evaluate equation (2.5). At a wavelength of 1.06μm, Valley et al. (1989) inferred a value of 1.0×10^{-16}cm^2 for the EL2CB cross section for our crystal. However, since we expect the value of this cross section to be somewhat larger for photon energies approaching the GaAs bandgap energy, it is necessary to independently measure this constant for the wavelength used in our experiments (960nm). In our crystal, we measure a small signal linear absorption coefficient of 2.2cm^{-1}. Assuming that the values given above for N-N^+_o, N^+_o, are correct, and that the value for σ_h/σ_e does not change with the increase in photon energy, we find an EL2CB cross section of 1.7×10^{-16}cm^2 for our crystal (and a VBEL2+ cross section of 1.3×10^{-16}cm^2). In Chapter VII, where we discuss

our results for semi-insulating GaAs, we will see that a knowledge of this constant is critical in accurately predicting the diffraction efficiency that is produced by the excess electron-ionized EL2 photorefractive nonlinearity.

2.2.2 Carrier Dephasing, Thermalization and Cooling

The results of Chapter III show that the photorefractive response that we observe in our experiments is dictated primarily by the mobilities of the photogenerated free carrier distributions. The carrier mobilities that are observe are average quantities over the free carrier distributions, which quantify the friction that the carriers experience during transport as a result of carrier scattering processes. As a result, the carrier mobilities (and the observed photorefractive response) are influenced by many factors, including the form of the carrier distributions and the characteristic temperature of the distributions. As we will see below, photogenerated free carriers can not initially be described by a Maxwell-Boltzmann or Fermi-Dirac distribution at the lattice temperature. Since we seek to understand the picosecond photorefractive response of semi-insulating GaAs and undoped CdTe, we must understand the carrier relaxation processes that are important for our experimental conditions, and compare the time scales for these processes with those of our experiments.

In general, a population of photogenerated free carriers is not initially in equilibrium with itself, or with the lattice. Instead, the carriers are initially localized in momentum space, having a fixed phase relationship among themselves and with the optical field that created them. Furthermore, the set of conduction and valence band states that

the carriers initially occupy is not initially dictated by a Maxwell-Boltzmann or Fermi-Dirac distribution, but by the material band structure and the frequency spectrum of the optical field. In addition, when the incident photon energy is larger than the transition energy, the free carriers are produced with excess energy. The free carriers relax, or come to equilibrium among themselves and with the lattice, via carrier scattering process. In the following paragraphs we describe carrier relaxation for our experimental conditions in terms of three simultaneous macroscopic processes. First we consider carrier depahsing and carrier thermalization, which are the processes by which the carrier momenta and energy are randomized (J. Shah, 1996). Finally, we consider carrier cooling, which is the process by which the carriers dissipate their excess energy to the lattice (J. Shah, 1996).

In our experiments, we propagate intense (~2.5 GW/cm^2) picosecond duration optical pulses through thick (~1-3 mm) GaAs and CdTe crystals. As we will see in section 2.2.6, intensity dependent nonlinear absorption limits the optical intensities that are transmitted through our crystals. As a result, averaged over the length of each crystal, we produce low to moderate carrier densities ($1x10^{14}$ cm^{-3} – $1x10^{16}$ cm^{-3}) at the center of our optical pulses. Carrier dephasing has been studied in GaAs at room temperature using photon echo measurements, and time-resolved pump probe spectroscopy (P.C. Becker et al.,1988, M.T. Portella et al., 1992). Both studies showed that, at the highest carrier densities generated in our experiments, carrier dephasing can be assumed to occur in times less than 100fs. While carrier dephasing has not been directly studied at the lowest carrier densities generated in our experiments, the work of P.C. Becker et al. suggests that, for low carrier densities, the carrier dephasing time is constant and is the LO phonon emission

time. This follows from the fact that, while carrier-carrier scattering is the dominant scattering process at high carrier densities, the dominant carrier scattering process at low carrier densities (in room temperature semi-insulating GaAs) is carrier-LO phonon scattering (F. Rossi et al., 1994, P.C. Becker et al., 1988, M.T. Portella et al., 1992). Since the LO phonon emission time is ~165fs (J.A. Kash, 1985), carrier dephasing can be assumed to occur instantaneously for our experimental conditions, so that the free carrier distributions can be considered isotropic in momentum space.

While carrier thermalization has been studied extensively in GaAs, nearly all of the studies that have been performed have been at high carrier densities ($1x10^{17}cm^{-3}$ – $1x10^{18}cm^{-3}$). For photogenerated carrier densities greater than or equal to $1x10^{16}cm^{-3}$, experimental results have shown that carrier-carrier scattering produces a thermal distribution of free carriers in times of less than 100fs (T. Elsaesser et al., 1991). Thus, for the highest carrier densities generated in our experiments, we can assume that the carriers thermalize instantaneously. Though carrier thermalization has not been studied at the lowest carrier densities that are generated in our experiments ($1x10^{14}cm^{-3}$), we can estimate the corresponding carrier thermalization time using a knowledge of the carrier scattering process that are dominant for our experimental conditions. As we noted above, for low carrier densities, carrier-LO phonon scattering is the dominant carrier scattering mechanism for our experimental conditions. For semi-insulating GaAs, the LO phonon emission time is roughly 165fs. If we assume that the energy and momenta of the free carriers are randomized after ~10 LO phonon collisions, this leads to a carrier thermalization time of roughly ~1.7ps. This time is consistent with the results of Monte

Carlo simulations of the carrier scattering processes in GaAs that have been reported in the literature (F. Rossi et al., 1994). Thus, at the lowest carrier densities that are generated in our experiments, carrier thermalization can not be considered instantaneous with respect to our 1ps pulses.

For our experimental conditions, the primary means of carrier cooling is polar optical phonon scattering (C. V. Shank, et al., 1979 and K. Seeger, 1985). Here the free carriers lose energy to the lattice by inducing LO lattice vibrations via the Fröhlich interaction. Under these circumstances, we can estimate the carrier cooling time (t_{ce}) using the simple relationship:

$$t_{ce} \approx N_{LO} t_{LO},$$

which states that the carrier cooling time is approximately equal to the product of the number of LO phonons which must be emitted to cool each carrier (N_{LO}), and the LO phonon emission time (t_{LO}). The GaAs LO phonon energy is ~35meV (J. A. Kash, 1985), and the LO phonon emission time has been measured at 165fs. Since free electrons are generated in these experiments by EL2 single-photon absorption with excess energies of ~0.5eV, and by two-photon absorption (to be discussed in sub-section 2.2.6) with excess energies of ~1.0eV, between 14 and 28 LO phonons must be emitted to cool the electrons. Using the equation given above, this implies carrier cooling times of 2ps - 5ps. Therefore, like carrier thermalization, carrier cooling can not be considered instantaneous with respect to our 1ps duration optical pulses.

In this thesis, the experimental results are compared with the results of a (relatively) simple carrier transport model in which the carriers are assumed to thermalize and cool instantaneously (see Chapter III). While the assumption of instantaneous carrier cooling and thermalization on 5ps time scales is not completely valid for our experimental conditions, it allows the experimental results to be compared with our model at times where carrier thermalization and cooling are complete. While the agreement between our model and the experimental results are good for times greater than ~10ps, the photorefractive experimental results for both materials show an enhancement to the space-charge field that is in poor agreement with the results of our model. In Chapter VI, where the CdTe experimental results are discussed, this transient feature is shown to be consistent with diffraction from a hot carrier photorefractive grating. This result is consistent with non-instantaneous carrier cooling on 1ps – 5ps time scales.

2.2.3 Carrier Recombination

Whereas optical carrier generation results in populations of free carriers, carrier recombination destroys the free electron and hole populations, restoring the neutral and ionized EL2 densities to their dark (before illumination) values. In this sub-section we discuss the dominant carrier recombination processes in semi-insulating GaAs for our experimental conditions. Since carrier recombination has been studied extensively in semi-insulating GaAs, the important carrier recombination constants have been measured and are readily available in the literature. In this section we use these constants, along with

our experimental conditions, to estimate the carrier recombination time for our experiments, and compare the carrier generation and recombination rates.

The three main carrier recombination processes prevalent in GaAs for our experimental conditions are shown in figure 2.2. In the first of these processes (I), free electrons recombine with free holes. Called electron-hole bimolecular recombination, this process destroys both the free electron and hole populations. The free electron population can also be destroyed through bimolecular recombination with ionized EL2 (II). As a result of this process, the ionized EL2 are neutralized. Finally, bimolecular recombination involving the free holes and neutral EL2 is also possible (III). This process destroys the free hole population and ionizes the neutral EL2. With recombination due to these three processes taken into account, the electron, hole and ionized EL2 rate equations (equations (2.1), (2.2) and (2.3)) become:

$$\frac{\partial n}{\partial t} = \frac{\sigma_e \left(N - N^+\right) I}{h\nu} - \gamma_{eh} np - \gamma_{et} nN^+ \ , \qquad (2.6)$$

$$\frac{\partial p}{\partial t} = \frac{\sigma_h N^+ I}{h\nu} - \gamma_{eh} np - \gamma_{hd} p(N - N^+) \ , \qquad (2.7)$$

and

$$\frac{\partial N^+}{\partial t} = \frac{\sigma_e (N - N^+) I}{h\nu} - \frac{\sigma_h N^+ I}{h\nu} - \gamma_{et} nN^+ + \gamma_{hd} p(N - N^+). \qquad (2.8)$$

In the above equations, γ_{eh}, γ_{et} and γ_{hd} are electron-hole, electron-ionized EL2 and hole-neutral EL2 recombination coefficients, respectively.

Since carrier recombination has been studied extensively in semi-insulating GaAs, the important constants are easily obtained from the literature. Von

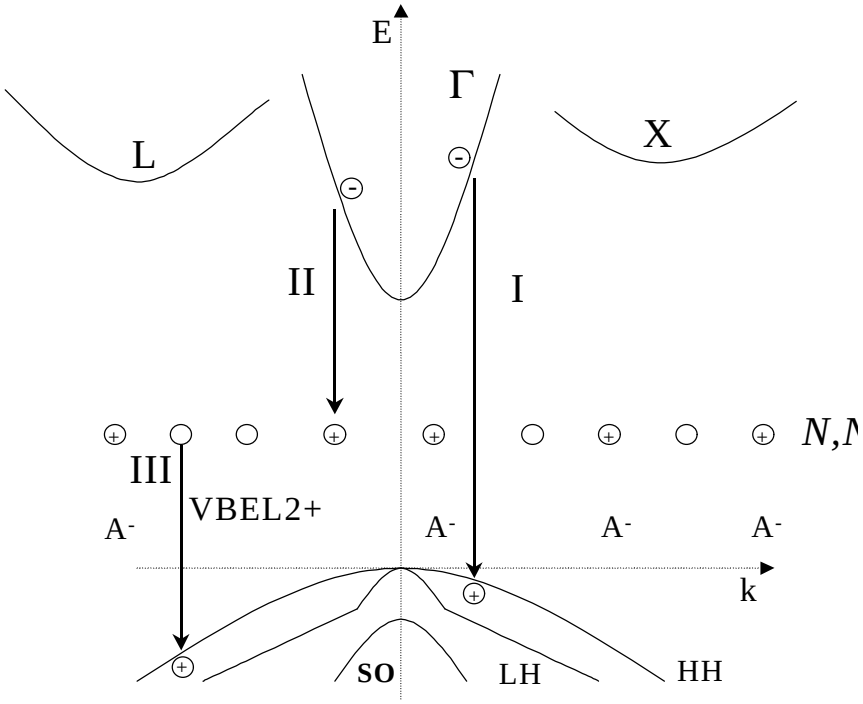

Figure 2.2 – Schematic diagram of the band structure of semi-insulating GaAs near k=0 illustrating the prevalent carrier recombination processes for our experimental conditions. As discussed in the text, these processes are electron-hole recombination (I), electron-ionized EL2 recombination (II) and hole-neutral EL2 recombination (III).

Lehmen and Ballantyne reported a value of $2x10^{-10}cm^3/s$ for the electron-hole bimolecular recombination coefficient (g_{eh}). The electron-ionized EL2 and hole-neutral EL2 recombination coefficients (g_{et} and g_{nd}) must be calculated from the respective recombination cross-sections of $4.3x10^{-16}cm^2$ and $2x10^{-18}cm^2$ reported by G. M Martin and S. Makram-Ebeid (1986). The electron-ionized EL2 and hole-neutral EL2 recombination coefficients are given by the product of the respective carrier thermal velocities ($(3kBT/m)^{½}$) and the recombination cross-sections. Using the lattice temperature and the carrier effective masses, we obtain electron and hole thermal

velocities of 4.4×10^7cm/s and 1.7×10^7cm/s, and electron-ionized EL2 (γ_{et}) and hole-neutral EL2 (g_{nd}) recombination coefficients of 2×10^{-8}cm^3/s and 3.5×10^{-11}cm^3/s, respectively.

To determine the dominant electron recombination process for our experimental conditions, we compare recombination processes I and II from figure 2.2 using our experimental conditions and the constants reported in the previous paragraph. As we have stated, in our experiments we generate average hole densities between 1×10^{14}cm^{-3} and 1×10^{16}cm^{-3} at the center of the optical beams. With the electron-hole bimolecular recombination constant (g_{eh}) of 2×10^{-10} cm^3/s, these densities yield a maximum recombination rate of 2×10^6s^{-1}. The maximum ionized EL2 density that can be generated is the "saturation" concentration of ~7×10^{15}cm^{-3} (EL2 absorption saturation will be discussed in the following sub-section). With the electron-ionized EL2 recombination constant (g_{et}) of 2×10^{-8}cm^{-3}/s, this density yields a maximum electron-ionized EL2 recombination rate of 1.5×10^8s^{-1}. Thus, in our experiments, electron-ionized EL2 recombination is the dominant electron recombination process. (Note: the discrepancy in the electron-hole and electron-ionized EL2 recombination rates is even larger when the material is excited with CW laser beams, and this allows electron-hole recombination to be ignored relative to electron-ionized EL2 recombination when considering steady-state excitation of the EL2.) Together, the maximum recombination rates given above imply a minimum electron recombination time of ~7ns.

To determine the dominant hole recombination process for our experimental conditions, we compare recombination processes I and III from figure 2.2 in the same way that we compared the electron recombination processes. Since the average electron

densities generated in our experiments are the same as the average hole densities ($1x10^{14}cm^{-3}$ and $1x10^{16}cm^{-3}$), electron-hole bimolecular recombination destroys the free hole population at the same maximum rate as it destroys the electron population ($2x10^{6}s^{-1}$). In order to correctly compare hole-neutral EL2 recombination with the other carrier recombination processes, we must calculate the hole-neutral EL2 recombination rates for the minimum and maximum optical fluences used in our experiments. We perform this calculation at low fluences because that is where hole-neutral EL2 recombination is maximum, while we perform this calculation at high fluences in order to facilitate comparison with the electron-hole recombination constant and the electron-ionized EL2 constant. At low excitation fluences, where the hole population is at its minimum value, the neutral EL2 density is at its maximum value of $1.2x10^{16}cm^{-3}$. With the hole-neutral EL2 recombination constant (g_{nd}) of $3.5x10^{-11}cm^{3}/s$, this density yields a maximum hole-neutral EL2 recombination rate of $5x10^{5}s^{-1}$. At high fluences, where the ionized EL2 density is at the saturated value (see section 2.2.4) of $6.8x10^{15}cm^{-3}$, the neutral EL2 density is at its minimum value of $6.6x10^{15}cm^{-3}$. This with the hole-neutral EL2 recombination constant give a minimum hole recombination rate of $2.5x10^{5}s^{-1}$. Comparison of these constants with the electron recombination constant given above shows that electron-hole recombination is the dominant hole recombination process at high fluences, while hole-neutral EL2 recombination is the dominant hole recombination process at low fluences. (This discrepancy is even larger when the material is excited with CW beams, so that electron-hole recombination can be ignored relative to hole-neutral EL2

recombination when considering steady-state excitation of the EL2.) Along with this, the minimum hole recombination time is 0.45μs at high fluences, and 4.5μs at low fluences.

The electron and hole populations can also be destroyed by Auger recombination. Under these circumstances, the electron and hole recombination rates are proportional to the square of the carrier density. Nather and Quagliano (1985) measured an Auger recombination constant of $1x10^{-27}cm^6/s$ in GaAs. With the range of electron and hole densities given above, this constant gives minimum and maximum Auger recombination rates of $10s^{-1}$ and $1x10^5s^{-1}$. Since the Auger recombination rate is negligible compared to the other recombination rates at all but the largest carrier densities, this process has been ignored in the description given above.

We can use the results of the above analyses to compare the carrier generation and recombination rates for our experiments. As we stated above, we generate free carrier densities between ($1x10^{14}cm^{-3}$–$1x10^{16}cm^{-3}$) in our experiments with 1.0ps duration FWHM optical pulses. When we assume that the electron density decays exponentially with the minimum recombination time of 7ns estimated above, approximately 33ns is required to reduce the electron density from $1x10^{16}cm^{-3}$ to $1x10^{14}cm^{-3}$. Thus, in our experiments, the carrier generation rates greatly exceed the carrier recombination rates.

The large discrepancy between the carrier generation and recombination rates is a fundamental difference between the experiments described in this thesis, and experiments conducted with CW laser beams. As we will see in the following sections, this discrepancy produces some important results. First, picosecond photoexcitation of our semi-insulating GaAs crystal leads to saturation of the EL2 single-photon absorption.

Second, photoexcitation leads to carrier accumulation and the free carrier refractive nonlinearity that is discussed in section 2.2.5. Separating the photorefractive nonlinearity from these and other competing optical nonlinearities poses the greatest experimental challenge in measuring picosecond photorefractive effects.

The above analyses lead to another important result: that carrier recombination can be neglected in modeling carrier transport and space-charge field formation. This can be seen by noting that the maximum field formation time in semi-insulating GaAs is 5ps for our 1.7μm grating period. Assuming the same 7ns minimum carrier recombination constant, the free electron population decays by only 0.1% during this time. As we will see in Chapter III, this reflects an important difference between picosecond photorefractive effects and CW photorefractive effects. Whereas recombination is necessary in generating the photorefractive nonlinearity that is measured with CW laser beams, it is not required to generate the picosecond photorefractive nonlinearities that are generated in these experiments.

2.2.4 Contrast: EL2 Related Light Absorption and Carrier Generation Under Steady-State and Transient Excitation Conditions

The use of picosecond optical pulses introduces some important differences between the experiments described in this thesis, and the more traditional photorefractive experiments, which are conducted with CW laser beams. Therefore, while we wish to acquaint the reader with the carrier generation processes that occur for our experimental conditions, we take the opportunity to compare and contrast these processes with those

that occur in experiments conducted with CW laser beams. In this section, we contrast EL2 absorption under steady-state (excitation with CW laser beams) and transient (excitation with picosecond optical pulses) excitation conditions. Since many of the differences between the steady-state and transient space-charge fields arise from the differences between CW and short-pulsed excitation, this discussion provides important background information for comparisons/contrasts that are made between them in Chapter III.

When CW and long pulsed laser beams are present, photoexcitation occurs over a period that is much longer than the carrier recombination time. Under these circumstances, the ionized EL2 and free electron and hole densities that are produced reflect an equilibrium that is established between the carrier generation and recombination processes. For these conditions, equations (2.6) and (2.7) can be used to obtain simple equations for the steady-state electron and hole densities:

$$n_{ss} = \frac{\sigma_e (N - N_{ss}^+) I}{h\nu g_{et} N_{ss}^+} \qquad (2.9)$$

and

$$p_{ss} = \frac{\sigma_h N_{ss}^+ I}{h\nu g_{hd} (N - N_{ss}^+)}. \qquad (2.10)$$

Here we have postulated that the free electron and hole densities are much smaller than the ionized EL2 density, so that electron-hole bimolecular recombination is negligible in equations (2.6) and (2.7).

In order to evaluate equations (2.9) and (2.10), we must know the steady-state ionized EL2 density (N^{+}_{ss}). The steady-state ionized EL2 density can not be determined in the same way that the steady-state electron and hole densities were determined, because equation (2.8) only combines the information in equations (2.6) and (2.7). Instead, we must use the condition of charge neutrality, along with the steady-state electron and hole densities to determine the steady-state ionized EL2 density. This procedure produces a cubic equation in N^{+}_{ss}:

$$N_{ss}^{+3}+\left[\frac{I}{h\nu}\left(\frac{\sigma_e}{\gamma_{et}}-\frac{\sigma_h}{\gamma_{hd}}\right)-N-A^{-}\right]N_{ss}^{+2}+\left[NA^{-}-\frac{2\sigma_e IN}{\gamma_{et}h\nu}\right]N_{ss}^{+}+\frac{\sigma_e IN^2}{\gamma_{et}h\nu}=0\,. \qquad (2.11)$$

When factored, the above equation yields expressions for the steady-state ionized EL2 density that are neither compact nor intuitive. However, if we estimate the magnitude of the different terms in equation (2.11), we can simplify the equation while making an important point about exciting our crystal with CW laser beams. Using the constants reported in the previous discussions, equation (2.11) becomes:

$$N_{ss}^{+3}-\left[I(9.9x10^{12})+1.3x10^{16}\right]N_{ss}^{+2}+\left[1.9x10^{31}-I(6.4x10^{26})\right]N_{ss}^{+}+4.3x10^{42}=0\,, \qquad (2.12)$$

where we have neglected the units so that the equation can be more easily displayed. For the range of beam intensities normally employed in CW photorefractive experiments (5 mW/cm^2 – 1 W/cm^2), the terms in equation (2.12) involving the beam intensity are much smaller than the terms involving the EL2 and acceptor densities. Thus, for typical CW excitation conditions, the ionized EL2 density should not be expected to change from its dark value. Neglecting the terms involving the beam intensity, equation (2.11) becomes:

$$N_{ss}^{+3} - \left[N + A^{-}\right]N_{ss}^{+2} + \left[NA^{-}\right]N_{ss}^{+} \approx 0. \quad (2.11)$$

This equation can be easily factored, yielding roots equal to 0, the total EL2 density (N) and the acceptor density (A^-). Of these roots, the acceptor density is the one with physical significance, since the acceptor density is equal to the dark density of ionized EL2 (N^+_o). Thus, for typical CW excitation conditions, the ionized EL2 departs little from the dark value of $1.4\text{x}10^{15}$ cm^{-3}. Under these circumstances the maximum electron and hole densities, which are respectively $2.1\text{x}10^{11}$ cm^{-3} and $1.2\text{x}10^{12}$ cm^{-3}, are much smaller than the neutral and ionized EL2 densities.

By contrast, when the material is excited with picosecond duration optical pulses, the photoexcitation rates are much larger than the carrier recombination rates, so that there is never a steady-state established between these processes. To determine the ionized EL2 and carrier densities for transient photoexcitation, we solve equations (2.6) – (2.8) while neglecting the carrier recombination terms. When the dark densities of electrons and holes are assumed to be zero, and the dark densities of neutral and ionized EL2 are assumed to be (N-A^-) and A^-, this procedure produces the following set of equations:

$$N^{+} = N_{sat}^{+} - (N_{sat}^{+} - A^{-})e^{-\frac{F}{F_{sat}}}, \quad (2.12)$$

$$n = \frac{\sigma_e}{h\nu}\left[\left(N - N_{sat}^{+}\right)F + F_{sat}\left(N_{sat}^{+} - A^{-}\right)\left(1 - e^{-\frac{F}{F_{sat}}}\right)\right], \quad (2.13)$$

and

$$p = \frac{\sigma_p}{h\nu}\left[N_{sat}^{+} F - F_{sat}\left(N_{sat}^{+} - A^{-}\right)\left(1 - e^{-\frac{F}{F_{sat}}}\right)\right]. \qquad (2.14)$$

In these equations, F is the incident pulse fluence,

$$F = \int_{-\infty}^{+\infty} I(t)dt\,, \qquad (2.15)$$

F_{sat} is the EL2 saturation fluence,

$$F_{sat} = \frac{h\nu}{\sigma_e + \sigma_h}, \qquad (2.16)$$

and N^{+}_{sat},

$$N_{sat}^{+} = \frac{\sigma_e N}{\sigma_e + \sigma_h}. \qquad (2.18)$$

is the saturation density of ionized EL2.

The above equations describe the following set of circumstances. The electron generation rates are initially larger than the hole generation rates, owing to the fact that the EL2CB cross section is larger than the VBEL2+ cross section, and the dark density of neutral EL2 is larger than the dark density of ionized EL2. However, since the electron generation rate is initially larger than the hole generation rate, the density of ionized EL2 is increased significantly, while the density of neutral EL2 is decreased significantly. The change in the neutral and ionized EL2 densities is accompanied by an increase in the hole generation rate, and a decrease in the electron generation rate. In fact, as the pulse fluence is increased, the ionized EL2 density is driven to a saturation value (N^{+}_{sat}) at which the electron and hole generation rates are equal. After the saturation density of ionized EL2 is

reached, photoexcitation can not change the density of ionized EL2, but instead results in the generation of electron-hole pairs in a step-wise two-photon absorption process in which the EL2 are the intermediary. This is in contrast to instantaneous two-photon absorption, where the excitation occurs instantaneously without the aid of the EL2 (discussed in sub-section 2.2.6).

Evaluation of equations (2.12)-(2.17) for our experimental conditions allows us to determine the importance of EL2 absorption saturation for our experimental conditions. From the values given previously for the photon energy and EL2 electron and hole cross-sections, the EL2 saturation fluence is approximately 0.7mJ/cm^2. Since fluences ranging from 50μJ/cm^2 to 2.5mJ/cm^2 are used in these experiments, we expect EL2 absorption saturation and EL2 step-wise two photon absorption to be visible in the experimental results at the middle and high end of the fluence range used in our experiments.

An important result of the above discussion is that, as photoexcitation drives the concentration of ionized EL2 to the saturation value, the effective EL2 absorption is changed. We can estimate the change in the EL2 linear absorption using equation (2.5) and the dark and saturated values of the ionized EL2 concentration. As we stated above, the small-signal linear absorption coefficient was determined to be 2.2cm^{-1}. Using the EL2 absorption cross sections and total density of EL2, we find a saturation density of ionized EL2 (N^+_{sat}) of 7.6x10^{15} cm^{-3}. When we use this value in equation (2.5) with the EL2 absorption cross sections, we find an effective absorption coefficient of 1.6cm^{-1}. Thus, saturation of the EL2 absorption causes a decrease in the linear absorption coefficient of roughly 30% (0.6cm^{-1}).

We can also use equations (2.12) – (2.14) to determine the range of carrier densities that are generated for our experimental conditions, and then compare these with the carrier densities determined for steady-state excitation conditions. Evaluation of equation (2.12) for the fluence range given above shows that, in these experiments, the ionized EL2 density is changed from its dark value of 1.4×10^{15} cm^{-3} to a value of 1.6×10^{15} cm^{-3} at low fluences and the saturation value (7.6×10^{15} cm^{-3}) at the highest fluences. This is in direct contrast to the steady-state results, where photoexcitation produced only a small change in the ionized EL2 concentration. Equations (2.13) and (2.14) also show that, for the fluence range given above, our optical pulses generate free electron and hole densities between $1 \times 10^{14} cm^{-3}$ – $1 \times 10^{16} cm^{-3}$ via EL2 absorption. While this clearly is in contrast to the steady-state case, where the maximum free carrier densities were on the order of $1 \times 10^{12} cm^{-3}$, it also indicates that photoexcitation with picosecond pulses results in carrier accumulation. In the following sub-section, we show that carrier accumulation leads to absorptive and refractive optical nonlinearities that we call the free carrier nonlinearities.

2.2.5 The Refractive and Absorptive Free-Carrier Nonlinearities

In the previous sub-section, the large discrepancy between the carrier generation and recombination rates associated with picosecond pulses in our GaAs crystal was shown to result in large free electron and hole populations. It is well known that the generation of free carriers in a semiconductor results in a modification to the material's absorptive and refractive properties. In this section, we discuss these free carrier nonlinearities. It is

important to note that these optical nonlinearities do not arise as a result of carrier transport and are thus separate from the photorefractive nonlinearity. Furthermore, since the free carrier density is well below the value at which the carrier wavefunctions begin to overlap (~$1x10^{19}$ cm^{-3}, C. Kittel and H. Kroemer, 1980), these nonlinearities are not due to exchange and correlation interactions in the electron-hole system (K. Bohnert et al., 1988).

Before discussing the absorptive and refractive free carrier nonlinearities, it is necessary to review material absorption and refraction, and their interdependence. Generally, when an incident optical field interacts with a linear medium, the field experiences some attenuation, and it induces a dipole moment in the medium that oscillates at the optical frequency and radiates light. The total field inside the material is then the sum of the incident and radiated optical fields. Since the radiated field generally has a different amplitude and phase than the incident field, the net effect is to change the amplitude and phase of the total field, which is observed as absorption and refraction.

The material's absorptive and refractive properties are interrelated, and this is most easily seen in the relationships between the real and imaginary components of the material's relative permittivity, the index of refraction, and the linear absorption coefficient. Referring to the discussion of the previous paragraph, the amplitude and phase changes that are incurred by the radiated wave are dictated by the real and imaginary components of the relative permittivity constant (ε_{rr} and ε_{ri}). These quantities are strong functions of the optical frequency around a material resonance, and they are related through the Kramers-Krönig relation,

$$\varepsilon_{rr}(\omega) - 1 = \frac{2}{\pi} \int_0^{\infty} \frac{\omega' \varepsilon_{ri}(\omega') d\omega'}{\omega'^2 - \omega^2}, \qquad (2.19)$$

which expresses the real component of the relative permittivity (at a given frequency ω) in terms of a sum over all frequencies, involving the imaginary component of the permittivity. The absorptive and refractive properties of the material that are observed are expressed in the linear absorption coefficient (α) and the index of refraction (n). These quantities are related to the real and imaginary components of the relative permittivity constant in the following way:

$$n = \left[\frac{1}{2} \left(\varepsilon_{rr} + \left[\varepsilon_{rr}^2 + \varepsilon_{ri}^2 \right]^{\frac{1}{2}} \right) \right]^{\frac{1}{2}} \qquad (2.20)$$

and

$$\alpha = \frac{2\omega}{c} \left[\frac{1}{2} \left(-\varepsilon_{rr} + \left[\varepsilon_{rr}^2 + \varepsilon_{ri}^2 \right]^{\frac{1}{2}} \right) \right]^{\frac{1}{2}}. \qquad (2.21)$$

For experimental conditions such as ours, where the imaginary component of the dielectric constant is much smaller than the real component, equations (2.20) and (2.21) can be written:

$$n = \sqrt{\varepsilon_{rr}}, \qquad (2.22)$$

and

$$\alpha = \frac{k \varepsilon_{ri}}{n}, \qquad (2.23)$$

where k is the vacuum wave number.

Photogeneration of free carriers can change the absorption in our semi-insulating GaAs crystal in several ways. We have already seen how photoexcitation with picosecond optical pulses drives the neutral and ionized EL2 densities from their dark values to "saturation" values, resulting in a 30% decrease in the effective linear absorption coefficient (see section 2.2.6). However, photogeneration of free carriers can produce three other changes in the material absorption. First, the carriers occupy valence and conduction band states, and, by preventing additional transitions to these states, change the absorption. This contribution to the free carrier absorption change is called band-blocking. The second absorptive change introduced by the free carrier population is due the fact that their optical properties are different from those of the bulk semiconducting material. Indeed, when the effective mass approximation is valid for the free carriers, they can be thought of as comprising a plasma, and having similar optical properties. Finally, the free carriers can absorb incident light and be promoted either to higher energy states within the same energy band, or to higher energy states in different conduction or valence bands. The former process, which is known as intraband free-carrier absorption, requires absorption of a phonon. However, the latter process, which is called interband free-carrier absorption, does not.

In our experiments, the excitation photon energy is smaller than the bandgap energy, while the excitation optical frequency is much larger than the plasma frequencies associated with the range of carrier densities generated. As a result, the absorption change resulting from the free carrier population is due mainly to free carrier absorption. The

change in the linear absorption coefficient due to free carrier absorption ($\Delta\alpha_{fc}$) can be written phenomenologically in terms of the free electron (n) and hole (p) densities:

$$\Delta\alpha_{fc} = n\sigma_{fe} + p\sigma_{fp} \qquad (2.24)$$

Here σ_{fe} and σ_{fp} are the free electron and hole absorption cross sections. The free carrier absorption cross sections and, hence, the absorptive change are dependent on the wavelength of incident radiation. For a wavelength of 1.06 μm, the sum of these cross sections has been determined to be approximately 9×10^{-18} cm^2 (G.C. Valley et al., 1989). With the range of carrier densities generated in our experiments, these cross sections produce maximum absorptive changes of 9×10^{-2} cm^{-1}. In addition to being too small to measure with our transient grating measurement technique, this absorption change is much smaller than the absorptive changes resulting from EL2 absorption saturation and instantaneous two-photon absorption (discussed in section 2.2.6). Thus, we conclude that free carrier absorption is unimportant in our experiments.

Several researchers have derived expressions for the free carrier index change. Their expressions are linear in the photogenerated free carrier density, which supports the use of the phenomenological expression involving the density of electron-hole pairs (N), and the index change per electron-hole pair (n_{eh}):

$$\Delta n = n_{eh} N \, . \qquad (2.25)$$

Auston et al. (1978) calculated the change in the real and imaginary parts of the dielectric constant resulting from the free carrier population, and then used these quantities to approximate the index change. Wherrett and Higgins directly calculated the free carrier

index change by summing the differential change in index caused by the removal of a single set of valence-to-conduction band states, over all the occupied states (1981). Both of these methods considered valence-to-conduction band transitions only, and an equilibrium distribution of free carriers at a lattice temperature of 0K. The index change per electron-hole pair resulting from the derivation by Auston et al. (1978) is:

$$n_{eh} = -\frac{2\pi e^2}{n_b m_r \omega^2} \frac{\omega_g^2}{\omega_g^2 - \omega^2}. \qquad (2.26)$$

Here m_r is the reduced mass of the electron-hole pairs, e is the electron charge, n_b is the background index of refraction, and ω_g and ω are the angular frequencies corresponding to the material bandgap energy and the incident light, respectively.

The discussions contained in section 2.2.6 and the previous paragraphs show that the largest absorption change that has been considered up to this point is due to EL2 saturation. However, in deriving the free carrier index change, Auston et al., assume only band-to-band transitions, so that equation (2.25) does not take into account EL2 saturation. Moreover, because EL2 absorption saturation produces a 14% absorption change, it might be expected to produce an index change that is comparable to, or larger than, the index change given by equations (2.25) and (2.26). However, a simple analysis of EL2 carrier generation in our crystal shows that EL2 absorption saturation does not cause a significant index change. As discussed in section 2.2.1, the number density (N, N-N^+) and cross sections (σ_e and σ_h) of the EL2 and $EL2^+$ are nearly equal. As a result, when free electrons are generated via the EL2CB transition, holes are nearly always generated via the VBEL2+ transition. Thus for our experimental conditions, the EL2 act

largely as an intermediary in the photogeneration of electron-hole pairs, and the index change is much like that which is produced when the carriers are produced by band-to-band transitions. This result has also been shown experimentally by Valley et al. in modeling transient energy transfer in semi-insulating GaAs (1988). In their study, the authors found that, in spite of the inaccuracies in the theoretical index change given by equations (2.25) and (2.26), the observed and predicted index changes differed only by a factor of 0.6 to 0.8. It must be noted that, while we use equations (2.25) and (2.26) in modeling the free carrier index change (see Chapter V), we seek only an order of magnitude estimate of this index change. This is because, in our numerical modeling, we seek to model the dynamics of the observed diffraction efficiencies, not the magnitudes of the nonlinearities.

The magnitude of the free carrier index change can be estimated using the experimental range of free carrier densities given above along with measured values for the index change per electron-hole pair. The index change per electron hole pair has been measured in semi-insulating GaAs in the 1.0 μm wavelength range (A.A. Said et al., 1992 and A.G. Cui, 1992). Using the Z-scan measurement technique at a wavelength of 1.06μm, and taking into account carrier generation due to the EL2 sites, A.G. Cui measured a value of -5.1×10^{-21} cm^3 for this constant. With the experimental range of carrier densities given above (1×10^{14} cm^{-3} – 1×10^{16} cm^{-3}), this constant predicts free-carrier index changes ranging from 5×10^{-7} to 5×10^{-5}. While the free carrier index change is smaller than the instantaneous bound-electronic index change (discussed in section 2.2.6) at all but the lowest excitation fluences, it is larger than the photorefractive index change at all but the

lowest excitation fluences (see Chapter III). As a result, the free carrier nonlinearity complicates the measurement of picosecond photorefractive nonlinearities.

A final point that must be made about the free carrier index change is that it can be assumed to be isotropic on picosecond time scales. This follows from the isotropy of the carrier effective masses in semi-insulating GaAs (Landolt and Börnstein, vol. 17, 1982), and the discussion of section 2.2.2, where we showed that carrier dephasing occurs instantaneously with respect to the time scales of our experiments. Since the free carrier index change is isotropic, the corresponding index grating does not produce a diffracted beam with a rotated polarization. In our transient grating measurement method, we use the polarization rotating properties of the photorefractive nonlinearity to separate it from the other competing optical nonlinearities (see Chapter V).

2.2.6 Instantaneous Two-Photon Absorption

In our experiments, we employ 960nm wavelength optical pulses with peak intensities as high as ~2.5GW/cm^2. As a result, another optical nonlinearity, instantaneous two-photon absorption, is prevalent in our experiments. As we will see in this section, this optical nonlinearity results in an additional light absorption and carrier generation mechanism that dominates over EL2 single photon absorption at high beam intensities. We use the term “instantaneous two-photon absorption” in order to distinguish this process from the step-wise two photon absorption process that was discussed previously in connection with EL2 absorption saturation.

The instantaneous two-photon absorption process is shown schematically in figure 2.3. As shown in the figure, the material simultaneously absorbs two photons of light, and one free electron and one free hole are produced in the conduction and valence bands. The two-photon absorption carrier generation rate involves the square of the beam intensity. Including this light absorption process, the electron and hole rate equations become:

$$\frac{\partial n}{\partial t} = \frac{\sigma_e \left(N - N^+\right) I}{h\nu} + \frac{\beta I^2}{2h\nu} \ , \qquad (2.27)$$

$$\frac{\partial p}{\partial t} = \frac{\sigma_h N^+ I}{h\nu} + \frac{\beta I^2}{2h\nu} \ , \qquad (2.28)$$

In these equations, β is the wavelength-dependent two-photon absorption coefficient of the material, and we have neglected electron and hole recombination for the reasons discussed in section 2.2.3. Since the two-photon related carrier generation rates are directly related to the square of the optical intensity, these processes have greater prevalence at higher beam intensities.

Including two-photon absorption, the beam propagation equation becomes:

$$\frac{dI}{dz} = -\sigma_e (N - N^+) I - \sigma_h N^+ I - \beta I^2 \ . \qquad (2.29)$$

The dependence of two-photon absorption on the square of the optical intensity means that beams of higher intensity incur a greater absorption than beams of lower intensity. In this way, two-photon absorption effectively limits the beam intensity that can be transmitted through the crystal. Optical limiting of the laser beams by two-photon absorption will be visible in the experimental results of Chapters VII and VIII.

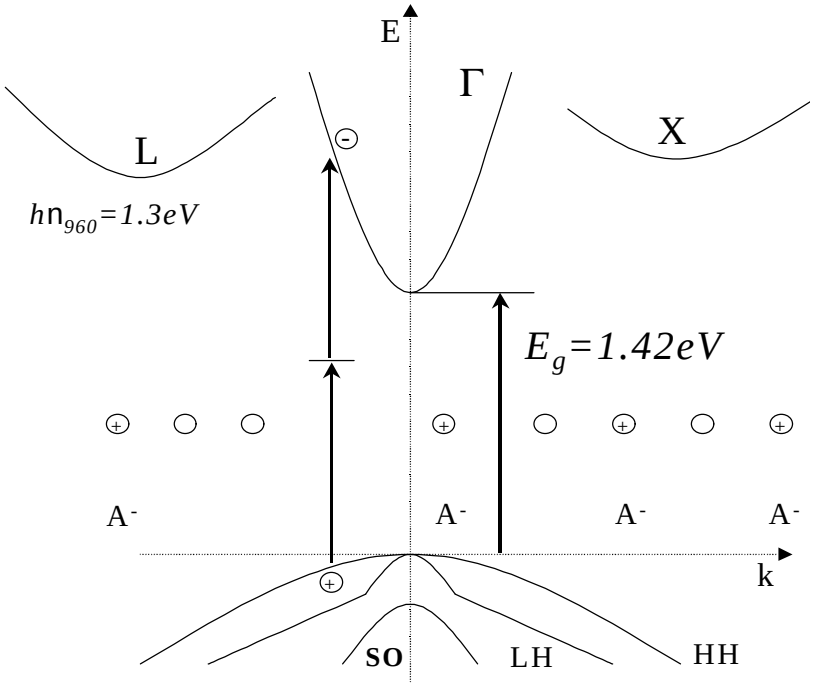

Figure 2.3 – Schematic diagram of the band structure of semi-insulating GaAs near k=0 illustrating the instantaneous two-photon absorption process. In this figure, other transitions involving the light-hole and split-off valence bands are possible, but not shown for clarity of presentation.

The two-photon absorption coefficient can be derived using second order, time-dependent perturbation theory. This coefficient is related to the imaginary part of the third-order susceptibility, $\chi^{(3)}$ through the equation (A. Yariv, 1989):

$$\beta(\omega_1,\omega_1)=\frac{2\omega_1}{n_b\varepsilon_o c^2}\,\mathrm{Im}\left[\chi^{(3)}(\omega_1,\omega_1)\right], \qquad (2.30)$$

where ω_1 and ω_2 are the angular frequencies of the incident photons, and all the other parameters have already been defined. Equation (2.30) involves SI units, so that β and $\chi^{(3)}$ are in units of m/W and m^2/V^2.

The two photon absorption coefficient in semi-insulating GaAs has been reported to be anisotropic (M. D. Dvorak, et al., 1994, S.J. Bepko, 1975, R. DeSalvo et al., 1993). For the cut of our semi-insulating GaAs crystal, as well as the crystal orientation and the polarization of the pump beams used in our experiments, these measurements suggest a value of roughly 19cm/GW for the two-photon absorption coefficient (M. D. Dvorak, et al., 1994).

In order to give the reader an idea of the importance of two-photon absorption in these experiments, the relative strengths of the single and two photon absorption processes under these circumstances can be compared. The solution to the single beam propagation equation shows that single and two photon absorption are equal at the critical intensity I_{crit}, given by the equation (T. F. Boggess et al., 1986):

$$I_{crit} = \frac{\alpha}{\beta(1-R_1)(1-e^{-\alpha\ell})}. \qquad (2.31)$$

The derivation that produces this equation assumes a constant linear absorption. The factor $(1-R_1)$ accounts for the loss of optical energy due to Fresnel reflection at the front surface of the sample, while the factor $(1-e^{-\alpha l})$ is the fractional loss of optical energy due to linear absorption over the length of the crystal. When the front surface reflection coefficient of 0.305 is used with the sample length of 0.317 cm and the values of α and β for this crystal, equation (2.31) yields a critical intensity of 0.33GW/cm^2. This intensity is in the middle of the range of beam intensities used in these experiments. Thus for the larger half of the optical fluences used in these experiments, two photon absorption is the dominant light absorption mechanism in semi-insulating GaAs.

2.2.6.1 The Instantaneous Bound-Electronic Refractive Nonlinearity

Semi-insulating GaAs also exhibits an instantaneous, intensity dependent refractive nonlinearity. At a wavelength of 960nm, this results mainly from the changes in absorption caused by the two-photon absorption process and the quadratic Stark effect (M. Sheik-Bahae et al., 1991). The relationship between the index change (Δn) and the optical intensity can be written:

$$\Delta n = n_2 I \quad . \qquad (2.32)$$

Here n_2 is the second-order index parameter, which is related to the real part of the instantaneous third order susceptibility $\chi^{(3)}$, through the equation:

$$n_2 = \frac{1}{\varepsilon_o c n_b^2} \mathrm{Re}\left[\chi^{(3)}(\omega_1, \omega_2)\right]. \qquad (2.33)$$

Here, as in the equation for the two-photon absorption coefficient, SI units are used so that n_2 and $\chi^{(3)}$ are in units of m^2/W and m^2/V^2. The second order index parameter has been measured in GaAs at wavelengths near 1.0μm (M. Shiek-Bahae et al., 1991). As part of their study on the dispersion of refractive bound-electronic nonlinearities in solids, the authors measured a second-order refractive index coefficient of -2.26×10^{-17} m^2/W (-2700 esu). Using this value and the peak optical intensity of 2.4 GW/cm^2 used in our experiments, equation (2.32) predicts an index change of 8×10^{-4}. This optical nonlinearity is clearly larger than the free carrier index change discussed in the last section.

The anisotropy in the two-photon absorption coefficient, which arises from the imaginary component of the third order susceptibility, suggests an anisotropy in the second-order index parameter, which we have seen arises from the real component of the

third-order susceptibility. However, while this has been predicted for GaAs and other III-V semiconductors (C. Flytzanis, 1970), to the knowledge of this author it has not been measured.

In keeping with the other discussions of this chapter, we can compare the magnitude of the instantaneous bound-electronic and free-carrier index changes, for our experimental conditions. In order to do this, we calculate the intensity at which the two optical nonlinearities are equal, and then compare this with the range of intensities used in our experiments. Using equation (2.25) and the measured value for n_{eh}, along with equation (2.32), we find that the free carrier and instantaneous bound electronic index changes are equal at the intensity (I_{neq}):

$$I_{neq} = \frac{2\sqrt{2}}{(1-R_1)\beta}\left[\frac{2\hbar\omega n_2}{\sqrt{\pi}\,t_o n_{eh}} - \alpha\right]. \qquad (2.34)$$

Here we have considered the instantaneous bound electronic index change that is generated at the peak of the optical pulse, and used the carrier density that is accumulated as a result of both single- and two-photon absorption over one half of a 1ps FWHM pulse with a Gaussian temporal profile. The quantity t_o is the HW1/e Gaussian width of the pulses, and again, for simplicity, we have assumed a constant linear absorption coefficient. When the measured values for n_{eh}, n_2, β and R_1 are used, equation (2.34) yields an intensity of 1.6GW/cm^2. Since we employ pulse intensities between 0.03GW/cm^2 and 2.4GW/cm^2 in these experiments, the instantaneous bound-electronic index change is expected to be comparable to, or larger than the free carrier index change at the largest intensities.

2.3 Undoped Cadmium Telluride (CdTe)

Figure 2.4 is a schematic diagram of the band structure of undoped CdTe near k=0. As is evident from the figure, the band structure of CdTe is similar to that of GaAs in many ways. First, like GaAs, CdTe is a direct bandgap semiconductor; its conduction band minimum and valence band maximum are both at k=0. As in GaAs, the valence to conduction band energy difference, 1.49eV (Landolt and Börnstein, vol.17b, 1982), is larger than the 1.3eV photon energy of the 960nm radiation that we employ in these experiments. Thus, direct, single photon induced band-to-band transitions do not occur in this material when the material is excited at 960nm.

The CdTe band structure is different from that of GaAs in one notable way. As seen in the figure, undoped CdTe possesses no optically active mid gap levels. Indeed, in the studies detailed in this thesis, we have observed no measurable linear absorption for our CdTe crystal at wavelengths near 1.0μm. Our measurements are corroborated by the fact that other studies have shown this same result, measuring linear absorption coefficients less than $0.1cm^{-1}$ at wavelengths near 1.0μm (M. S. Petrovic et al., 1989).

Although it is not possible to generate free electrons and holes in undoped CdTe by linear absorption at the 960nm excitation wavelength, the use of intense picosecond pulses allows carriers to be generated in this material via two-photon absorption. This process, which is shown schematically in figure 2.4, occurs in the same way that was discussed in the description of carrier generation in GaAs. Thus, in undoped CdTe, the

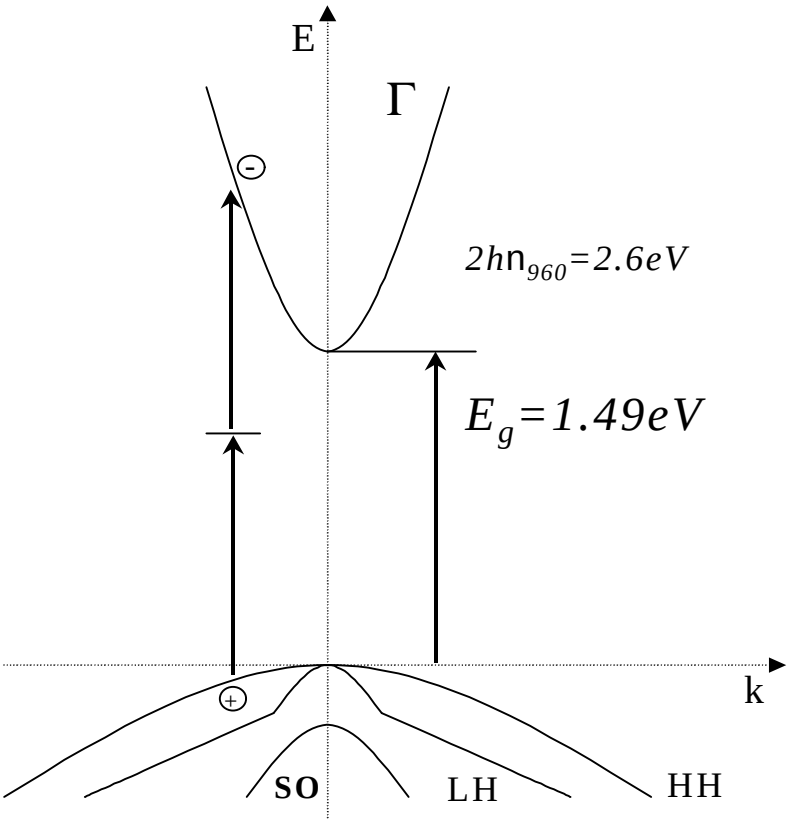

Figure 2.4 – Band structure diagram for undoped CdTe illustrating the lone carrier generation and light absorption process for our experimental conditions, instantaneous two-photon absorption. Shown in this figure is the Γ conduction band valley and the light-hole (LH), heavy-hole (HH) and split-off (SO) valence bands. The X and L conduction band valleys are not pictured because transitions to these bands are extremely unlikely for our experimental conditions.

carrier generation equations are written:

$$\frac{\partial n}{\partial t} = \frac{\beta I^2}{2\hbar\omega}\ , \qquad (2.35)$$

and

$$\frac{\partial p}{\partial t} = \frac{\beta I^2}{2\hbar\omega}\ . \qquad (2.36)$$

Clearly, since two-photon absorption is the predominate means of carrier generation in undoped CdTe, any free-carrier related optical nonlinearities must be due to equal

populations of electrons and holes (assuming the absence of dark densities of electrons and holes).

The lack of measurable linear absorption in this semiconductor means that the incident optical radiation is depleted entirely by two photon absorption. As a result, the beam propagation equation can be written:

$$\frac{dI}{dz} = -\frac{\beta I^2}{2h\nu}. \qquad (2.37)$$

As in semi-insulating GaAs, the two photon absorption coefficient in CdTe has been observed to be anisotropic (M. D. Dvorak et al., 1994). For our experimental conditions, which include the crystal cut and orientation, as well as the orientation of our pump beams the above work implies a value of 17cm/GW for the two-photon absorption coefficient. Since the measured value of the two-photon absorption coefficient is near to the value of 19cm/GW applicable to GaAs, instantaneous two-photon absorption of our 960nm optical pulses results in similar carrier densities in both materials.

Comparison of the carrier generation and beam propagation equations for GaAs and CdTe clearly illustrates the advantage of studying the optical nonlinearities in CdTe in addition to those in GaAs. While GaAs possesses free-carrier related optical nonlinearities that result from both optically-active midgap levels and instantaneous two-photon absorption, CdTe possesses free-carrier related optical nonlinearities that result only from the latter of these carrier generation processes. Thus, in addition to simplifying the analysis of experimental results, the use of undoped CdTe also allows the nonlinearities that result from instantaneous two-photon absorption to be independently characterized.

In this thesis, the use of this material will allow the photorefractive nonlinearity resulting from the electron-hole (Dember) space-charge field to be unambiguously observed for the first time.

To the knowledge of this author, carrier relaxation has not been studied in undoped CdTe. However, CdTe is a polar semiconductor like GaAs, so that carrier-LO phonon scattering can be expected to play an important role in carrier dephasing and thermalization, along with carrier-carrier scattering. Indeed, this has been shown in studies involving other II-VI materials, such as CdS (P. Motisuke, et. al., 1975) and CdSe (J. Shah, 1974). Since the parameters that determine the carrier-carrier and carrier-LO phonon scattering rates are of the same order of magnitude in GaAs and CdTe, it is therefore reasonable to assume that carrier dephasing in CdTe occurs instantaneously with respect to our experiments, while carrier thermalization occurs in times less than 4ps. We can estimate the carrier cooling time in undoped CdTe in the same way that it was estimated in semi-insulating GaAs, using the LO phonon emission time and energy and the excess energy of the carriers. Free carriers are generated in CdTe with excess energies of ~1eV. Using the CdTe LO phonon energy of 21meV (Landolt and Börnstein, vol. 17b, 1982) and assuming that the CdTe LO phonon emission time is approximately equal to the GaAs LO phonon emission time, the estimated carrier cooling time for CdTe is ~5ps. Thus, as in GaAs, carrier cooling does not occur instantaneously with respect to our experiments.

Carrier recombination has been studied to a limited degree in undoped CdTe. While the electron-hole bimolecular recombination coefficient has not been determined for

CdTe, Petrovic et al. reported carrier recombination times of 12ns (1989) in undoped CdTe. This time is on the order of those reported for semi-insulating GaAs, which indicates that the carrier recombination rates in undoped CdTe are much smaller than the carrier generation rates. Thus, as in semi-insulating GaAs, photoexcitation results in the accumulation of free carriers, and absorptive and refractive free carrier nonlinearities.

We can estimate the magnitude of the free carrier absorptive and refractive nonlinearities and the instantaneous bound-electronic refractive nonlinearities in undoped CdTe in the same way that they were estimated for semi-insulating GaAs. As in semi-insulating GaAs, the absorptive change resulting from the free carrier population is due mainly to free carrier absorption. A free carrier absorption coefficient of $1x10^{-18}$ cm^2 has been reported for undoped CdTe (K. Zanio, 1978). With the carrier densities generated in our experiments ($1x10^{14}$ cm^{-3} – $1x10^{16}$ cm^{-3}), this yields a maximum absorption change of $1x10^{-2}$ cm^{-1}. Thus, as in semi-insulating GaAs, the free carrier induced absorption change is too small to measure, and is therefore neglected. While the index change per photogenerated electron-hole pair has not been measured in undoped CdTe, we can use equation (2.26) to estimate its magnitude. Using a band gap energy of 1.49eV, a background index of refraction of 2.87 (Landolt and Börnstein, vol 11, 1979), and electron and hole effective masses of 0.1 and 0.4 (K. Zanio, 1978), we estimate an index change per electron hole pair of $-2x10^{-21}$ cm^3. With the carrier densities generated in our experiments, this leads to free carrier index changes between $–2x10^{-7}$ and $–2x10^{-5}$. As in GaAs, the free carrier index change can be expected to be easily visible in our experimental results. The second order index parameter (n_2) has been measured in CdTe

at a wavelength of 1.06μm (M. Sheik-Bahae et al., 1989). The value determined for this constant, which is -2.95×10^{-17} m^2/W, can be used with our peak intensities to estimate the magnitude of the instantaneous bound-electronic index change in undoped CdTe. As noted in the paragraphs above, we use optical intensities as high as $2.5 GW/cm^2$ in our experiments. With the value cited above for n_2, we estimate a maximum instantaneous bound electronic index change of $\sim 7 \times 10^{-4}$. Like the free carrier index change, the instantaneous bound-electronic index change in CdTe is large. As in GaAs, the presence of both of the free carrier and instantaneous bound electronic index changes will complicate the measurement of picosecond photorefractive effects. While we expect the second order index parameter to be anisotropic in CdTe, to the knowledge of this author, this has not been measured.

2.4 Summary

We have discussed carrier generation in semi-insulating GaAs and undoped CdTe as a result of excitation with our intense 960nm optical pulses. While carriers are generated in both materials via instantaneous two-photon absorption, carriers are also generated in semi-insulating GaAs as a result of single photon induced transitions involving the EL2 midgap levels. In our experiments the excitation fluences are large enough to saturate the EL2 absorption, a result that produces a 30% decrease in the effective linear absorption coefficient, and causes carriers to be generated via step-wise two-photon absorption involving the EL2 levels.

Aside from instantaneous two-photon absorption and EL2 absorption saturation, semi-insulating GaAs and undoped CdTe exhibit a variety of other optical nonlinearities. Since the carrier generation rates in our experiments are much larger than the carrier recombination rates, photoexcitation produces populations of free carriers in the 10^{14} cm^{-3} -10^{16} cm^{-3} range (averaged over the length of our crystals), along with subsequent absorptive and refractive nonlinearities. While the absorptive change induced by the free carrier populations is small, the refractive index change is not. In fact, the free carrier index change is as large as $1x10^{-5}$ at the highest carrier densities generated in our experiments. Due to the fact that we use intense picosecond pulses in our experiments, we generate an additional instantaneous bound electronic index change. Like the free carrier index change, the instantaneous bound electronic index change is large (Δn as large as 10^{-4}). For our experimental conditions the free carrier index changes is isotropic. In Chapter V, this will be shown to produce an important result: for our experimental conditions, the free carrier does not produce a diffracted optical signal with a polarization rotation. Similarly, while the second-order index parameter is expected to be anisotropic in both semi-insulating GaAs and undoped CdTe, this nonlinearity produces no polarization rotation for our experimental conditions (W. A. Schroeder et al., 1992).

CHAPTER III

CARRIER TRANSPORT, THE FORMATION OF SPACE-CHARGE FIELDS AND THE LINEAR ELECTROOPTIC EFFECT

3.1 Introduction

The photorefractive effect arises from the electrooptic response of a material to a space-charge field that is generated by the migration of photogenerated charge carriers. Having discussed carrier generation (and the associated optical nonlinearities) in GaAs and CdTe for our experimental conditions, we turn our attention, in this chapter, to carrier transport, the generation of space-charge fields, and the photorefractive effect. The experiments described in this thesis are intended to contrast studies with similar goals that have investigated the steady-state space-charge field and photorefractive effect. For this reason, and because the formation of the steady-state space-charge field has received much theoretical attention, it is fitting that we begin our discussion by reviewing these results. Following this, we focus on the *transient* space-charge fields that we generate in our experiments. Finally, we discuss the electrooptic response of GaAs and CdTe, and some basic properties of the photorefractive nonlinearities produced in these materials.

3.1.1 Initial Conditions

The experiments described in this thesis are performed with an arrangement of optical beams that is similar to that shown in figure 3.1. In our experiments, two parallel-polarized, temporally and spatially coincident laser pulses generate a modulated intensity pattern of the form,

$$I(x) = \frac{I_0}{2}\left[1 + m\cos\left(\frac{2\pi x}{\Lambda_g} + \Delta\phi\right)\right] \qquad (3.1)$$

inside the material. In equation (3.1), the intensity, I_0, is the sum of the squares of the two complex optical field magnitudes ($\frac{1}{2}cn\varepsilon_0(|E_1|^2+|E_2|^2)$). The phase difference between the optical electric fields determines the phase of the grating ($\Delta\phi$) and the grating spacing, Λ_g, is dependent on the wavelength of radiation (inside the material), λ, and the half-angle between the beams, θ, through the equation:

$$\Lambda_g = \frac{\lambda}{2\sin\theta}. \qquad (3.2)$$

The quantity m, which is given by the equation,

$$m = \frac{2r}{1+r^2} \qquad (3.3)$$

dictates the depth of the intensity modulation. Here r is the ratio of the magnitudes of the two optical electric fields. The carrier and space-charge field dynamics discussed in this chapter will consider the initial conditions dictated by the arrangement of the optical beams shown in figure 3.1.

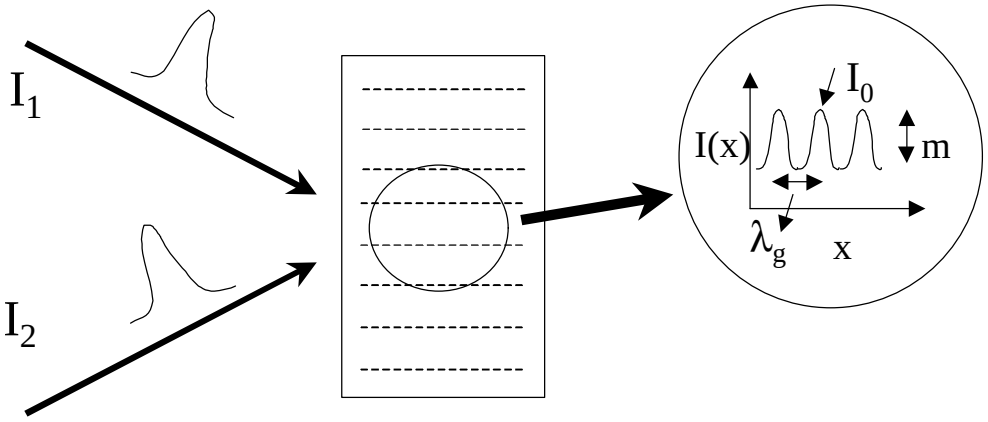

Figure 3.1 – Initial conditions for our experiments. As described in the text, two spatially- and temporally-coincident optical pulses form a modulated intensity pattern inside our crystals. From this modulated intensity pattern, the photorefractive and other induced gratings are formed.

3.2 The Steady-State Space-Charge Field

For the reasons discussed in Chapter I, a wealth of theoretical work has been done to understand the characteristics of the steady-state space-charge field. We begin by reviewing the relevant results of this work. In the same way that EL2 absorption was contrasted for steady-state and transient excitation conditions in Chapter II, the results presented here will be compared and contrasted with the results presented in section 3.3.

The physical model for the photorefractive effect, which includes carrier generation, drift and diffusion, and recombination, is well developed and verified after over 30 years of study. Charge migration was first proposed as a mechanism for forming the photorefractive nonlinearity by Chen, who postulated that this effect arose from the drift of photogenerated electrons in the internal field of the material (1969). Chen's model was the basis for subsequent theories, first by Amoedi (1971), who showed that diffusive charge migration and its balance with drift due to the induced space-charge field, were

important in field formation. Later, Glass et al., (1974) proposed the bulk photovoltaic effect as an additional mechanism for field formation. Kukhtarev included all of the above contributions, and solved the carrier generation and transport equations in the steady-state to yield general expressions for the fundamental Fourier component of the space-charge field, and its response time (N. V. Kukhtarev et al., 1979). Separately, Feinberg applied a different physical model, known as the "hopping model", to explain the formation of the photorefractive nonlinearity in $BaTiO_3$. (J. Feinberg et al., 1980). Though this theory produced results that were similar to those of the charge migration model, it was different from the charge migration model in that it was statistical in nature. For a review of the theoretical development of the steady-state space-charge field, the reader is referred to "Theory of Photorefractive Effects in Electrooptic Crystals" by G.C. Valley and J.F. Lam (1988).

The photorefractive nonlinearity that is observed in semi-insulating GaAs under CW excitation conditions arises, in the most simple circumstances, from a steady-state balance between the formation and decay processes depicted in figure 3.2. In this example, there is no applied electric field, and the photovoltaic effect is neglected because it has been shown to have a negligible effect on space-charge field formation in semiconductors (Glass, 1974). Linear absorption of the sinusoidal intensity pattern of figure 3.1 produces sinusoidal population densities of free electrons and ionized EL2. As we discussed in Chapter II, in semi-insulating GaAs the photoionized EL2 population exists along with a background (dark) density of ionized EL2 that is compensated by an

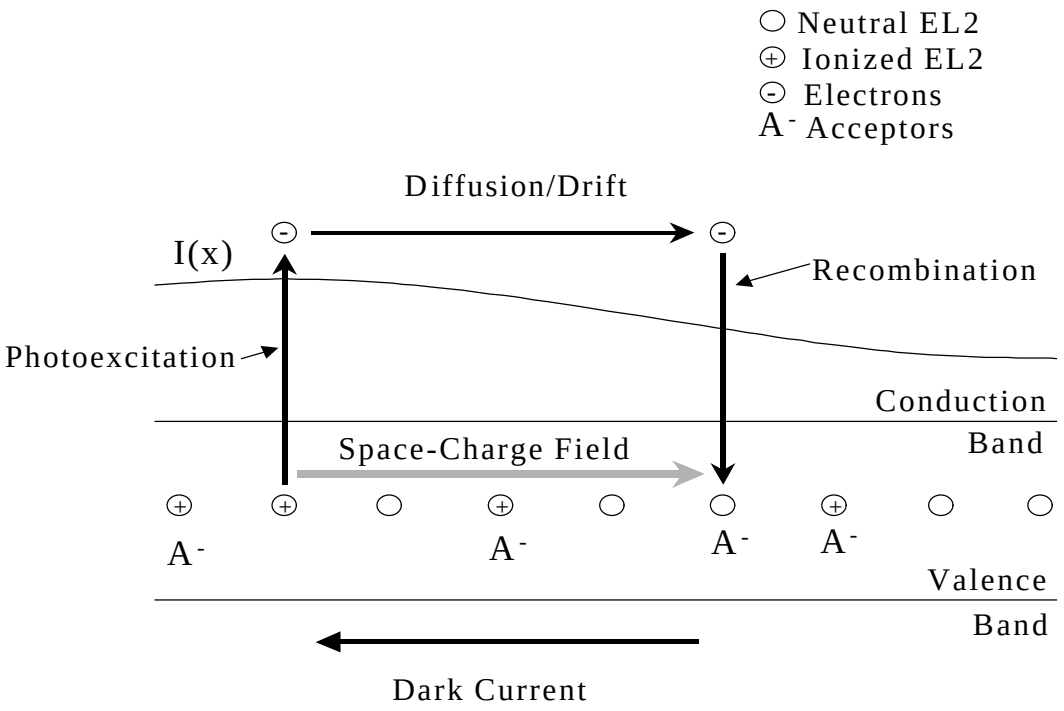

Figure 3.2 – Formation of the steady-state space-charge field in semi-insulating GaAs. Included are the modulated intensity pattern, the dark current, the neutral and ionized El2 (hole generation is neglected).See text for description.

equal density of negatively charged acceptors. The space-charge field is formed by three processes that occur concurrently with carrier generation. First, the photogenerated electrons diffuse (as a result of the gradient in carrier density) from regions of high concentration to regions of low concentration. Second, when a non-zero space-charge field is present, the electrons drift in the field, and the drift current density is in the opposite direction as the diffusion current density. Finally, the electrons recombine with the ionized EL2. As a result of carrier generation, drift and diffusion, and recombination, a charge separation is established in which the ionized EL2 population is modulated above and below the density required to compensate for the acceptors. This charge separation results in a periodic space-charge field, and the space-charge field has a spatial frequency component that is equal to that of the incident irradiance pattern (equation (3.2)).

Through the material's linear electrooptic effect, the periodic space-charge field results in a photorefractive index grating.

The charge separation and space-charge field that are described above decay as a result of the dark current, as shown in figure 3.2. Here thermally-generated free electrons drift as a result of the space-charge field and then recombine with the ionized EL2, thereby restoring the ionized EL2 population to that required to compensate the acceptor population. Destruction of the EL2/acceptor charge separation via the dark current occurs slowly, so that the photorefractive nonlinearity is generally long-lived. Indeed, while the dark current will destroy the photorefractive nonlinearity in semi-insulating GaAs on ~0.1ms time scales, in ferroelectric materials, where the electron mobilities are smaller and the optically-active donor sites are farther below the conduction band edge, photorefractive nonlinearities can be generated that are semi-permanent. The long-lived nature of the photorefractive nonlinearity allows a steady-state effect to be observed with CW laser beams of a few milliwatts, which is one of its most unique and important properties. As discussed in Chapter I, this property of the photorefractive nonlinearity makes it promising for optical device applications, and easy to study.

For a situation such as that described above, where there is no applied electric field and only a single charge carrier is present, the fundamental Fourier component of the steady-state space-charge field (E_{scss}) is given by the equation:

$$E_{scss} = -\frac{imE_D}{1+E_D/E_q}\left(1-e^{-t/\tau_{effss}}\right) \qquad (3.4)$$

In this equation *m* is the modulation ratio (equation (3.3)), E_q and E_D are the limiting space-charge fields,

$$E_q = \frac{e\Lambda_g N_T}{2\pi\varepsilon}, \qquad (3.5)$$

and

$$E_D = \frac{2\pi k_B T}{\Lambda_g e}, \qquad (3.6)$$

and τ_{effss} is the effective time constant for steady-state formation,

$$\tau_{effss} = \frac{1+(2\pi r_D/\Lambda_g)^2}{1+(2\pi l_s/\Lambda_g)^2}\tau_{die}. \qquad (3.7)$$

In equation (3.7), r_D, τ_{die} and l_s are, respectively, the length an electron travels before recombination, the dielectric relation time ($\tau_{die} = \varepsilon/ne\mu$), and the Debye length ($l_s = [\varepsilon k_B T/(N_T e^2)]^{1/2}$). The dielectric relaxation time and the Debye length will be discussed in greater detail in the paragraphs below. The effective trap density, N_T, which is the number of traps that are available for recombination under CW illumination, is related to the dark densities of neutral (N-N^+_D) and ionized traps (N^+_D) through the equation:

$$N_T = \frac{N_D^+(N-N_D^+)}{N_D^+ + (N-N_D^+)}.$$

In our semi-insulating GaAs crystal, where the dark densities of neutral and ionized EL2 are 1.2×10^{16} cm^{-3} and 1.4×10^{15} cm^{-3}, respectively, the effective trap density is 1.25×10^{15} cm^{-3}.

The magnitude of the steady-state space-charge field is dependent on the relative importance of drift and diffusion in carrier transport. This is reflected in equations (3.4) – (3.6) and that the magnitude of E_{scss} is dependent only on l_g through E_q and E_D, which are limiting fields that are generated when diffusion and drift, respectively, dominate carrier transport. In the limit of small grating periods, diffusion dominates carrier transport, so that diffusion and then recombination *completely destroy* any modulation in the photogenerated carrier density. This results in the maximum possible charge separation between the ionized EL2 and acceptor populations, which produces the field magnitude given by equation (3.5). The dependence of this field magnitude on the effective trap density illustrates the fact that the maximum attainable steady-state space-charge field is limited by the amount of charge that can be trapped in the material. In the limit of large grating spacings, electronic drift balances diffusion, so that diffusive decay of the modulated carrier density ceases, and the modulated free carrier density is destroyed only by recombination. In this limit, the field magnitude, which is given by equation (3.6), is inversely proportional to grating spacing, and independent of any material parameters.

An important point to note about the steady-state space-charge field magnitude is that it is 90^o out of phase with the incident intensity pattern, as indicated by the presence of the factor ($-i$) in equation (3.7). In chapter IV, this will be shown to result in energy transfer between beams in the two beam geometry shown in figure 3.1. The energy transfer properties of the photorefractive grating, which are another important characteristic of this nonlinearity, make photorefractive gratings useful for coherent operations such as image amplification and phase locking of lasers.

Equation (3.7) shows that the rise time of the steady-state space-charge field (τ_{efss}) reduces to the dielectric relaxation time in the limit of large grating periods. This can be easily understood by noting that drift dominates carrier transport and field formation at large grating periods (see above), and that the dielectric relaxation time is the characteristic time for the build-up of the space-charge field (see below). At smaller grating spacings, where the ratios of the diffusion and Debye lengths to the grating period can not be neglected, the rise time is material-dependent.

The dielectric relaxation time can be written in terms of the carrier excitation rate ($\alpha I/h\nu$) and recombination time (τ_R) to illustrate two important points:

$$\tau_{die} = \frac{\varepsilon h\nu}{e\alpha I\mu\tau_R}. \qquad (3.8)$$

Here h is Planck's constant, ε is the material permittivity, ν is the frequency of the optical beam, and α is the material's linear absorption coefficient. First, as equation (3.8) shows, the steady-state field forms more quickly when the carrier mobility-lifetime product ($\mu\tau_R$) is large. As discussed in Chapter I, this corresponds to a large photorefractive efficiency, which is the charge separation that can be generated on a per-carrier basis (see Chapter I). Second, equation (3.8) shows that that the field formation time is inversely proportional to the optical intensity (I). Since the steady-state space-charge field is formed under excitation conditions where the carrier generation rate is much smaller than the carrier diffusion and recombination rates, this is not surprising. However, due to its dependence on the optical intensity, the steady-state formation time can not be regarded as the fundamental formation time of the space-charge field. Instead, the fundamental

formation time is the time required for a single charge carrier to diffuse across the grating period. This can only be observed in experiments where the carrier generation rates are much larger than the carrier diffusion and recombination rates, which is the case in the transient photorefractive experiments described in this thesis.

The Dielectric Relaxation Time and Debye Length

The dielectric relaxation time is an important constant in the temporal dynamics of both the transient and steady-state space-charge fields. Therefore, since an understanding of the dielectric relaxation time is key in understanding the space-charge field dynamics, it is necessary to briefly review this constant before proceeding. In addition, since the Debye length is related to the dielectric relaxation time, we also discuss this constant in the context of our experiments.

The dielectric relaxation time is generally defined as the time constant associated with the exponential decay of a perturbation in a material's majority carrier density (and the resulting space-charge field), where the mechanism responsible for destroying the carrier density perturbation is drift due to the induced space-charge field (K. Seeger, 1985). Not surprisingly, the dielectric relaxation time is proportional to the material permittivity, and inversely proportional to the carrier density and mobility ($\tau_{die} = \varepsilon/ne\mu$). In this thesis, solution of the carrier transport equations yields the dielectric relaxation time as the time constant for an equivalent but converse process: the *build-up* of the space-charge field due to the diffusion of free carriers. As we will see, the space-charge fields that are generated in our experiments can have a significant effect on carrier transport. Thus, for the purposes of this thesis, we define the dielectric relaxation time as

the characteristic time for the build-up of the space-charge field, such that drift plays a significant role in carrier transport. Similarly, since the Debye length is generally defined as the length that carriers diffuse in the dielectric relaxation time (K. Seeger, 1985), in the context of our experiments, the Debye length can be thought of as the characteristic distance that carriers can travel in forming an appreciable space-charge field.

3.3 The Transient Space-Charge Fields

Having reviewed the steady-state space-charge field, we now discuss the magnitude and dynamics of the transient space-charge fields that are generated in our experiments. We have already shown in Chapter II that for our experimental conditions, excitation of the semi-insulating GaAs and undoped CdTe crystals produces, respectively, electrons, holes and ionized EL2, and electrons and holes. Thus, in this section we discuss two illustrative transient space-charge fields; the field between equal populations of ionized EL2 and electrons, and the Dember field, which is the field between equal populations of electrons and holes. In each case, in order to give the reader an intuitive and reasonably accurate description of the picosecond carrier and field dynamics, we begin by discussing the solution to the carrier transport and field equations in the low modulation limit. However, while this approximation allows these equations to be solved analytically, our experiments are conducted with a (high) unity modulation ratio. Therefore, we follow this procedure by numerically solving the carrier transport and field equations in the high modulation limit. This section should be considered the most

important of this chapter, as it provides background that is necessary for understanding fluence- and probe delay-dependencies of the diffraction efficiencies that we measure.

3.3.1 Fundamental Equations

The equations that are used for modeling transient space-charge field formation are well established. These equations, which include the carrier generation equations developed in Chapter II along with equations and terms to include the effects of carrier transport and space-charge field formation, have been used to model photorefraction (A.L. Smirl et al., 1988) and transient energy transfer (G.C. Valley, 1988) on picosecond time scales. These equations are:

$$\frac{\partial n}{\partial t} = \frac{\beta_e \left(N - N^+\right) I}{h\nu} + \frac{\beta I^2}{2h\nu} + \frac{1}{e}\nabla \cdot j_e, \tag{3.9}$$

$$\frac{\partial p}{\partial t} = \frac{\beta_h N^+ I}{h\nu} + \frac{\beta I^2}{2h\nu} - \frac{1}{e}\nabla \cdot j_p, \tag{3.10}$$

$$\frac{\partial N^+}{\partial t} = \frac{\beta_e (N - N^+) I}{h\nu} - \frac{\beta_h N^+ I}{h\nu}, \tag{3.11}$$

$$j_e = \mu_e k_B T \nabla n + e\mu_e E_{sc} n, \tag{3.12}$$

$$j_p = -\mu_p k_B T \nabla p + e\mu_p E_{sc} p, \tag{3.13}$$

and

$$\nabla \cdot E_{sc} = \frac{e}{\varepsilon}\left(p + N^+ - n - A^-\right). \tag{3.14}$$

Every quantity in these equations has been previously defined except j_e, j_p, and μ_p, which are the electron and hole current density vectors, and the hole mobility. Equations (3.9)

and (3.10) can be seen to be continuity equations involving the carrier generation rates, and the divergence of the carrier current densities. Since the photovoltaic transport length is much less than the diffusion lengths in semiconductors, carrier transport due to the photovoltaic effect has been neglected from equations (3.12) and (3.13) (A.M. Glass and J. Strait, 1988). Equation (3.14) is simply Gauss' Law, which relates the divergence of the space-charge field to the charge density and permittivity constant.

In comparing equations (3.9) – (3.14) with the carrier generation equations of Chapter II, it is immediately obvious that equations (3.9) – (3.12) do not consider carrier recombination. This is because the carrier recombination times that are characteristic of these experiments are much larger than the field formation times. For example, as was shown in Chapter II, the minimum electron recombination time in our semi-insulating GaAs crystal is ~7ns. In contrast, the maximum field formation time in GaAs, which is the time required for free electrons to diffuse across the grating period, is ~5ps. The large discrepancy between the carrier recombination and diffusion times is key to an important difference between the steady-state and transient space-charge fields. Since the steady-state space-charge field arises from a charge separation between immobile species, carrier recombination plays a vital part in field formation (see section 3.2). However, as we will see in the remainder of this chapter, the transient space-charge fields arise from charge separations involving free carriers, so that carrier recombination is not necessary in forming these fields. This result will be shown to have several important ramifications in the discussions that follow.

It must be further noted that in this analysis, we will assume that carrier thermalization (the process by which the photogenerated electrons come to equilibrium amongst themselves) and cooling (the process by which the electrons come to equilibrium with the lattice) occur instantaneously. In making this assumption, we assume that carrier transport occurs at a constant lattice temperature of 300K and that the carrier mobilities are the measured drift mobilities. For the purpose of estimation in this chapter, we use values of $5000cm^2/V\text{-}s$ and $400cm^2/V\text{-}s$ (G.C. Valley et al., 1989), respectively, for the electron and hole mobilities in GaAs, and electron and hole mobilities of $1050cm^2/V\text{-}s$ and $90cm^2/V\text{-}s$, respectively, for CdTe (M. S. Petrovic et al., 1991). In Chapter VII and VIII, where we discuss our undoped CdTe and semi-insulating GaAs experimental results, we use the ambipolar decay constant to independently measure the hole mobilities for these materials. In using the above carrier mobilities, we are assuming that the carriers are in thermal equilibrium at the lattice temperature throughout our experiments. As we discussed in Chapter II, this assumption is not completely valid. However, making this assumption allows us to describe carrier transport and field formation with a (relatively) simple set of equations.

In equations (3.9) – (3.14), carrier transport is taken into account through the divergence of the electron and hole current densities which are given by equations (3.12) and (3.13). Since the space-charge fields are generated as a result of carrier transport, many of the concepts that are discussed in this chapter are directly related to the terms in equations (3.12) and (3.13), and their interplay. Therefore, before proceeding, it is necessary to discuss these equations in greater detail. The electron and hole current

densities each contain components describing the diffusion of carriers due to spatial gradients in carrier density ($\tilde{N}n$ and $\tilde{N}p$) and drift due to the generated space-charge field. Both current densities show that free electrons and holes diffuse from areas of greater concentration to areas of lesser concentration. In the case of the electron current density, this follows from the fact that the motion of the electrons is in the direction *opposite* from the direction of the electron current density. In our experiments, where there is no applied electric field, electronic diffusion displaces negative charge to areas where the electron concentration is least, resulting in a space-charge field vector that points from the maxima of the t=0 carrier distributions to the minima of the t=0 carrier distributions. In light of this and the direction of the electron motion relative to the electron current density, equation (3.12) shows that electronic drift *opposes* electronic diffusion. However, equation (3.13) shows that hole drift is in the same direction as hole diffusion, and therefore acts with diffusion to destroy the gradient in carrier density. Thus, in the experiments described in this thesis, electronic diffusion is opposed by electronic drift due to the space-charge field, while hole diffusion and drift are in the same direction.

The interplay between the electronic diffusion and drift currents has already been shown to be important in the formation of the steady-state space-charge field. In the remainder of this section, we will see that this interplay is key in the formation of both the transient space-charge fields. Not surprisingly, in the case of the transient space-charge field between free electrons and ionized EL2, the diffusion/drift interplay produces similar results as were seen with the steady-state space-charge field. In the case of the transient space-charge field between electrons and holes, this interplay will be shown to cause the

free electrons and holes to diffuse together. Called ambipolar diffusion, this process destroys the space-charge field between electrons and holes.

3.3.2 Transient Space-Charge Fields – Electrons and Ionized EL2

The carrier and field equations given above (equations (3.9) – (3.14)) are solved in Appendix C in the limit of a small modulation, and where the free carriers are assumed to be generated instantaneously. In solving these equations, we find that they are most easily discussed in terms of two limits of carrier transport. These limits, which we call the diffusion and drift limits, are dictated by the carrier density, and reflect the importance of electronic drift (due to the space-charge field) in carrier transport. Since the relative importance of diffusion and drift are dependent on carrier density, it is necessary to define a critical carrier density at which diffusion and drift contribute easily. Thus, before discussing the solutions to equations (3.9) – (3.14), it is necessary to discuss this carrier density.

Diffusion and Drift – The Critical Carrier Density

In solving the equations (3.9) – (3.14) we find that the magnitude and dynamics of the electron density and space-charge field depend on two constants:

$$\Gamma_{die} = \frac{n_0 \mu_e e}{\varepsilon}, \qquad (3.15)$$

and

$$\Gamma_{Dn} = \frac{(2\pi)^2 \mu_e k_B T}{\lambda_g^2 e}, \qquad (3.16)$$

which are the inverse of the dielectric relaxation time and the time required for electrons to diffuse across the grating period. Clearly, the magnitude and dynamics of the carrier density and field will be dominated by the dielectric relaxation rate at high carrier densities, and by the electronic diffusion rate at low carrier densities. The electronic diffusion and dielectric relaxation rates are equal at the critical carrier density:

$$n_{0crit} = \frac{(2\pi)^2 k_B T \varepsilon}{e^2 \Lambda_g^2}, \qquad (3.17)$$

that is ~$2.5 \times 10^{14} cm^{-3}$ for semi-insulating GaAs. For carrier densities less than n_{0crit}, $\Gamma_{Dn} > \Gamma_{die}$, and electronic diffusion dominates the carrier and field dynamics. Conversely, for carrier densities above this value, $\Gamma_{die} > \Gamma_{Dn}$, and electronic drift dominates the carrier and field dynamics. In the following paragraphs we consider the solution to the above equations in these two limits: when $\Gamma_{Dn} >> \Gamma_{die}$, and when $\Gamma_{die} >> \Gamma_{Dn}$.

$\Gamma_{Dn} >> \Gamma_{die}$ – The Diffusion Limit of Carrier Dynamics

At low carrier densities, where $\Gamma_{Dn} >> \Gamma_{die}$, the time dependent modulated free electron density (equation (C.16)) reduces to;

$$n_1(t) \approx n_1(0) e^{-\Gamma_{Dn} t}. \qquad (3.18)$$

Under these circumstances, the modulated free electron density can be seen to decay exponentially with a time constant that is characteristic of the diffusion of electrons across the grating period. At $t=\infty$, the modulated free carrier density is zero, so that a spatially uniform free electron density exists within the material. This free electron density will persist in the material until it is destroyed by electron/ionized EL2 recombination (see

Chapter II), and this has been shown to result in the steady-state space-charge field (see section 3.2). Recalling the discussion of section 3.3.1, the above situation corresponds to one where, at all times, carrier transport is dictated by the diffusion current density. Under these circumstances, diffusion results in a space-charge field, but the field is never large enough so that electronic drift significantly opposes diffusion, and diffusion completely destroys the modulated carrier density. Thus, the limit where $\Gamma_{Dn} >> \Gamma_{die}$ corresponds to the diffusion limit of carrier transport.

In the limit where $\Gamma_{Dn} >> \Gamma_{die}$, the transient space-charge field (equation (C.17)) reduces to;

$$E_{sctr} \approx -imE_q'\left(1-e^{-\Gamma_{Dn}t}\right). \qquad (3.19)$$

Here E_q' is given by the equation:

$$E_q' = \frac{e\ell_g N_1^+}{2\pi\varepsilon}. \qquad (C.18)$$

Equation (3.19) shows that the space-charge field forms exponentially with a time constant characteristic of the diffusion of free electrons across the grating period. Using values for the grating period (1.7μm) and the electron drift mobility, we can see that the characteristic field formation time (Γ_{Dn}^{-1}) in GaAs is roughly 5.5ps. Referring to the discussions of the previous section, this can be considered the fundamental formation time for the photorefractive nonlinearity in semi-insulating GaAs.

Equation (3.19) shows that, at t=∞, when the modulated free carrier density has been completely destroyed, the field magnitude is E_q'. The field E_q' can be seen to be nearly identical to E_q (equation (3.5)), the steady-state field magnitude that results when

diffusion dominates carrier transport. Like E_q, E_q' is the maximum space-charge field that can be generated at any grating spacing. However, while E_q was produced from a charge separation between negatively charged acceptors and a modulated density of ionized EL2, E_q' results from a charge separation between a spatially uniform density of free electrons and a modulated density of ionized EL2. As a result, while the maximum steady-state space-charge field is limited by the density of charge that can be trapped in the material (through the effective trap density, N_T), the maximum transient space-charge field is limited by the density of neutral EL2 that can be photoionized (N_1^+). This difference is not surprising, and follows from the role that recombination plays in forming the steady-state and transient space-charge fields.

Close inspection of E_q' (equation (C.18)) might seem to indicate that it is possible to generate an arbitrarily large space-charge field through transient excitation (through the presence of N_1^+). If this were possible, it would be a major contrast between E_q' and the equivalent steady-state field E_q (equation (3.5)), which is limited by the amount of charge that can be trapped in the material. However, in practical situations, the magnitude of E_q' is limited by saturation of the EL2 transition. Recalling the discussion of section 2.2.4, under transient excitation conditions, the maximum density of ionized EL2 that can be generated by photoexcitation is N^+_{sat} (equation (2.17)), the ionized EL2 density where the hole generation rate is equal to the electron generation rate. Therefore, the maximum free electron/ionized EL2 space-charge field that can be generated in our semi-insulating GaAs crystal is:

$$E'_{q\max} = \frac{e\Lambda_g N^+_{sat}}{2\pi\varepsilon}.$$

We can estimate the magnitude of E'_{qmax} using the value for N^+_{sat} (given in section 2.2.4), along with our grating spacing of 1.7μm, and the GaAs permittivity ($12.04 \times 8.854 \times 10^{-14}$ F/cm). These values yield a field magnitude of ~27kV/cm.

It is important to note that, while E'_{qmax} is the maximum free electron/ionized EL2 transient space-charge field that can be generated in our semi-insulating GaAs for the experimental conditions, it is *not* the space-charge field magnitude that would be observed in the diffusion limit of carrier dynamics. This follows from the fact that the value of N^+_{sat} (6.8×10^{15}cm^{-3}), which is an order of magnitude larger than n_{0crit}, so that the criteria for diffusion limited dynamics ($\Gamma_{Dn} >> \Gamma_{die}$) is not met. In order to estimate the field magnitude that would be observed in the diffusion limit of carrier dynamics, we use a carrier density which is less than n_{0crit}, along with the grating spacing and permittivity value given above. Using a carrier density of 1×10^{12}cm^{-3} (corresponds to $\Gamma_{die}=7.5 \times 10^{9}$s^{-1}), equation (C.18) yields a field value of ~4V/cm.

<u>$\Gamma_{die} >> \Gamma_{Dn}$ – The Drift Limit of Carrier Dynamics</u>

For carrier densities above the critical carrier density, where $\Gamma_{die} >> \Gamma_{Dn}$, the time dependent modulated free electron density reduces to:

$$n_1(t) \approx n_1(0). \qquad (3.20)$$

This result describes the situation where electronic diffusion quickly produces a large enough space-charge field so that the electronic drift and diffusion current densities

balance, and electronic diffusion ceases. Under these circumstances, the modulated carrier density decays only slightly before this balance is met, so that the modulated carrier density changes little from its initial value. This is the drift limit of carrier transport that was described previously.

In this same limit ($\Gamma_{die} >> \Gamma_{Dn}$), $E_D/E'_q << 1$, and the transient space-charge field (equation (C.17)) reduces to;

$$E_{sctr} \approx -imE_D\left(1-e^{-\Gamma_{die}t}\right). \qquad (3.21)$$

Thus, the field rises exponentially to the magnitude, E_D (equation (3.6)), and the formation constant is Γ_{die}^{-1}. We can arrive at the drift-limited field magnitude separately by considering the situation described in the previous paragraph, where the electronic drift and diffusion current densities balance. Under these circumstances,

$$ne\mu_e E_{sctr} = \mu_e k_B T \nabla n. \qquad (3.22)$$

If we use equations (C.10) and (3.20) to determine the carrier density, and use the relationship between the n_0 and n_1 components of the carrier density, we find that the magnitude of the space-charge field is given by E_D. For a grating spacing of 1.7μm and a lattice temperature of 300K, equation (3.6) yields a drift-limited field magnitude of ~95V/cm (m=0.1).

Equation (3.21) shows that the drift limited field formation constant is the dielectric relaxation time ($\Gamma_{die}^{-1} = \tau_{die} = \varepsilon/n_0 e\mu_e$). This is not surprising, since the dielectric relaxation time is the characteristic time for field formation due to the diffusion of free carriers. At the highest excitation fluences used in these experiments, we generate carrier

densities as high as ~$1x10^{17}$ cm^{-3} in our GaAs crystal. Under these circumstances, G_{die} ($7.5x10^{13}$ s^{-1}) is much greater than G_{Dn} ($1.8x10^{11}s^{-1}$), so that the resulting space-charge field forms according to the drift limit of carrier dynamics, and the corresponding dielectric relaxation time is ~13fs. If we use this dielectric relaxation time together with the electron diffusion coefficient for semi-insulating GaAs, we can determine the Debye length ($l_s = [D_n t_{die}]^{1/2}$), which is the distance that free carriers can diffuse in forming the space-charge field. Using the Einstein relation between the electron mobility and diffusion coefficient ($D_n = \mu_e k_B T/e$), we find a Debye length of ~$1.2x10^{-2}$ μm for this carrier density. Thus, for the peak carrier densities generated in our experiments, the modulated carrier density decays little before the diffusion/drift balance is reached, and equation (3.20) is an excellent approximation.

Together with the discussions of the previous paragraphs, equations (3.6) and (3.22) give an idea of how hot carrier transport leads to an increased transient space-charge field magnitude. As discussed above, the drift-limited space-charge field magnitude is dictated by the diffusion/drift current density balance (equation (3.22)). Under these circumstances, the space-charge field magnitude is given by E_D (equation (3.6)). If we assume that carrier thermalization occurs instantaneously with respect to carrier transport, then the free electron population is represented by a Fermi-Dirac distribution function with an elevated temperature. Then, the electron diffusion current density is increased as a result of its dependence on carrier temperature. However, since the drift-limited field magnitude is determined by the balance described above, the space-charge field magnitude must increase in order for this balance to be met. This can be

easily seen by noting that E_D increases as the electron temperature increases. Thus, in the drift limit of carrier dynamics, hot carrier transport results in an increased space-charge field.

Carrier Density Dependence of Space-Charge Field Magnitude

In considering the electron/ionized EL2 transient space-charge field, it is important to consider the dependence of the space-charge field on carrier density. In later chapters, where the experimental results are considered, the behavior described here will be compared with diffraction efficiency versus fluence data to aid in associating the diffracted signal with the photorefractive nonlinearity.

The carrier density dependence on the space-charge field magnitude is given by the magnitude of the transient space-charge field (equation (C.17)), and equations (3.6) and (C.18). The transient space-charge field magnitude is plotted in figure 3.3 as a function of dc carrier density (n_0) for a grating spacing of 1.7 μm, and a modulation ratio of 0.1. In addition, we have included two lines on the plot; lines to illustrate E_q' and the critical carrier density at which diffusion and drift play equal parts in forming the field.

The carrier density dependence of the space-charge field follows directly from the field magnitude in the diffusion and drift limits of carrier transport. At low carrier densities, in the diffusion limit of carrier transport, the space-charge field magnitude follows E_q', and depends linearly on the free carrier density (equations (C.18) and (3.19)). At high carrier densities, in the drift limit of carrier transport, the space-charge field magnitude is constant at E_D, and is therefore independent of carrier density (equations

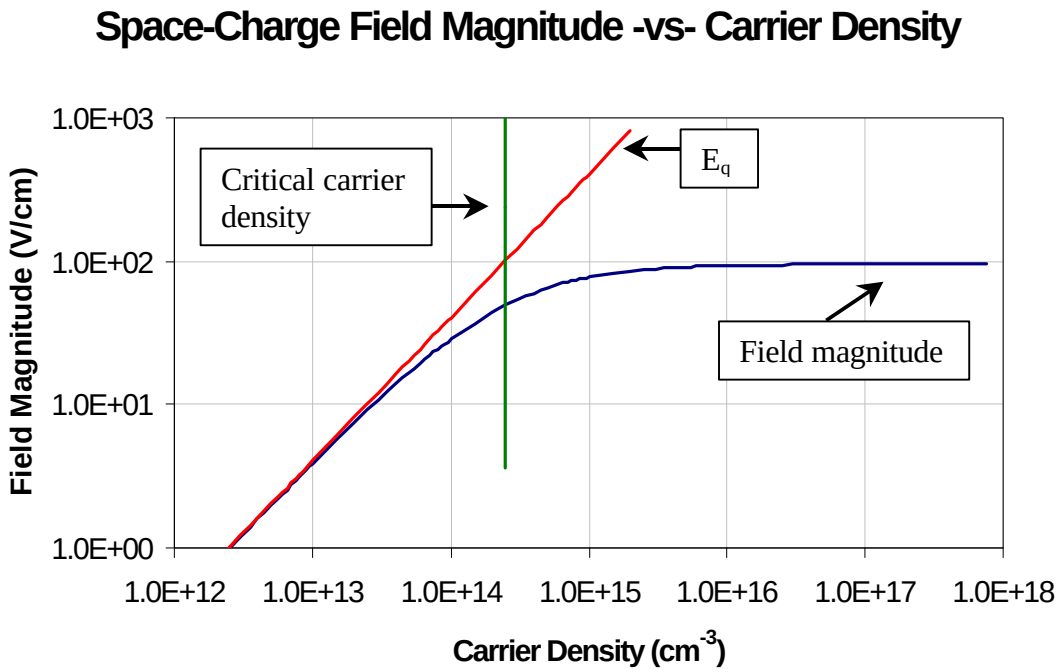

Figure 3.3 – Dependence of the space-charge field magnitude on dc carrier density for a 1.7μm grating period. The space-charge field is due to equal populations of electrons and ionized EL2.

(3.6) and (3.21)). At intermediate carrier densities, the space-charge field magnitude increases sub-linearly with carrier density. In our experiments, we generate free carrier densities that are always greater than or equal to the critical carrier density. Thus, while our experimental results are expected to exhibit drift-limited carrier dynamics, when we monitor the fluence dependence of the photorefractive diffraction efficiencies, we expect the diffraction efficiencies to increase at a rate less than the carrier generation rate.

3.3.3 Electrons and Holes

In this section, we summarize the solution to equations (3.9) – (3.14) for equal populations of electrons and holes, which is considered in section C.4. As in the previous section, it is convenient to discuss the solution to these equations in terms of the diffusion

and drift limits of carrier dynamics. However, since ambipolar diffusion is an important concept in discussing the solutions to these equations in both limits, we begin by reviewing this transport process. The space-charge field that is generated between electrons and holes is the Dember field, and arises as a result of the disparity between the diffusion rates of these species. Since this field is between two mobile species, it decays in times less than 1ns (for typical conditions in GaAs and CdTe) and is therefore unique to transient photorefractive experiments. In our experiments, large populations of electrons and holes are generated in both GaAs and CdTe as a result of the carrier generation processes discussed in Chapter II. Thus both materials can be expected to exhibit a substantial Dember field-related photorefractive nonlinearity.

Ambipolar Diffusion

Before discussing the solutions to equations for the case of electrons and holes, it is necessary to review ambipolar diffusion, and the interplay that occurs between the electron and hole current densities. Just as the interplay between the electron diffusion and drift current densities dictated the magnitude and dynamics of the electron/ionized EL2 space-charge field, the magnitude and dynamics of the electron/hole space-charge field are dictated by the interplay between the electron and hole current densities.

Recalling the discussion of section 3.3.1, the modulated electron density decays faster than the modulated hole density, a result that gives rise to a charge separation and space-charge field. However, while the drift portion of the electron current density acts to oppose electron diffusion, the drift portion of the hole current density acts to enhance hole

diffusion. As a result, when the magnitude of the space-charge field is large enough, the electron and hole current densities balance, and the electron-hole pairs diffuse together as a single equivalent carrier species. This transport process, which is called ambipolar diffusion, is responsible for destroying the modulated electron and hole carrier densities, as well as the space-charge field.

To gain a better analytical understanding of ambipolar diffusion, we can use the electron and hole current densities (equations (3.12) – (3.13)) to form an equivalent current density (j_{eq}) for the electron-hole pairs. Since the same space-charge field appears in both current densities, the equivalent current density can be formed by first solving for the electron current density (j_e) in terms of the space-charge field, and then substituting this result into the hole current density (j_p). Following this, if we use the fact that the current densities balance ($j_e + j_p = 0$) for the situation of interest, we find the equivalent current density, j_{eq}:

$$j_{eq} = \mu_A k_B T \nabla n, \qquad (3.23)$$

in terms of the gradient in the electron-hole pair density (∇n), and the ambipolar mobility (μ_A) of the electron-hole pairs. The ambipolar mobility is related to the electron and hole densities (n, p), the electron and hole mobilities (μ_e, μ_h) and the modulations of the electron and hole densities (m_e, m_h) through the equation:

$$\mu_A = \frac{(m_h p + m_e n)\mu_e \mu_h}{n\mu_e + p\mu_h}. \qquad (3.24)$$

Thus, equations (3.23) and (3.24) show that the overall effect of the electron-hole (Dember) space-charge field is to force the carriers to diffuse together as a single

equivalent species. This diffusion, which destroys the modulated density of electron-hole pairs and the modulated space-charge field, occurs according to the ambipolar mobility. The ambipolar mobility can range in value from the hole mobility to the electron mobility, depending on the density of carriers present, and the carrier modulation. In the paragraphs below, we will discuss the ambipolar mobility in light of our experimental conditions and the diffusion and drift limits of carrier and field dynamics.

$\Gamma_{Dn}\,\Gamma_{Dp} >> \Gamma_{die}, \Gamma_{dip}$ – The Diffusion Limit of Carrier Dynamics

For carrier densities much less than the critical carrier density of $2.5\text{x}10^{14}\text{cm}^{-3}$ (n_{0crit}, equation (3.33)), $\Gamma_{Dn}\,\Gamma_{Dp} >> \Gamma_{die}, \Gamma_{dip}$, and equations (C.22) – (C.24) reduce to:

$$n_1(t) \approx n_1(0)\left[e^{-\frac{\Gamma_{DA}t}{2}}\left(\frac{\Gamma_{Dp}}{\Gamma_{Dn}+\Gamma_{Dp}}\right)+\left(\frac{\Gamma_{Dn}}{\Gamma_{Dn}+\Gamma_{Dp}}\right)e^{-\Gamma_{Dn}t}\right], \tag{3.25}$$

$$p_1(t) \approx p_1(0)\left[e^{-\frac{\Gamma_{DA}t}{2}}\left(\frac{\Gamma_{Dn}}{\Gamma_{Dn}+\Gamma_{Dp}}\right)+\left(\frac{\Gamma_{Dp}}{\Gamma_{Dn}+\Gamma_{Dp}}\right)e^{-\Gamma_{Dn}t}\right], \tag{3.26}$$

and

$$E_{sctr} \approx -imE'_{qnp}\left(e^{-\frac{\Gamma_{DA}}{2}t}-e^{-\Gamma_{Dn}t}\right). \tag{3.27}$$

The space-charge field magnitude E'_{qnp} is:

$$E'_{qnp}=\frac{e\Lambda_g n_1(0)}{2\pi\varepsilon}\left[\frac{\mu_e-\mu_p}{\mu_e+\mu_p}\right], \tag{3.28}$$

and is defined as such because of its similarity to E_q and E'_q. The constant $\Gamma_{DA,}$ which is the ambipolar diffusion rate for the 1.7μm grating period and equal populations of

electrons and holes, is defined in a similar way as the electron and hole diffusion rates ($\Gamma_{DA} = \tau_{DA}^{-1} = (2\pi)^2 \mu_A k_B T / \lambda_g^2 e$). The ambipolar mobility that is used in Γ_{DA} is that which results from equation (3.24), when equal populations of electrons and holes and equal electron and hole carrier density gradients are present:

$$\mu_A = \frac{2\mu_n \mu_p}{\mu_n + \mu_p}. \qquad (3.29)$$

For the materials studied in this thesis, the electron mobility is roughly an order of magnitude larger than the hole mobility ($\mu_e/\mu_p \approx 12.5$ for semi-insulating GaAs, $\mu_e/\mu_p \approx 11.5$ for undoped CdTe). Thus, in deriving the above equations we have used the fact that, in both materials, $\Gamma_{Dn} \sim 10\Gamma_{Dp}$, so that $\mu_A \sim 2\mu_p$ and $\Gamma_{DA}/2 \sim \Gamma_{Dp}$. Though the constant $\Gamma_{DA}/2$ is nearly equal to Γ_{Dp}, we have used $\Gamma_{DA}/2$ in the above equations for reasons that will be made obvious in the paragraphs below.

Equations (3.25) and (3.26) describe the dynamics of the modulated electron and hole populations in terms of two exponentially-decaying components. In both cases, the rates associated with these terms are the electronic diffusion rate (Γ_{Dn}), and one half the ambipolar diffusion rate ($\Gamma_{DA}/2$). In both equations, the fraction of the modulated carrier density that decays according to each rate is given by the ratio of the electron and hole diffusion rates to their sum. For example, since $\Gamma_{Dn}/(\Gamma_{Dn} + \Gamma_{Dp})$ is approximately equal to one for our experimental conditions, equation (3.25) tells us that a very large fraction of the modulated free electron density decays according to the electron diffusion rate. In contrast, since $\Gamma_{Dp}/(\Gamma_{Dn} + \Gamma_{Dp})$ is much less than one, equation (3.26) tells us that a very

small fraction of the modulated hole density decays according to the same rate. This result is not surprising, since the hole mobility is much less than the electron mobility.

Equations (3.25) - (3.27) give the following picture of carrier transport and space-charge field formation. Since the electron mobility is larger than the hole mobility, the modulated electron density is destroyed more quickly than the modulated hole density, a result that gives rise to a charge separation and space-charge field. In equations (3.25) and (3.49), this is reflected in the fact that the fraction of the modulated electron population which decays via the electron diffusion rate ($G_{Dn}/(G_{Dn} + G_{Dp})$) is much larger than the fraction of the modulated hole population that decays via the same rate ($G_{Dp}/(G_{Dn} + G_{Dp})$). As can be seen from equation (3.28), this disparity also dictates the peak magnitude of the space-charge field ($G_{Dn} - G_{Dp}/(G_{Dn} + G_{Dp}) = m_n - m_p/(m_n + m_p)$). Even though the space-charge field is weak (due to the low carrier density), it still affects carrier transport by causing the electrons to diffuse together with the holes at the ambipolar mobility. This is reflected in the equations for the modulated electron (3.25) and hole (3.26) densities by the presence of the exponentially-decaying term involving one half the ambipolar diffusion rate. However, as can be seen by comparing the two terms in equation (3.25), ambipolar diffusion does not significantly affect the decay of the modulated electron density until $t \geq 3t_{Dn}$. As a result, since the modulated electron density has decayed to less than e^{-3} of its initial value by this time, the ambipolar mobility is equal to one half the value given by equation (3.29), which is what is expected for an electron modulation of zero ($m_e \neq 0$, equation (3.24)).

Thus in the low carrier density limit, the modulated electron and hole densities decay nearly independently. While the space-charge field rises with the decay of the modulated electron population, it decays with the decay of the modulated hole population. The peak space-charge field reflects a charge separation where the modulated hole density is nearly equal to its initial value, and the modulated electron density is nearly equal to zero. The characteristic rise time of the diffusion-limited Dember field can be approximated by the electron diffusion time, which is ~5.5ps in semi-insulating GaAs and ~26ps in undoped CdTe (for a 1.7μm grating period). The space-charge field decays with the decay of the modulated hole population, which is ~69ps for semi-insulating GaAs and ~310ps for undoped CdTe for our 1.7μm grating periods. Equation (3.28) can be used to estimate the peak magnitude of the diffusion-limited Dember field in both semi-insulating GaAs and undoped CdTe. Using a modulated free carrier density of $1x10^{12}cm^{-3}$, we estimated a field magnitude of ~4V/cm for the electron/ionized EL2 field. Using this value, along with the electron and hole mobilities for semi-insulating GaAs (μ_e = $5000cm^2$/V-s, μ_p = $400cm^2$/V-s), we find a field magnitude of ~3.4V/cm. For undoped CdTe, we use the same carrier density, a relative permittivity of 10.4 (K. Zanio, 1978), and the electron and hole mobilities ($1050cm^2$/V-s and $90cm^2$/V-s) (M. Petrovic et. al, 1991), to find a field magnitude of ~4.0V/cm.

Γ_{die} Γ_{dip} >>Γ_{Dn}, Γ_{Dp} – The Drift Limit of Carrier Dynamics

In the drift limit of carrier dynamics ($n_0 >> n_{0crit}$, G_{die} G_{dip} >>G_{Dn}, G_{Dp}), equations (C.22) – (C.24) reduce to:

$$n_1(t) \approx n_1(0)\left[e^{-\Gamma_{DA}t}\left(\frac{\Gamma_{die}+\Gamma_{dip}-\Gamma_{Dn}}{\Gamma_{die}+\Gamma_{dip}}\right)+\left(\frac{\Gamma_{Dn}}{\Gamma_{die}+\Gamma_{dip}}\right)e^{-(\Gamma_{die}+\Gamma_{dip}-\Gamma_{DA})t}\right], \tag{3.30}$$

$$p_1(t) \approx p_1(0)\left[e^{-\Gamma_{DA}t}\left(\frac{\Gamma_{die}+\Gamma_{dip}-\Gamma_{Dp}}{\Gamma_{die}+\Gamma_{dip}}\right)+\left(\frac{\Gamma_{Dp}}{\Gamma_{die}+\Gamma_{dip}}\right)e^{-(\Gamma_{die}+\Gamma_{dip}-\Gamma_{DA})t}\right], \tag{3.31}$$

and

$$E_{sctr} \approx -imE_{Dnp}\left(e^{-\Gamma_{DA}t}-e^{-(\Gamma_{die}+\Gamma_{dip}-\Gamma_{DA})t}\right). \tag{3.32}$$

The space-charge field magnitude E_{Dnp} is:

$$E_{Dnp} = \frac{2\pi k_B T}{\lambda_g e}\left[\frac{\mu_e-\mu_p}{\mu_e+\mu_p}\right], \tag{3.33}$$

which is similar to the space-charge field E_D which appeared in the results for the steady-state and electron/ionized EL2 space-charge fields. Like all the other space-charge fields, the Dember space-charge field is 90° out of phase with the incident irradiance profile.

As in the diffusion limit, equations (3.30) – (3.32) describe the electron, hole and space-charge field dynamics in terms of two exponentially-decaying terms that are characteristic of the system. In this limit, the rates that characterize these terms are the ambipolar diffusion rate (Γ_{DA}), and a composite rate which involves the electron and hole dielectric relaxation rates and the ambipolar diffusion rate ($\Gamma_{die} + \Gamma_{dip} - \Gamma_{DA}$), but is approximately equal to the electron dielectric relaxation rate ($\Gamma_{die} > \Gamma_{dip} >> \Gamma_{DA}$). Just as in the diffusion limit, ratios involving the electron and hole diffusion rates (Γ_{Dn}, Γ_{Dp}) and the sum of the electron and hole dielectric relaxation rates ($\Gamma_{die} + \Gamma_{dip}$) determine the fraction of the modulated electron and hole densities that are associated with each decay. In the

drift limit of carrier dynamics, G_{die} and G_{dip} are at least 2 orders of magnitude larger than G_{DA}, a fact that leads to two important results regarding equations (3.30) – (3.32). First, the exponential decay associated with the composite rate of G_{die}, G_{dip} and G_{DA} can be thought of as occurring instantaneously compared to the decay associated with the ambipolar diffusion rate (G_{DA}). Second, the fractions of the modulated electron and hole populations that decay according to the composite rate are very small compared to the fractions that decay according to the ambipolar diffusion rate.

Equations (3.30) – (3.32) give a picture of carrier and space-charge field dynamics that is similar to that which was seen for the diffusion limit. As in the diffusion limit, diffusive decay of the modulated electron density occurs more quickly than diffusive decay of the modulated hole density. This is reflected in equations (3.30) and (3.31) by the fact that the fraction of the modulated electron density that decays according to the composite rate ($G_{Dn}/(G_{die} + G_{dip})$) is larger than the corresponding fraction of the modulated hole density ($G_{Dp}/(G_{die} + G_{dip})$). The diffusive decay of the electrons and holes quickly leads to a large space-charge field (due to the high carrier density), and the rise time of the field is commensurate with the initial decay of the modulated electron and hole densities. The field reaches it peak value as the electron and hole current densities balance, and thereafter the modulated electron and hole densities decay together via ambipolar diffusion. Under these circumstances, since the modulated electron and hole densities balance before significant decay occurs, the ambipolar mobility is given by equation (3.29).

Equations (3.30) – (3.33) can be used to estimate the rise and decay times of the space-charge field, and the peak field magnitude. Assuming a carrier density of $1x10^{17}cm^{-3}$, we find a field formation time of ~10fs for semi-insulating GaAs and ~55fs for undoped CdTe. Assuming a 1.7μm grating period and the electron and hole mobilities given before, we find an ambipolar decay time of ~35ps for semi-insulating GaAs and ~155ps for CdTe. For a modulation ratio of 0.1, these values yield peak Dember field magnitudes of 81V/cm in semi-insulating GaAs, and 78V/cm in undoped CdTe.

3.3.4 High Modulation Effects

The previous sections considered the carrier and space-charge field dynamics in the small modulation limit. However, our experiments were performed at a unity (high) modulation depth. Thus, the carrier and field dynamics reflected by our experimental results will be slightly different from those that have been presented. In this section we consider these differences. Whereas in the previous section we truncated the Fourier series for the carrier densities, ionized EL2 population and space-charge field after the n=1 components, in this discussion we include higher-order components. Since the resulting equations for the carrier densities and space-charge field can not be solved analytically, we solve these equations numerically and compare the results with those derived in the small modulation limit. Together with the small signal transient grating diffraction efficiency and the relationships between the free carrier density and space-charge field and the free-carrier and photorefractive index changes, the equations given in this section form the basis for the transient-grating diffraction efficiency model that is discussed in Chapter VI.

In modeling the carrier and field dynamics in the high modulation limit, we must include a sufficient number of terms in the Fourier series for the carrier densities and space-charge field so that our numerical model will accurately represents the carrier and field dynamics. However, because there is no reference against which to measure the accuracy of our numerical model, we must use the following method for terminating the Fourier series. We know that as higher-order Fourier components of the space-charge field are considered, the magnitude of the n=1 field component will increase. If we assume that the lower-order components for the carrier densities and field have a higher magnitude than the higher-order components, then when a sufficient number of higher-order components have been included (equation (3.27)), the magnitude of the n=1 component of the space-charge field will converge to a given value. As an arbitrary limit, we choose to truncate the Fourier series directly after the addition of a higher-order carrier and field component changes the peak (n=1) field magnitude by less than 1%. In practice, we find that as we add the n=2,3,4, and 5 components, the peak field magnitude increases successively by 28%, 5%, 1% and 0.3%. Thus, since addition of the n=5 component causes the peak field magnitude to change by only 0.3%, we terminate the Fourier series for the carrier densities and space-charge field after this component.

When the Fourier series for the electron and hole densities and space-charge field are truncated after the n=5 components, the following equations result for the electrons:

$$\frac{\partial n_1}{\partial t} = \frac{-k_g^2 \mu_e k_B T}{e} n_1 + \frac{\mu_e k_g}{2}(2n_0 E_{sc1} + n_1 E_{sc2} - n_2 E_{sc1} + n_2 E_{sc3} - n_3 E_{sc2} + n_3 E_{sc4} - n_4 E_{sc3} + n_4 E_{sc5} - n_5 E_{sc4}), \quad (3.34)$$

$$\frac{\partial n_2}{\partial t} = -\frac{4k_g^2 \mu_e k_B T}{e} n_2 + \mu_e k_g (2n_0 E_{sc2} + n_1 E_{sc1} + n_1 E_{sc3} - n_3 E_{sc1} + n_2 E_{sc4} - n_4 E_{sc2}$$

$$+ n_3 E_{sc5} - n_5 E_{sc3}) \quad (3.35)$$

$$\frac{\partial n_3}{\partial t} = -\frac{9k_g^2 \mu_e k_B T}{e} n_3 + \frac{3\mu_e k_g}{2} (2n_0 E_{sc3} + n_1 E_{sc2} + n_2 E_{sc1} + n_1 E_{sc4} - n_4 E_{sc1}$$

$$+ n_2 E_{sc5} - n_5 E_{sc2}) \quad (3.36)$$

$$\frac{\partial n_4}{\partial t} = -\frac{16k_g^2 \mu_e k_B T}{e} n_4 + 2\mu_e k_g (2n_0 E_{sc4} + n_1 E_{sc3} + n_2 E_{sc2} + n_3 E_{sc1} + n_1 E_{sc5}$$

$$- n_5 E_{sc1}), \quad (3.37)$$

$$\frac{\partial n_5}{\partial t} = -\frac{25k_g^2 \mu_e k_B T}{e} n_5 + \frac{5\mu_e k_g}{2} (2n_0 E_{sc5} + n_1 E_{sc4} + n_4 E_{sc1} + n_2 E_{sc3} + n_3 E_{sc2}), \quad (3.38)$$

holes,

$$\frac{\partial p_1}{\partial t} = \frac{-k_g^2 \mu_e k_B T}{e} p_1 - \frac{\mu_e k_g}{2} (2p_0 E_{sc1} + p_1 E_{sc2} - p_2 E_{sc1} + p_2 E_{sc3} - p_3 E_{sc2} + p_3 E_{sc4}$$

$$- p_4 E_{sc3} + p_4 E_{sc5} - p_5 E_{sc4}), \quad (3.39)$$

$$\frac{\partial p_2}{\partial t} = -\frac{4k_g^2 \mu_e k_B T}{e} p_2 - \mu_e k_g (2p_0 E_{sc2} + p_1 E_{sc1} + p_1 E_{sc3} - p_3 E_{sc1} + p_2 E_{sc4} - p_4 E_{sc2}$$

$$+ p_3 E_{sc5} - p_5 E_{sc3}) \quad (3.40)$$

$$\frac{\partial p_3}{\partial t} = -\frac{9k_g^2 \mu_e k_B T}{e} p_3 - \frac{3\mu_e k_g}{2} (2p_0 E_{sc3} + p_1 E_{sc2} + p_2 E_{sc1} + p_1 E_{sc4} - p_4 E_{sc1}$$

$$+ p_2 E_{sc5} - p_5 E_{sc2}) \quad (3.41)$$

$$\frac{\partial p_4}{\partial t} = -\frac{16k_g^2 \mu_e k_B T}{e} p_4 - 2\mu_e k_g (2p_0 E_{sc4} + p_1 E_{sc3} + p_2 E_{sc2} + p_3 E_{sc1} + p_1 E_{sc5}$$

$$- p_5 E_{sc1}), \quad (3.42)$$

$$\frac{\partial p_5}{\partial t} = -\frac{25 k_g^2 \mu_e k_B T}{e} p_5 - \frac{5 \mu_e k_g}{2}(2 p_0 E_{sc5} + p_1 E_{sc4} + p_4 E_{sc1} + p_2 E_{sc3} + p_3 E_{sc2}), \quad (3.43)$$

and the space-charge field:

$$E_{sc1} = \frac{e}{\varepsilon k_g}(p_1 - n_1), \quad (3.44)$$

$$E_{sc2} = \frac{e}{2\varepsilon k_g}(p_2 - n_2), \quad (3.45)$$

$$E_{sc3} = \frac{e}{3\varepsilon k_g}(p_3 - n_3), \quad (3.46)$$

$$E_{sc4} = \frac{e}{4\varepsilon k_g}(p_4 - n_4), \quad (3.47)$$

$$E_{sc5} = \frac{e}{5\varepsilon k_g}(p_5 - n_5), \quad (3.48)$$

where k_g is the wave number associated with the grating spacing Λ_g.

In solving equations (3.34) – (3.48), we note three high modulation effects. First, as can be seen from figure 3.4, the peak field magnitude is roughly 30% higher than predicted by equations (3.6) and (3.55) when a modulation ratio of near unity is considered. Second, the field formation time increases by as much as 60% from that predicted by equations (3.37) and (3.54). Finally, the Dember space-charge field exhibits an initial, fast decay that is followed by the exponential decay that is predicted by equation (3.32). As discussed in section 3.3.3, the time constant for the latter decay is the ambipolar diffusion time for the grating period.

We can understand the high modulation effects that are noted above by recalling that in the drift limit, the formation constant for the space-charge field is the dielectric relaxation time, and this constant is dependent on carrier density. In the high modulation limit, there is a large variation in the free carrier density from the peaks to the valleys of the carrier modulations, and this leads to a large spatial variation in the field formation time. At the peaks of the modulated carrier densities, where the field formation time is fastest, the electrons diffuse only a short distance before the electron/hole current density balance occurs. However in the valleys, where field formation is much slower, the electrons diffuse much farther before the current density balance occurs. While this results in a longer field formation time and a larger overall charge separation (and n=1 space-charge field), it produces another important result. Since the maximum charge separation is not uniform across the grating spacing, higher-order harmonics of the carrier densities and space-charge field are generated.

The third of the high modulation effects that we observe, the fast decay of the electron-hole space-charge field, is shown in figure 3.4 for the CdTe carrier mobilities and a 1.7μm grating period. While we have included a reference line illustrating the decay of the space-charge field in the low modulation limit, the data are plotted on a semi-logarithmic scale, so that the exponential decay of the low-modulation space-charge field follows a straight line. The initial, fast decay of the high modulation space-charge field can be understood in the following way. Once the peak charge separation is reached and the field begins to decay, the higher-order components of the carrier

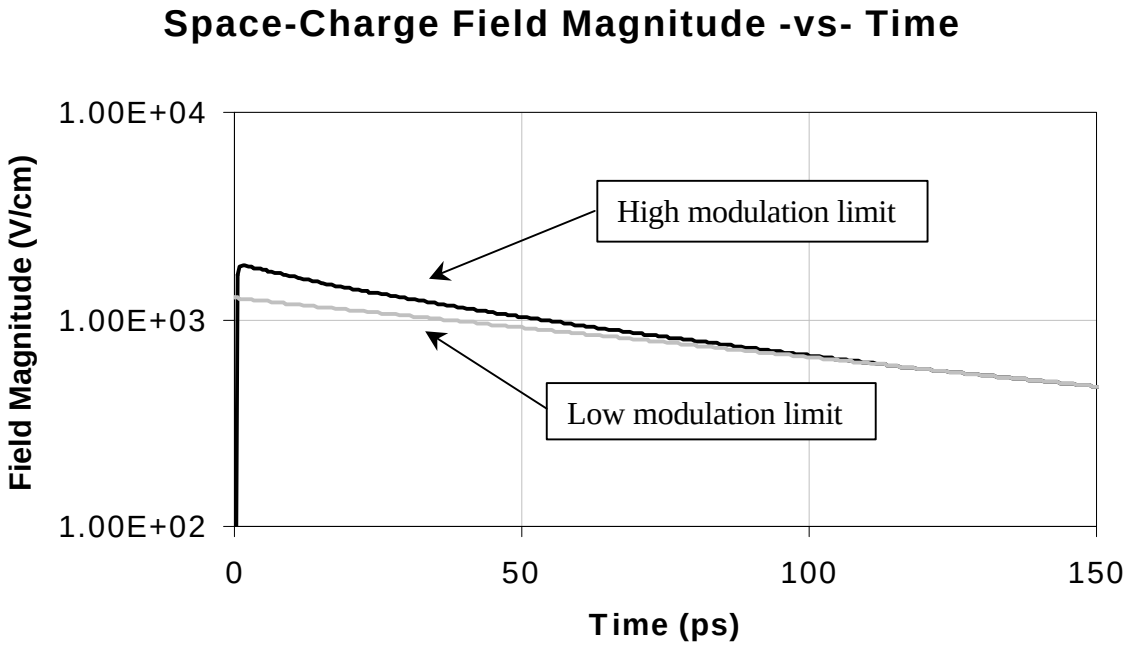

Figure 3.4 – Decay of the electron-hole space-charge field magnitude in the high and low modulation limits. As discussed in the text, the initial fast decay of the field in the high modulation limit follows from the dependence of the n=1 space-charge field on higher-order harmonics of the carrier densities.

densities decay more quickly than the n=1 component. This result follows from the fact that for successively higher harmonics of the carrier densities, the associated ambipolar diffusion times decrease by a factor of n from the ambipolar diffusion time associated with the grating spacing ($t_{DA} = \Lambda_g^2 e/((2\pi)^2 \mu_A k_B T)$). Since the n=1 component of the space-charge field depends on the higher-order carrier densities (through the n=1 electron and hole densities), an initial, fast decay of this space-charge field results. Since the ambipolar diffusion time is dependent on the square of the grating period, and is inversely proportional to the ambipolar mobility, we expect this decay to be most visible in the CdTe results (CdTe has a lesser hole mobility than GaAs) for the longest grating period (3.8μm).

Since our experimental results show an initial enhanced photorefractive diffraction efficiency that is consistent with hot carrier effects, we can not observe the slower field formation and larger field magnitude discussed above. However, we do observe the initial, fast decay of the Dember space-charge field that was described. This is most easily seen in the data for undoped CdTe, where the constant associated with the decay of the photorefractive diffraction efficiency is slightly less than the constant for the decay of the free carrier diffraction efficiency.

3.4 The Linear Electrooptic Effect in Zincblende Semiconductors

The linear electrooptic effect is an optical nonlinearity in which the application of an electric field results in an index change whose magnitude is linearly proportional to the field strength. This optical nonlinearity, which is expressed in the material-dependent electrooptic tensor, only occurs in materials that lack inversion symmetry, and generally results in an anisotropic index change. The linear electrooptic effect is important for the purposes of this thesis because, with space-charge fields such as those discussed in the previous section, it also produces the photorefractive nonlinearity. The purpose of this section is to consider some of the general electrooptic properties of zincblende semiconductors, the magnitude of the photorefractive index changes in these materials, and the properties of the index gratings which result from the generation of space-charge fields such as those discussed in the previous section.

3.4.1 Basic Electrooptic Properties of Zincblende Semiconductors

Zincblende semiconductors such as GaAs and CdTe lack inversion symmetry and, as a result, exhibit a linear electrooptic effect. Since these materials have $\bar{4}3m$ crystal symmetry, the only non-zero components which their (contracted) electrooptic tensors possess are the equal r_{41}, r_{52}, and r_{63} components (i.e., $rij=0$ except r_{41}, r_{52}, and $r_{63} \neq 0$) (A. Yariv, 1985 and S. Namba, 1961). The symmetry of the electrooptic effect in zincblende semiconductors will be later shown to result in anisotropic photorefractive index gratings which, when generated in a properly oriented crystal and probed with a beam of the correct polarization, produce a polarization rotation of exactly 90°. Photorefractive polarization rotation is an important part of the transient-grating measurement technique used in our experiments: the 90° polarization produced by this nonlinearity allows it to be separated from the other competing nonlinearities which do not produce a polarization rotation.

As in other materials, the linear electrooptic nonlinearity in both GaAs and CdTe has electronic and ionic contributions (C. Flytzannis, 1969, I. P Kaminow, 1974, and C.C. Shih and A. Yariv, 1982). These contributions, which are functions of the spectral content of the applied and optical electric fields, give rise to second harmonic generation and Raman effects, respectively. In our experiments, the space-charge fields are generated in times long enough to allow both the electronic and ionic components to contribute to the linear electrooptic response. Including both of these contributions, GaAs and CdTe have

r_{41} elements equal to 1.43pm/V and 5.5pm/V, respectively at a wavelength of approximately 1μm (A. Yariv, 1985).

3.4.2 Magnitude of the Photorefractive Index Change in GaAs and CdTe

In the experiments performed in this thesis, the semi-insulating GaAs and undoped CdTe crystals are orientated so that the photorefractive index change is given by the equation:

$$\Delta n = \frac{1}{2} n_b^3 r_{41} E_{sc} . \qquad (3.49)$$

All of the parameters used in this equation have been identified previously. This equation can be used with (1) the background indices of refraction in GaAs and CdTe, (2) the values given previously for the electrooptic coefficients, and (3) the space-charge field, to estimate the magnitude of the photorefractive index change in these materials. In the drift limit of carrier dynamics, both the electron-ionized EL2 and electron-hole space-charge fields have peak magnitudes of approximately 1kV/cm when a unity modulation is considered. Using this field value with the electrooptic coefficients given above and the background indices of 3.47 for GaAs and 2.82 for CdTe (A. Yariv, 1985), equation (3.49) yields a maximum index changes of 6×10^{-6} in CdTe and 3×10^{-6} in GaAs. These index changes are small in magnitude, but also an order of magnitude smaller than the index changes that are produced by the instantaneous bound electronic and free carrier nonlinearities under similar (high excitation) conditions (see Chapter II). In Chapter V, we will see that this result places two important requirements on our measurement

method. First, since the photorefractive index change is small, we must use thick crystals in our transient grating measurement technique in order to generate measurable photorefractive effects over a wide range of excitation intensities. Second, since the photorefractive nonlinearity is smaller than the other competing nonlinearities, our measurement technique must allow the photorefractive nonlinearity to be separated from the other competing nonlinearities.

3.4.3 Generation of Photorefractive Index Gratings

When periodic space-charge fields such as those described in the previous section are generated in an electrooptic material, a photorefractive index grating is produced. Since the photorefractive index grating arises from the space-charge field, it differs in phase from the modulated intensity pattern in the same way. Thus, for our experimental conditions, the space-charge fields and photorefractive index gratings generated in both semi-insulating GaAs and undoped CdTe differ in phase from the incident intensity pattern by 90°. This phase difference produces the maximum steady-state energy transfer between beams in the simple two beam arrangement shown in figure 3.1, and makes the photorefractive nonlinearity ideal for applications such as those discussed in Chapter I.

3.5 Summary

In this chapter we have discussed the dynamics of the free carrier populations and space-charge fields that are generated under picosecond excitation conditions, and in the low and high modulation limits. Our discussion has considered space-charge fields arising from equal populations of electrons and (immobile) ionized El2, and from equal

populations of electrons and holes. For both of these space-charge fields, the magnitude and dynamics of the field depends on the balance between the carrier diffusion and drift current densities, which is dictated by the carrier densities that are present. In the low carrier density limit, which we have called the diffusion limit, carrier transport and field formation is dominated by the diffusive decay of the modulated carrier populations. As the carrier density is increased above the critical value, which we have determined to be roughly $2.5x10^{14}cm^{-3}$ for semi-insulating GaAs, the magnitude of the space-charge field increases, and the drift current density plays an increasingly important role in carrier transport and field formation. The high carrier density (drift) limit is characterized by a balance between the diffusion and drift portions of the carrier current densities. While the diffusion/drift current density balance causes transport to cease in the case of the electron/ionized EL2 space-charge field, it gives rise to ambipolar diffusion of the electron-hole pairs in the case of the electron-hole (Dember) space-charge field. While the electron-ionized EL2 space-charge field is long-lived, the electron-hole space-charge field decays on picosecond time scales.

The equations that we derive predict maximum space-charge fields of roughly ~1kV/cm for both the materials studied in this thesis. Using literature values for the linear electrooptic coefficients in semi-insulating GaAs and undoped CdTe, this results in maximum photorefractive index changes of roughly $3\text{-}6x10^{-6}$ in these materials.

CHAPTER IV

TWO BEAM COUPLING AND TRANSIENT ENERGY TRANSFER

4.1. Introduction

We have shown in Chapters II and III how illumination of our semi-insulating GaAs and undoped CdTe crystals leads to a variety of absorptive and refractive optical nonlinearities. We have also shown that when our materials are illuminated with two temporally and spatially coincident optical pulses, absorptive and refractive gratings are induced as a result of these optical nonlinearities. However, the optical fields that are responsible for generating these gratings can themselves interact with the induced gratings, a result that can give rise to energy and phase coupling between the beams. In this chapter we consider these two-beam coupling effects in the context of our transient photorefractive experiments.

We begin by reviewing the equations for beam propagation in the two-beam geometry that was shown in Chapter III, in the presence of induced index and absorption gratings and under steady-state conditions. We use these equations to give qualitative descriptions of energy transfer in the steady-state and transient regimes, and then apply the results of these discussions to our picosecond photorefractive measurements. We show that the unique energy transfer properties of the photorefractive grating, which arise from its dependence on the material's electrooptic tensor, allow it to be distinguished

from the other competing effects, including transient energy transfer and energy coupling due to the EL2 absorption grating. This discussion culminates in a description of what has been the only method for measuring picosecond photorefractive effects in semiconductors prior to the experiments described in this thesis. Moreover, while the two-beam coupling method outlined in this chapter allows picosecond photorefractive effects to be measured, it requires the induced gratings to be 'written' and 'read' by the same optical pulses. This precludes an unambiguous measurement of the time evolution of this nonlinearity and therefore dictates the need for the new three-beam, transient-grating measurement method that is discussed in Chapter V.

4.2. Energy Transfer in The Steady-State

Before discussing energy transfer in the steady-state, we outline the process for deriving the equations that describe this phenomenon. This discussion will also serve as a background for section 6.2, where we discuss the beam propagation equations that describe our experiments.

The equations that describe self-diffraction are derived using coupled wave theory (H. Kogelnik, 1969). In general, this theory describes the coupling of 'reference' and 'signal' electric fields via phase-matched interactions with induced index or absorption gratings. In the two-beam coupling effects that we will discuss in this chapter, we consider the coupling of two incident fields such as those shown in the simple two-beam geometry given in chapter III. For convenience, this geometry is shown again in figure 4.1. Since the fields are responsible for generating the permittivity change, they are automatically phase-matched to the induced grating. In addition, since the crystal is

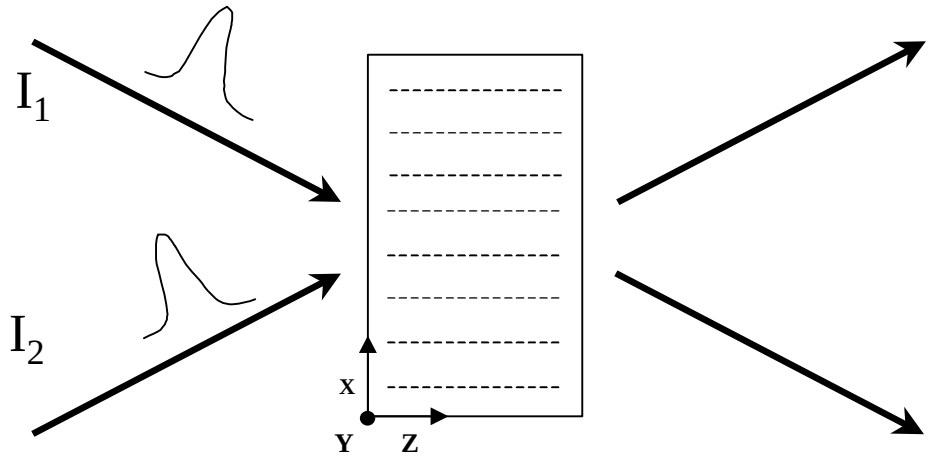

Figure 4.1 – Two-beam geometry used in two-beam coupling and transient energy-transfer experiments.

thick, the coupling that each field experiences is limited to the first-order Bragg reflection from the permittivity grating.

We assume that the electric field inside the material takes the form:

$$E = E_{+1}(z,t)e^{i(k_x x + k_z z - \omega t)} + E_{-1}(z,t)e^{-i(-k_x x + k_z z - \omega t)} + cc\,, \qquad (4.1)$$

where we have assumed that the field magnitudes are complex quantities, oriented along the y direction (perpendicular polarization), and that the fields propagate as plane waves. To derive propagation equations for $E_{\pm 1}$, we substitute equation (4.1) into the wave equation. We assume that the material's relative permittivity takes the form:

$$\varepsilon_r = \varepsilon_{rr} + i\varepsilon_{ri} + \Delta\varepsilon_r(e^{i2k_x x} + e^{-i2k_x x})\,, \qquad (4.2)$$

which allows for linear absorption of the fields through the imaginary part of the dielectric constant (ε_{ri}). We have also included a real induced permittivity grating ($\Delta\varepsilon_r$), which occurs as a result of the interaction of the optical fields with the material (the spatial frequency of $\Delta\varepsilon_r$ is that of the modulated intensity pattern). We have assumed a

general form for the induced permittivity change so that we can derive a general result for energy transfer under steady-state conditions. While we have assumed that the induced permittivity change is real (refractive), this analysis is easily extended to consider permittivity changes that are imaginary (absorptive). Generally, the permittivity grating has a phase that is determined by the material process that is responsible for producing the optical nonlinearity. To simplify this analysis, we set this phase to zero, and measure all other phases relative to the phase of the permittivity grating.

In order to derive simple propagation equations, we make some standard assumptions about the electric fields and the material. First, we assume that the magnitudes of the electric fields do not vary in the x and y directions ($\partial^2 E/\partial x^2$, $\partial E/\partial x$, $\partial^2 E/\partial y^2$, $\partial E/\partial y = 0$). This is equivalent to assuming that the material is infinitely large in the x and y directions, and that the fields propagate along the z direction inside the material. This is a good assumption for experiments like ours, since the optical spot size is made to be small compared to the size of the crystal, and the half-angle between beams that is required to produce our 1.7μm gratings small (< 5° inside the crystal). Next, we assume that the variation of the electric field magnitude with respect to z and t is small compared to the z component of the spatial propagation frequency (k_z) and the optical frequency (ω). This simplifies the process of determining the spatial and temporal derivatives of the fields; terms involving the first and second derivatives of the field magnitude with respect to time ($\partial^2 E/\partial t^2$, $\partial E/\partial t$) can be neglected compared to terms involving $\omega^2 E$, and terms involving the second derivative of the field magnitude with respect to z ($\partial^2 E/\partial z^2$) can be neglected with respect to $k_z^2 E$ and k_z ($\partial E/\partial z$). For

experiments like ours, the validity of this assumption follows from the fact that the optical pulse duration (~1ps) is long compared to the oscillation period of the fields (~2×10^{-14} s), and that any changes to the optical beam intensities are incurred over distances long compared to the inverse of the spatial frequency of the fields (k^{-1} ~ 0.01μm). Finally, it is important to note that, since we are considering energy transfer under steady-state conditions, we assume that the induced permittivity change is constant with respect to time.

The process outlined above produces the following propagation equations for the two complex electric fields:

$$\frac{\partial E_{+1}}{\partial z} = -\frac{\alpha}{2}E_{+1} + i\frac{k\Delta\varepsilon_r}{2}E_{-1}, \qquad (4.3)$$

$$\frac{\partial E_{-1}}{\partial z} = -\frac{\alpha}{2}E_{-1} + i\frac{k\Delta\varepsilon_r}{2}E_{+1}, \qquad (4.4)$$

where we have assumed that the z component of the spatial propagation frequency (inside the material) is approximately equal to its magnitude ($|k| \sim k_z$), used the relationship between the magnitudes of the spatial propagation frequency inside the material and in free space ($k=n_b k_0$), and used the relationship between the linear absorption coefficient and the imaginary component of the relative permittivity ($\alpha = k\varepsilon_{ri}/n_b^2$). These equations can be put into terms that are more easily understood if we assume that each electric field has the general form:

$$E = |E(z)|e^{i\phi(z)},$$

and that any phase change incurred by the fields occurs on spatial scales large compared to the propagation frequency of the optical fields. By substituting this form into

equations (4.3) and (4.4), we can get equations for the two beam intensities and phases of the two fields ($I_{\pm 1}$, $\phi_{\pm}$):

$$\frac{dI_{+1}}{dz} = -\alpha I_{+1} + \frac{k_0 \Delta\varepsilon_r}{n_b} |E_{+1}||E_{-1}| \sin\Delta\phi \ , \qquad (4.5)$$

$$\frac{dI_{-1}}{dz} = -\alpha I_{-1} - \frac{k_0 \Delta\varepsilon_r}{n_b} |E_{-1}||E_{+1}| \sin\Delta\phi \ , \qquad (4.6)$$

$$\frac{d\phi_{+1}}{dz} = \frac{k_0 \Delta\varepsilon_r}{2n_b} \frac{|E_{-1}|}{|E_{+1}|} \cos\Delta\phi \ , \qquad (4.7)$$

$$\frac{d\phi_{-1}}{dz} = \frac{k_0 \Delta\varepsilon_r}{2n_b} \frac{|E_{+1}|}{|E_{-1}|} \cos\Delta\phi \ . \qquad (4.8)$$

In the above equations, $\Delta\phi$ is the phase difference between the modulated intensity pattern (ϕ_+-ϕ_-) and the induced grating, measured relative to the phase of the induced grating. Since the quantity $\Delta\phi$ is measured relative to the phase of the induced grating, it is generally determined by the material process that is responsible for forming the grating. As examples of this, we can consider the instantaneous bound electronic and photorefractive nonlinearities discussed in Chapters II and III. The instantaneous bound-electronic index change for semi-insulating GaAs is $-n_2 I$ (see Chapter II). As a result, the corresponding index grating is 180° out of phase with the modulated intensity pattern. However, in contrast, the photorefractive index change is proportional to the induced space-charge field, which we have seen is 90° out of phase with the incident intensity

pattern. As we will see below, these two index gratings can be expected to effect the beams in different ways in the geometry given in figure 4.1.

Equations (4.5) – (4.8) illustrate two important points about energy transfer under steady-state conditions. First, the equations show that the beam intensities are coupled through the induced permittivity change, and the beams can experience gain or loss as a result of this coupling. Equations (4.5) and (4.6) show that energy transfer between the beams is maximum when the modulated intensity pattern and induced permittivity grating differ in phase by 90°. This result, which should be considered one of the most important of this discussion, can be explained in the following way. Equations (4.3) and (4.4) show that each electric field has two components; the field component in the absence of beam-coupling, which decays according to Beer's law, and the component that results from the coupling of the two fields via the induced permittivity grating (equations (4.3) and (4.4)). The equations show that, independent of any other factors, the scattered field component is shifted in phase by 90° relative to the transmitted field component. However, the phase of the scattered electric field is also shifted by the phase difference between the modulated intensity pattern and the induced permittivity grating. While the phase difference Δf is subtracted in determining the magnitude of E_{+1}, it is added in determining the magnitude of E_{-1}. Thus, the case where Δf is +90° describes a situation where the scattered contribution to E_{+1} is 180° out of phase with respect to the transmitted component, so that E_{+1} experiences loss. In contrast, for the same conditions, the scattered component to E_{-1} is in phase with the transmitted component, so that E_{-1} experiences gain.

Equations (4.5) – (4.8) show that, for the general permittivity change considered in equation (4.2), the direction of energy transfer is from the strong beam to the weak beam. This can be understood by noting that for $E_{-1} > E_{+1}$, $\phi_+ > \phi_-$, and equations (4.5) and (4.6) hold, so that I_{+1} experiences gain while I_{-1} experiences the same amount of loss. On the other hand, when $E_{+1} > E_{-1}$, equations (4.7) and (4.8) show that $\phi_- > \phi_+$ so that $\Delta\phi$ reverses sign, and I_{-1} experiences gain while I_{+1} experiences the same amount of loss.

A similar derivation can be performed for the general case of an imaginary (absorptive) induced permittivity change ($\Delta\varepsilon_r \rightarrow i\Delta\varepsilon_i$). Under these circumstances, the process outlined above produces the following equations for the beam intensities and phases of the two fields:

$$\frac{dI_{+1}}{dz} = -\alpha I_{+1} - \frac{k\Delta\varepsilon_i}{2}\left|E_{+1}\right|\left|E_{-1}\right|\cos\Delta\phi \ , \qquad (4.9)$$

$$\frac{dI_{-1}}{dz} = -\alpha I_{-1} - \frac{k\Delta\varepsilon_i}{2}\left|E_{-1}\right|\left|E_{+1}\right|\cos\Delta\phi \ , \qquad (4.10)$$

$$\frac{d\phi_{+1}}{dz} = \frac{k\Delta\varepsilon_i}{2}\frac{\left|E_{-1}\right|}{\left|E_{+1}\right|}\sin\Delta\phi \ , \qquad (4.11)$$

$$\frac{d\phi_{-1}}{dz} = -\frac{k\Delta\varepsilon_i}{2}\frac{\left|E_{+1}\right|}{\left|E_{-1}\right|}\sin\Delta\phi \ . \qquad (4.12)$$

Where, again, $\Delta\phi$ is the phase difference between the modulated intensity profile and the permittivity grating, measured relative to the phase of the permittivity grating.

Equations (4.9) – (4.12) show that, in contrast to the case where a refractive permittivity grating is present, there is no real energy transfer between the beams when an absorption grating is present. However, it is easy to see that for phase differences

between 90° and 270° ($cos\Delta f$ negative), the net result of the grating will be to reduce the effective absorption that the beams encounter in propagating through the material, an effect that will appear to couple energy into each beam. The effective absorption of the material will be least when the maxima of the modulated intensity pattern are spatially coincident with the areas of minimum absorption, a situation that corresponds to a phase difference of 180°. It is important to note that in practical situations, the maximum nonlinear absorption change is always smaller than the linear absorption coefficient. Thus, it is not possible for the beams to experience intensity gain in propagating through the material.

Equations (4.9) and (4.10) also show that when the intensities of the two beams are different, the effective absorption that each beam experiences is different, and energy appears to be coupled from beam to the other. This can be seen by considering the case where Δf is 180°, and $|E_{+1}|$ is larger than $|E_{-1}|$. For these conditions, we can relate $|E_{+1}|$ and $|E_{-1}|$ through a proportionality constant M ($|E_{+1}|=M|E_{-1}|$, $M>1$), and re-write equations (4.9) and (4.10):

$$\frac{dI_{+1}}{dz} = -(\alpha - \frac{k\Delta\varepsilon_i}{2M})I_{+1}, \qquad (4.13)$$

$$\frac{dI_{-1}}{dz} = -(\alpha - \frac{kM\Delta\varepsilon_i}{2})I_{-1}, \qquad (4.14)$$

Clearly, since M is greater than 1, beam I_{-1} experiences a lesser absorption than I_{+1}, so that energy appears to be transferred from beam I_{+1} to I_{-1}. In contrast, for the same conditions and a phase difference of 0° (Δf =0°), I_{-1} experiences a greater absorption, so that energy appears to be transferred from I_{-1} to I_{+1}. The “energy transfer” properties of

absorptive gratings have been observed experimentally in photorefractive beam coupling studies involving GaAs (K. Walsh et al., 1987) as well as $BaTiO_3$ (R. S. Cudney et al., 1990).

4.3 Transient Energy Transfer

Up to this point, we have considered the transfer of energy that occurs under steady-state conditions for the simple two-beam geometry shown in Chapter III. However, for the transient conditions that we have described throughout this thesis, it is possible for energy transfer to occur in circumstances where, according to the discussion of section 4.2, energy transfer is forbidden. In this section we give a description of this process, which is called transient energy transfer. However, whereas in section 4.2 we derived a set of equations that described steady-state energy transfer, in this section we give a qualitative description of transient energy transfer. In discussing transient energy transfer we are not considering energy transfer under transient conditions due to the photorefractive grating. As we have seen in Chapter III, photorefractive gratings generated under steady-state and transient conditions differ in phase from the incident intensity pattern by 90°. As a result, both transient and steady-state photorefractive gratings can transfer energy by the means described in section 4.2.

Transient energy transfer was first observed in nonlinear wave mixing experiments using a solution of carbon tetrachloride and iodine (F. Gires, 1968). This phenomenon was first attributed to the process that will be described below by W.L. Rother (W.L. Rother, 1970). Transient energy transfer has been observed in a variety of semiconducting materials, including Silicon (V.L. Vinetskii, et. al., 1976), Cadmium

Sulfide (S.G. Odulov et. al., 1978) and semi-insulating GaAs (G.C. Valley and A.L. Smirl, 1988).

In describing transient energy transfer, we consider the case where two optical pulses of unequal intensity generate a refractive index grating that is nominally in phase with the incident intensity pattern. From the discussion of the previous section, we know that steady-state energy transfer is forbidden for this situation. However, as we will see, if the duration of the optical pulses is on the order of or shorter than the relaxation time of the optical nonlinearity, then energy transfer occurs. In describing transient energy transfer, we consider the illustrative situation where three consecutive slices of the two optical pulses propagate through two layers of the material, as shown in figures 4.2a-d. For convenience, we assume that the spatial extent of the pulse slices in the material is equal to the thickness of the material layers. We also assume that the pulses are perfectly coherent before they interact with the material. That is, the phase relationship along each optical field is given by the relationship $e^{i\{\mathbf{k}\cdot\mathbf{r}-\omega t\}}$ ($\mathbf{k}$ and ω are the wave vector and angular frequency of the fields).

As shown in figure 4.2a, at time t_1 when the front slice of each pulse encounters the first layer of the material, there is no index grating ($\Delta\varepsilon_r = 0$), so that the pulses form the grating and are depleted via linear absorption. At time t_2, as the front slice of each pulse encounters the second layer of the material, the same process is repeated (figure 4.2b). However, at the same time, the second slice of each pulse encounters the first layer of the material. The second slice of each pulse is depleted via linear absorption, and interacts with the existing index grating according to equations (4.5) – (4.8). Since the

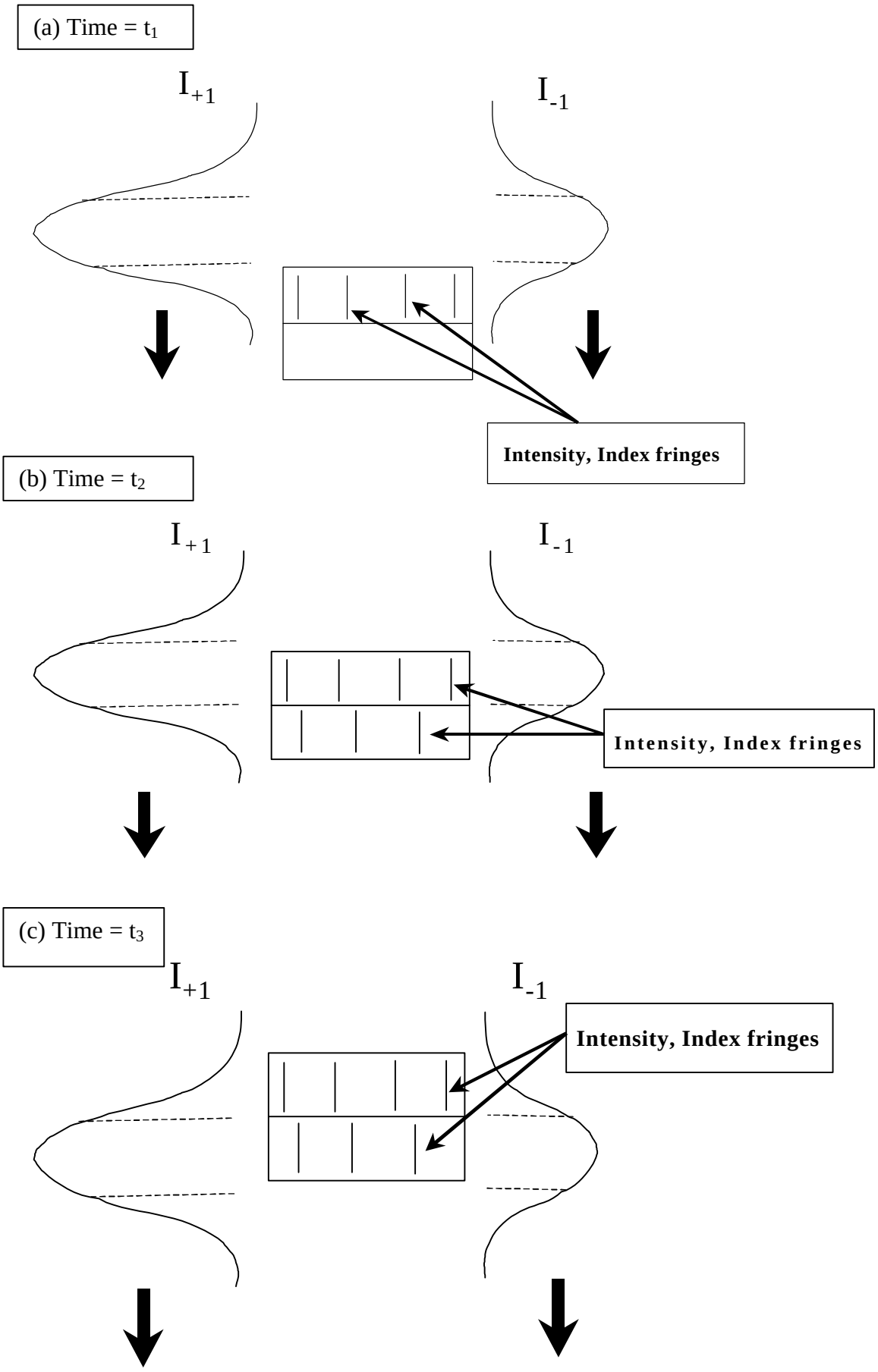
(a) Time = t_1
I_{+1}
I_{-1}
Intensity, Index fringes
(b) Time = t_2
I_{+1}
I_{-1}
Intensity, Index fringes
(c) Time = t_3
I_{+1}
I_{-1}
Intensity, Index fringes

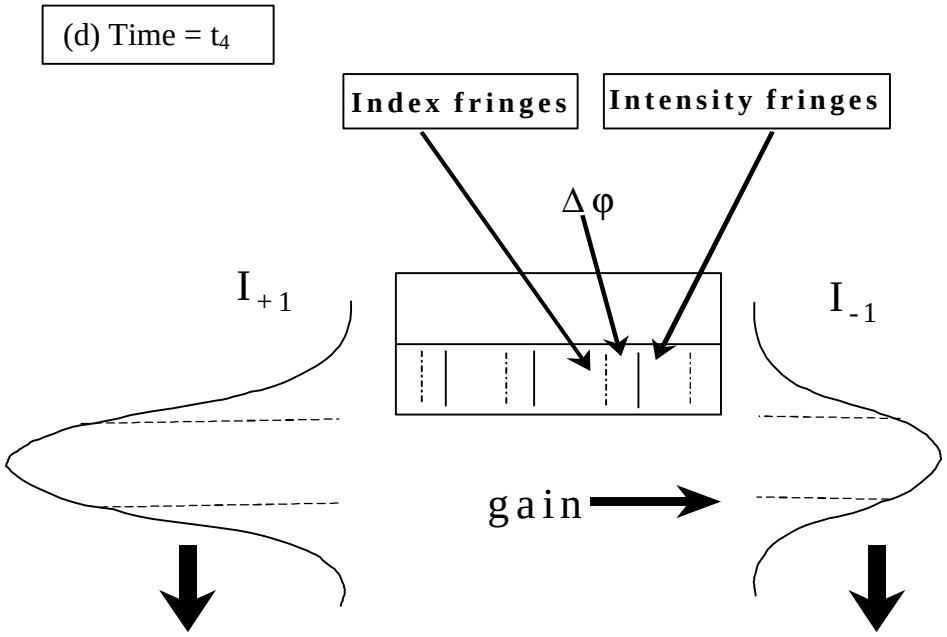

Figure 4.2a-d – Transient Energy Transfer. See the text for description.

phase difference between the modulated intensity pattern and index grating is zero, there is no transfer of energy as a result of the interaction of the fields with the grating. Though there is no energy coupling between the beams, equations (4.7) and (4.8) tell us that under these circumstances, the two optical fields incur the maximum possible phase change as a result of their interaction with the grating. However, more importantly, since the magnitudes of the fields are unequal, the fields incur unequal phase changes (as discussed in section 4.2, the weaker field receives the larger phase change).

At time t_3, which is depicted in figure 4.2c, the third pulse slices encounter the first layer of the material, and they are depleted via linear absorption and interact with the grating in the same way as described above for the second slice of the pulses. At the same time, as the second pulse slices propagate to the second layer of the material, they are depleted via linear absorption and interfere to form a modulated intensity pattern and index grating. However, since the second pulse slices incurred unequal phase changes in

propagating through the first layer of the material, the maxima of the index grating are shifted relative to the maxima of the index grating that was formed by the first pulse slices. Following this, the index grating in the second material layer is generally a superposition of the index grating written by the first slice of the pulses, and the phase shifted grating written by the second slice of the pulses.

At time t_4, which is shown in figure 4.2d, the third pulse slices reach the second layer of the material and encounter the two component index grating. If the relaxation time of the optical nonlinearity is instantaneous with respect to the duration of the pulses, than component of the index grating that is due to the first pulse slices will have completely decayed, and is thus zero. Under these circumstances, the phase difference between the existing index grating and the modulated intensity profile generated by the third slice of the pulses is zero, and the material/field interaction proceeds as described above for the first layer of the material. However, if the relaxation time of the optical nonlinearity is on the order of or longer than the duration of the optical pulses, then both components of the index grating are non-zero. The index grating that exists under these conditions is out of phase with the incident intensity profile, a result that leads to energy transfer between the beams. Since the phase of the weak beam is larger than the phase of the strong beam, equations (4.5) and (4.6) show that energy is transferred from the strong beam to the weak beam.

The above description illustrates three important points about transient energy transfer. First, transient energy transfer produces energy coupling between beams where it is forbidden under steady-state conditions. Second, the transfer of energy occurs when

the optical pulses generate and interact with the index grating in a time on the order of, or shorter than the relaxation time of the optical nonlinearity, and is therefore inherently a transient process. Finally, transient energy transfer only occurs when the intensities of the two beams are unequal, and energy transfer is always from the strong beam to the weak beam. For this reason, we have used beams of equal intensity in generating the nonlinear optical gratings in our experiments. As we showed in Chapter III, this results in high modulation effects.

4.4 Picosecond Beam Coupling in Semi-Insulating GaAs and Undoped CdTe

So far, our discussions of steady-state and transient beam coupling have been general concerning the induced index and absorption gratings that give rise to these effects. However, in this section, we depart from this by considering beam coupling due to the optical nonlinearities that are present in our semi-insulating GaAs and undoped CdTe crystals, for our experimental conditions. As we will see, the photorefractive nonlinearity has some characteristics that distinguish it from the other optical nonlinearities that we have discussed for semi-insulating GaAs and undoped CdTe. These characteristics allow transient photorefractive effects to be measured using the experimental method that is described in this section. Moreover, while it is possible to measure picosecond photorefractive effects using this measurement technique, this method of measurement is not suitable for our experiments because it does not allow the photorefractive nonlinearity to be time-resolved.

4.4.1 Beam Coupling Due to the Instantaneous Bound Electronic, Free-Carrier and EL2 Absorptive Nonlinearities

From the discussions of Chapter II, we recall that excitation with our picosecond duration optical pulses produces a host of index and absorption changes such as the free carrier index change, the instantaneous bound electronic index change, EL2 absorption saturation, and instantaneous two-photon absorption. In this section we discuss the results of sections 4.2 and 4.3 in light of these nonlinearities.

For both semi-insulating GaAs and undoped CdTe, the instantaneous bound-electronic refractive index change is $-n_2 I$. As a result, the instantaneous bound electronic index grating is clearly 180° out of phase with the incident irradiance pattern, and will therefore not transfer energy under steady-state conditions. In addition, as is indicated by its name, the response of this nonlinearity is instantaneous relative to the duration of our optical pulses, so that it will not transfer energy via transient energy transfer. Similarly, as we saw in Chapter II, the free carrier index change is negative in both semi-insulating GaAs and undoped CdTe, and proportional to the free carrier density ($-n_{eh}N$). Since the modulated free carrier density is in phase with the modulated intensity pattern, the free carrier index grating is therefore also 180° out of phase with the incident intensity pattern and will not transfer energy under steady-state conditions. However, unlike the instantaneous bound-electronic nonlinearity, the response of the free carrier nonlinearity is not instantaneous relative to the duration of our optical pulses. This follows from the discussions of Chapter III, where we showed that the decay constant for the modulated free carrier density in semi-insulating GaAs and undoped CdTe is 38ps and 110ps

respectively for our experimental conditions. Thus, unlike the instantaneous bound electronic grating, the free carrier index grating will transfer energy via transient energy transfer in picosecond two-beam coupling experiments.

In Chapter II we showed that excitation with our picosecond duration optical pulses can saturate the EL2 absorption, causing the linear absorption coefficient in semi-insulating GaAs to decrease by roughly 30% at the middle and high beam intensities used in our experiments. Since the absorption is decreased at high intensities, excitation with a modulated intensity profile produces an EL2 absorption grating that is 180° out of phase with the incident intensity profile. Thus, the EL2 absorption grating will produce energy transfer effects that will be manifest in two beam coupling measurements. As discussed in section 4.2, these effects include a decreased absorption for both beams.

Instantaneous two photon absorption can also effect picosecond beam coupling measurements, although not through an associated absorption grating. This follows from the fact that a weak picosecond pulse experiences greater attenuation due to two-photon absorption when a temporally and spatially coincident pulse of greater intensity is present. Thus, the presence of a more intense picosecond pulse causes the transmission of a weak picosecond pulse to decrease.

4.4.2 Beam Coupling Due to the Photorefractive Nonlinearity

From the discussions of Chapter I and Chapter III, we know that the photorefractive nonlinearity arises from a material's electrooptic response to an internal space-charge field that is generated by the transport of photogenerated charge carriers. In Chapter III, we showed that the periodic space-charge field that is generated from a

modulated free carrier density is 90° out of phase with that carrier density, for both steady-state and transient conditions. Since the modulated carrier density is in phase with the modulated intensity pattern from which it arises, the space-charge field is 90° out of phase with the modulated intensity pattern, so that the photorefractive grating will produce the maximum energy transfer for the configuration shown in figure 4.1.

While it is easy to see that the phase difference between the photorefractive grating and modulated intensity profile is optimum for two-beam coupling, we must also determine the direction of energy transfer for this grating. Equations (4.5) and (4.6) show that this follows from the sign of the induced permittivity change, which is dictated by the electrooptic properties of the crystal. The electrooptic response of the material is determined using the linear electrooptic properties of the crystal in the index ellipsoid formalism. For $\bar{4}3m$ materials like our GaAs and CdTe crystals, the general equation for the index ellipsoid can be expressed in matrix form (A. Yariv, 1985):

$$\begin{bmatrix} x & y & z \end{bmatrix} \begin{bmatrix} \frac{1}{n_b^2} & r_{41}E_z & r_{41}E_y \\ 2r_{41}E_z & \frac{1}{n_b^2} & r_{41}E_x \\ r_{41}E_y & r_{41}E_x & \frac{1}{n_b^2} \end{bmatrix} \begin{bmatrix} x \\ y \\ z \end{bmatrix} = 1. \quad (4.15)$$

All of the factors in this equation have been defined previously, and the *x*, *y* and *z* axes, which are the (100), (010) and (001) crystallographic directions, *do not* correspond to the *x*, *y* and *z* axes shown in figure 4.1. The induced changes in the crystal's optical

properties are determined by diagonalizing the central matrix in this equation. The resulting eigenvectors are the new principal axes of the crystal (the crystal directions where no birefringence is observed), and the eigenvalues are used to determine the change in index along each of these directions.

Referring to figure 4.1, our semi-insulating GaAs crystal is cut so that the x, y and z axes shown in this figure are, respectively, the (001), (110) and $(\bar{1}10)$ crystallographic directions. For this orientation of the crystal and optical beams, it is clear that the space-charge field will be generated along the (001) crystal axis, so that $E_z=E_{sc}$ in equation (4.15), while $E_x=E_y=0$. When we diagonalize the matrix for this crystal orientation, we find the new principal axes (x',y',z') for the crystal:

$$x' = (0,0,1),$$

$$y' = \frac{1}{\sqrt{2}}(1,1,0),$$

and,

$$z' = \frac{1}{\sqrt{2}}(1,-1,0).$$

Which correspond to the *x*, *y* and -*z* axes in figure 4.1. We also find that, while the index of refraction is not changed along the x axis in figure 4.1, the indices of refraction along the *y* and *z* directions (in figure 4.1) are respectively, n_b-½$n_b^3 r_{41} E_{sc}$ and n_b+½$n_b^3 r_{41} E_{sc}$. Since the incident fields are perpendicularly polarized, they experience an index change equal to $-½n_b^3 r_{41} E_{sc}$, and equations (4.5) and (4.6) can be re-written:

$$\frac{dI_{+1}}{dz} = -\alpha I_{+1} + \Gamma \left| E_{+1} \right\| \left| E_{-1} \right|, \qquad (4.16)$$

$$\frac{dI_{-1}}{dz} = -\alpha I_{-1} - \Gamma \left| E_{-1} \right\| E_{+1} \left| . \right. \qquad (4.17)$$

In the above equations, Γ is the photorefractive coupling constant:

$$\Gamma = k_0 n_b^3 r_{41} E_{sc} \sin 90^\circ , \qquad (4.18)$$

and we have used the relationship between the index change and the real permittivity change ($\Delta\varepsilon_r = 2n_b \Delta n$). Thus, equations (4.16) – (4.17) show that for this crystal orientation, energy is transferred from I_{-1} to I_{+1}. In contrast, if we keep the orientation of the beams that is shown in figure 4.1, but rotate the crystal by 180°, we find the opposite result. For this crystal orientation, the space-charge field is formed along the $(00\bar{1})$ axis, resulting in the same set of principal axes as before, but with index changes of $+\frac{1}{2} n_b^3 r_{41} E_{sc}$ and $-\frac{1}{2} n_b^3 r_{41} E_{sc}$ respectively, along the *y* and *z* axes. For this crystal orientation, the sign of the index change that the perpendicularly polarized beams experience is positive, so that the photorefractive coupling constant changes sign, and energy is transferred from I_{+1} to I_{-1}.

The above analysis shows that for the photorefractive grating, the direction of energy transfer is dependent on the crystal orientation, which dictates the direction that the space-charge field is applied within the material, and the material's subsequent electrooptic response to the field. This important result, which arises from the electrooptic properties of the photorefractive nonlinearity, is in contrast to the other competing nonlinear effects, which are independent of the crystal orientation. From an experimental point of view, the most difficult aspect of picosecond photorefractive measurements in semiconductors is separating the effects of the photorefractive

nonlinearity from the other competing (and larger magnitude) effects. As we will see in the next subsection, these unique energy transfer properties of the photorefractive nonlinearity allow us to make this separation. For the same reason, namely separating the photorefractive nonlinearity from the other competing effects, we utilize the electrooptic nature of the photorefractive nonlinearity in the transient grating measurement technique that is discussed in Chapter V. However, whereas it is the electrooptic energy transfer properties of the photorefractive grating that allow it to be distinguished using the two beam coupling method, it is the electrooptic polarization rotation properties of this nonlinearity that allow it to be distinguished using the transient grating method of Chapter V.

4.4.3 Measurement of Picosecond Photorefractive Effects Using the Two Beam Coupling Method

In this section we outline the two beam coupling method for measuring picosecond photorefractive effects in semiconductors. This method, which was developed by A.L. Smirl, has been the only method for measuring picosecond photorefractive measurements in semiconductors, prior to the experiments described in this thesis. This method of measurement has been used to measure picosecond photorefractive effects in semi-insulating GaAs, CdTe:V, and InP:Fe using picosecond optical pulses (A. L. Smirl et al., 1988, G. C. Valley et al., 1989, W. A. Schroeder et al., 1991). This method of measurement has also been used to measure picosecond photorefractive effects in undoped CdTe (M. S. Petrovic et al. 1991).

Referring to Figure 4.1, in the two-beam coupling method, we measure the change in transmission that a weak beam experiences in the presence and absence of a second strong beam. We write the change is transmission:

$$\frac{\Delta T_{pr}}{T_{pr}} = \frac{T_{prw} - T_{prwo}}{T_{prwo}}.$$

Here T_{prw} is the transmission that the weak beam, which we call the probe beam, experiences with the strong beam, which we call the pump beam, present. For reference to figure 4.1, we assume that I_{+1} is the probe beam, while I_{-1} is the pump beam. The quantity T_{prwo} is the transmission of the probe beam in the absence of the pump beam. When we consider the photorefractive nonlinearity together with the other optical nonlinearities discussed in sub-section 4.4.1, the differential equations that describe beam propagation will take the form of equations (4.17) and (4.18), with terms added to account for beam depletion via instantaneous two photon absorption, and loss or gain due to the induced absorptive or refractive gratings. For this set of circumstances, we can write a general solution for the propagation of the probe beam:

$$I_{pr}(z) = I_{pr0} e^{-\alpha z \pm \Gamma z \pm \Delta \alpha} \quad .$$

Here I_{pr0} is the probe intensity as it enters the crystal, while α is the linear absorption coefficient, Γ is the photorefractive coupling constant, and $\Delta\alpha$ is the change in the probe absorption due to all of the other nonlinear effects. We can then write the transmission of the probe beam with and without the pump present as:

$$T_{prwo} = e^{-\alpha \ell} \qquad \text{(pump not present)}$$

$$T_{prw} = e^{-\alpha \ell \pm \Gamma \ell \pm \Delta \alpha \ell} \qquad \text{(pump present),}$$

and the normalized change in probe transmission as:

$$\frac{\Delta T_{pr}}{T_{pr}} = e^{\pm \Gamma \ell \pm \Delta a \ell} - 1. \qquad (4.19)$$

Here it is important to note that, while we have assumed that Γ and Δa are constant, the values that are extracted for these quantities are spatial averages over the beam profile and sample length, and temporal averages over the pulse duration.

We measure picosecond beam coupling effects in the limit where the normalized change in probe transmission is small. Under these circumstances, we make use of the exponential expansion, and equation (4.19) can be written:

$$\frac{\Delta T_{pr}}{T_{pr}} = \pm \Gamma \ell \pm \Delta a \ell . \qquad (4.20)$$

We measure the normalized change in probe transmission at the two crystal orientations described in section 4.4.2, which we call crystal orientations 0 and p. We note that for these two crystal orientations, the photorefractive coupling constant is maximum, but it is positive for crystal orientation 0 while it is negative for crystal orientation p. In contrast, as we noted in sections 4.4.1 and 4.4.2, the other contributions to the probe transmission have the same magnitude and sign for the two crystal orientations. Thus, we isolate the photorefractive contribution to the probe transmission by subtracting the normalized change in probe transmission for the two crystal orientations:

$$\left(\frac{\Delta T_{pr}}{T_{pr}} \right)_0 - \left(\frac{\Delta T_{pr}}{T_{pr}} \right)_p = 2\Gamma \ell . \qquad (4.21)$$

Conversely, we isolate the other contributions to the probe transmission by adding the normalized change in probe transmission:

$$\left(\frac{\Delta T_{pr}}{T_{pr}}\right)_0 + \left(\frac{\Delta T_{pr}}{T_{pr}}\right)_p = 2\Delta a\ell . \qquad (4.22)$$

The measurement method that is described above allows the photorefractive contribution to the change in probe transmission to be separated from the other effects that are present in semiconductors on picosecond time scales. We emphasize that, as it is described above, the relationship between the photorefractive coupling constant and the probe transmission for the two crystal orientations is valid only when the overall change in the probe transmission is small. We also emphasize that the photorefractive coupling constant that is measured represents an average over the spatial extent of the pulses, the length of the sample, and the duration of the pulses.

Two-beam coupling is a unique nonlinear optical phenomenon in that the same optical fields that generate the induced gratings also experience a change of amplitude and/or phase by interacting with the gratings. However, for this same reason, the two-beam coupling measurement method has some important limitations. For example, since the incident optical pulses must both be present in order to produce the beam coupling effects that we use to measure the photorefractive nonlinearity, we can only measure the evolution of this nonlinearity over the temporal duration of the pulses. In addition, since the two-beam coupling measurement method requires that we create and sample the photorefractive nonlinearities with the same optical fields, the results that we obtain reflect a complex convolution of the generation and sampling processes. Since the goal

of this thesis is to time resolve the photorefractive nonlinearity over a wide range of times in order to obtain an unambiguous measure of its evolution, the two-beam coupling measurement method is not suitable for our experiments. Instead, we seek a three-beam, transient-grating measurement method where we generate the photorefractive gratings with two pulses, and then probe the gratings with a third, phase-matched probe pulse that is delayed with respect to the other pulses. The transient grating measurement method that is used for these measurements is the subject of Chapter V.

4.5 Conclusions

In this chapter we have considered two-beam coupling and transient energy transfer. For the simple two beam geometry shown in this chapter, we find that energy transfer between beams only occurs when there is a phase difference between the induced gratings, and the modulated intensity profile that is produced by the beams. For our experimental conditions, steady-state energy transfer only occurs as a result of the photorefractive nonlinearity. While this provides a means for measuring photorefractive effects in zincblende semiconductors, such measurements are complicated by competing effects such as transient energy transfer, which can occur as a result of the free-carrier grating, induced absorption gratings, and non-linear absorption of the optical beams. Moreover, while the two-beam coupling measurement method allows the picosecond photorefractive effects to be separated from these competing effects, since it does not allow the photorefractive nonlinearities to be unambiguously time resolved for a wide range of delays, it is not suitable for our experiments.

CHAPTER V

THE PHOTOREFRACTIVE POLARIZATION ROTATION TRANSIENT-GRATING MEASUREMENT METHOD

5.1 Introduction

In Chapter IV, we reviewed the two-beam coupling measurement method and showed that it is not suitable for our experiments. There we stated that for our experiments, we seek a three-beam, transient grating measurement method where the photorefractive gratings are generated with two spatially and temporally coincident pulses, and then probed with a third, phase-matched probe pulse. In this chapter we discuss the transient-grating measurement method that we use in our experiments. We begin with some general points about transient-grating measurement methods, and then consider three aspects of our measurement technique. We consider first the requirements that the goals of this thesis place on our measurement technique, along with a general description of how we meet these requirements. Second, we discuss some important details about the method of measurement, including the generation, phase-matching, and overlap of the probe beam.

5.2 Measurement of Optical Nonlinearities Using Transient-Grating Methods

Before discussing the various aspects of our transient-grating measurement technique, it is necessary to provide a general introduction to this method of measuring optical nonlinearities. In transient-grating experiments, we use two temporally and spatially coincident optical pulses, incident with an angle 2θ between them, to produce a modulated intensity pattern inside the material, as was shown in figure 3.1. As we have seen in Chapters II, III, and IV, the incident optical pulses, which we call pump pulses, induce refractive index and absorption gratings as a result of the nonlinear optical response of the material. A third, Bragg-matched probe pulse of low intensity, incident at an arbitrary delay with respect to the pump pulses, interacts with the induced gratings to produce a diffracted beam. In transient-grating experiments, we measure the intensity of the diffracted beam relative to that of the probe beam, which provides a measure of the diffraction efficiency of the induced gratings.

Our experiments are conducted in a regime where the beam propagation length (3×10^{-3}m) is much larger than the period of the induced gratings (2-4μm), and where the diffraction efficiency of the induced gratings is much less than unity. As we will see in Chapter VI, under these circumstances the diffraction efficiency (η) can be written in terms of the index change (Δn) and absorptive change ($\Delta\alpha$) (H. J. Eichler et al., 1986):

$$\eta(t) = \left(\frac{\pi\Delta n(t)\ell}{\lambda}\right)^2 + \left(\frac{\Delta\alpha(t)\ell}{4}\right)^2. \qquad (5.1)$$

Where ℓ is the propagation length, λ is the probe wavelength, and t is the delay of the probe pulses with respect to the pump pulses. It is clear from equation (5.1) that the

magnitude of the diffraction efficiency can be used to determine the magnitude of the index and absorption changes that are induced in the material. However, more importantly for our experiments, we can measure the temporal dynamics of the index and absorption changes by measuring the diffraction efficiency as a function of the delay of the probe pulse. As we have stated, we seek to measure the dynamics of one of many optical nonlinearities that are generated in semi-insulating GaAs and undoped CdTe, the photorefractive nonlinearity. As we will see in the discussions that follow, this experimental goal poses some experimental challenges.

5.3 Requirements

In reviewing the results of Chapters II and III, we find that our experimental goal dictates substantial requirements on the measurement method, in terms of its inherent time resolution, its ability to separate the photorefractive nonlinearity from the other competing picosecond optical nonlinearities, and its inherent signal to noise ratio. In this section we discuss these requirements. Here we show that our experimental goals can be met with a two-color, forward-probing, transient grating measurement method that utilizes the polarization rotation properties of the photorefractive nonlinearity.

5.3.1 Minimum Resolvable Time - Forward-Probing Geometry

The requirement that is placed on our transient-grating measurement technique for minimum resolvable time is dictated by the time required for the formation and decay of the photorefractive nonlinearities, which we have seen to be 5ps-150ps in semi-insulating GaAs and undoped CdTe (see Chapter III). However, a related requirement arises from the fact that the photorefractive index change is small (see Chapter III). Since the

photorefractive index change is small, we must maximize the diffraction efficiency in order to ensure that we can make measurements at a wide range of pump pulse intensities. As can be seen from equation (5.1), we do this by using a thick crystal (maximizing ℓ). Thus, while our experimental goals dictate the requirement for a minimum resolvable time of ~5ps, the overall magnitude of the photorefractive index change dictates an additional requirement for a thick crystal.

Two frequently used transient grating geometries, the Raman-Nath geometry and the Degenerate Four Wave Mixing (DFWM) geometry, are shown in figures 5.1a and b. The Raman-Nath geometry offers the advantage of a high inherent time resolution, along with the additional advantage that the probe beam does not have to be Bragg-matched to the gratings in order for a diffracted signal to be produced. However, since these advantages come at the expense of using a thin crystal, this transient-grating geometry is not adequate for our experiments. On the other hand, the DFWM geometry shown in figure 5.1b offers a large crystal length, and relative ease in Bragg-matching the probe beam to the induced gratings (the probe beam is simply aligned so that it counterpropagates with the pump pulse E_2). However, it has been shown that the minimum resolvable time for this geometry is equal to the time of flight of the optical pulses in the crystal ($t_{min}=n\ell/c$) (Trebino and Siegman, 1985), which is roughly 10ps – 35ps in our GaAs and CdTe crystals. Thus, like the Raman-Nath transient-grating geometry, the DFWM geometry is inadequate for our experiments.

A Bragg-matched forward-probing transient-grating geometry such as shown in figure 5.2 is best suited for our experiments. Here the pump and probe beams co-propagate through the crystal, so that the pump-probe delay is constant over the

(a) Raman-Nath Geometry (b) "DFWM" Geometry

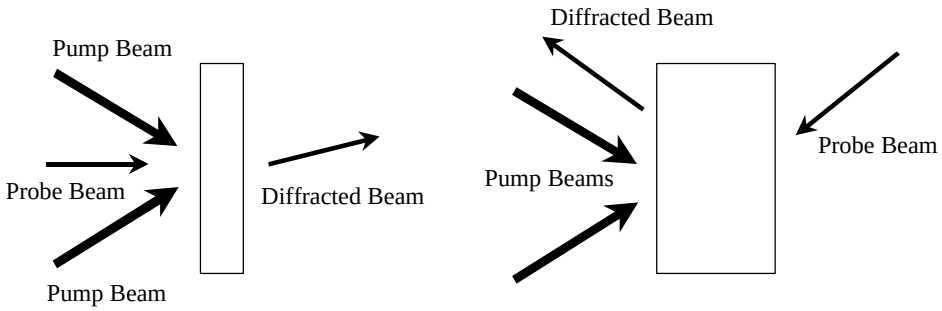

Figure 5.1a and b – The Raman-Nath and "DFWM" transient-grating geometries. See the text for description.

propagation length of the crystal. As a result, the time resolution of this transient-grating geometry is independent of the crystal length, and limited only by the duration of the pump and probe pulses (and effects such as dispersion or pulse broadening) (Trebino and Siegman, 1985). Thus, using this transient-grating geometry, a high time resolution can be maintained while the diffraction efficiency is maximized.

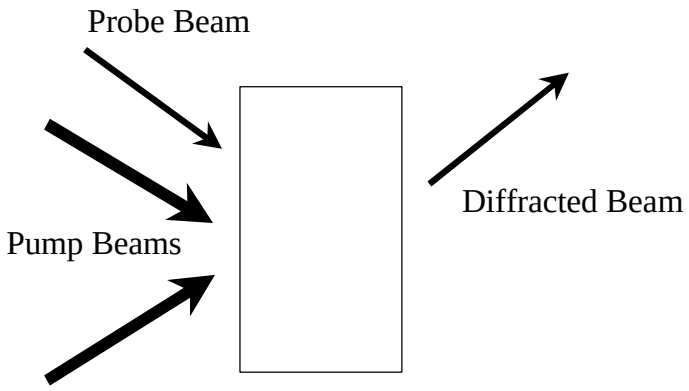

Figure 5.2 – Forward-probing transient-grating geometry used in our experiments. See the text for description.

5.3.2 Separation of the Photorefractive and Competing Nonlinearities: Photorefractive Polarization Rotation

As we showed in Chapters II and III, the picosecond photorefractive nonlinearities in semi-insulating GaAs and undoped CdTe coexist with other optical nonlinearities that are of comparable or greater magnitude. As a result, another requirement that is placed on our measurement technique is that is must allow the photorefractive nonlinearities to be separated from the other picosecond optical nonlinearities. In our transient-grating measurement method, we accomplish this using photorefractive polarization rotation (A. L. Smirl et al., 1989, D. Liu and L.J. Cheng, 1989, P. Yeh, 1987). Like the energy transfer properties of the photorefractive grating observed in two-beam coupling, these polarization rotation properties follow directly from the electrooptic nature of the photorefractive effect. In the following paragraphs, we solve the index ellipsoid equation for our semi-insulating GaAs crystal orientation and show how scattering of the probe beam from the photorefractive gratings generates a diffracted beam with a 90° polarization rotation. In Appendix B, we use the same method to illustrate a similar result for our undoped CdTe crystal. The conclusions that are reached in this section should be considered among the most important of this chapter. Moreover, an understanding of photorefractive polarization rotation is critical to understanding the experimental results of Chapters VII and VIII.

The crystal orientation that is used in our experiments is that which has been used to demonstrate high contrast optical switching using photorefractive polarization rotation (A. L. Smirl et al., 1989). Shown in figure 5.3 along with the orientation of the pump beams, this arrangement of crystal and beams results in the generation of a periodic space-

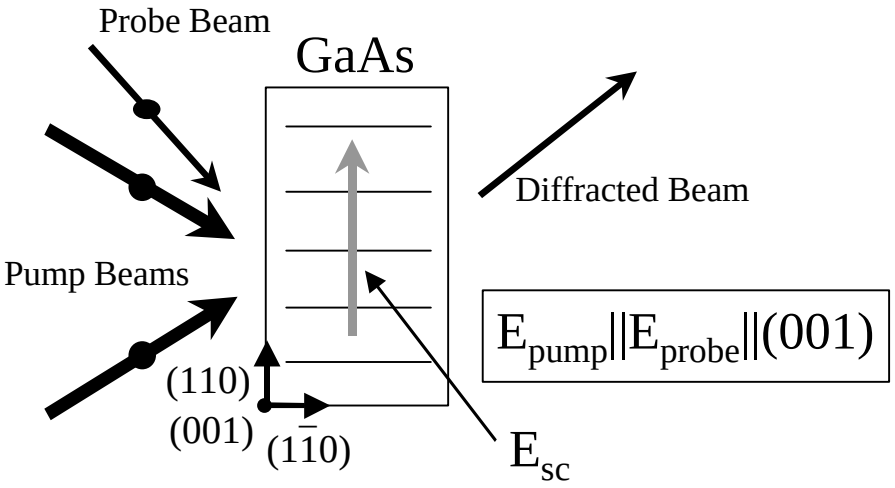

Figure 5.3 – Crystal and beam orientation used in these experiments. See the text for description.

charge field in the (110) crystal direction. Under these circumstances, the equation for the index ellipsoid (equation (4.15)) becomes:

$$\begin{bmatrix} x & y & z \end{bmatrix} \begin{bmatrix} \frac{1}{n_b^2} & 0 & \frac{r_{41}E_{sc}}{\sqrt{2}} \\ 0 & \frac{1}{n_b^2} & \frac{r_{41}E_{sc}}{\sqrt{2}} \\ \frac{r_{41}E_{sc}}{\sqrt{2}} & \frac{r_{41}E_{sc}}{\sqrt{2}} & \frac{1}{n_b^2} \end{bmatrix} \begin{bmatrix} x \\ y \\ z \end{bmatrix} = 1, \qquad (5.2)$$

where the space-charge field has been assumed to have the form:

$$\overrightarrow{E_{sc}} = \frac{E_{sc}}{\sqrt{2}}(\hat{x} + \hat{y}),$$

and we have temporarily ignored the periodicity of the space-charge field for simplicity. In the above equations, all of the other factors have been previously defined, except $\hat{x}$ and $\hat{y}$ which are the unit vectors in the (100) and (010) crystallographic directions. As in the two-beam coupling analysis of Chapter IV, we diagonalize the central matrix in equation

(5.2) to determine the new principal axes of the crystal and the index changes along each of the crystal directions. This procedure leads to the following set of principal axes in our semi-insulating GaAs crystal:

$$x' = (-1,1,0), \qquad (5.3)$$

$$y' = \frac{1}{\sqrt{2}}(-1,-1,\sqrt{2}), \qquad (5.4)$$

and

$$z' = \frac{1}{\sqrt{2}}(1,1,\sqrt{2}). \qquad (5.5)$$

In addition, this process shows that, while the index of refraction is unchanged along the *x'* axis, it is increased along the *y'* axis by $\frac{1}{2}n_b^3 r_{41} E_{sc}$ and decreased by the same amount along the *z'* axis. As a result, when a periodic space-charge field is generated along the (110) crystal direction, photorefractive index gratings are generated along the crystal axes defined by equations (5.4) and (5.5). Since the index changes along these crystal directions are equal in magnitude but opposite in sign, the resulting index gratings are equal in magnitude but differ in phase by 180°, as shown in figure 5.4.

Close analysis of figure 5.3 shows that the two new principal axes defined by equations (5.4) and (5.5) lie in the plane parallel to the input and output faces of the crystal, and are along the diagonal directions which connect opposite corners of each crystal face. As a result, as shown in figure 5.5, s- and p-polarized radiation has equal components along the *y'* and *z'* axes for the crystal orientation shown in figure 5.3. As we know from the analyses of Chapter IV, an optical beam that is diffracted from an induced

grating has a phase that reflects the phase of the induced grating. Thus, when an s- or p-polarized probe beam diffracts from the photorefractive gratings that are generated for this

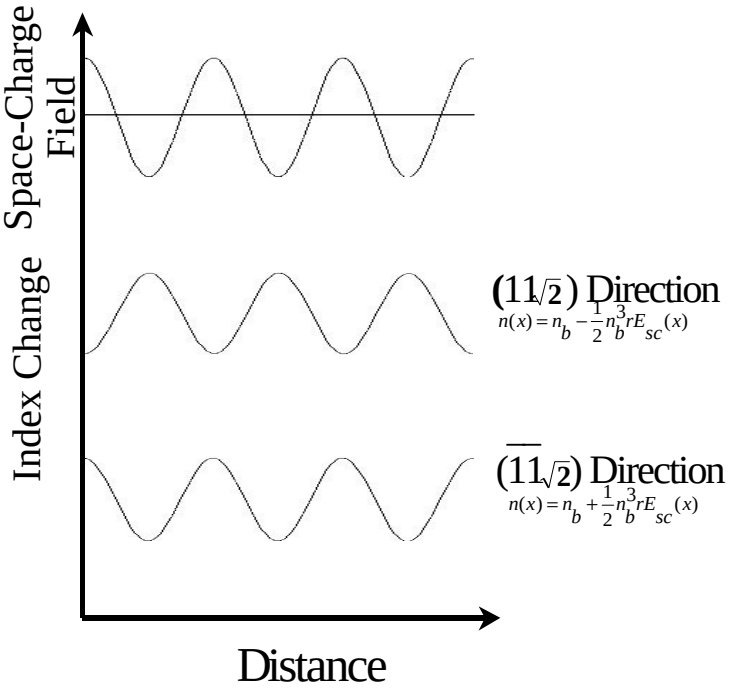

Figure 5.4 – The space-charge field that is generated in our crystal, and the resulting index gratings. See the text for description.

crystal orientation, the result is a diffracted beam that has a phase shift of 180° introduced between the field components in the directions defined by equations (5.4) and (5.5). Since the probe optical field has *equal* components along these directions, and the y' and z' photorefractive gratings are of equal magnitude, the diffracted beam that is produced has a polarization rotation of *exactly 90°* relative to the probe electric field (also shown in figure 5.5).

We emphasize that the result that is described above, a diffracted beam with a 90° polarization-rotation, arises from the linear electrooptic nature of the photorefractive

effect. Since the second-order index parameter exhibits no measurable isotropy (see section 2.2.6.1), and the free carrier de-phasing occurs instantaneously on the time scales

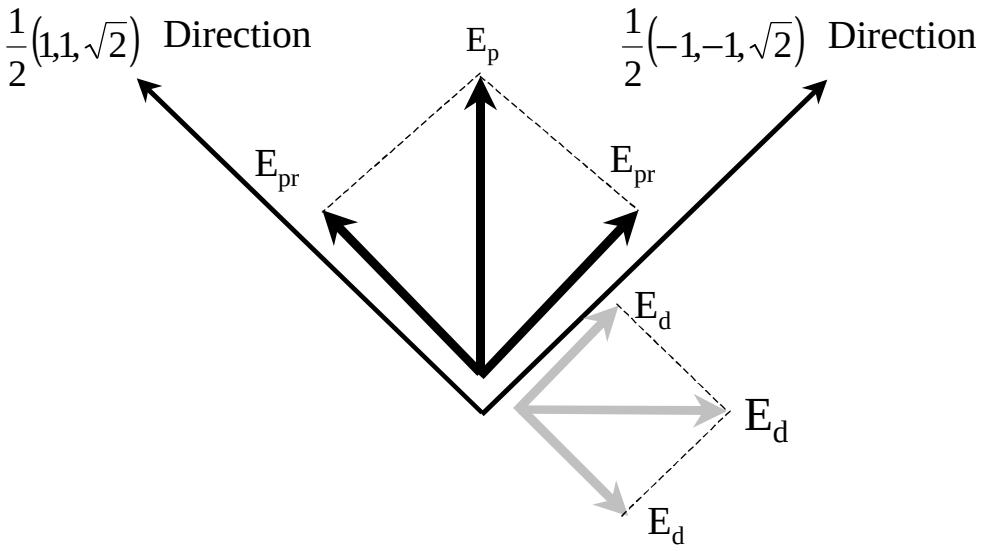

Figure 5.5 – Orientation of the probe electric field along the new principal axes in our GaAs crystal. As discussed in the text, this results in a diffracted beam with a polarization rotation of exactly 90°.

of our experiments, neither of these induced gratings will produce a similar result. We can thus separate the photorefractive contribution to the diffracted signal by placing a polarizer-analyzer pair in the probe and diffracted beams shown in figure 5.2. While the polarizer ensures that the probe beam is s-polarized, the analyzer separates the s- and p-polarized components of the diffracted beam.

5.3.3 Sensitivity – Two-Color Measurements

A third requirement for our transient-grating measurement technique is that it must allow measurements to be made with a high sensitivity. This requirement follows from the fact that the expected magnitude of the picosecond photorefractive nonlinearity in our materials is small (see Chapter III).

In transient-grating experiments, sensitivity is gained by measuring the diffracted beam in a way such that there is a minimum of optical background noise present. In the forward-probing geometry shown in figure 5.2, this can be done by making the pump and probe beams s-polarized and then using a polarizing prism to separate the portion of the beam that is diffracted from the photorefractive grating (p-polarized) from the transmitted pump beam (s-polarized). However, a simple analysis shows that under these circumstances, the portion of the transmitted pump pulse that will leak through the polarizing beamsplitter will be of equal or greater intensity than the p-polarized diffracted beam that is produced by the photorefractive grating. For example, the maximum optical fluences that are used in our experiments are roughly $1mJ/cm^2$. If we assume that the pump pulses incur a maximum absorption of 90% in propagating through the crystal, and that the extinction ratio of the polarizing beam splitter is typical of those that are commercially available (10,000:1) (Spindler & Hoyer, 1999), this leads to pump pulse leakage of roughly $10nJ/cm^2$. So that our results can be analytically compared with established sets equations describing Four Wave Mixing, the probe pulses must be at least 100 times weaker than the pump pulses, leading to a maximum probe pulse fluence of $10\mu J/cm^2$. If we assume no absorption of the probe or diffracted beams, and a maximum photorefractive diffraction efficiency of 10^{-4}, this leads to a p-polarized diffracted signal with a fluence that is a factor of ten smaller than the pump pulse leakage ($1nJ/cm^2$). Thus, using polarizing optics in the forward probing geometry will not allow a sensitivity that is adequate for our experiments, and we must therefore seek another method of reducing optical background noise to produce high experimental sensitivity.

In light of the experimental constraints that we have already discussed in this chapter, high sensitivity measurements can be most easily be enabled by using a two-color, Bragg-matched, forward-probing transient-grating geometry. Since the Bragg-matched probe pulse is of a different wavelength, the diffracted beam will be spatially separated from the pump pulses, leading to a background-free direction for measurement. However, in addition to allowing a background-free direction for measurement, use of the second color beam also provides a background-free wavelength for measurement. This allows for the use of commercially available spike filters to isolate the diffracted beam from the pump beams and thus greatly add to the sensitivity of the experiments.

5.4 The Photorefractive Polarization-Rotation Transient-Grating (PPRTG) Measurement Technique

In the preceding section, we showed that the picosecond photorefractive nonlinearities in semi-insulating GaAs and undoped CdTe could be separated and time-resolved with a forward-probing, two-color, Bragg-matched transient-grating measurement technique employing photorefractive polarization rotation. In this section we describe the actual technique used in our experiments, including the generation, phase matching and overlap of the 1.06μm wavelength probe beam. From this point on, our measurement technique will be referred to as the Photorefractive Polarization-Rotation Transient-Grating (PPRTG) measurement technique.

5.4.1 Writing and Reading of the Photorefractive and Other Gratings

The complete arrangement of the semiconductor crystal and optical beams used in these experiments is shown in figure 5.6. The induced gratings are generated by two spatially-

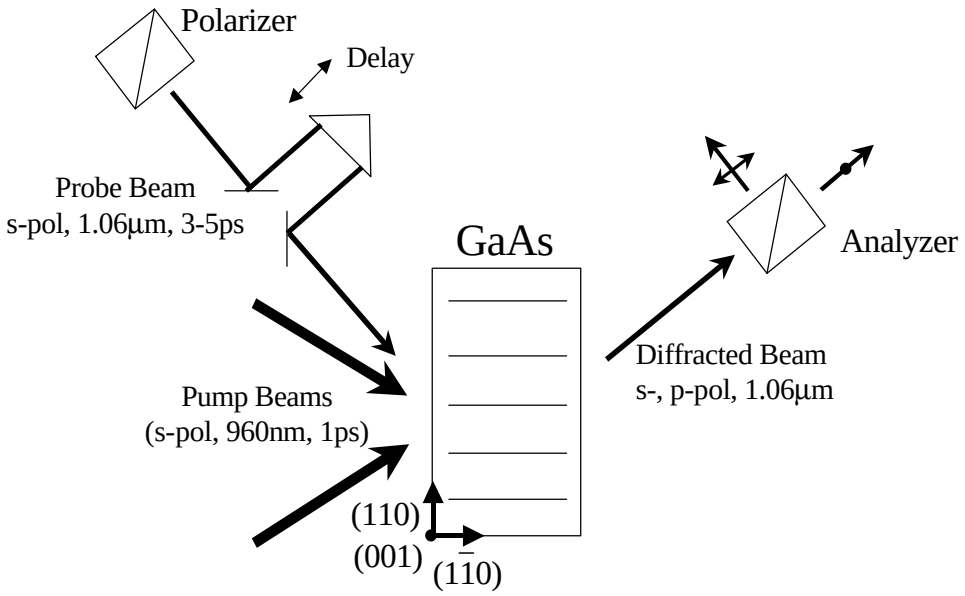

Figure 5.6 – Crystal and beam orientation for the Photorefractive Polarization Rotation Transient-Grating (PPRTG) measurement technique.

and temporally-coincident s-polarized pump beams from the amplified laser system. Or laser system produced energetic 960nm, 1ps duration laser pulses with Gaussian spatial profiles (1/e radius ~0.5 mm) (T. S. Stark et al., 1988). In our experiments, the pump beams were given equal intensities in order to eliminate transient energy transfer effects (see Chapters III and IV).

It is important to note that before data was taken each day, a pre-determined procedure was followed in order to allow an accurate determination of the pump beam fluences and intensities. This included scans to determine the beam sizes, as well as autocorrelation measurements to approximate the pulse duration.

Finally, an accurate determination of the picosecond nonlinear response of GaAs required that the residual (non-amplified) 82MHz pulses be eliminated from the 10Hz amplified pulse train (The processes described in Chapter III result in photorefractive and free-carrier gratings in GaAs that decay on microsecond (μs) time scales). In our

experiments, this was accomplished using a Pockels cell, which electrooptically rotated the polarization of the amplified pulses, along with a polarizing prism. The Pockels cell was electronically synchronized with our 10Hz regenerative amplifier.

As we discussed in the previous section, the gratings were read in these experiments with a Bragg-matched probe beam of a second color in order to give the measurements a greater sensitivity. By passing the probe beam through a variable delay stage consisting of a retro-reflecting corner cube mounted on a translation stage, it was possible to probe the gratings at a chosen time either before, during or after their generation. The generation, Bragg-matching and synchronization of the probe beam will be discussed in greater detail in the following sub-section. Also shown in figure 5.6 is the polarizer-analyzer pair in the probe and diffracted beams. The polarizer was used (along with a half-wave plate) to ensure that the probe beam was s- or p- polarized, while the analyzer is used to separate the different polarization components of the diffracted beam. It should be noted that in experiments where the free-carrier nonlinearity is measured, the polarization of the probe beam is made orthogonal to the polarization of the pump beams. This is done so that the analyzer can be used to isolate the diffracted radiation from the transmitted pump radiation. In contrast, in experiments where the photorefractive nonlinearity is measured, the rotated polarization component is made background-free by orienting the polarization of the probe beam so that it is parallel to that of the pump beams.

5.4.2 Generation and Bragg-Matching of the 1.06μm Probe Beam

One conclusion of section 5.3 was that our measurements require the use of a probe beam of a second color. In this sub-section, we discuss the generation and Bragg-matching of the probe beam. In addition, we consider the determination of pump-probe overlap, and the probe pulse duration.

In order to keep the probe beam from experiencing a large amount of absorption, it is advantageous to choose a wavelength that will not induce single-photon band-to-band transitions in either GaAs or CdTe. Furthermore, it is desirable to derive the probe beam from the 10Hz laser beam, so that the probe pulses can be easily synchronized with the pump pulses. Two methods of generating the desired signal were explored: Continuum Generation (CG) by self-phase modulation (R. R. Alfano, 1989), and Stimulated Raman Scattering (SRS) (M. D. Levenson and S. S. Kano, 1988). Of these methods, SRS was chosen because it was more efficient in producing a probe beam of a specific wavelength.

The SRS down conversion process is shown scematically in figure 5.7. The 1.06μm, down-shifted beam is generated by splitting off a portion (50%) of the amplified 960 nm amplified beam and gently focusing it through a 3cm cuvette filled with benzene. Of the liquids available for SRS, benzene was chosen because its CH vibrational line was capable of producing 1.06μm radiation from the 960nm pump pulses (G. Eckhardt, 1966). The use of a 1.06μm probe wavelength was chosen due to the commercial availability of spike filters centered on the Nd:YAG and Nd:Glass laser lines. The radiation is then sent through a spike filter, centered at 1.06μm, to separate the 1.06μm radiation from the unshifted 960nm light. Unfortunately, benzene is also highly Kerr active, so that the intense picosecond radiation induces phase modulation effects. In order to remove the

spatial phase distortions resulting from the Kerr effects, a spatial filter was employed. Spatial filtering of the beam was achieved by focusing the beam on a small pinhole, and then passing the transmitted far-field diffraction pattern through another aperture in order to eliminate all but the central maximum of its Airy disc pattern. Including spatial filtering, the overall conversion efficiency of the down-shifting process was ~1%. Finally, in order

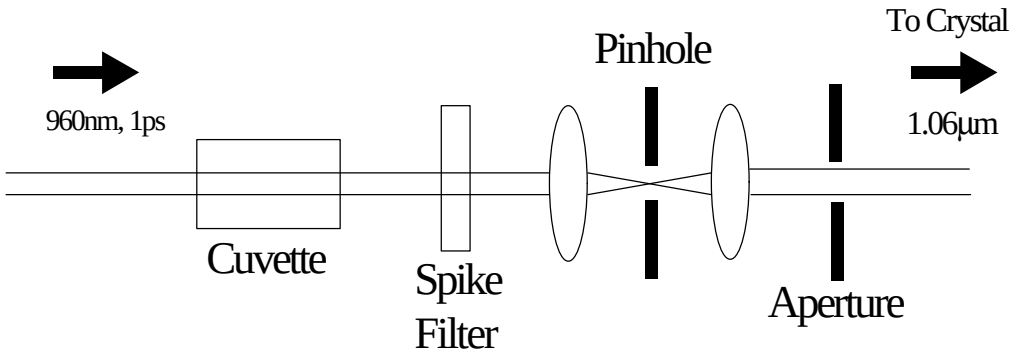

Figure 5.7 – Diagram of the optical apparatus used to produce the 1.06μm beam. See the text for description.

to ensure that the probe beam had a high-quality spatial profile for our experiments, the pinhole was imaged onto the sample site.

The lenses, pinhole and aperture that are shown in figure 5.7 make up a spatial filtering apparatus that ensures that the probe beam profile is gaussian or near-gaussian within the crystal. Though not shown, the vertical and horizontal shapes of the probe beam are both near-gaussian with ~0.3mm 1/e radii. Here it should be noted that the size of the probe beam was purposely chosen to be smaller than the pump beam (3/5 smaller in this case). In addition to allowing regions of the highest index change to be probed (so that a larger diffraction efficiency is produced), this helped minimize walk-off effects due to the finite sizes of the pump and probe beams.

As stated above, measurements were made in the Bragg-regime (crystal lengths large compared to the grating spacing). As a result, the probe beam had to be Bragg-matched to the gratings in order to observe nonlinear diffraction. The correct incidence angle, θ, for the probe beam was first calculated with the Bragg relation, $\lambda = 2\Lambda_g \sin\theta$ (Λ_g is the grating spacing and λ is the probe wavelength). The probe beam was then aligned to be incident on the crystals at these angles, with small adjustments made periodically for maximum diffraction efficiency.

Overlap between the pump and probe pulses was determined by measuring the differential transmission of the probe pulses through the semiconductor crystals in the presence of one of the pump pulses. Figure 5.8 shows a typical differential transmission versus probe delay plot. When the pump and probe beams are overlapped, the intense 960nm radiation causes the weak, 1.06μm radiation pulses to be more strongly absorbed through the instantaneous two-photon absorption process. The pump and probe pulses are synchronized when the transmission of the probe pulses is minimum. This is because two-photon-related absorptive loss of the probe pulses is maximum when the overlap between the pump and probe pulses is maximum.

The differential transmission plot can also be used to determine the duration of the probe pulses. The differential transmission feature is expected to follow the inverted second-order correlation function between the intensity profiles of the pump and probe pulses. In light of this, and the fact that the duration of the pump pulses is independently determined to be less than 1ps (this is known by measuring the intensity autocorrelation of the pump pulses at the sample site), the shape of the differential transmission feature shown in figure 5.8 shows a FWHM (full width at half minimum) of ~4.0ps. It should be

noted that in our experiments, probe pulse widths varied between 3ps and 5ps. Since the duration of the pump pulses was consistently ~1ps, 3ps – 5ps represents the minimum time that can be resolved with our measurement technique. It should also be noted that the slight asymmetry seen in the differential transmission feature of figure 5.8 was present in nearly all plots of this type. This feature reflects an asymmetry in the intensity profile of the probe pulses, which is expected from the transient nature of the SRS process (C. S. Wang, 1985).

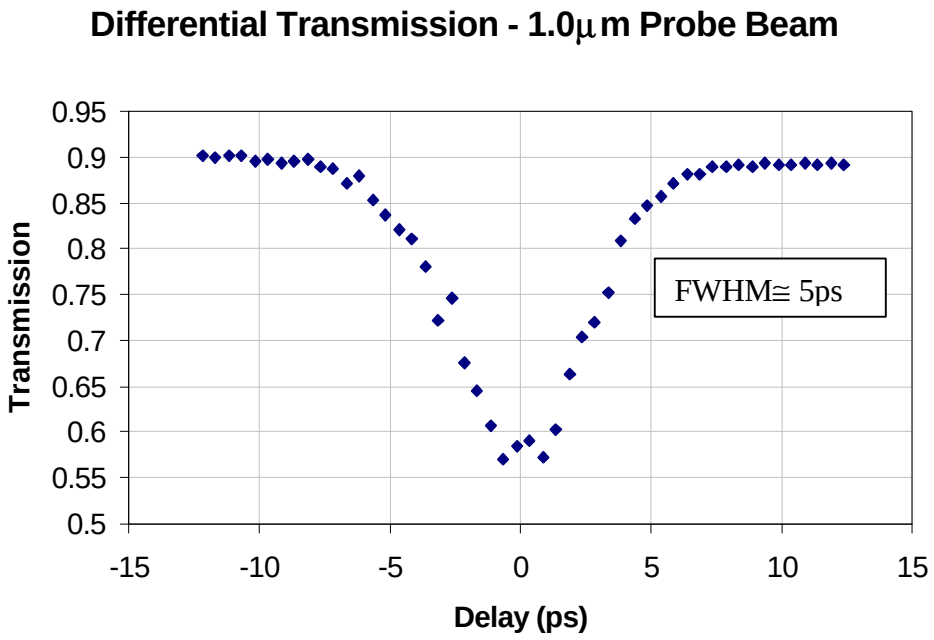

Figure 5.8 – Plot of differential transmission versus probe delay for the Raman-shifted probe beam. The duration of the down-shifted pulses, which the figure shows is approximately 5ps, is the minimum resolvable time for our measurement technique.

5.5 Conclusions

In this chapter we have discussed the measurement technique that we use in our experiments. We considered the requirements that the goals of our study places on the measurement technique, and showed that these requirements are met in a two-color,

Bragg-matched, forward-probing transient-grating measurement technique involving photorefractive polarization rotation. The use of a probe beam of a second color is an important part of our measurement technique. Therefore, we considered the generation, phase matching and overlap of our probe pulses. With this, we considered the duration of our probe pulses, which is the minimum time that can be resolved in our experiments.

CHAPTER VI

NUMERICAL MODELING OF EXPERIMENTAL RESULTS

6.1. Introduction

As part of our investigation of the picosecond photorefractive effects in semi-insulating GaAs and undoped CdTe, it is necessary to numerically model our experimental results. In this chapter we consider the method that we use in achieving this goal. A detailed model for the diffraction efficiencies we measure must necessarily consider the nonlinear response of the material, as well as the propagation of the pump, probe and diffracted beams in the presence of linear and nonlinear absorption and laser-induced index gratings. However, as we show in this chapter, our goal, which is to model the probe-delay dependencies of the diffraction efficiencies, can be accomplished in a much more simple way. We begin by deriving equations that describe the propagation of the pump, probe and diffracted beams, as well as the n=0,1, and 2 components of the photogenerated carrier densities. Following this, we show that in the limit of small diffraction, and for probe delays greater than 5ps, we can model the temporal dynamics of the diffraction efficiencies using the carrier and field equations of Chapter III, along with the relationship between the carrier densities and the free-carrier index change, and the space-charge field and the photorefractive index change. In semi-insulating GaAs, where the relative densities of electrons, holes and ionized EL2 depend on fluence,

we find that we must also solve the beam propagation equation.

6.2 Beam Propagation and Carrier Density Equations

Figure 6.1 shows the configuration of our PPRTG measurement technique that was presented in Chapter V. As we discussed there, in order to measure the dynamics of the photorefractive and other induced index changes, we measure the diffraction efficiency of the induced gratings as a function of the probe pulse delay (with respect to the pump pulses). As shown in figure 6.1, the quantity that we measure, which is the ratio of the voltages of two photodiodes, is related to the ratio of the temporal and spatial integral of the probe and diffracted intensities:

$$\eta_{n,r}(\tau) \propto \frac{\iint I_{dn,dr}(\tau, r, t)\, 2\pi r\, dr\, dt}{\iint I_{pr}(r,t)\, 2\pi r\, dr\, dt}, \qquad (6.1)$$

where τ is the probe pulse delay, the *dr* integral is over the surface of the photodiodes, the *dt* integral is over the duration of the probe and diffracted pulses, and it is understood that the probe intensity is measured before the front face of the crystal, and the rotated and non-rotated diffracted intensities are measured behind the rear surface of the crystal. The probe and diffracted intensities (I_{pr}, I_{dn}, I_{dr}) are related to the probe and diffracted electric fields (E_{pr}, E_{dn}, E_{dr}) through the relationship:

$$I_{pr,dn,dr}(r,t) = \left[\frac{1}{2}\varepsilon_0 c n_b\right]^2 \left|E_{pr,dn,dr}(r,t)\right|^2, \qquad (6.2)$$

where all the factors in this equation have been previously defined.

From equations (6.1) and (6.2), it is clear that that any model of the diffraction efficiency must necessarily consider the magnitudes of the probe and diffracted electric

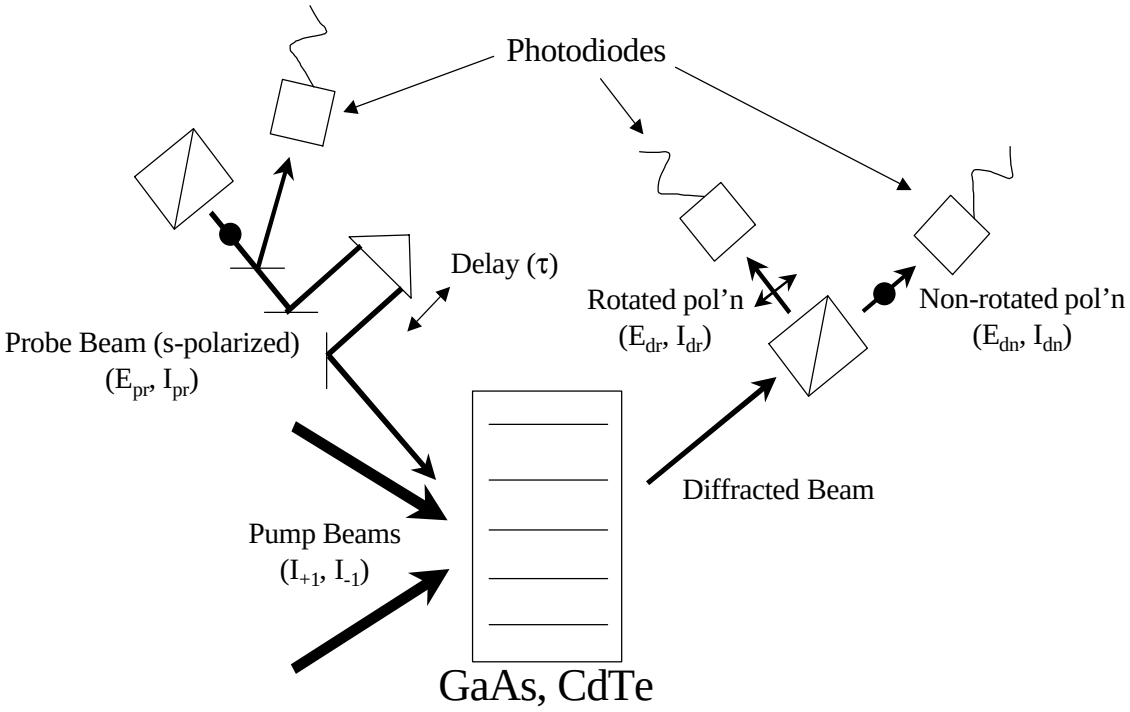

Figure 6.1 – Experimental set-up depicting the quantities that we measure, the rotated and non-rotated diffraction efficiencies. The diffraction efficiencies involve the ratio of the diffracted and probe intensities, as described in the text.

fields. The magnitudes of these fields are coupled though the induced index and absorption changes, which arise from the material response to the pump beams. Thus, in modeling the diffraction efficiency, we must also consider these things. In the following discussion, we consider the propagation of the pump, probe and diffracted beams. While the response of the material is described in the discussions of Chapters II and III, our model for the carrier and field dynamics takes, as input, the n=0,1, and 2 components of the photogenerated electrons, holes and ionized EL2. Since these quantities follow directly from the pump beam intensities, we consider their magnitude along with the pump beams.

6.2.1 Pump Beam Equations

In our experiments, we employ 960nm wavelength pump beams with a 1.0mm (*1/e*) spatial width. Since the 6.5m confocal parameter associated with these beams is much larger than our 1mm-3mm crystal lengths, we can assume that the pump beams propagate through the crystals as plane waves. In addition, in order to generate and probe grating wavelengths between 1.7μm and 3.8μm in our GaAs and CdTe crystals, the pump and probe beams propagate inside the crystals at angles less than ~5° relative to the normal to the plane of incidence. Thus, we can also assume that the pump beams co-propagate along the direction normal to the plane of incidence. Under these circumstances, we can use the method outlined in section 4.2 in order to derive propagation equations for the pump beams. When we allow for instantaneous two-photon absorption through the imaginary component of the third-order susceptibility, this procedure results in the following equations:

$$\frac{dI_{+1}}{dz} = -\sigma_e (N - N^+) I_{+1} - \sigma_h N^+ I_{+1} - \beta I_{+1}^2 - 2\beta I_{+1} I_{-1}, \qquad (6.3)$$

and

$$\frac{dI_{-1}}{dz} = -\sigma_e (N - N^+) I_{-1} - \sigma_h N^+ I_{-1} - \beta I_{-1}^2 - 2\beta I_{-1} I_{+1}, \qquad (6.4)$$

where we have adopted the same conventions used in Chapter IV, calling the z direction the propagation direction, and denoting the pump beams as I_{-1}.

Equations (6.3) and (6.4) account for single-photon absorption at the EL2 sites as well as self- and cross-beam instantaneous two-photon absorption. While these equations apply to semi-insulating GaAs, the equations for undoped CdTe result when we eliminate

EL2 absorption (σ_e,σ_h, N, N^+=0). As we noted in Chapter II, the neutral and ionized EL2 densities can vary with fluence for our excitation conditions, so that these equations must be solved self-consistently with the equations for the EL2 densities. We also noted in Chapter II that the two photon absorption coefficient (β) has been observed to be crystal-orientation dependent in both semi-insulating GaAs and undoped CdTe (M. D. Dvorak et al., 1994). For our experiments in semi-insulating GaAs, where we employ s-polarized pump beams (E|| (001) crystallographic axis), these studies suggest a value of 19cm/GW for the two-photon absorption coefficient. Likewise, in our experiments in undoped CdTe, where we employ s-polarized pump beams (E|| $(11\bar{2})$ crystallographic axis), the same studies suggest a value of 17cm/GW for the two-photon absorption coefficient.

Before proceeding, several additional points must be made about equations (6.3) and (6.4). First, it must be noted that we have not allowed for energy coupling between the two pump beams. This is because the means for energy coupling, photorefractive beam coupling and transient energy-transfer, are not allowed for our experimental conditions. For transient energy-transfer, this follows from the fact that the pump beams have equal intensities (see section 4.3). In the case of the photorefractive effect, beam coupling is not allowed for our crystal orientation (see section 5.4). It must be noted that while photorefractive energy coupling is not allowed for our crystal orientation, the pump beams will experience photorefractive polarization rotation in the way that is discussed in Chapter V. However, we neglect this in equations (6.3) and (6.4) because the overall magnitude of this effect is small, and results in no significant effect to the modulated intensity pattern that is produced by the pump pulses.

Second, in modeling our experiments, we do not consider non-linear optical effects that alter the phase structure of the optical electric fields and affect the ability of the pulses to form the modulated optical intensity pattern. As a result, while the pump beams will experience intensity-dependent self- and cross-phase modulation through the real part of the third order susceptibility (refractive instantaneous bound-electronic nonlinearity), we have neglected these effects in equations (6.3) and (6.4). Instead, we assume that the pump pulses are perfectly coherent at 960nm, so that the modulated optical intensity pattern is perfectly formed. Since we employ pump pulses of equal intensity, self- and cross-phase modulation effects are expected to affect both beams equally.

Third, in describing the propagation of the pump beams, we do not consider nonlinear optical effects involving the refractive instantaneous bound-electronic nonlinearity which rotate the polarization of the pump beams (W. A. Schroeder et al., 1992). This follows from a simple analysis involving the crystal orientation, pump beam orientation, and tensor properties of the cubic $\bar{4}3m$ third order susceptibility, which show that interactions of this type are not allowed for our experimental conditions.

Finally, while it is possible for the 1.06μm probe pulse probe pulse to interfere with either of the pump pulses and form modulated intensity patterns and induced gratings, we do not consider interactions of this type. This is because the probe pulse intensity is much weaker than the pump pulse intensities, so that any induced gratings of this type would have a much smaller magnitude than those generated by the pump pulses.

6.2.2 Carrier Density and Ionized EL2 Equations

In Chapter III, we used the Fourier series formalism to derive equations that describe the dynamics of the carrier densities and space-charge fields. However, in modeling the carrier and field dynamics in this way, it is necessary to determine the initial Fourier components of the electron, hole and ionized EL2 densities for use in these equations. In this section, we derive rate equations for the n=0, 1 and 2 densities of the electrons, holes and ionized EL2. We use the functional form for the modulated intensity pattern, along with the carrier generation equations of Chapter II, to produce these equations.

As we noted above, the rate equations for the Fourier components of the carrier densities and ionized EL2 are derived using the functional form for the modulated intensity pattern (equation (3.1), *m*=1), along with the carrier generation equations of Chapter II (equations (2.27), (2.28) and (2.3)). If we allow the density of ionized EL2 to be modulated as a result of saturation, we find the following equations for the electrons:

$$\frac{\partial n_0}{\partial t} = \frac{\mathsf{s}_e}{h\mathsf{n}}\left[N - N_{dc}^{+} - \frac{N_{ac}^{+}}{2}\right]I_0 + \frac{3}{4}\frac{\mathsf{b}I_0^2}{h\mathsf{n}}, \qquad (6.5)$$

$$\frac{\partial n_1}{\partial t} = \frac{\mathsf{s}_e}{h\mathsf{n}}\left[N - N_{dc}^{+} - N_{ac}^{+}\right]I_0 + \frac{\mathsf{b}I_0^2}{h\mathsf{n}}, \qquad (6.6)$$

$$\frac{\partial n_2}{\partial t} = \frac{\mathsf{s}_e}{h\mathsf{n}}\left[-\frac{N_{ac}^{+}}{2}\right]I_0 + \frac{\mathsf{b}I_0^2}{4h\mathsf{n}}, \qquad (6.7)$$

holes:

$$\frac{\partial p_0}{\partial t} = \frac{\mathsf{s}_h}{h\mathsf{n}}\left[N_{dc}^{+} + \frac{N_{ac}^{+}}{2}\right]I_0 + \frac{3}{4}\frac{\mathsf{b}I_0^2}{h\mathsf{n}}, \qquad (6.8)$$

$$\frac{\partial p_1}{\partial t} = \frac{\sigma_h}{h\nu}\left[N_{dc}^{+} + N_{ac}^{+}\right] I_0 + \frac{\beta I_0^2}{h\nu}, \qquad (6.9)$$

$$\frac{\partial p_2}{\partial t} = \frac{\sigma_h}{h\nu}\left[\frac{N_{ac}^{+}}{2}\right] I_0 + \frac{\beta I_0^2}{4h\nu}, \qquad (6.10)$$

and ionized EL2:

$$\frac{\partial N_0^{+}}{\partial t} = A^{-} + \frac{\sigma_e}{h\nu} N I_0 - (N_{dc}^{+} + \frac{N_{ac}^{+}}{2})\frac{I_0}{F_{sat}}, \qquad (6.11)$$

$$\frac{\partial N_1^{+}}{\partial t} = \frac{\sigma_e}{h\nu} N I_0 - (N_{dc}^{+} + N_{ac}^{+})\frac{I_0}{F_{sat}}, \qquad (6.12)$$

$$\frac{\partial N_2^{+}}{\partial t} = -\frac{N_{ac}^{+}}{2}\frac{I_0}{F_{sat}}. \qquad (6.13)$$

We emphasize that though equations (6.5) – (6.13) describe the carrier and ionized EL2 densities in terms of Fourier components, in treating carrier generation due to the EL2 sites, these equations contain the same information as equations (2.12) – (2.14). However, we note that the above equations must be solved together with equation (2.12), which yields the maximum ionized EL2 density in the crystal. This, quantity, which we refer to as N^{+}_{peak}, is used with the dark density of ionized EL2 (A^{-}) to determine the constant and modulated components of our assumed ionized EL2 density:

$$N_{ac}^{+} + N_{dc}^{+} = N_{peak}^{+},$$

$$N_{dc}^{+} - N_{ac}^{+} = A^{-}.$$

All of the other parameters in equations (6.5) – (6.13) have been previously defined, including I_0, the peak intensity in the crystal, which is the combined intensity of both pump beams (see equation (3.1)). As with the beam propagation equations (equations

(6.3) and (6.4)), the CdTe carrier generation equations follow when we do not consider EL2 absorption (σ_e,σ_h, N, N^+=0).

In modeling the attenuation of the pump beams and the subsequent generation of free carriers, it is necessary to ensure that the photogenerated carrier densities balance the light that is absorbed. We can see this balance easily in equations (6.3) – (6.13) if we express equations (6.3) and (6.4) in terms of the modulated intensity pattern. This is done by summing the electric field equations that are associated with equations (6.3) and (6.4) to obtain a propagation equation for the total pump electric field inside the material. We then use this equation to form a propagation equation for the total intensity inside the material, noting that the modulated intensity is formed by cross-terms between the two pump fields. When we allow the neutral and ionized EL2 densities to be modulated, this balance is directly seen.

6.2.3 Probe and Diffracted Field Equations

The equations of section 6.2.1 describe the propagation of the pump beams through the crystal, and the effect that the material has on the beams is taken into account completely by the linear and non-linear absorption terms. Conversely, the effect that the pump beams have on the material is described in the equations of section 6.2.2, and Chapters II and III. In this section, we consider the only remaining element in modeling our experiments: the propagation of the probe and diffracted beams in the presence of linear and nonlinear absorption and diffraction due to the induced gratings. Since the quantities that we observe in our experiments, the rotated and non-rotated diffraction

efficiencies, follow directly from the propagation equations for the probe and diffracted beams, this forms a very important part of our model.

As we discussed in Chapter V, the 1.06μm wavelength probe beam that we use in our experiments is focused to a 0.6mm (*1/e*) spatial width. Since the 2.1m confocal parameter associated with the propagation of this beam is much larger than our 1mm-3mm crystal lengths, we can assume, as in the case of the pump beams, that the probe and diffracted beams propagate through our crystals as plane waves. Furthermore since the phase matching angle for our induced gratings is less than ~6.5° relative to the normal to the plane of incidence, we can assume that the probe and diffracted beams co-propagate with the pump beams along the direction normal to the plane of incidence. Under these circumstances, we can use the process described in section 4.2 to derive equations for the probe and diffracted electric fields. As in section 4.2, we model the coupling between the probe and diffracted beams in terms of phase-matched interactions with the induced gratings. This procedure produces the following equations for the rotated and non-rotated components of the probe (E_{prr}, E_{prn}) and diffracted (E_{dr}, E_{dn}) electric fields:

$$\frac{\partial E_{prn}}{\partial z} = -\frac{\alpha}{2} E_{prn} - \frac{\beta}{2}\left(I_{+1} + I_{-1}\right)E_{prn} + \frac{i2\pi\Delta n_{fc}}{\lambda} E_{dn} + \frac{i2\pi\Delta n_{ibe}}{\lambda} E_{dn}, \tag{6.14}$$

$$\frac{\partial E_{prr}}{\partial z} = -\frac{\alpha}{2} E_{prr} - \frac{\beta}{2}\left(I_{+1} + I_{-1}\right)E_{prr} + \frac{i2\pi\Delta n_{pr}}{\lambda} E_{dr}, \tag{6.15}$$

$$\frac{\partial E_{dn}}{\partial z} = -\frac{\alpha}{2} E_{dn} - \frac{\beta}{2}\left(I_{+1} + I_{-1}\right)E_{dn} + \frac{i2\pi\Delta n_{fc}}{\lambda} E_{prn} + \frac{i2\pi\Delta n_{ibe}}{\lambda} E_{prn}, \tag{6.16}$$

and,

$$\frac{\partial E_{dr}}{\partial z} = -\frac{\alpha}{2} E_{dr} - \frac{\beta}{2}\left(I_{+1} + I_{-1}\right)E_{dr} + \frac{i2\pi\Delta n_{pr}}{\lambda} E_{prr} . \qquad (6.17)$$

Here λ is the vacuum wavelength of the probe and diffracted fields, and Δn_{pr}, Δn_{fc}, and Δn_{ibe}, the index changes associated with the photorefractive, free-carrier and instantaneous bound-electronic nonlinearities, are defined respectively by equations (3.56), equations (2.25) and (2.26), and equations (2.32) and (2.33). In the case of the refractive instantaneous bound-electronic nonlinearity, the induced index change in equations (6.14) and (6.16) arises from the third-order susceptibility tensor associated with the pump and probe wavelengths (equation (2.33), 960nm, 1.06μm).

As we noted at the beginning of this discussion, the propagation equations for the probe and diffracted beams form an important part of our model. Thus, there are several points about the above equations that are worthy of discussion. First, we have assumed in equations (6.14) – (6.17) that the fluences associated with the probe and diffracted fields are small enough so that no EL2 saturation occurs, so that α is the small-signal linear absorption coefficient at the wavelength of the probe and diffracted fields (1.06μm). In addition since the optical intensities associated with the probe and diffracted fields are small, we have neglected self- and cross-instantaneous two-photon absorption between the probe and diffracted beams. However, we have allowed for instantaneous two-photon absorption of the probe and diffracted beams due to the presence of the pump beams, so that β is the non-degenerate two-photon absorption coefficient for the wavelengths of 960nm and 1.06μm. Clearly, this effect is negligible except for probe delays less than ±5ps.

Second, equations (6.14) – (6.17) show that the probe and diffracted fields are coupled through the induced index gratings. While equations (6.16) and (6.17) show that the diffracted beam is generated as a result of the interaction of the probe beam with these gratings, equation (6.15) and the last two terms on the right of equation (6.14) allow for energy coupling back into the probe beam in the limit of large diffraction. Moreover, equations (6.16) and (6.17) show that, while the non-rotated (polarization) component of the diffracted beam arises from interactions with the refractive instantaneous bound-electronic and free-carrier gratings, the sole contribution to the rotated (polarization) component is due to the photorefractive grating. As we noted in Chapters II and V, the free-carrier grating produces no polarization rotation because the associated optical nonlinearity is isotroptic on picosecond timescales. Furthermore, since the probe electric field is polarized parallel to the pump fields, interactions between the pump and probe beams due to the refractive instantaneous bound-electronic nonlinearities can not result in a beam with a rotated polarization (W.A. Schroeder et al., 1992).

Third, in discussing the terms describing nonlinear diffraction in equations (6.14) – (6.17), it is important to note that the lengths of our crystals (1-3mm) are large compared to the periods of the induced gratings that we probe (1.7μm-3.8μm). As a result, the free-carrier instantaneous bound-electronic and photorefractive index changes that are responsible for nonlinear diffraction in equations (6.14) – (6.17) follow from the n=1 Fourier components of the free carrier population, optical intensity, and space-charge field.

Finally, close examination of equations (6.14) – (6.17) in light of the discussions of Chapter IV shows that we have neglected the effects of absorption gratings in these equations. More specifically, while our pump pulses produce absorption gratings that are present due to EL2 absorption saturation and instantaneous two-photon absorption (due to the presence of the modulated intensity pattern, the probe and diffracted beams see a change in absorption: $\Delta\alpha = \beta I_0$), we have neglected the effects of these gratings. Using the magnitude of the absorption change ($\Delta\alpha \sim 0.7 cm^{-1}$) associated with EL2 absorption saturation, equation (5.1) shows that the diffraction efficiency associated with this grating is small relative to the diffraction efficiencies associated with the refractive index gratings present in our experiments. In addition, the magnitude of this grating can be considered constant over the range of probe delays used in our experiments, so that it will not affect our diffraction efficiency versus probe delay results. Conversely, the magnitude of the absorption grating associated with instantaneous two-photon absorption can be large, but it is only significant between probe delays of ±5ps. In terms of the probe delay-dependence of the diffraction efficiency, this grating will affect our results in the same way as the refractive instantaneous bound-electronic grating. Since these nonlinearities convey no information about the carrier or field dynamics that produce the photorefractive nonlinearity, and since we have allowed for the presence of the refractive instantaneous bound-electronic nonlinearity in equation (6.16), the contribution of this absorption grating is neglected.

6.2.4 Summary

Using the pump, probe and diffracted beam equations given in this section, as well as the materials equations given here and in Chapters II and III, we can model the dynamics of the diffraction efficiencies that we observe with a high degree of fidelity. These equations must be solved self-consistently for each probe delay, for the length of each crystal, and for each element of the spatial profile of the beams. Clearly, we can only solve these equations numerically, so that modeling of our experimental results is clearly a complicated endeavor. However, as we show in the following section, we can simplify this process by making some observations that follow from our experimental conditions.

6.3 Modeling Method

The set of equations given in section 6.2 can be used to perform high fidelity modeling of our experiments. However, while it is desirable to model our results with a high degree of fidelity, as we noted in section 6.2, such fidelity comes with a high degree of complexity. It is therefore necessary to investigate ways of simplifying the modeling method outlined in section 6.2. As we show in this section, this can be done for our experimental conditions, so that we can model the observed diffraction efficiencies for probe delays greater than ~5ps using the carrier and field equations that are derived in Chapter III, along with the small-signal diffraction efficiency and the relationship between the carrier density and free-carrier index change, and space-charge field and photorefractive index change.

6.3.1 Time Resolving the Rise of the Photorefractive Nonlinearities in Semi-insulating GaAs and Undoped CdTe

We begin by discussing the rise of the photorefractive nonlinearities in semi-insulating GaAs and undoped CdTe for our experimental conditions and show that the expected rise time of the space-charge field is always comparable to, or less than, the duration of our probe pulses. Thus, while we are therefore relegated to modeling only the decay of the photorefractive nonlinearities in our materials, this results in a considerable simplification to the equations for the probe and diffracted beams.

An important simplification to equations (6.14) – (6.17) can be made by estimating the expected formation time of the photorefractive nonlinearities generated in our materials. While we stated, for the purposes of estimation in Chapter II, that we generate average carrier densities between $10^{14}cm^{-3}$ and 10^{16} cm^{-3} in our materials, it is necessary for the purposes of discussion to cite a more specific estimation of the carrier densities generated in our materials. Using the beam propagation equations along with the parameters given in Chapter II, we find that we generate carrier densities between $3x10^{15}cm^{-3}$ and $3x10^{17}cm^{-3}$ in CdTe, and carrier densities between $2x10^{14}cm^{-3}$ and $1x10^{17}$ cm^{-3} in semi-insulating GaAs (at the center of our pump pulses). As we discussed in Chapter III, for these carrier densities we expect the space-charge fields to follow drift-limited dynamics, where the field forms in the (carrier density-dependent) dielectric relaxation time. Using the carrier densities given above, along with the parameters given in Chapter III, we find that the space-charge fields can be expected to form in times less than ~2.5ps for our experimental conditions. Since the space-charge fields form in times

less than the FWHM intensity duration of our probe pulses, we do not expect to be able to time-resolve the formation of the photorefractive nonlinearities generated in our materials. As a result, in modeling the probe delay dependencies of the diffraction efficiencies, we are relegated to modeling the decay of the diffraction efficiencies in these materials at probe delays greater than ~5ps. For probe delays greater than 5ps, we can neglect the terms in equations (6.14)-(6.17) that describe pump-intensity dependent absorption of the probe and diffracted beams, as well as the contribution to the non-rotated diffracted beam due to the instantaneous bound-electronic grating.

In the data for both GaAs and CdTe, we observe an enhancement to the rotated component of the diffraction efficiency that is consistent with diffraction from a photorefractive grating that is formed by hot carrier transport. In semiconductors, the free carrier mobilities are linearly proportional to the momentum relaxation time (t_m), which increases with increasing carrier temperature in materials like GaAs and CdTe, where polar optical phonon scattering is the dominant scattering mechanism (K. Seeger, 1985). Thus, in our materials, an increased carrier temperature leads to increased carrier mobilities. Since the dielectric relaxation time is inversely proportional to the carrier mobility, we observe a faster photorefractive rise time than is estimated above, especially at higher excitation fluences. As a result, even if we numerically solved equations (6.14) – (6.17) for the full range of probe delays, the predictions of our model would be in disagreement with the experimental results for probe delays less than ~5ps, where carrier cooling is incomplete.

6.3.2 Small-Signal Approximation

The second simplification that we can make to the equations given in section 6.2 follows from the fact that, at all times in our experiments, we measure diffraction efficiencies that are much less than unity. Under these circumstances, we can neglect equation (6.15), and the terms in equation (6.14) that describe nonlinear diffraction from the non-rotated diffracted beam to the probe beam. Taking this into account, along with the discussions of section 6.3.1, the equations for the probe and diffracted beams can be re-written:

$$\frac{\partial E_{pr}}{\partial z} = -\frac{\alpha}{2} E_{pr}, \qquad (6.18)$$

$$\frac{\partial E_{dn}}{\partial z} = -\frac{\alpha}{2} E_{dn} + \frac{i 2\pi \Delta n_{fc}}{\lambda} E_{pr}, \qquad (6.19)$$

and,

$$\frac{\partial E_{dr}}{\partial z} = -\frac{\alpha}{2} E_{dr} + \frac{i 2\pi \Delta n_{pr}}{\lambda} E_{pr}. \qquad (6.20)$$

These equations can be easily solved to yield expressions for the small-signal rotated and non-rotated diffraction efficiencies:

$$\eta_n = \left(\frac{2\pi \Delta n_{fc} \ell}{\lambda} \right)^2, \qquad (6.21)$$

and

$$\eta_r = \left(\frac{2\pi \Delta n_{pr} \ell}{\lambda} \right)^2, \qquad (6.22)$$

where ℓ is the length of the crystal, and it is understood that the diffraction efficiencies (η_{nr} and η_{r}) and the corresponding index changes (Δn_{fc}, Δn_{pr}) are functions of the probe delay (t).

The results contained in equations (6.21) and (6.22) are important because they encapsulate the physics contained in equations (6.18) – (6.20) into two (relatively) simple analytical expressions for the quantities that we observe, the diffraction efficiencies associated with the non-rotated and rotated polarization components of the diffracted beam. In principle, we can use these equations, along with equations that describe the dynamics of the free-carrier and photorefractive index changes, to model the dynamics of the non-rotated and rotated diffraction efficiencies. A dynamical picture of the free-carrier and photorefractive index changes is given by the equations derived in Chapter III, which describe the dynamics of the free-carrier populations and space-charge fields. To model the dynamics of the photorefractive and free-carrier index changes, these equations are used with the equations that relate the free-carrier and photorefractive index changes to the free-carrier density and space-charge field magnitude. While the carrier and field equations of Chapter III assume free-carrier populations that are generated instantaneously, use of these equations is justified, since the carrier populations are generated by 1ps duration pulses, which is instantaneous relative to the decays that are expected in our experiments (35ps – 750ps).

6.3.3 Spatial and Beam Propagation Effects

While it would seem that equations (6.21) and (6.22) offer a simple way of modeling our diffraction efficiency versus probe delay results, we must take caution in using this approach. It is important for us to note that the observed diffraction efficiencies reflect index changes that must be thought of as averages over the spatial profile and temporal duration of the probe pulses, as well as averages over the propagation length of the crystal. Thus, in using equations (6.21) and (6.22) to model the observed diffraction efficiencies, we must consider effects due to the spatial profiles of the pump pulses, as well as propagation effects related to the pump beams.

As we discussed in section 5.4.3, we minimize effects with the spatial profiles of the pump and probe beams by choosing a probe beam with a (*1/e*) radius that is 60% of that of the pump beams. As a result, we can model the diffraction efficiencies in terms of the peak intensities of the pump pulses. However, since we use long crystal lengths, and since our pump beams can be depleted via instantaneous two photon absorption, averaging effects over the crystal lengths might be expected to have a non-negligible effect on our experimental results. For example, due to the presence of instantaneous two-photon absorption, our pump beams experience optical limiting as they propagate through the crystal, an effect that leads to a non-negligible variation in pump intensity between the front and back faces of the crystal and a similar variation in the photogenerated free carrier densities. Since the decay of the free-carrier populations and electron-hole space-charge field can be carrier density-dependent, this can lead to the following result: the photorefractive diffraction efficiency that is measured at a given

probe pulse delay is an average over a set of gratings encountered at different points along the propagation length, at various stages of decay.

By recalling the carrier generation discussions of Chapter II, as well as the carrier transport and field formation discussions of Chapter III, we can estimate the effect that the propagation length has on the diffraction efficiencies that we observe. As we saw in Chapter II for undoped CdTe, the sole carrier generation mechanism, which is instantaneous two-photon absorption, produces equal populations of electrons and holes. In addition, as we saw in Chapter III and in section 6.3.1, the carrier densities that we generate in undoped CdTe are large enough so that our experimental results can be expected to exhibit drift-limited carrier and field dynamics. In the drift limit of carrier and field dynamics, the decay of the free carrier populations and electron-hole space-charge field occur by ambipolar diffusion, and the associated time constant is the same for all carrier densities, since equal populations of electrons and holes are always present. Thus, we conclude that in undoped CdTe, the decay of the induced index changes will not vary over the length of the crystal for our experimental conditions.

The result of the previous paragraph, that the decay of the free-carrier and photorefractive index changes do not vary over the crystal length for our experimental conditions, leads to the following method for modeling our CdTe results. For each excitation fluence, we numerically solve the beam propagation equation to determine the average electron and hole densities that are generated over the crystal length. We then use these carrier densities in the carrier and field equations of Chapter III to determine the dynamics of the n=1 electron density and space-charge field. Following equations (6.21)

and (6.22) and the equations that relate the free carrier density and space-charge field to the corresponding index changes, we square these quantities and then fit them to the non-rotated and rotated diffraction efficiencies.

The situation is not as simple in semi-insulating GaAs. As we saw in Chapter II, beam depletion and carrier generation in semi-insulating GaAs occur by linear and instantaneous two-photon absorption, and the relative importance of these two carrier generation mechanisms varies as a function of fluence over the propagation length. However, more importantly, excitation of our crystal generally produces unequal populations of electrons and holes, and the relative magnitude of the electron and hole densities varies with fluence over the crystal length. Since the drift-limited dynamics of the free carrier populations and electron-hole space-charge field vary with the relative magnitudes of the electron and hole populations, the dynamics of the non-rotated and rotated diffraction efficiencies can be expected to vary over the length of the crystal.

In order to consider propagation effects involving the pump beams, we can use the following procedure in modeling our semi-insulating GaAs results. We numerically solve the beam propagation equations (equations (6.3) and (6.4)) using the peak beam intensities, and assuming a constant linear absorption. For each excitation fluence, we divide the crystal into slices ($d\ell$) over which the optical fluence decreases by 20% from its initial value. For each slice, we use the equations given in section 6.2.2 to determine the n=0,1, and 2 components of the electron, hole, and ionized EL2 densities. These carrier densities are then used in the carrier and field equations of Chapter III to determine the dynamics of the n=1 component of the space-charge field and electron

density. For each incident fluence, we use the dynamics of the carrier densities and field for each crystal slice, along with the slice thickness to form the sum of the square of the field or carrier density and slice thickness ($\sum\left(\Delta n_{fc}, \Delta n_{pr} d\ell\right)^2$). This result is then fit to the diffraction efficiency for the corresponding fluence and polarization component.

In concluding this discussion, we note that Appendix B contains source listings for the computer codes used in modeling our experimental results. In modeling the CdTe results, we use "beamprop.for" to determine the average carrier densities, and "cdte5.for" to determine the carrier and field dynamics. In modeling our semi-insulating GaAs results, we use "carrgen.for" to determine the crystal slices and carrier densities, and then "gaas5.for" to determine the carrier and field dynamics.

6.4 Conclusions

In this chapter we have considered the numerical modeling of our experimental results. We began by deriving a set of equations that describe the propagation of the pump, probe and diffracted beams, as well as the photogenerated EL2 and carrier densities. With the equations that were derived in Chapter III, which describe the dynamics of the free carriers and space-charge fields, these equations form a detailed model for our experiments. We found that while the set of equations that comprise our model can not be solved analytically, we can simplify the equations for the probe and diffracted beams by noting that our diffraction efficiencies are always much less than unity, and by modeling the dynamics of the diffraction efficiencies only for probe delays greater than 5ps. With these two simplifications, we solved the equations for the probe

and diffracted beams to yield analytical expressions for the rotated and non-rotated diffraction efficiencies. We then showed that, with numerical solutions to the equations of Chapter III that describe carrier and field dynamics, these expressions for the diffraction efficiencies could, in principle, be used to model our experimental results.

In modeling our results for semi-insulating GaAs, we must take into account propagation effects with the pump beams. We outlined a method for this that involved numerically solving the beam propagation equations, in order to divide the crystal into slices. For each slice, the procedure described above is followed, with the carrier and field equations of Chapter III numerically solved for each crystal slice. These results are used to form a sum involving the square of each slice thickness and the photorefractive of free-carrier index change, which is fit to the experimental results. In the case of undoped CdTe, where equal population densities of electrons and holes are always present, the modeling method is much more simple. The beam propagation is solved to determine the average carrier densities that are generated over the crystal length. These carrier densities are used in the carrier and field equations of Chapter III, in order to determine the dynamics of the free-carrier or photorefractive index change. This result is squared and then fit to our experimental results.

CHAPTER VII

UNDOPED CdTe - THE DEMBER SPACE-CHARGE FIELD

7.1. Introduction

With this chapter we begin our presentation of the experimental results. Here we consider the results obtained using our PPRTG measurement technique and the more simple of the two materials that we are studying, undoped CdTe. Since the undoped CdTe crystal used in our experiments exhibits no measurable linear absorption at the laser operating wavelength of 960nm, free carriers can only be produced in this material by instantaneous two-photon absorption. Since instantaneous two-photon absorption always produces equal populations of electrons and holes, our experimental results for undoped CdTe provide unambiguous evidence of a photorefractive nonlinearity that arises entirely as a result of the Dember space-charge field.

We begin by presenting data for the non-rotated polarization component of the diffracted beam and then follow this by presenting the data for the rotated component. After considering the non-rotated and rotated data sets, we conclude by comparing our CdTe experimental results with predictions made by our numerical model. Whereas our discussions of the non-rotated and rotated diffraction efficiencies focus mainly on data for

the 1.7μm grating period, our modeling discussion considers these and the results taken at a grating period of 3.8μm.

As we will see, the data for the non-rotated component of the diffraction efficiency exhibits sharply-peaked and decaying features that are consistent with diffraction from instantaneous bound electronic and free carrier gratings. The data for the rotated polarization component of the diffracted beam exhibits crystal-orientation and fluence dependencies consistent with diffraction from a photorefractive grating.

7.2 Non-Rotated Polarization Component: The Free-Carrier and Instantaneous Bound-Electronic Nonlinearities

In this section we consider the experimental results obtained by monitoring the non-rotated component of the diffracted beam in the way discussed in Chapter V. The experimental results shown in this section were taken with the space-charge field generated parallel to the $(\bar{1}10)$ crystallographic direction, where diffraction from the photorefractive grating produces a beam with a rotated polarization component. Thus, the diffraction efficiencies shown in this section *are not* due to the photorefractive grating.

7.2.1 Temporal Dynamics

The dynamics of the non-rotated component of the diffracted signal are shown in figure 7.1a-c for a range of fluences and a grating spacing equal to 1.7μm. In each of these figures, the diffraction efficiency is plotted against the delay of the probe beam. As can be seen most easily from the two lower fluence plots (figures 7.1b and c), the

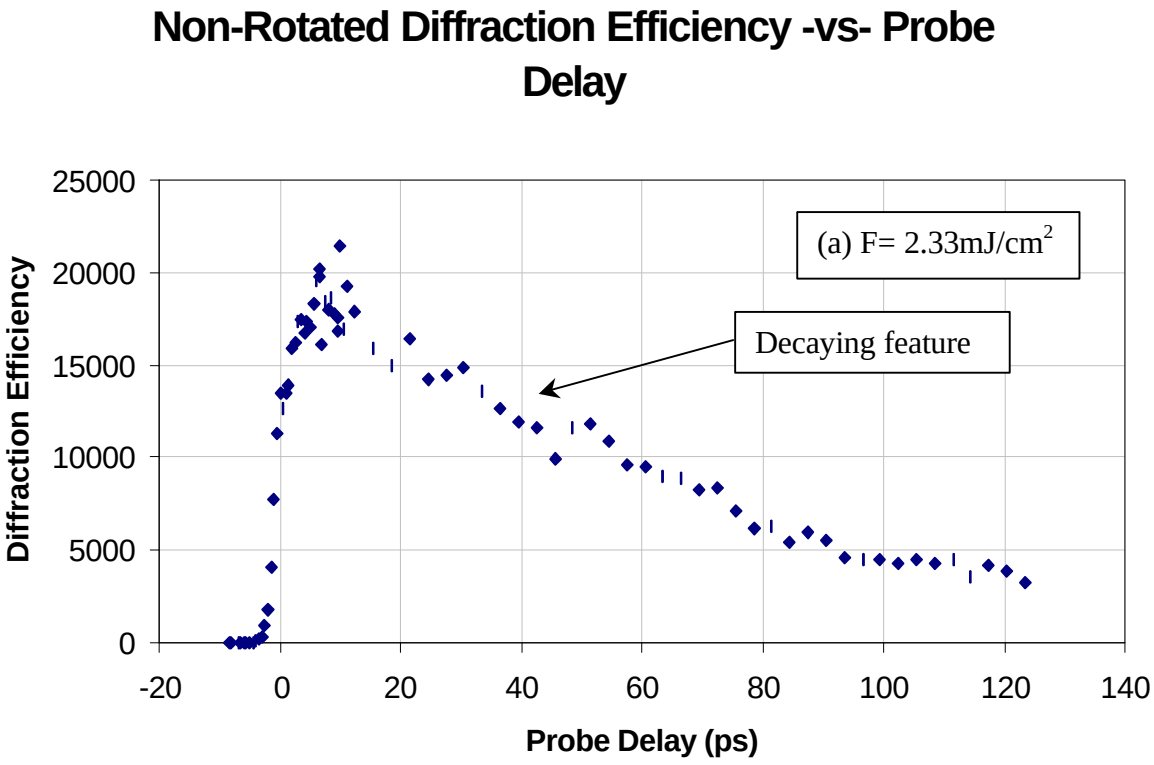
Non-Rotated Diffraction Efficiency -vs- Probe Delay
Diffraction Efficiency
25000
20000
15000
10000
5000
0
-20
0
20
40
60
80
100
120
140
Probe Delay (ps)
(a) F= 2.33mJ/cm2
Decaying feature

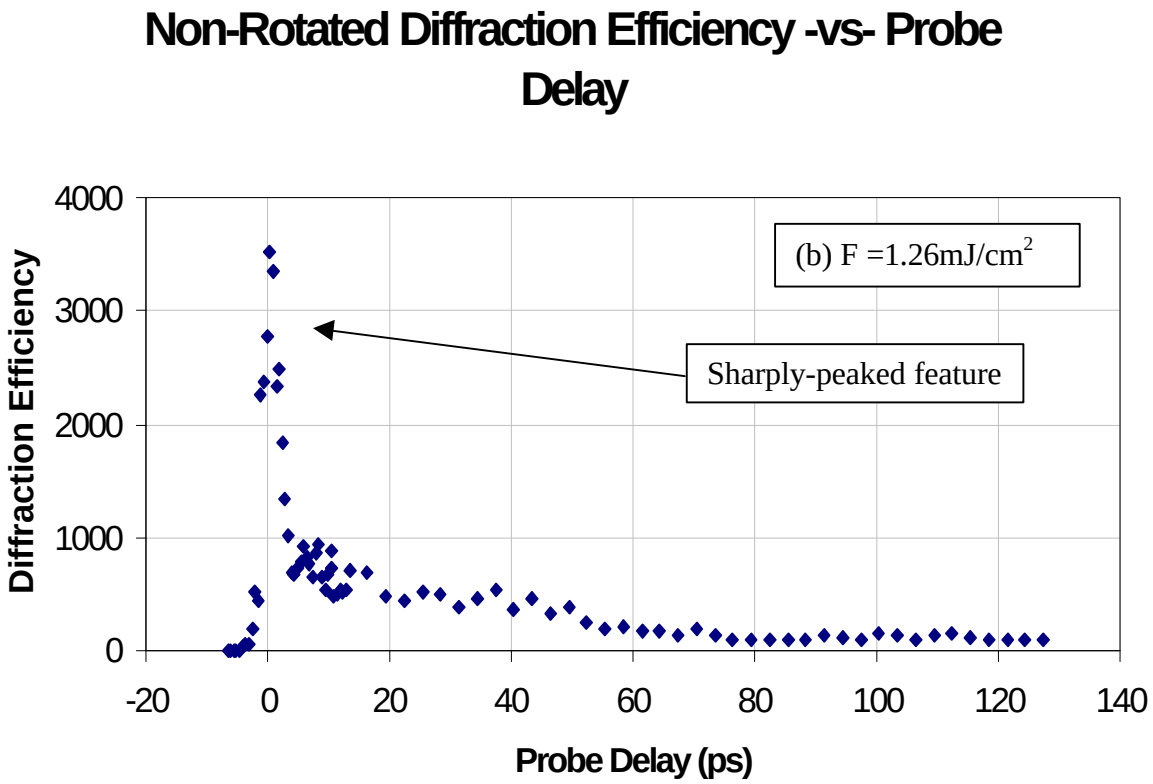
Non-Rotated Diffraction Efficiency -vs- Probe Delay
Diffraction Efficiency
4000
3000
2000
1000
0
-20
0
20
40
60
80
100
120
140
Probe Delay (ps)
(b) F =1.26mJ/cm2
Sharply-peaked feature

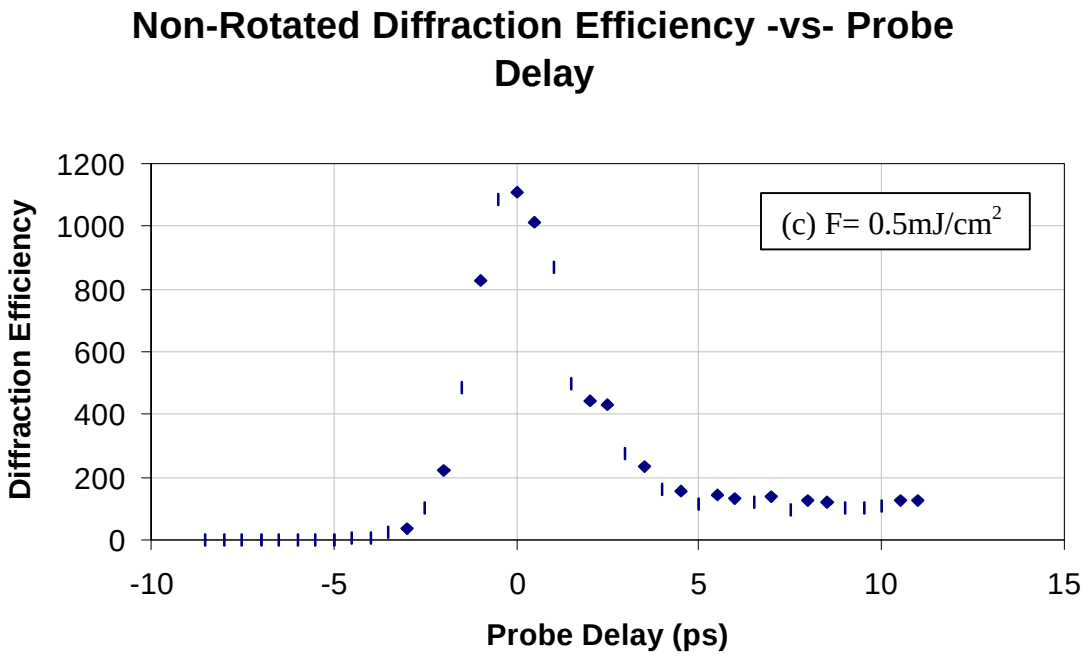

Figure 7.1a-c – Non-rotated diffraction efficiency versus probe delay for fluences of (a) 2.33mJ/cm^2, (b) 1.26mJ/cm^2 and (c) 0.50mJ/cm^2. In all cases, the fluences listed on the figure is the peak excitation fluence (i.e., the fluence at the peak of the are the modulated fluence profile).

diffracted signal possesses two components with distinctly different temporal dependencies.

The first of these features, a sharply-peaked signal which is centered at a probe delay of 0ps, is most evident in the lower fluence plots. A comparison of figure 7.1c with figure 5.8 reveals that this sharply-peaked diffraction efficiency roughly follows the shape of the probe pulse intensity profile. In light of the fact that the temporal shape of the diffraction efficiency is generally determined by the correlation function involving the probe pulse intensity profile and the square of the induced index change (which involves both the fundamental material response and the pump pulses), the similarity between these plots indicates that this feature arises from a grating whose onset and decay are both

instantaneous with respect to the duration of the probe pulses. Though not shown for the sake of brevity, this diffraction efficiency exhibited the fluence dependence expected for the instantaneous bound electronic nonlinearity. Thus, both the fluence and temporal dependencies of this feature suggest that it arises from a refractive index grating generated through the instantaneous bound-electronic nonlinearity. Since this feature tells us nothing of the free-carrier or space-charge field dynamics of the material, it is not of further interest in this discussion.

The second feature in figures 7.1a-c, the decaying diffraction efficiency, is of interest in this study. Since this decaying diffraction efficiency dominates the sharply-peaked signal at the highest fluences, the rise of this feature can only be studied with the data shown in figures 7.1a-c. As shown, the rise of the decaying diffraction efficiency closely follows the shape of the integral of the probe pulse intensity profile. This diffraction efficiency reaches half of its peak value at a delay of 0ps and its maximum at small positive probe delays. This response is consistent with diffraction from a grating that is created cumulatively in a time that is shorter than the duration of the probe pulses, and that decays in a time much longer than the duration of the probe pulses. This is the general behavior that is expected for a free carrier grating in undoped CdTe. The free-carrier populations are cumulatively generated over the 1ps duration of the pump pulses by instantaneous two-photon absorption. In the drift limit of carrier dynamics, the free carrier populations decay by ambipolar diffusion, and the decay constant of 70ps that is predicted using the literature value for the hole mobility ($90 cm^2/V\text{-}s$) and our 1.7μm grating spacing is approximately equal to the value of 65ps that we observe.

Though the decaying diffraction efficiency shown in figure 7.1a exhibits the decay constant expected for a drift-limited free carrier grating, it is necessary to more rigorously compare the dynamics of this feature that are observed at 1.7μm, 3.0μm, and 3.8μm grating periods with the expected behavior. We can do this by noting that in the drift limit, and when the modulated free carrier population is also destroyed by carrier recombination, the observed decay rate ($1/\tau$) of the free-carrier diffraction efficiency can be written (R.K. Jain and M.B. Klein, 1983):

$$\frac{1}{\tau} = \frac{2}{\tau_r} + \frac{8\pi^2 D_A}{\Lambda_g^2}. \qquad (7.1)$$

Here τ_r is the carrier lifetime, and D_A is the ambipolar diffusion coefficient (discussed in Chapter III). Thus, a plot of the observed decay rate as a function of the grating constant ($8\pi^2/\Lambda_g^2$) will yield a linear plot whose slope is the diffusion coefficient and whose y-intercept is twice the carrier recombination rate. We can therefore make a plot of this type, and then compare our measured values with those reported in the literature. The result of this procedure is shown in figure 7.2. In this plot, the solid line is the result of a least-squares fit of the data, and yields an ambipolar diffusion coefficient of 4.83cm^2/s and a carrier recombination time of 1ns. Both of these values are close to the reported values for these constants of 3.0 cm^2/s and 12.5ns ±9ns (M.S. Petrovic et al., 1989). While this further supports the identification of the decaying diffraction efficiency with a drift-limited free-carrier grating, it provides an independent measure of these constants for use in our model of the carrier and field dynamics.

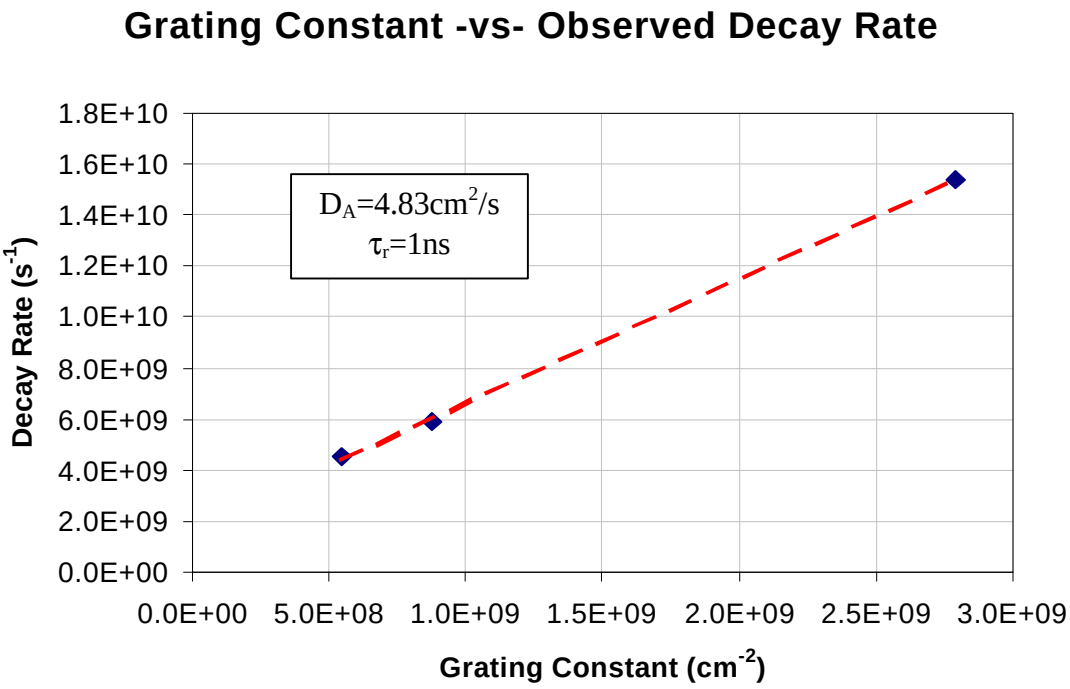

Figure 7.2 – Grating constant ($8\pi^2/\lambda^2_g$) versus observed decay rate. As discussed in the text, the slope of the resulting plot yields the ambipolar diffusion coefficient, while the y-intercept yields twice the carrier recombination time.

Two other characteristics of the dynamics of the decaying diffraction efficiency also support the association of this feature with diffraction from a free-carrier grating. First, separately for each of the three grating periods, the decay constant associated with the decaying feature was observed to be the same over the range of fluences where a measurable decaying feature was present. As we discussed in Chapter VI, this is the behavior that is expected for a drift-limited free-carrier grating in undoped CdTe. This follows from the dependence of the ambipolar decay time on the relative densities of electrons and holes, and the fact that instantaneous two-photon absorption always produces equal populations of electrons and holes. Also included in this is the fact that

the dominant carrier recombination process in our undoped CdTe crystal is electron-hole bimolecular recombination, so that neither species is preferentially depleted. Second, for all of the data sets where a measurable decaying feature was present, the decay was seen to be purely exponential. This is the behavior that is expected for materials like undoped CdTe, where photogeneration produces only electrons and holes, and no ionized midgap levels. As will be shown in Chapter VIII, this is not the case in semi-insulating GaAs. As we saw in Chapter II, photoexcitation produces population densities of electrons, holes, and ionized EL2, causing space-charge fields between the electrons and holes, and between the electrons and ionized El2. Since the EL2 are immobile, the EL2-associated space-charge field is long-lived, and in the drift-limit of carrier dynamics, results in a free-carrier grating that is constant on picosecond time scales. Thus, rather than decaying to zero, the free-carrier diffraction efficiency in semi-insulating GaAs decays to a constant value.

7.2.2 Fluence Dependence of the Free-carrier Diffraction Efficiency

Whereas we examined the temporal dynamics of the decaying diffraction efficiency in the previous sub-section, in this sub-section we examine the fluence dependence of this feature. Since the fluence-to-the-fourth-power dependence that is measured for this feature is that which is expected for a free-carrier grating that is generated by two-photon absorption, this data serves to further strengthen the association between the decaying feature in our data, and diffraction from a free-carrier grating.

It is beneficial to begin this discussion by considering the expected diffraction efficiency-versus-fluence behavior that a two-photon absorption generated free-carrier grating is expected to exhibit. In Chapter VI, the small-signal transient-grating diffraction efficiency was shown to be proportional to the square of both the index change and interaction length. In addition, in Chapter II, the free-carrier index change was shown to be proportional to the carrier density. Therefore, in undoped CdTe, where carriers are generated by two-photon absorption according to the square of the beam intensity, the free-carrier diffraction efficiency is expected to be proportional to the product of the fourth power of the fluence, and the square of the interaction length.

The fluence dependence of the decaying diffraction efficiency is shown in figure 7.3. The data shown in this figure are taken at a fixed probe delay of 5ps, where the sharply-peaked signal does not contribute to the measured diffraction efficiency. As shown, the diffraction efficiency follows the F^4 fluence dependence closely over the lower and middle portion of the range of fluences for which diffraction is observed. However, as the fluence is increased past 1.0mJ/cm^2, the diffraction efficiency deviates from this dependence, increasing at a lower rate than predicted by the F^4 dependence.

The high-fluence deviation can be understood by recalling that, in addition to producing free carriers, two-photon absorption depletes the optical beams and introduces an optical absorption depth that is inversely proportional to the beam intensity ($\ell = 1/\beta I$). In transient-grating experiments, the intensity-dependent absorption depth introduces an intensity-dependent effective interaction length. At low fluences, where the effective

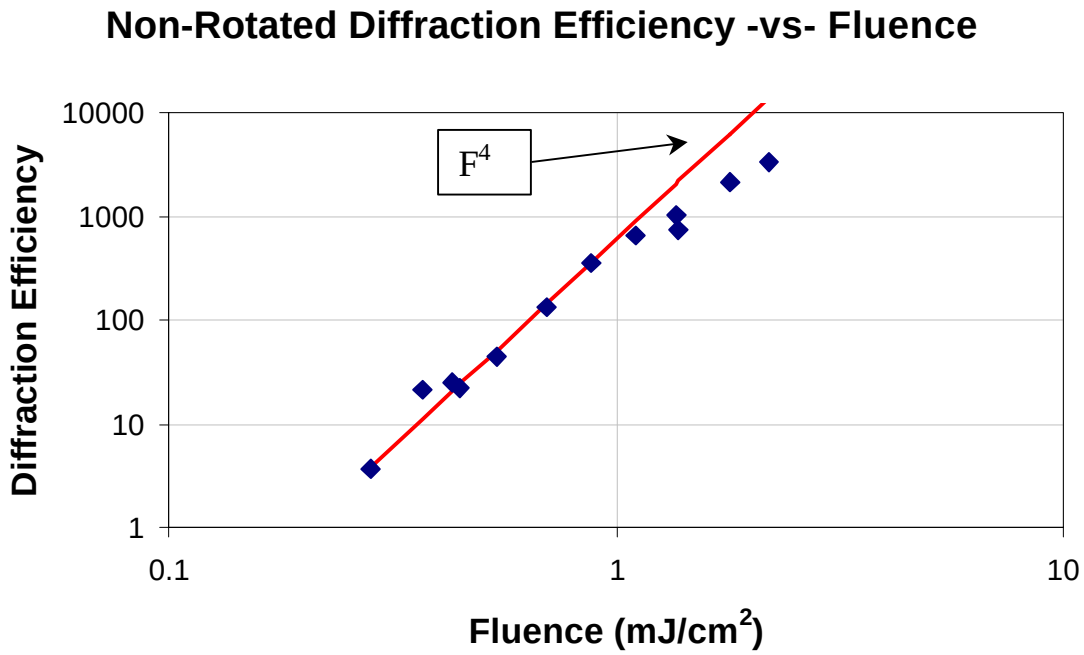

Figure 7.3 – Non-rotated diffraction efficiency versus fluence for a fixed probe delay of 5ps. Shown in the figure, the data follow the F^4 dependence expected for a free-carrier grating.

interaction length longer than the crystal length, the diffraction efficiency reflects the square of the index change. However at high fluences, where the effective interaction length is shorter than the crystal length, the diffraction efficiency reflects the fluence dependence of both the index change and the interaction length. While the index change increases with increasing fluence, the interaction length decreases with increasing fluence, and the result is that the diffraction efficiency increases more slowly than the square of the index change. Thus, the decaying diffraction efficiency follows the fluence dependence expected for a free-carrier grating generated by two-photon absorption in the presence of beam depletion.

7.3 Rotated Polarization Component: The Dember Photorefractive Nonlinearity

In this section we present the experimental results pertaining to the rotated polarization component of the diffracted beam. The experimental results shown in this section were obtained using our PPRTG measurement technique, an s-polarized probe beam, and a crystal orientation where the space-charge field was parallel to the $(1\bar{1}0)$ crystal axis. As is shown in Appendix A, for this crystal orientation the photorefractive grating is expected to produce a diffracted beam with a rotated polarization component.

7.3.1 Crystal Orientation-Dependence of the Rotated Polarization Component

In this section, we discuss the crystal orientation-dependence of the rotated polarization component of the diffracted signal. From the discussions of Chapter II and V, and Appendix A, it is generally expected that only the photorefractive grating will produce a diffracted signal with a rotated polarization component, and that the associated diffraction efficiency will exhibit a strong crystal orientation-dependence.

In figure 7.4, the diffraction efficiency associated with the rotated polarization component is plotted versus probe delay for an s-polarized probe beam, and two orientations of our 1.0mm CdTe crystal: $E_{sc}\|(1\bar{1}0)$ and $E_{sc}\|(11\bar{2})$. For clarity, we summarize the polarization rotation properties of our CdTe crystal, which are discussed in Appendix B. When the probe electric field is s-polarized and the crystal is oriented so that the space-charge field is generated along the $(1\bar{1}0)$direction, the photorefractive grating produces a diffracted beam whose polarization is rotated by exactly 90°. In contrast,

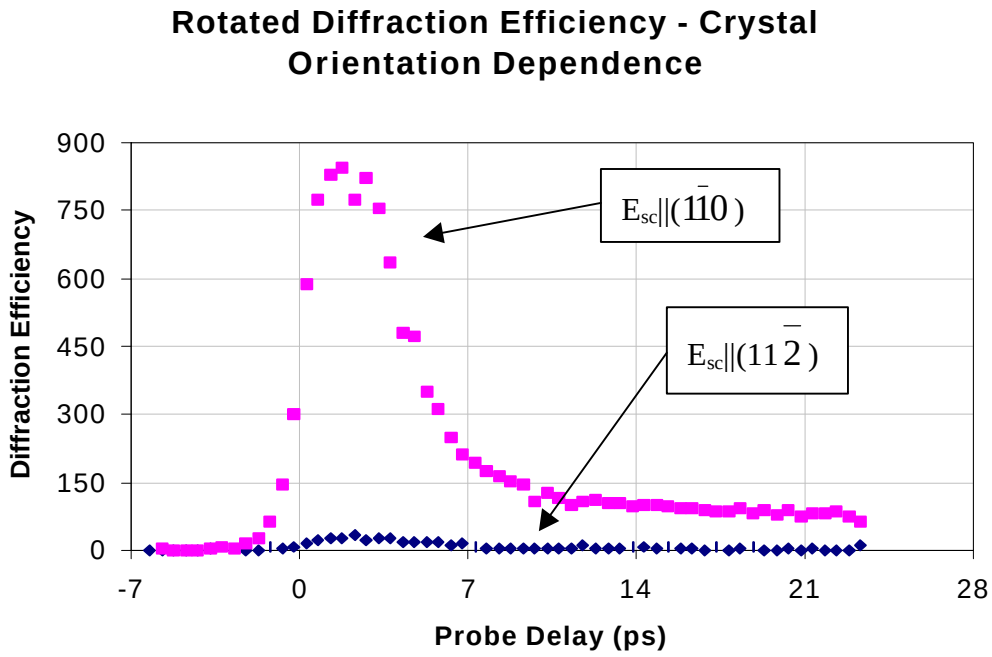

Figure 7.4 – Crystal orientation dependence of the rotated diffraction efficiency. As discussed in the text, the data shows the crystal orientation dependence expected for the photorefractive nonlinearity.

when the probe beam is s-polarized and the crystal is oriented so that the space-charge field is parallel to the $(11\bar{2})$ direction, the photorefractive grating produces a diffracted beam whose polarization is not rotated. As discussed in Chapters II and V, neither the free-carrier or instantaneous bound-electronic gratings are capable of producing a polarization rotation for our experimental conditions.

The diffraction efficiency data shown in figure 7.4 clearly follows the dependence expected for the photorefractive grating. While the diffraction efficiency exhibits a clear rise, peak and decay when the space-charge field is parallel to the $(1\bar{1}0)$ crystal direction, the diffraction efficiency decreases dramatically when the space-charge field is oriented along the $(11\bar{2})$ direction. Thus, the diffraction efficiency data shown in this section can

be attributed entirely to the photorefractive nonlinearity.

7.3.2 Temporal Dynamics

The dynamics of the photorefractive diffraction efficiency are shown in figure 7.5 for incident fluences of (a) 2.33mJ/cm^2, (b) 1.12mJ/cm^2 and (c) 0.47mJ/cm^2 and a grating period of 1.7μm. Visible in each of the data sets shown in figures 7.5a-c are a transient feature which peaks at small probe delays, and a decaying feature similar to that seen in the data for the non-rotated diffraction efficiency.

Transient Photorefractive Diffraction Efficiency

The first of the features that is visible in figures 7.5a-c, the transient feature, is clearly not related to the instantaneous bound electronic diffraction efficiency of the previous section for the following reasons. Firstly, this feature exhibits a cumulative rise, peaking at small positive probe delays, followed by a decay that is fastest at high fluences, and slowest at low fluences. This is in contrast to the instantaneous bound-electronic diffraction efficiencies shown in the previous section, which peak at a probe delay of 0ps and follow the shape of the probe pulse at all fluences. In addition, as is evident from figure 7.4, this diffraction efficiency exhibits the crystal orientation dependence expected for the photorefractive nonlinearity. In contrast, as we discussed in Chapter V, the instantaneous bound-electronic nonlinearity allows no such polarization rotation for the experimental conditions. Finally, this diffraction efficiency exhibits a fluence dependence that is characteristic of the photorefractive nonlinearity. Although not shown, this dependence is easily distinguished from the F^2 dependence of the instantaneous bound-

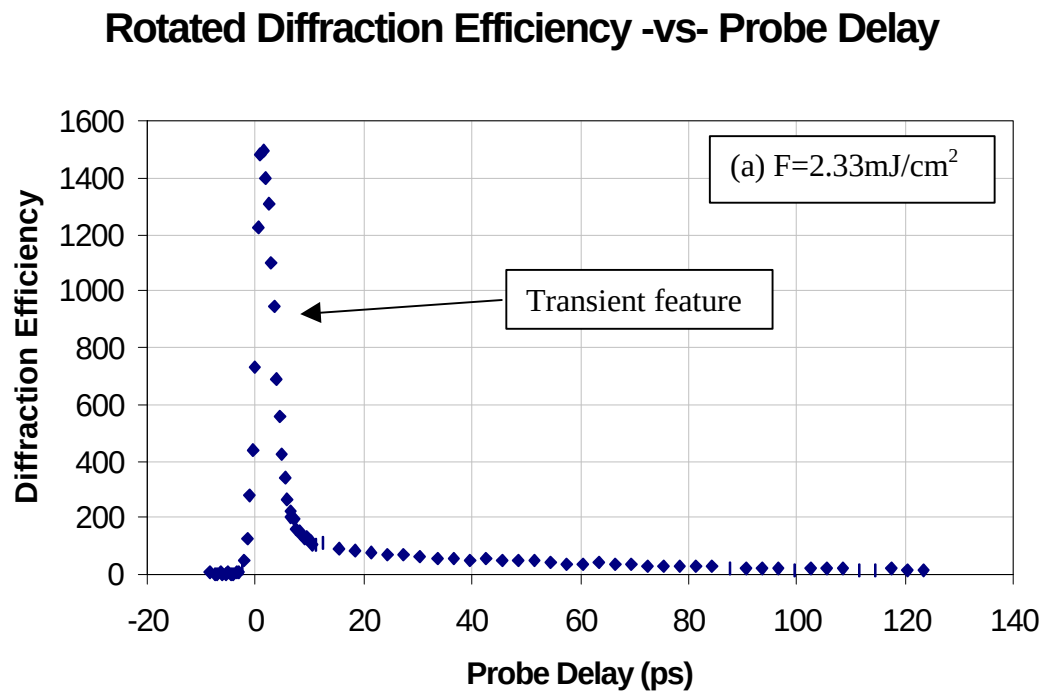
Rotated Diffraction Efficiency -vs- Probe Delay
(a) F=2.33mJ/cm2
Transient feature
Diffraction Efficiency
Probe Delay (ps)
1600
1400
1200
1000
800
600
400
200
0
-20
0
20
40
60
80
100
120
140

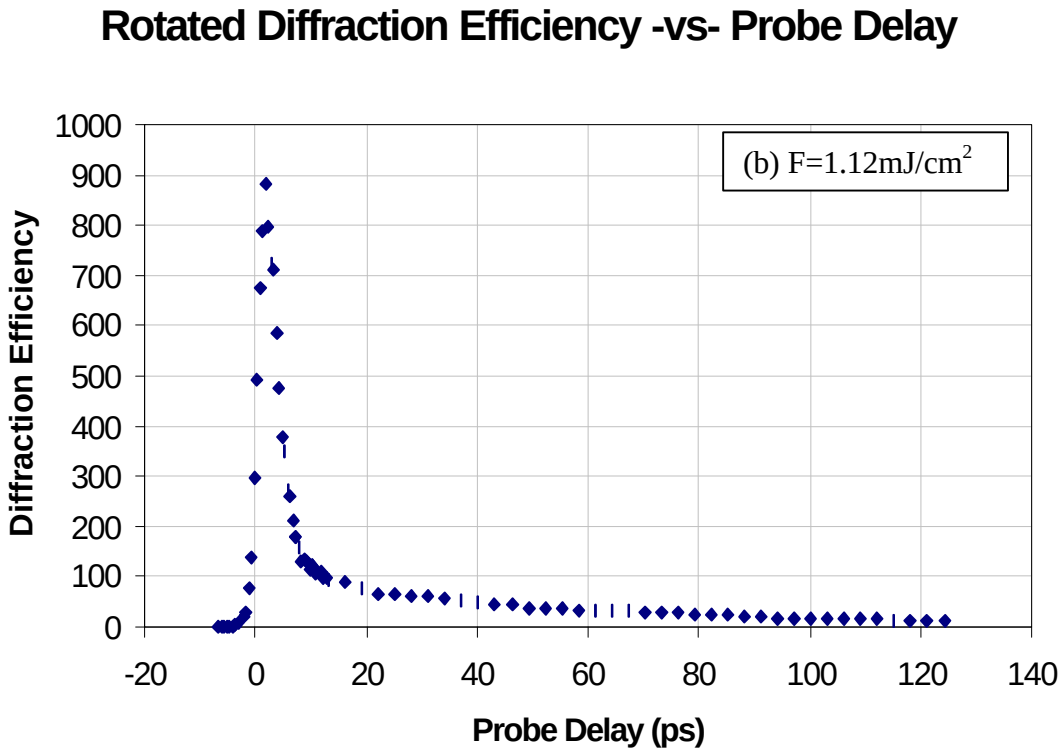
Rotated Diffraction Efficiency -vs- Probe Delay
(b) F=1.12mJ/cm2
Diffraction Efficiency
Probe Delay (ps)
1000
900
800
700
600
500
400
300
200
100
0
-20
0
20
40
60
80
100
120
140

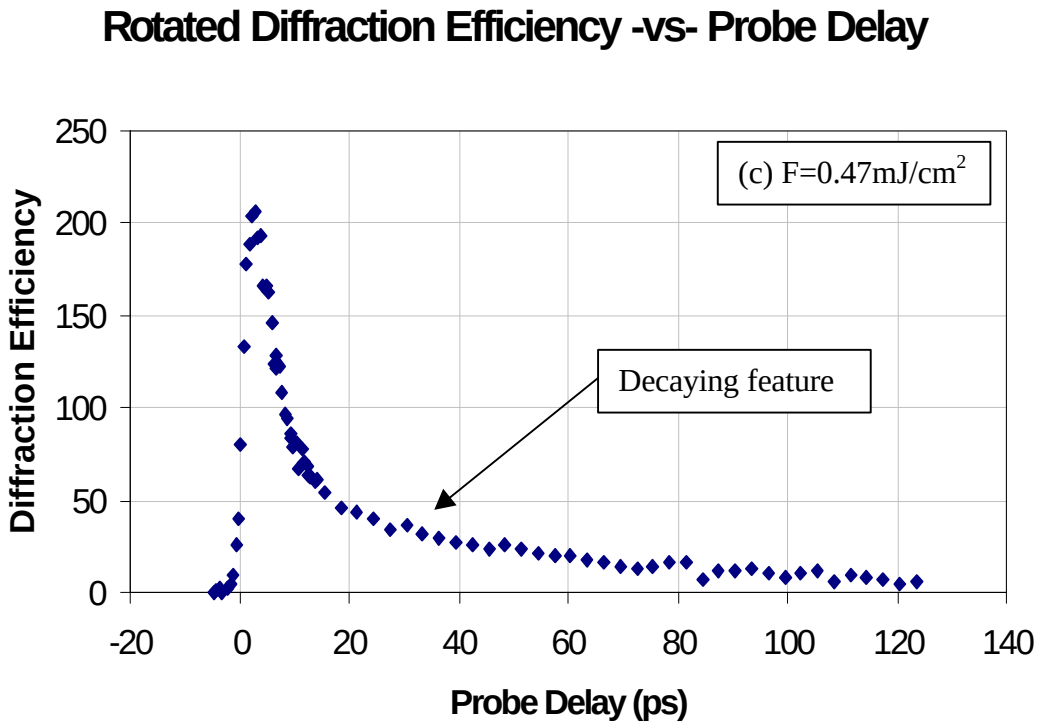

Figure 7.5a-c – Rotated diffraction efficiency versus probe delay for fluences of (a) 2.33mJ/cm^2, (b) 1.12mJ/cm^2, and (c) 0.47mJ/cm^2. In all cases, the fluences listed on the figure is the peak excitation fluence (i.e., the fluence at the peak of the are the modulated fluence profile).

electronic diffraction efficiency.

Comparison of the data of figure 7.5 with results obtained for the same experimental conditions in InP:Fe yields evidence as to the origin of the transient photorefractive diffraction efficiency. Such a comparison is made in figure 7.6, which is a plot of the photorefractive responses of both CdTe and InP:Fe at approximately equal excitation fluences. At 960nm, the photorefractive response of both materials is due to the Dember Space-charge field. In undoped CdTe, where there are no optically-active midgap levels, this is due to the fact that the intense 960nmpulses used in these experiments can generate electron-hole pairs by instantaneous two-photon absorption.

Because the photon energy of the 960nm radiation is ~1.3eV, and the bandgap energy of this material is 1.49eV, these carriers are produced with an excess energy of roughly 1eV.

The situation is completely different in InP:Fe. In this material, iron doping produces optically-active Fe^{2+}/Fe^{3+} centers which can absorb near infrared radiation and produce free carriers (P.B. Klein et al., 1984). In our InP:Fe crystal, the linear absorption coefficient due to these species is approximately $1.0cm^{-1}$ at the probe wavelength of 1.06μm (G.C. Valley et al., 1989). However, at 960nm, this material exhibits an additional linear absorption ($a \cong 10cm^{-1}$ at 960nm) because the laser photon energy is sufficient to couple the tails of the valence and conduction bands (the InP band-gap energy is 1.34eV (Landolt-Börnstein, vol.17, 1982)). This results in a strong single-photon band-to-band generation of electron-hole pairs which, under the experimental conditions, dominates the photoexcitation of free carriers due to both linear absorption at the Fe^{2+}/Fe^{3+} mid-gap sites and instantaneous two-photon absorption. Since these carriers are generated through the coupling of the valence and conduction band tails, they have no excess energy. As shown in figure 7.6, the transient feature is not present in the InP:Fe results. Thus, we postulate that this feature arises from hot carrier effects.

Though a detailed description of hot carrier transport and space-charge field formation is beyond the scope of this thesis, a simple analysis of the drift-limited carrier dynamics can be used to show that the transient photorefractive diffraction efficiency is consistent with diffraction from a photorefractive grating produced by hot electrons (W. A. Schroeder et al., 1991). In Chapter III, we showed that the drift-limited Dember field magnitude is linearly proportional to the temperature:

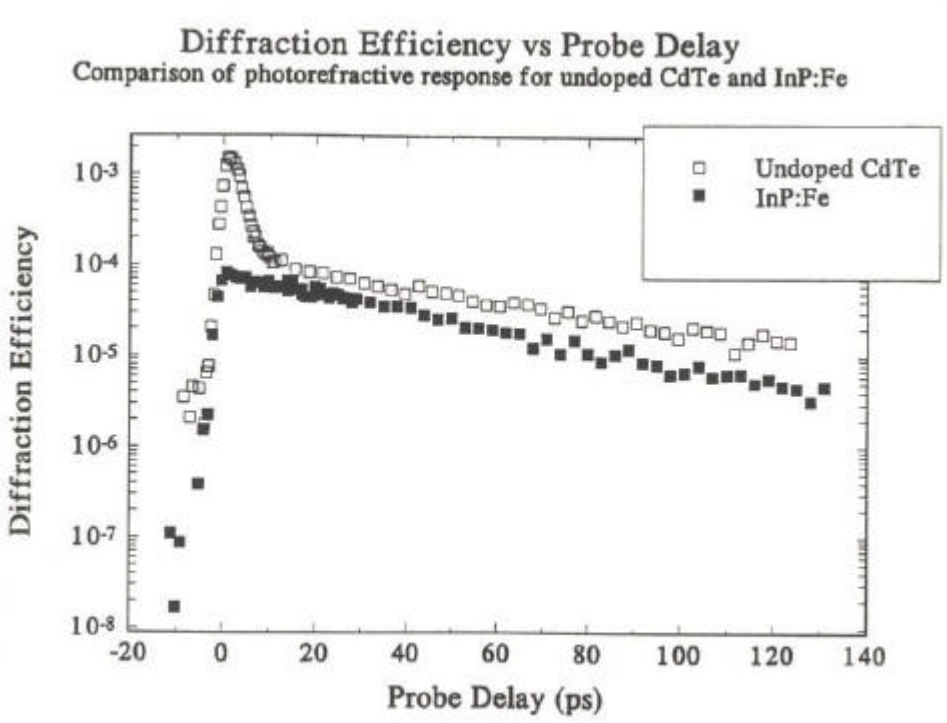

Figure 7.6 – Plot of diffraction efficiency versus probe delay contrasting the grating dynamics observed in undoped CdTe (open squares) and InP:Fe (filled squares) for similar excitation fluences (2.33mJ/cm2 and 2.25mJ/cm2). As discussed in the text, this gives information as to the origin of the transient diffraction efficiency that we observe in our undoped CdTe results.

$$E_{Dnp} = \frac{2\pi k_B T}{\Lambda_g e}\left[\frac{m_e - m_p}{m_e + m_p}\right], \qquad (3.33)$$

When the carriers can be assumed to thermalize faster than they cool (this is an excellent assumption at the highest carrier densities generated in our experiments), they can be represented by Maxwell-Boltzmann distributions with an elevated temperature. Since the electron effective mass is roughly 4 times the hole effective mass, the electrons and holes are photoexcited with, respectively, roughly 0.8eV and 0.2eV of the 1eV excess energy. Considering the electrons only, this corresponds to an equivalent initial carrier temperature

of ~6000K, which is roughly 20 times larger than the lattice temperature (300K). Thus, we would expect for hot carrier effects to produce a significant enhancement to the space-charge field magnitude.

We can also consider the effect of hot carrier transport on space-charge field formation in terms of the interplay between the electron and hole current densities that was discussed in Chapter III. There we showed that the electron-hole space-charge field is generated as a result of the discrepancy between the electron and hole mobilities, and the field reaches its peak value when it becomes large enough to cause the electron and hole current densities to balance. As we noted in Chapter VI, in zincblende semiconductors, where polar optical phonon scattering is the dominant carrier scattering mechanism, an increased carrier temperature results in an increased carrier mobility. Since the electrons receive the majority of the excess energy, their mobility is enhanced more than the hole mobility. While the increased electron mobility causes the field to form more quickly (the dielectric relaxation time is inversely proportional to the carrier mobility), it and the increased electron temperature together produce a larger electron diffusion current density. Thus, a larger electron diffusion current density means that the balance described above is reached at a larger space-charge field magnitude.

Once the field reaches its maximum value, it decays by two processes that occur simultaneously. First, as we described in Chapter III, the electron-hole pairs decay by ambipolar diffusion to destroy the modulated space-charge field. For the grating periods used in our experiments, this occurs more slowly than the second process, the cooling of the carriers. As the carriers cool, the space-charge field decays from its enhanced value to

the lattice temperature value, so that the balance described above is dynamically maintained. At high carrier densities, where the dielectric relaxation time is much shorter than the carrier cooling time, the carriers can respond instantaneously to the cooling of the carriers, and the decay of the hot carrier space-charge field is the cooling time of the carriers (we estimate this to be 5ps in section 2.3). However, at lower carrier densities, where the opposite situation holds, the decay of the hot carrier space-charge field is the dielectric relaxation time of the carriers, which is as long as 20ps for our lowest carrier densities. This is the trend that we observe in our experimental results: we see the decay of the transient photorefractive diffraction efficiency decrease as the excitation fluence is decreased. While we can not resolve this decay at higher fluences, at lower fluences this decay is comparable to the expected dielectric relaxation time. Thus the rise, magnitude and decay of the transient photorefractive diffraction efficiency of figures 7.5 shows the qualitative features expected for a hot carrier photorefractive grating.

In light of the above discussion, it might seem surprising that we do not see evidence of hot carrier transport in the non-rotated polarization data presented in section 7.2. Based of the above discussions, we would expect these effects to be manifest as a fast decay of the free-carrier grating for times less than ~5ps. However, by using the discussions of section 3.3.3, we can show that the overall effect of hot carrier transport on the free carrier decay is minimal. From section 3.3.3, we recall that the Debye length can be thought of as the distance that free electrons travel before the field magnitude reaches its maximum value. Assuming that this occurs before the carriers cool, we can use the electron temperature given above, along with the dependence of the Debye length on

carrier temperature ($T^{1/2}$) to estimate the increase in this quantity. Using a carrier density of $1x10^{17}cm^{-3}$, along with the electron temperature given above of 6000K, we find that the Debye length increases to $\sim 5.5x10^{-8}m$. Since this is still only about 3% of our smallest grating period, we conclude that the effect of hot carrier transport on the decay of the modulated free-carrier population is minimal, so that its effect on the free-carrier grating decay is unobservable.

The above discussion leads to an important contrast that must be made between the free-carrier and photorefractive nonlinearities. While we have seen that hot carrier transport causes a negligible increase in the decay of the free carrier population so that the overall effect on the free-carrier grating is minimal, our experimental results clearly show that hot carrier transport has a non-negligible effect on the magnitude of the photorefractive effect that is observed. This is because, while the free-carrier grating is dependent on the modulated carrier density, the photorefractive grating is dependent on the modulated space-charge field. According to Gauss' law, the modulated space-charge field is proportional to the modulated charge separation, summed over the grating period. Thus, instead of being sensitive to the modulated carrier density, the photorefractive grating is sensitive to *differences* in the modulated carrier populations through the space-charge field. Therefore, though an effect such as hot carrier transport might produce a small overall change in the modulated free electron density, when the resulting charge separation that is summed over the grating period, the overall effect can be substantial.

Decaying Photorefractive Diffraction Efficiency

In addition to the transient photorefractive diffraction efficiency discussed above, the data in figure 7.5 also reflect a decaying photorefractive diffraction efficiency. When closely examined, the dynamics of this decaying photorefractive diffraction efficiency are similar to those of the free-carrier grating decay discussed in the previous section. Most importantly, the 55ps decay constant is in the range of values expected for ambipolar diffusion of electron-hole pairs across the 1.7μm grating period. In addition, like the decay of the free-carrier grating, the decay of this photorefractive diffraction efficiency is both fluence-independent and exponential. According to the discussions of Chapter III, this is the behavior that is expected for a Dember photorefractive nonlinearity that is due to equal populations of electrons and holes.

The slight difference between the decay of the free-carrier and photorefractive diffraction efficiencies is expected. Indeed, for larger grating periods we see larger discrepancies between the decay of the free-carrier and Dember photorefractive diffraction efficiencies. This will be discussed in section 7.4, where we discuss our modeling of the experimental results.

7.3.3 Fluence Dependence of the Photorefractive Diffraction Efficiency

Having discussed the temporal dynamics of the diffraction efficiency associated with the rotated polarization component, we now consider its fluence dependence. Here it is important to note that it is the fluence dependence of the transient photorefractive diffraction efficiency that we measure. As we will see, this diffraction efficiency exhibits

the fluence dependence that is expected for a drift-limited Dember photorefractive nonlinearity generated by two-photon absorption.

In analyzing our diffraction efficiency versus fluence results, we must be able to compare our data with results that are expected for the photorefractive nonlinearity. As we have already seen, the diffraction efficiency is proportional to the square of the induced index change and the interaction length. Therefore, in order to make this comparison, we must relate the incident fluence to the magnitude of the photorefractive index change. This can be done using the relationship between the carrier density and space-charge field magnitude that was discussed in Chapter III. Here we note that the induced index change is linearly proportional to the space-charge field magnitude, and that the photogenerated carrier density increases according to the square of the incident fluence.

Recalling the discussion of Chapter III, the space-charge field magnitude is linearly proportional to the carrier density at low carrier densities (the diffusion limit), but increases sub-linearly as the carrier density is increased, and is independent of carrier density at high carrier densities (the drift limit). As we discussed in Chapter VI, our lowest photogenerated carrier densities are comparable to the critical carrier density where diffusion and drift are equally important in field formation. Thus, in the absence of effects which decrease the effective interaction length for the nonlinear diffraction process, we expect to the diffraction efficiency to increase at a rate less than F^4 at our lowest fluences, but be independent of fluence at our highest fluences.

The fluence dependence of the rotated diffraction efficiency is shown in figure 7.7. For reference, a line with F^4 dependence is shown with the data. In addition, in order to

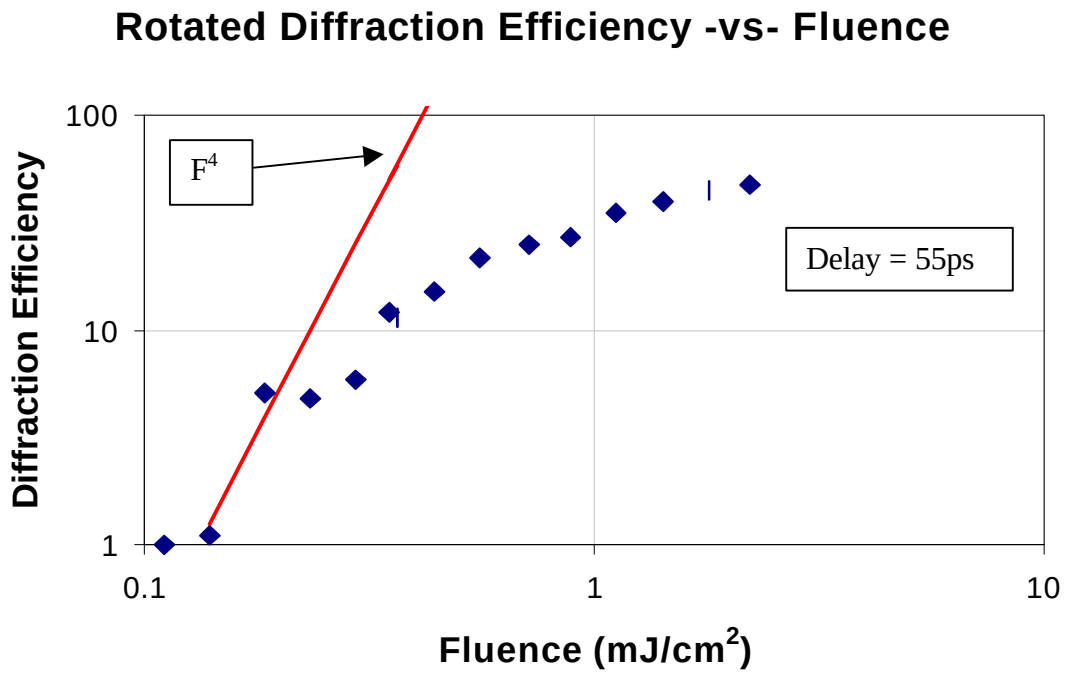

Figure 7.7 – Rotated diffraction efficiency versus fluence for a fixed probe delay of 55ps. As discussed in the text, the data are consistent with diffraction from a drift-limited photorefractive grating.

neglect hot carrier effects, the diffraction efficiency is measured at a fixed probe delay of 55ps. The data exhibit the behavior that is expected for a Dember photorefractive nonlinearity between the diffusion and drift limits. While the rate of increase of the diffraction is less than F^4 at the lowest fluences, it is sub-linear through the middle and upper fluences, increasing by a factor of less than 2 as the fluence is increased by a factor of roughly 3. Looking again at figure 3.3, this behavior is expected for a drift-limited photorefractive grating. This result is consistent with the results of the previous sections, where we observed drift-limited free-carrier and photorefractive grating dynamics.

7.4 Modeling

In this section we discuss the modeling of our CdTe experimental results. As we discussed in Chapter VI, we model these results using the relationship between the small-signal transient grating diffraction efficiency and the induced index change, and the relationship between the free-carrier and photorefractive index changes and the n=1 modulated carrier densities and space-charge field. The parameters that we use in modeling our CdTe results are summarized in table 7.1.

Parameter	Value	Reference
ε_r	10.4	K. Zanio, 1978
n_b	2.82	Landolt-Börnstein, 1982
μ_e	1050cm^2/V-s	M. S. Petrovic et al., 1991
μ_h	93cm^2/V-s	This work
β	17cm/GW	M. D. Dvorak et al., 1994
τ_r	1ns	This work

Table 7.1 – Parameters used in modeling our undoped CdTe experimental results.

Figures 7.8a and b show the experimental results for the decay of the free-carrier grating at grating periods of 1.7μm and 3.8μm, along with the predictions of our model (solid line). In generating the model predictions, we have used the procedure described in Chapter VI with the values given in table 7.1. While it is the results from our model in the high modulation limit that are shown in these figures, in both limits the model describes the same result: exponential decay of the free carrier populations via ambipolar diffusion, with the time constant given by the ambipolar diffusion time for the grating period. As can be seen from the plots, in all cases the results of our model fit the data very well,

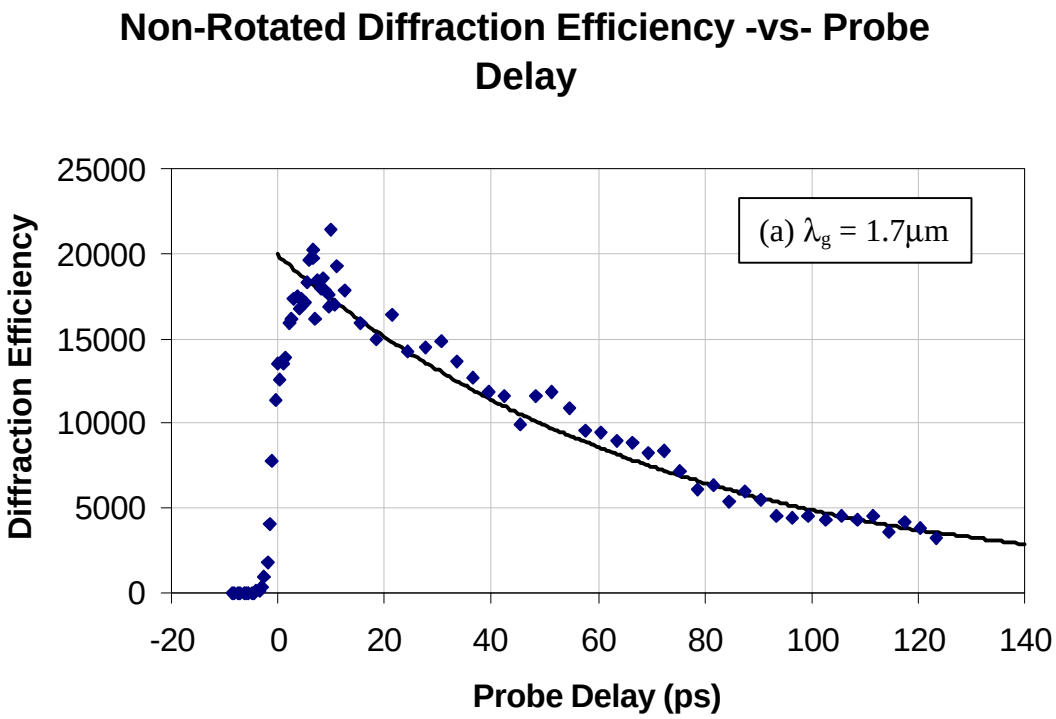

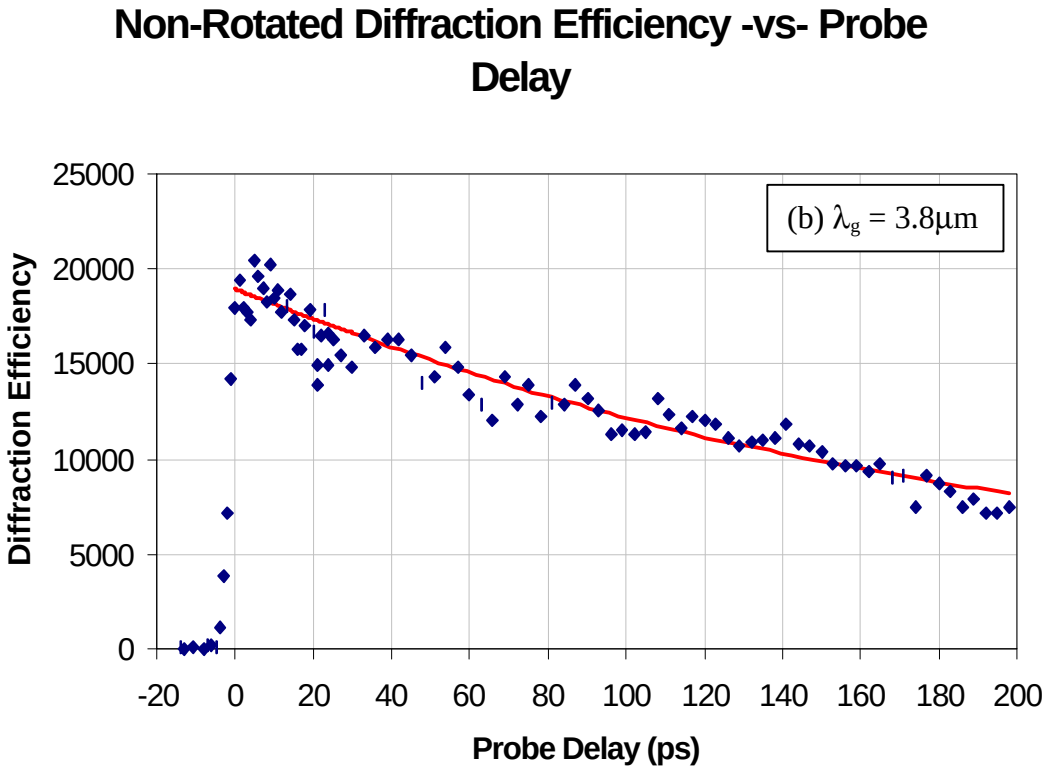

Figure 7.8a and b – Non-rotated diffraction efficiency versus probe delay plots comparing the predictions of our model with experimental results at grating periods of (a) 1.7μm and (b) 3.8μm.

indicating that our model accurately accounts for the dynamics of the n=1 modulated free carrier population.

The dynamics of the photorefractive diffraction efficiency are shown in figure 7.9a and b for grating periods of 1.7μm and 3.8μm, along with fits from our model in both the high (black lines) and low (gray lines) modulation limits. Here we have followed the same procedure as outlined above, except that it is the square of the modulated space-charge field that we have fit to the experimental results. Immediately obvious from all three figures is the disagreement between our model and the experimental results for short probe delays. Since we have shown that the transient feature in our data arises from hot carrier effects, and our model considers only free carriers at the lattice temperature, this disagreement is not surprising. Moreover, because we expect this disagreement, and in order to better facilitate a comparison between the model and experimental results at longer probe delays, we have plotted the data so that the peak of the transient photorefractive diffraction efficiency is not visible.

In comparing the output of our model with the photorefractive experimental results at probe delays greater than ~10ps, it is clear that the fit between the data and the low modulation prediction is not good at both grating periods. In contrast, the agreement between the data and our model in the high modulation limit is excellent at the 1.7μm grating period, and good at the 3.8μm grating period. As we noted in Chapter III, in the low modulation limit, the electron-hole space-charge field decays with the modulated free carrier densities, by ambipolar diffusion and with a decay constant given by the ambipolar

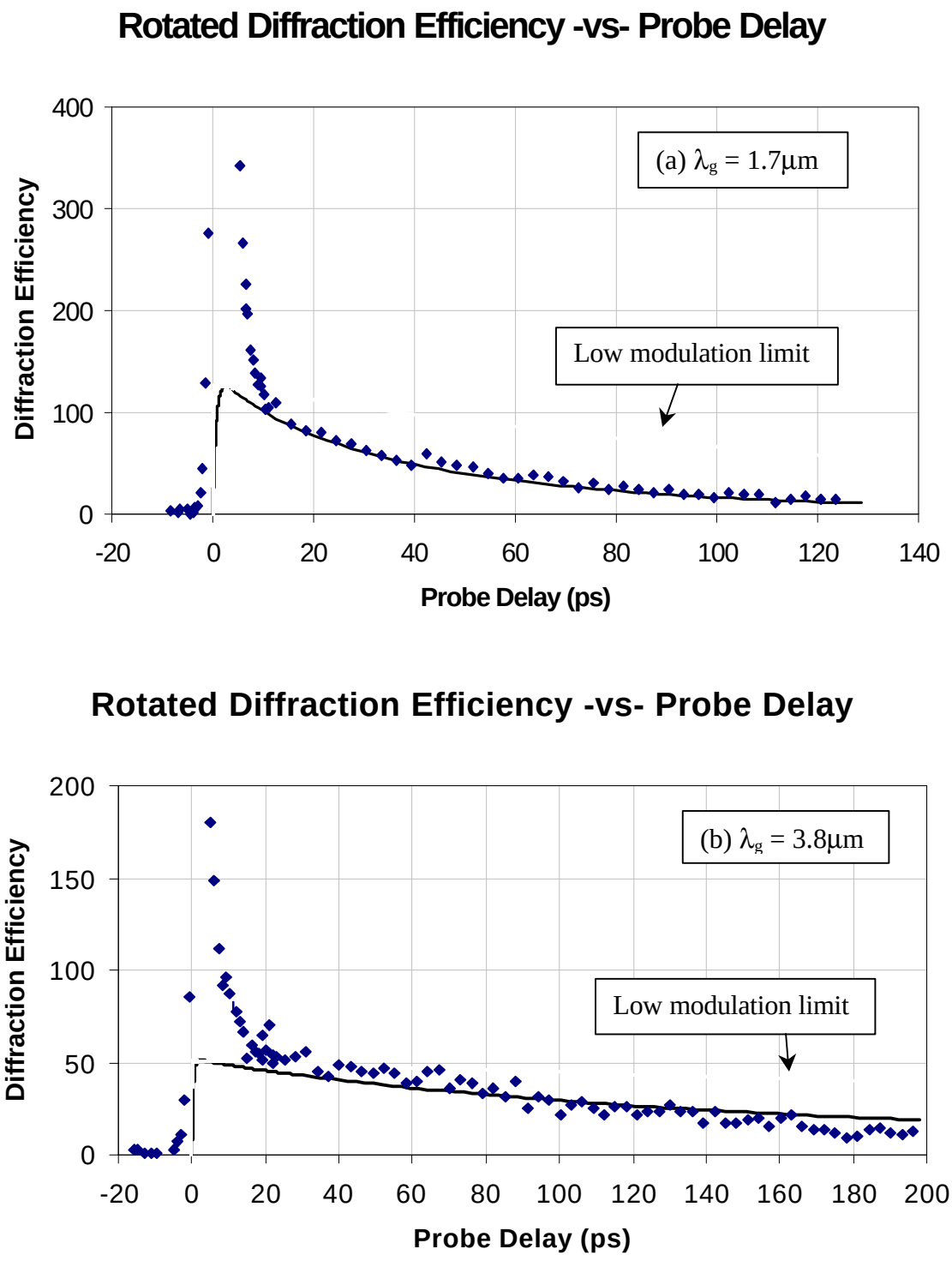

Figure 7.9a and b – Rotated diffraction efficiency versus probe delay plots comparing the predictions of our model with experimental results at grating periods of (a) 1.7μm and (b) 3.8μm. Gray lines are predictions in the low modulation limit, while black lines are predictions in the high modulation limit.

diffusion time for the grating period. However, inspection of the data in figures 7.9a and b reveals that the photorefractive diffraction efficiencies decay more quickly than the rate dictated by ambipolar diffusion. Indeed, in the case of the 3.8μm grating period results, where the predicted ambipolar decay is roughly 380ps, we observe a decay constant of 110ps. Due to the large discrepancy between the observed and predicted constants, and the fact that the agreement between the observed and predicted free carrier results is excellent, this discrepancy can not be counted as experimental error.

To understand the discrepancy between the data and the low modulation predictions, we must review the discussion given in Chapter III that details drift-limited field formation in the high modulation limit. Recalling the discussion of section 3.3.4, the high modulation effects that we observe arise from the fact that under these circumstances there is a wide discrepancy in the field formation time (the dielectric relaxation time) between the minima and maxima of the modulated intensity profile. Consequently, as the field is formed, higher-order spatial harmonics of the carrier densities and space-charge field are generated that are coupled to the n=1 component of the space-charge field (through the n=1 components of the carrier densities, as illustrated in equations (3.34)-(3.48)). Once the field reaches its maximum value, the higher order components of the carrier densities are destroyed by ambipolar diffusion according to the ambipolar diffusion rates for the higher order harmonics of the grating period. As we saw in Chapter III, this produces an initial decay of the space-charge field that is faster than the rate dictated by ambipolar diffusion for the fundamental grating period. This decay persists until the higher order components of the carrier densities are destroyed, and thereafter the n=1

modulated carrier densities decay according to the ambipolar diffusion rate for the fundamental grating period. Since the ambipolar diffusion time is proportional to the square of the grating period, as the grating period is increased, a longer time is required for the higher order components of the carrier densities to decay.

From the above discussion, two points about our predicted and observed results are immediately obvious. First, since the decay of the photorefractive diffraction efficiency is fundamentally a process involving many spatial harmonics of the carrier densities and field, it is not surprising that the low modulation predictions, which consider only the fundamental component of the carrier densities and field, do not accurately predict the decay. Second, it is clear that these high modulation effects are more clearly illustrated in our experimental results for the longer grating periods because at longer grating periods, the time required for the decay of the higher order carrier density harmonics is a larger fraction of the maximum probe delay. For example, at the 1.7μm grating period, where our maximum probe delay is roughly 150ps, the ambipolar diffusion time for the n=3 harmonic is 21ps. However, at the 3.8μm grating period, where our maximum probe delay is roughly 200ps, the ambipolar decay time for the n=3 harmonic is 105ps. For the same reason, it is clear that for our experimental conditions, these high modulation effects will be less prominent as the electron mobility is increased. Thus, we expect this effect to be less prominent in our results for semi-insulating GaAs.

7.5 Summary

In this chapter we have presented the experimental results obtained using the

PPRTG measurement technique and our 1.0mm undoped CdTe crystal. Our results for the non-rotated polarization component show evidence of index gratings resulting from the instantaneous bound-electronic and free carrier gratings. Data for the free carrier grating exhibits the behavior expected for a drift-limited population of electrons and holes, and our independent measurement of the ambipolar diffusion coefficient and carrier lifetime produce values that are in good agreement with those that have been previously reported.

Our experimental results for the rotated polarization component of the diffracted beam provide the first unambiguous illustration of a Dember photorefractive nonlinearity. Although the presence of this photorefractive response has been assumed in order to explain the results of picosecond two-beam coupling experiments, this photorefractive nonlinearity has not previously been unambiguously resolved. In addition, the transient feature that is present in our experimental results for the rotated polarization component shows the most clear evidence to date of a hot carrier photorefractive nonlinearity. Though we have not used a rigorous treatment of hot carrier transport and space-charge field formation to make this identification, we have used qualitative arguments to show that the characteristics of this transient feature are those that are expected for a hot carrier photorefractive nonlinearity.

Additionally, we have modeled our experimental results using the small-signal transient-grating diffraction efficiency, and the carrier and field equations that were derived in Chapter III. The results of our model are in excellent agreement with the free-carrier experimental results in both the low and high modulation limits, and for the range

of grating periods used in our experiments. Since our model considers carrier transport at the lattice temperature, it is not surprising that the results of our model are in poor agreement with the photorefractive experimental results for probe delays less than about 10ps. For probe delays longer than about 10ps, we observe decay constants associated with the photorefractive diffraction efficiency that are shorter than expected for ambipolar decay. While this trend is not predicted by our model in the low modulation limit, we obtain good agreement between the data and our model in the high modulation limit. On the whole, modeling of our photorefractive results provides a unique illustration of the interplay between the different Fourier components of the carrier densities and space-charge field in forming the fundamental component of the space-charge field.

CHAPTER VIII

PICOSECOND PHOTOREFRACTIVE RESPONSE OF SEMI-INSULATING GaAs

8.1. Introduction

In this chapter we consider the experimental results that have been obtained with the PPRTG measurement technique, and our 3.17mm semi-insulating GaAs crystal. As we have noted throughout this thesis, semi-insulating GaAs is the more complicated of the two materials that we are studying. Like undoped CdTe, semi-insulating GaAs exhibits substantial instantaneous two-photon absorption at the laser wavelength of 960nm. However, as we have discussed, single photon absorption can occur at the EL2 midgap levels, resulting in populations of electrons, holes and ionized EL2. Thus, not only does the EL2 absorption serve as an independent source for the electron-hole free-carrier and Dember photorefractive nonlinearities, but it also serves as a source for a second contribution to the photorefractive and free-carrier nonlinearities involving the excess photogenerated electrons and ionized EL2.

As in the previous chapter, we begin by considering the experimental results for the non-rotated polarization component of the diffracted beam. Following this, we consider the results for the rotated polarization component, and then conclude by discussing the modeling of our semi-insulating GaAs results. As before, while our main

emphasis in discussing the rotated and non-rotated diffraction efficiencies is on data taken at a grating period of 1.7μm, our modeling discussion considers these and the results taken at a grating period of 3.8μm.

As in undoped CdTe, the results pertaining to the non-rotated polarization component exhibit sharply-peaked and decaying features that are consistent with diffraction from instantaneous bound-electronic and electron-hole free-carrier gratings. However, we see an additional feature in the non-rotated results that is consistent with diffraction from a long-lived free-carrier grating. This behavior is that which is expected for semi-insulating GaAs, and is also reflected in the results for the rotated polarization component. Here, in addition to the transient and decaying features that were present in the CdTe data, we also see a long-lived feature that is consistent with diffraction from an electron-EL2 photorefractive grating.

8.2 Non-Rotated Polarization Component: Instantaneous Bound-Electronic and Free-Carrier Nonlinearities

In this section, we discuss the experimental results obtained using our PPRTG measurement technique, and by monitoring the non-rotated polarization component of the diffracted beam. The data shown in this section were taken with the space-charge field generated parallel to the (110) direction, where diffraction from the photorefractive grating produces a beam with a rotated polarization component. Since we are monitoring the non-rotated polarization component of the diffracted beam, these results *can not* be attributed to the photorefractive grating.

8.2.1 Temporal Dynamics

The temporal dependence of the non-rotated diffraction efficiency is shown in figures 8.1a-c for a range of incident fluences. As shown, the data share some of the same characteristics as the non-rotated diffraction efficiency observed in undoped CdTe: a sharply-peaked feature that is most easily seen in figures 8.1b and c, and a decaying feature that is most easily seen in figures 8.1a and b. The temporal- and fluence-dependencies of the sharply peaked feature indicate that it results from diffraction from the refractive instantaneous bound-electronic grating. Since it does not reflect the carrier or field dynamics of the material, it is not of interest and will not be considered further. In addition, there is a third component of the non-rotated diffraction efficiency that is not seen in the CdTe results: a long-lived feature. As we show in the following paragraphs, the temporal-dependencies of these features indicate that they are produced by diffraction from free-carrier gratings arising from the decaying electron-hole population, and a long-lived population of free electrons.

As in the non-rotated CdTe data shown in the previous chapter, the decaying feature of figure 7.1a shows the cumulative rise and slow decay that are expected for diffraction from a free-carrier grating. Preliminary inspection of this feature reveals a decay constant of ~30ps, which is in the range of values expected for ambipolar diffusion of electrons and holes in GaAs across our 1.7μm grating period. While it is therefore reasonable to assume that the decaying feature of figure 8.1a arises from a drift-limited

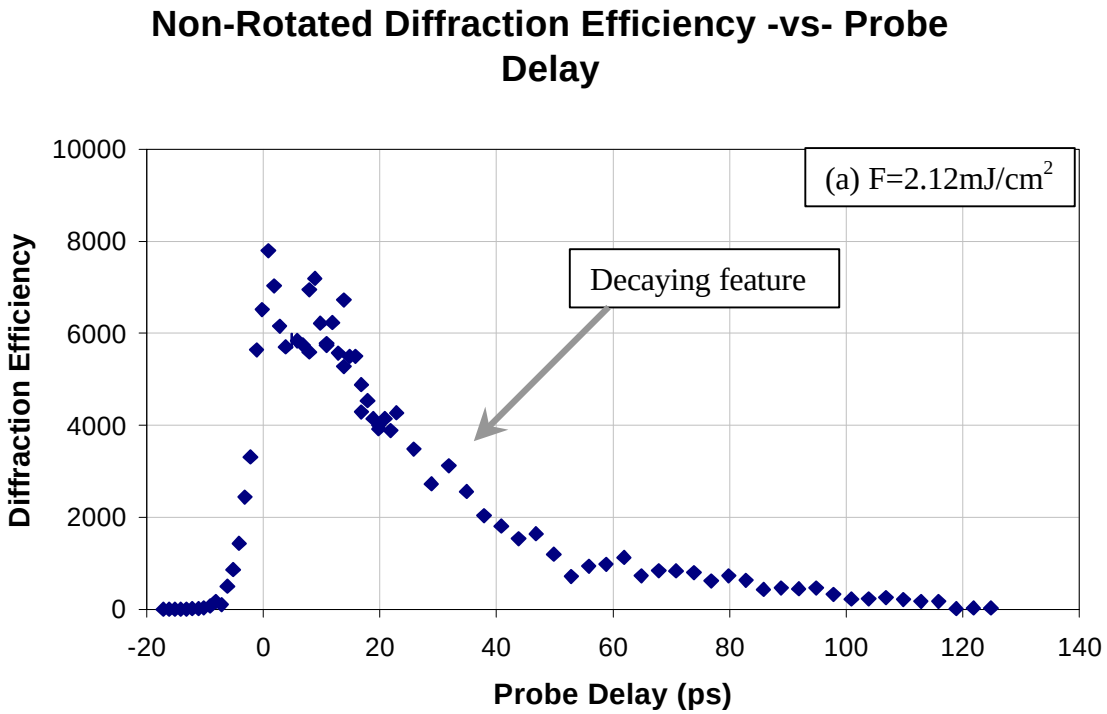
Non-Rotated Diffraction Efficiency -vs- Probe Delay
(a) F=2.12mJ/cm2
Decaying feature
Diffraction Efficiency
Probe Delay (ps)
10000
8000
6000
4000
2000
0
-20
0
20
40
60
80
100
120
140

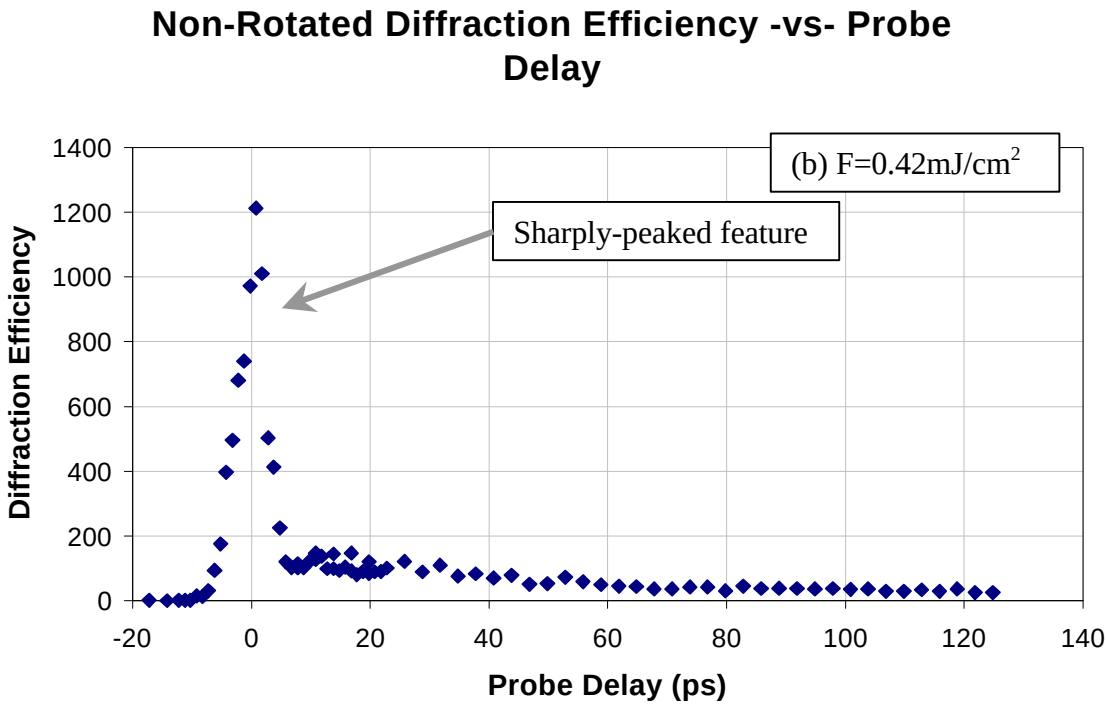
Non-Rotated Diffraction Efficiency -vs- Probe Delay
(b) F=0.42mJ/cm2
Sharply-peaked feature
Diffraction Efficiency
Probe Delay (ps)
1400
1200
1000
800
600
400
200
0
-20
0
20
40
60
80
100
120
140

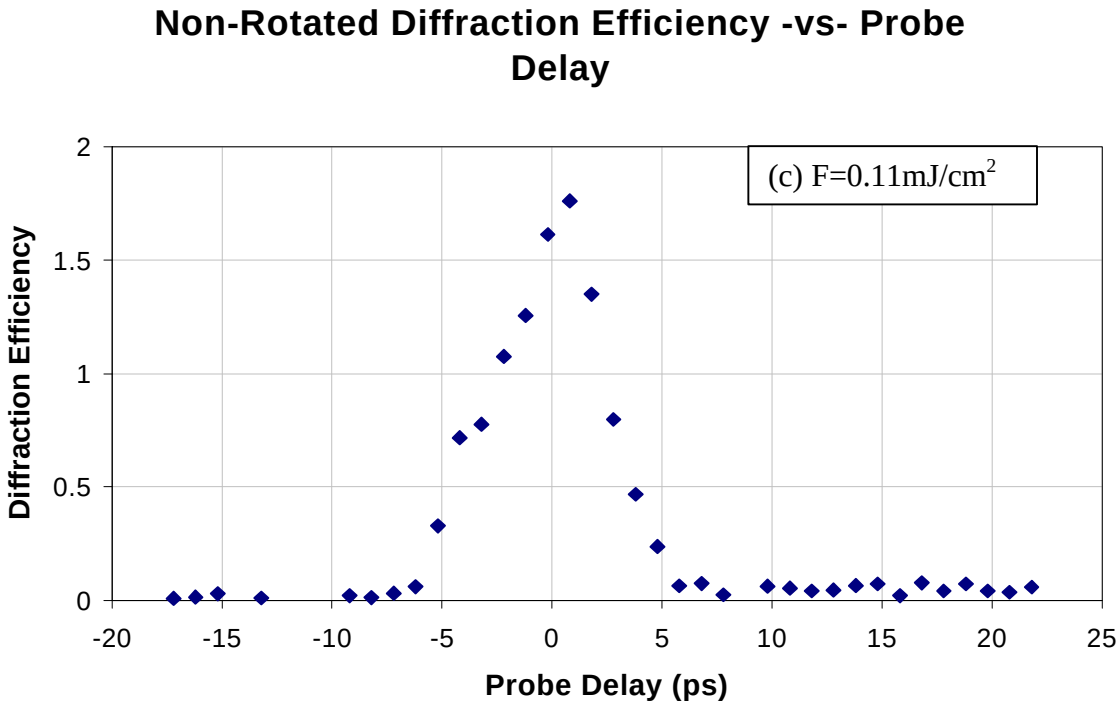

Figures 8.1a-c – Non-rotated diffraction efficiency versus probe delay for incident fluences of (a) 2.12mJ/cm^2, (b) 0.42mJ/cm^2, and (c) 0.11mJ/cm^2. The data show sharply-peaked, decaying and constant features.

free-carrier grating in GaAs, it is necessary to make this association more rigorously. This can be done in the way described in Chapter VII, by using the observed decay rate of this feature to measure the ambipolar diffusion coefficient, and then comparing our measured value with values reported in the literature. However, in performing this analysis we must be cautious of two things. First, since the decaying diffraction efficiency exists in the presence of a constant component, we must be careful that the presence of the constant component does not influence our determination of the decay rate. Second, the ambipolar diffusion coefficient depends on the relative densities of electrons and holes, and EL2 light absorption produces population densities of electrons and holes whose proportions vary

depending on the excitation fluence. As a result, we must be careful to use decay rates that are observed when similar population densities of electrons and holes are present.

At the incident fluence of 2.12mJ/cm^2, the fluence and corresponding intensity are high enough over the crystal length so that the dominant carrier generation mechanisms are instantaneous two-photon absorption and step-wise two-photon absorption at the EL2 sites. As a result, for this fluence, we can say that the decaying diffraction efficiency arises from a free-carrier grating where the electron and hole populations are nearly equal. For the same reason, at the shorter probe delays, we expect the magnitude of the constant component of the diffraction efficiency, which is proportional to the square of the photoionized EL2 density (see section 8.2.2), to be much smaller than the magnitude of the decaying component (proportional to the square of the electron and hole populations). We therefore measure the decay of this feature at the shorter probe delays and find a decay constant of roughly 27ps.

For the 3.8μm grating period (data shown in section 8.4), we find that the electron and hole populations are nearly equal at the incident fluence of 1.56mJ/cm^2. Since we measure the diffraction efficiency at probe delays that are at most 1.5 times longer than the expected ambipolar decay constant of ~133ps, it is reasonable to assume that over the range of our measurements, the decaying component of the diffraction efficiency is much larger than the magnitude of the constant component. Using the decay constant of ~137ps that we observe at this grating period, together with the constant of 27ps observed at 1.7μm, we find an ambipolar diffusion coefficient of 13.7cm^2/s, which corresponds to a hole mobility of roughly 265cm^2/V-s. Since this hole mobility is within the range of values

reported in the literature for this constant ($140cm^2/V\text{-}s$ to $400cm^2/V\text{-}s$, (W. Walukiewicz et al, 1982, J. S. Blakemore, 1982, K. Takeda, et al., 1985, and H. J. Lee and D. C. Cook, 1983)), we can associate the dynamics of our decaying non-rotated diffraction efficiency with those of a drift-limited free-carrier grating.

As we stated above, the non-rotated diffraction efficiency data exhibits a long-lived feature that is not present in the CdTe results. This feature can be most easily seen by in the data of figure 8.1b, where the magnitudes of the decaying and constant components are comparable. Shown in figure 8.2, we have graphed the data of figure 8.1b on a semi-logarithmic plot for probe delays where the free-carrier nonlinearity is the main contributor to the diffraction efficiency. Also included on the plot are two lines representing an exponential decay, and an exponential decay to a constant value. Since we have already shown that the dynamics of the decaying feature are consistent with diffraction from a drift-limited free-carrier grating, we have used the decay constant that is expected for ambipolar diffusion of electrons and holes across the grating period (~27ps). From the figure it is clear that the data more closely follows the line representing ambipolar decay to a constant value. While we could fit the data with a decay that is purely exponential (no constant value), this would require a much longer decay constant, which is clearly not justified, given the discussion of the previous paragraph.

The decay of the free-carrier diffraction efficiency to a constant value is expected in semi-insulating GaAs. As we showed in Chapter II, light absorption in our semi-insulating GaAs crystal produces a greater density of electrons and holes, and the excess electron density is compensated by a density of photoionized EL2 ($n\text{-}p=EL2^{+}_{ph}$). As a

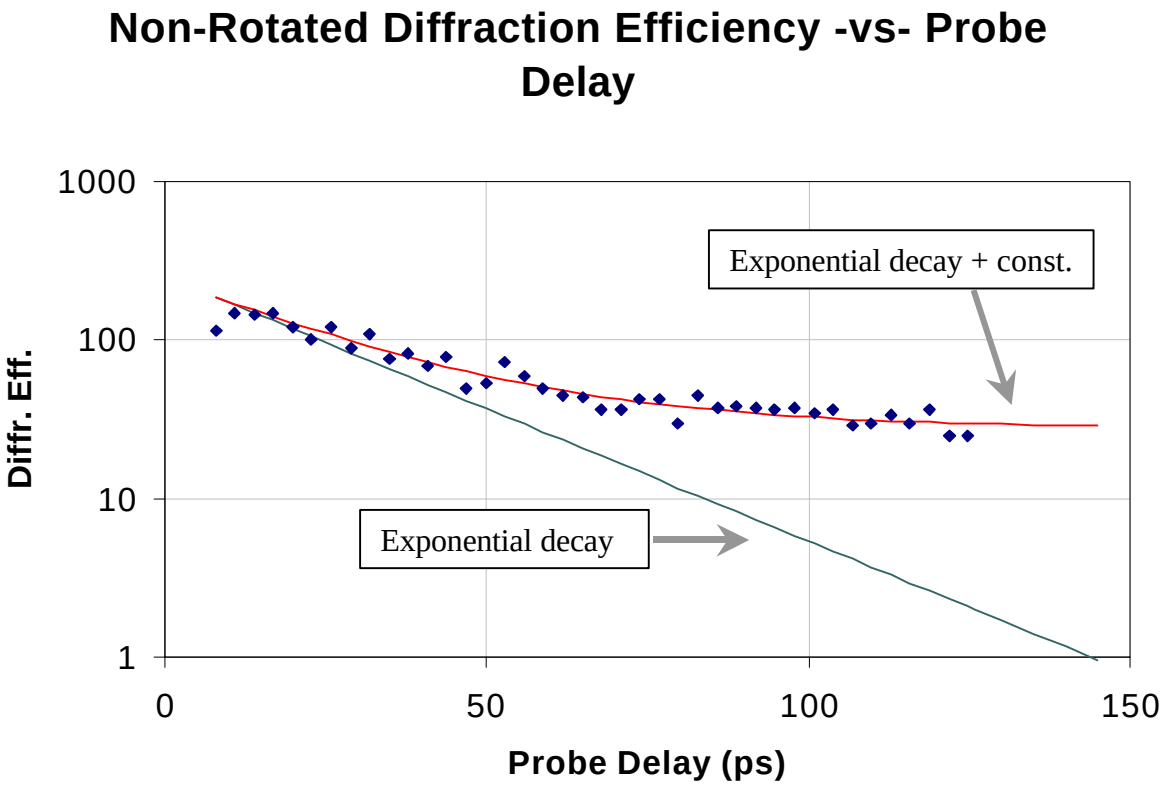

Figure8.2 – Semi-logarithmic plot of non-rotated diffraction efficiency versus probe delay for an incident fluence of 0.42mJ/cm^2 and probe delays greater than 7ps. The data show that the non-rotated diffraction efficiency decays to a constant value.

result, semi-insulating GaAs exhibits a two-component space-charge field on picosecond time scales, and we can think of these fields as being between equal densities of electrons and holes, and the excess electrons and photoionized EL2. While we have already seen that the drift-limited electron-hole space-charge field decays by ambipolar diffusion, we showed in section 3.3.4 that the drift-limited electron-ionized EL2 space-charge field results in a t=∞ modulated electron density (in the absence of carrier recombination). As we noted in Chapter III, it is this free electron population that is destroyed by carrier

recombination to produce the ionized EL2-acceptor space-charge field that is observed in experiments with CW laser beams.

8.2.2 Fluence Dependencies of the Decaying and Constant Diffraction Efficiencies

In the previous section we showed that the temporal dependence of the decaying and constant diffraction efficiencies are consistent with diffraction from free-carrier gratings due to electrons and holes and excess electrons. We can further strengthen these associations by examining the fluence dependencies of these features. We consider first the fluence dependence of the decaying diffraction efficiency and then consider the fluence dependence of the constant diffraction efficiency.

In considering the fluence dependence of the decaying diffraction efficiency, it is beneficial to begin our discussion as we have in the other discussions of this type; by considering the expected fluence dependence of this diffraction efficiency. However, whereas the expected dependence of the electron-hole diffraction efficiency took a relatively simple form in undoped CdTe, its form is clearly much more complicated in semi-insulating GaAs. Unlike undoped CdTe, where free carriers are generated solely by instantaneous two-photon absorption, free carriers are generated in our semi-insulating GaAs crystal by linear absorption at the EL2 sites, and instantaneous two-photon absorption. Furthermore, while the relative importance of these carrier generation mechanisms changes as the fluence is increased, we have also seen that the EL2 absorption saturates at high fluences, resulting in a change in the effective linear absorption coefficient, and step-wise two-photon absorption with the EL2 sites as the intermediary.

Finally, due to the presence of nonlinear absorption, we expect the fluence dependence of the diffraction efficiency to reflect an effective transient-grating interaction length that is fluence-dependent (discussed in section 2.2.- and 7.2.2). In light of these complexities, it is clear that it is necessary to use our numerical models to make a rigorous association between our data and the expected behavior.

The fluence dependence of the decaying diffraction efficiency is shown in figure 8.3. Here the diffraction efficiency has been measured at a constant probe delay of 10ps, where the instantaneous bound-electronic nonlinearity does not contribute to the diffraction efficiency. The data of figure 8.3 are accompanied by a line that is the "expected dependence" of the diffraction efficiency, as determined by numerical modeling of beam propagation and carrier generation in semi-insulating GaAs. Here we have used the beam propagation equation to determine the variation of the optical intensity (and fluence) over the crystal length (assuming a constant linear absorption). The optical intensity and fluence have in turn been used in equations (6.5) –(6.7) to calculate the n=1 photogenerated electron density for each *dz* element of the crystal. The propagation length dependence of the carrier density is then used to estimate the small-signal diffraction efficiency, which is proportional to the square of the product of the carrier density and interaction length. As can be seen from the figure, the agreement between the data and model is good. Thus, the fluence dependence of the decaying diffraction efficiency is that which is expected for an electron-hole free carrier grating, based on a simple model of the diffraction efficiency.

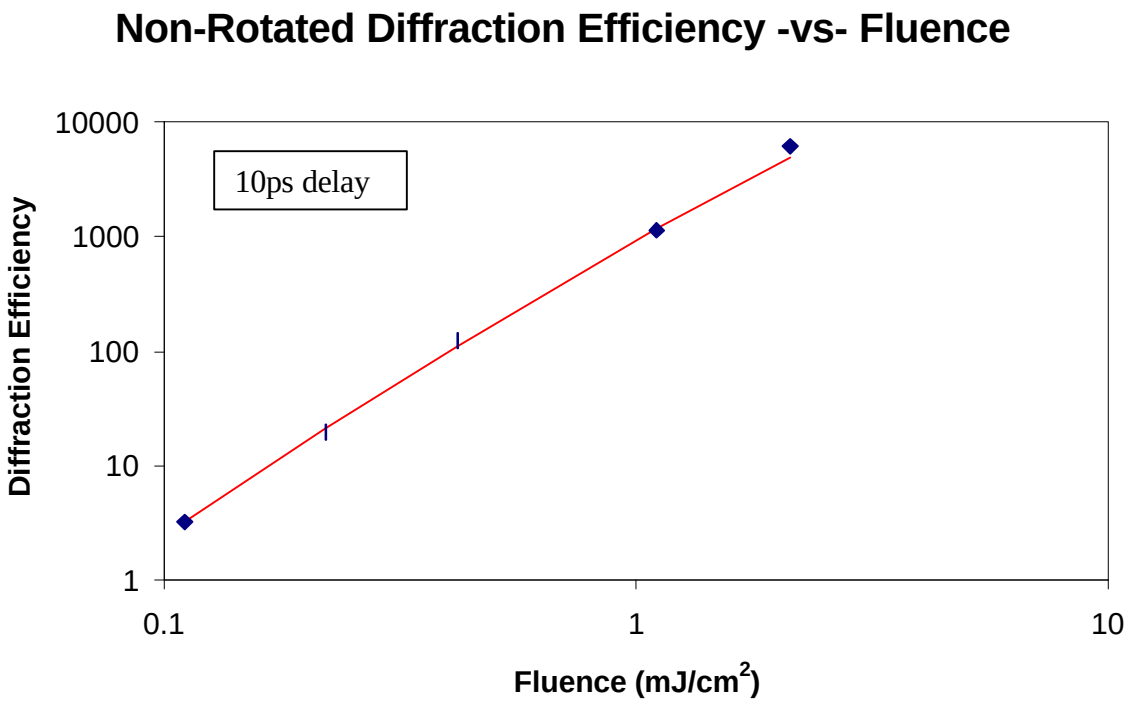

Figure8.3 - Diffraction efficiency versus fluence for the non-rotated component of the diffracted beam and a constant probe delay of 10ps. The data (filled diamonds) follow the expected dependence (line) for an electron-hole free-carrier grating, based on a simple model for the small-signal diffraction efficiency.

In order to understand the expected dependence of the constant diffraction efficiency, we can recall the dynamics for this feature discussed in the previous section, along with the carrier generation properties of our semi-insulating GaAs crystal. We showed in the previous section that the dynamics of this component are consistent with diffraction from a long-lived free-carrier grating, arising from the excess electron population that is generated as a result of absorption at the EL2 sites. Since the diffraction efficiency follows the square of the excess electron population, and the excess electron population balances the photoionized EL2 density, we expect the fluence

dependence of the constant diffraction efficiency to follow the square of the fluence dependence of the photoionized EL2 density. We can use equation (2.12), along with the fact that the photoionized EL2 density is the density of ionized EL2 minus the dark density of ionized EL2 (N^+-A^-), to glean the expected fluence dependence of the constant component (η_c):

$$\eta_c \propto \left[1 - e^{\frac{-F}{F_{sat}}}\right]^2 . \qquad (8.1)$$

Here F_{sat} is the EL2 saturation fluence, which is 0.7mJ/cm^2 (see Chapter II).

Figure 8.4 shows the fluence dependence of the constant diffraction efficiency. Here the data are taken at a constant probe delay of 130ps, where the contribution from the decaying component of the diffraction efficiency is minimized. Also included in the figure is a line depicting the dependence expected for the long-lived free-carrier grating. As can be seen from the figure, the line offers an excellent fit to the data for the middle range of fluences. The disagreement at low fluences is due to noise in the data (the diffraction efficiencies at these fluences are near the minimum measurable value). At the highest fluences, the disagreement is due to the fact that, even after 130ps, the magnitude of the decaying component is comparable to the magnitude of the constant component. Thus, the fluence dependence of the constant diffraction efficiency is that which is expected for a free-carrier grating due to excess electrons generated at the EL2 sites.

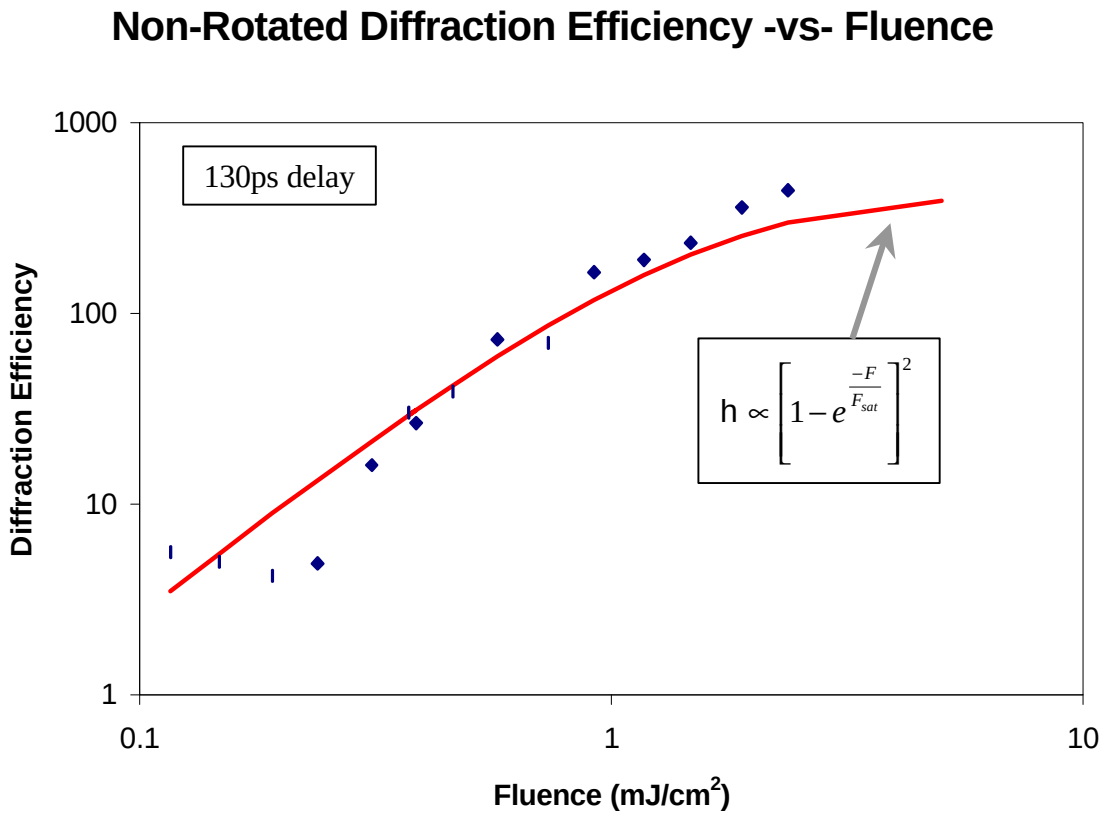

Figure 8.4 – Diffraction efficiency versus fluence for the non-rotated component of the diffracted beam and a constant probe delay of 130ps. The data follow the trend expected for a long-lived free carrier grating due to the excess electrons photogenerated at the EL2 sites.

8.3 Rotated Polarization Component: Dember and Electron-EL2 Photorefractive Nonlinearities

In this section, we discuss the experimental results for the rotated polarization component of the diffracted beam in our 3.17mm semi-insulating GaAs crystal. These results were obtained by monitoring the rotated polarization component of the diffracted beam as discussed in Chapter V.

Before discussing the experimental results for the rotated polarization component,

it is useful to consider the behavior that we can expect to observe, based on the non-rotated results of the previous section. In the previous section, we saw decaying and constant components to the non-rotated diffraction efficiency. We showed that these features exhibited the temporal and fluence dependencies that are expected for free-carrier gratings due to the electron and hole and excess electron populations generated in our semi-insulating GaAs crystal. As a result, we anticipate that the rotated diffraction efficiency, which we expect to portray the photorefractive nonlinearity, will also exhibit decaying and constant features. However, whereas the components to the non-rotated diffraction efficiency arise from decaying and constant free-carrier populations, the decaying and constant components of the rotated diffraction efficiency will arise from electron-hole and electron-ionized EL2 space-charge fields. Furthermore, since we have already shown that the density of photogenerated carriers exceeds the critical value, we expect the electron-hole and electron-ionized EL2 space-charge fields to exhibit drift-limited temporal and fluence dependencies.

8.3.1 Crystal Orientation Dependence

We begin our discussion of the rotated diffraction efficiency by considering its crystal orientation dependence. Here we show that the rotated diffraction efficiency exhibits the crystal orientation dependence expected for a photorefractive nonlinearity.

The polarization rotation properties of our semi-insulating GaAs crystal are discussed in Chapter V, and can be summarized as follows. Radiation that is scattered from the photorefractive grating has a polarization rotation of *exactly 90°* when the

incident radiation is s- or p-polarized, and when the space-charge field is generated along the (110) crystal direction. However, when the space-charge field is generated parallel to the (001) crystal direction, the photorefractive grating produces no polarization rotation for either s- or p-polarized probe radiation. The photorefractive grating is the only grating that is capable of producing this result; as we saw in Chapter II, the instantaneous bound electronic and free-carrier gratings do not produce a polarization rotation for our experimental conditions.

The crystal orientation dependence of the rotated diffraction efficiency is shown in figure 8.5. As is shown, the rotated diffraction efficiency exhibits the crystal orientation-dependence expected for a photorefractive grating. While a substantial rotated diffraction efficiency is seen when the crystal is oriented with the space-charge field parallel to the (110) direction, the rotated diffraction efficiency decreases dramatically when the crystal is oriented with the space-charge field parallel to the (001) direction. Thus, the rotated diffraction efficiency can be attributed entirely to the photorefractive grating.

8.3.2 Temporal Dynamics

The probe delay dependence of the rotated diffraction efficiency is shown in figure 8.6a-d for a range of incident fluences and a grating period of 1.7μm. Like the non-rotated results, the rotated results show some of the same features that are present in the CdTe data: a transient feature and a decaying feature. In Chapter VII, where we discussed the transient component of the diffraction efficiency, we showed that the magnitude,

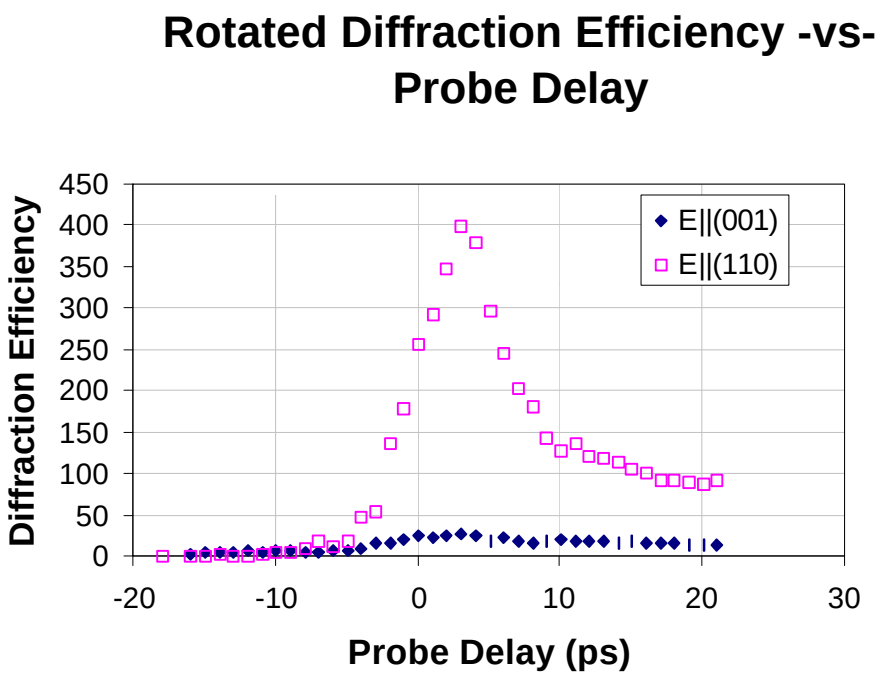

Figure 8.5 – Diffraction efficiency versus probe delay for two orientations of our semi-insulating GaAs crystal: $E_{sc}||(110)$ (open squares) and $E_{sc}||(001)$ (filled diamonds). The rotated diffraction efficiency exhibits the crystal orientation dependence expected for the photorefractive nonlinearity.

formation time, and decay time of this feature are consistent with diffraction from a hot carrier photorefractive grating. The transient feature shown in figures 8.6a-c exhibits the same characteristics as were observed in the CdTe results. Since free carriers generated in semi-insulating GaAs by instantaneous two-photon absorption and linear absorption at the EL2 sites have a significant excess energy, we postulate that this component arises from diffraction from a hot-carrier photorefractive grating. Since a detailed description of hot carrier photorefractive effects is beyond the scope of this thesis, we will not consider this feature further. For a qualitative explanation of hot carrier photorefractive effects, the reader is referred to the description that is given in Chapter VII.

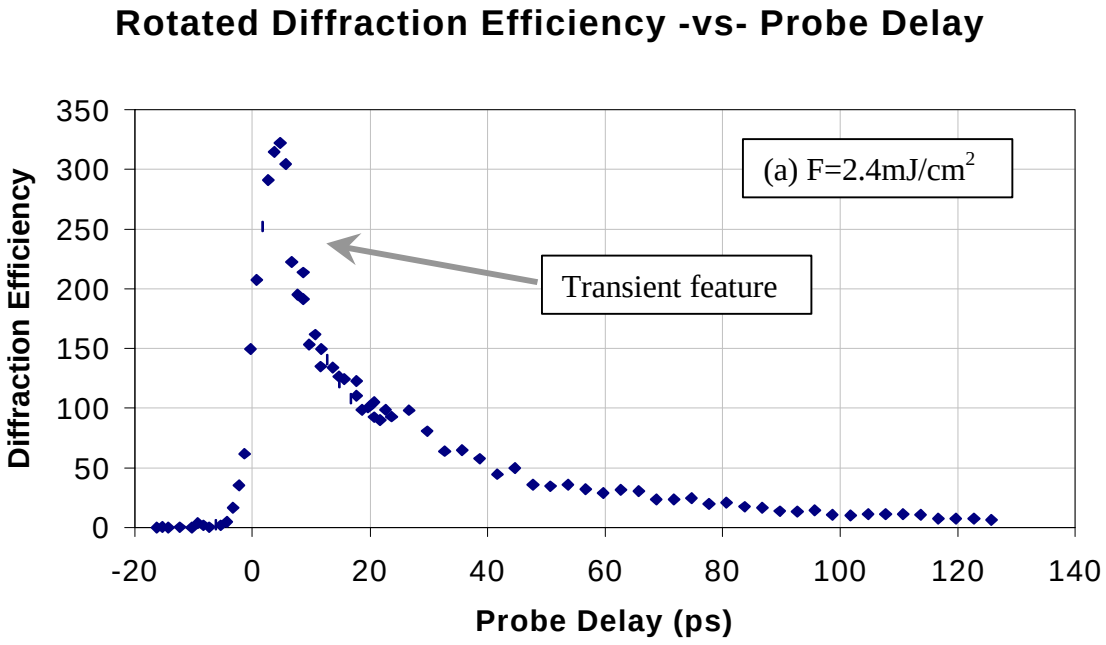
Rotated Diffraction Efficiency -vs- Probe Delay
Diffraction Efficiency
Probe Delay (ps)
(a) F=2.4mJ/cm2
Transient feature
350
300
250
200
150
100
50
0
-20
0
20
40
60
80
100
120
140

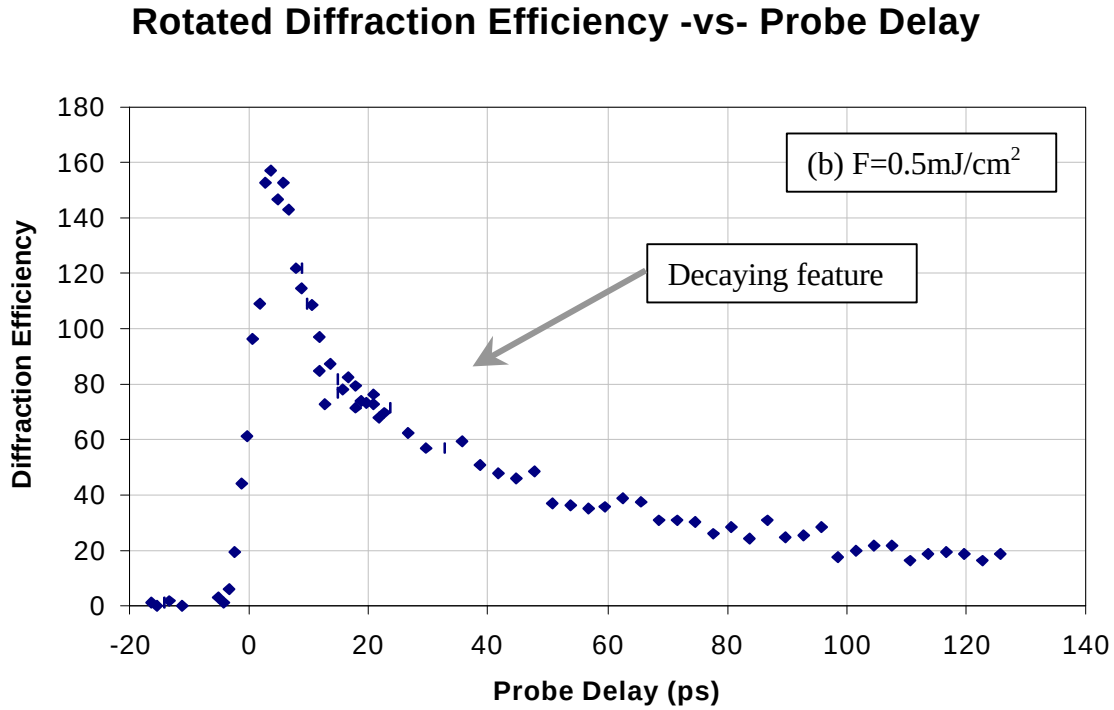
Rotated Diffraction Efficiency -vs- Probe Delay
Diffraction Efficiency
Probe Delay (ps)
(b) F=0.5mJ/cm2
Decaying feature
180
160
140
120
100
80
60
40
20
0
-20
0
20
40
60
80
100
120
140

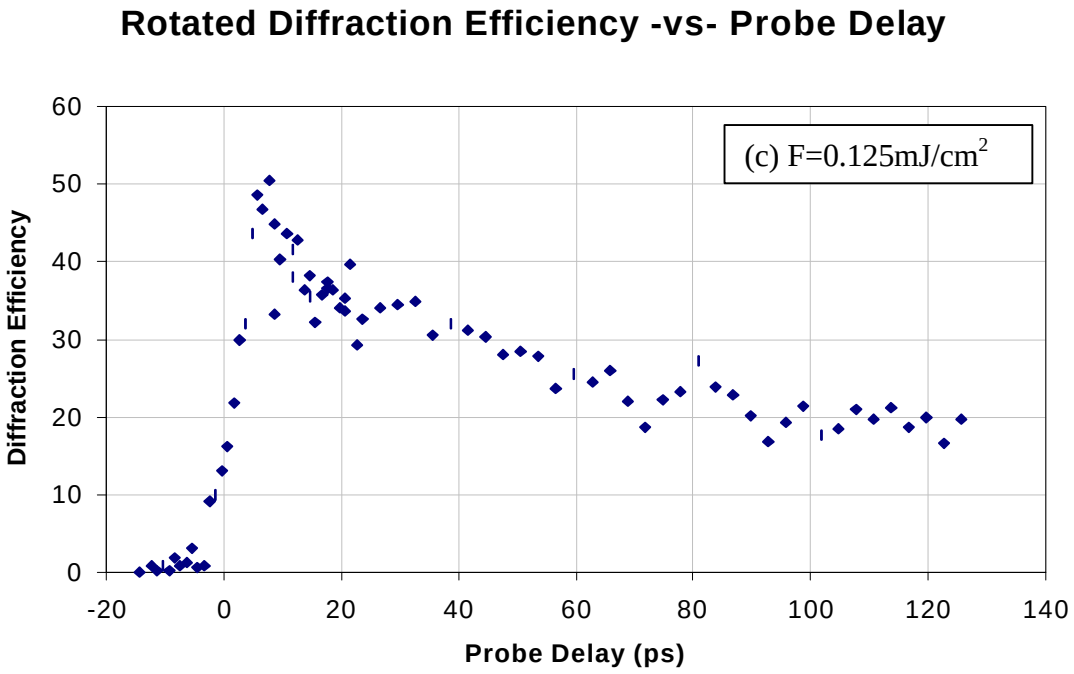

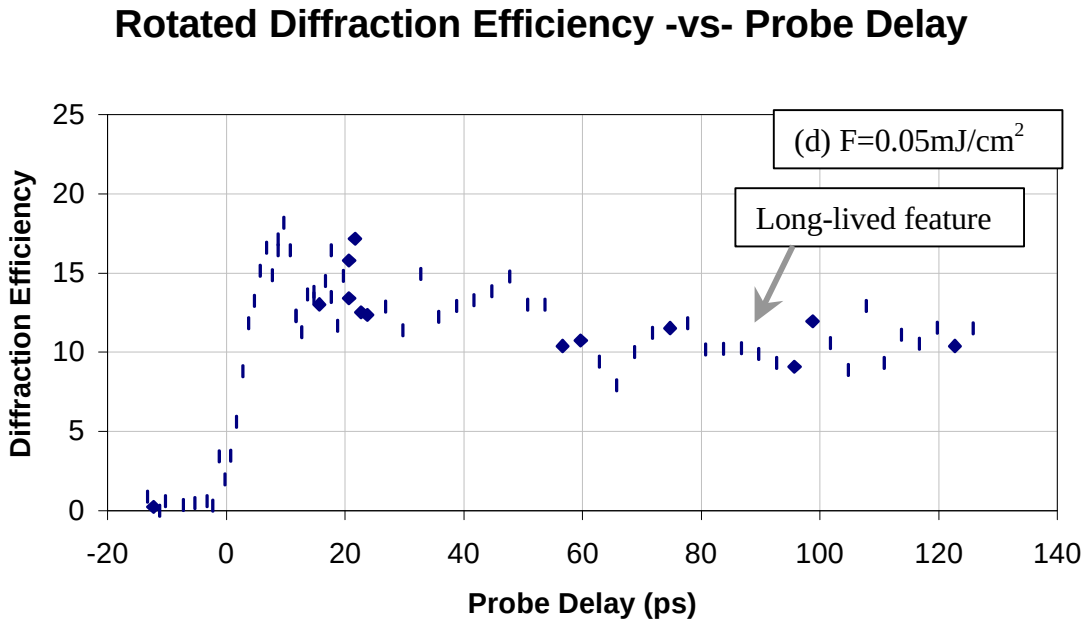

Figure 8.6a-d – Rotated diffraction efficiency versus probe delay for a range of incident fluences ((a) 2.4mJ/cm^2, (b) 0.5mJ/cm^2, (c) 0.125mJ/cm^2, (d) 0.05mJ/cm^2). The data exhibit transient, decaying and long-lived features.

Visible especially in figures 8.6a and b is a decaying photorefractive diffraction efficiency that is similar to that which was observed in the undoped CdTe results. The presence of this feature, which can be associated with a Dember (electron-hole) photorefractive grating, is not surprising. Instantaneous two-photon absorption, the predominant carrier generation mechanism in semi-insulating GaAs at these fluences (2.4mJ/cm^2, and 0.5mJ/cm^2), produces equal populations of electrons and holes. In addition, since these fluences are near to or larger than the EL2 saturation fluence, light absorption at the EL2 sites results in step-wise two-photon absorption, and populations of electrons and holes that are nearly equal. The decay constant that is observed for this feature is that which is expected for a drift-limited Dember photorefractive grating. It is nearly equal to that observed for the electron-hole free-carrier grating (~28ps at 2.4mJ/cm^2), and in the range of values expected for ambipolar diffusion of electron-hole pairs across our 1.7μm grating period. In addition, the observed constant also decreases with decreasing fluence, behavior that is expected in light of the dependence of the ambipolar diffusion constant on the electron and hole densities, and the carrier generation properties of our semi-insulating GaAs crystal.

It is important to note that, while the decay constants for the electron-hole free-carrier and photorefractive gratings are nearly equal at the 1.7μm grating period, we find that the electron-hole photorefractive grating decays more quickly than the electron-hole free-carrier grating at the 3.8μm grating period. This feature of the data, which was also observed in the CdTe results, arises from interplay between the fundamental and higher-

order Fourier components of the carrier densities in the decay of the n=1 space-charge field. Our experimental results for the 3.8μm grating period will be discussed in section 8.4. For an explanation of this effect, the reader is referred to the discussion given in Chapter VII.

While exhibiting features that are similar to those that are present in the CdTe results, the semi-insulating GaAs data of figures 8.6a-d are fundamentally different from the CdTe results in an important way. As is most visible from figure 6.7d, the rotated diffraction efficiency in semi-insulating GaAs decays to a constant value. The presence of this feature, which can be associated with diffraction from a photorefractive grating arising from the space-charge field between the excess electrons and photoionized EL2, is not surprising. As we noted in section 8.2.1, light absorption in our semi-insulating GaAs crystal results in populations of electrons, holes and photoionized EL2, where the density of electrons exceeds the density of holes, but is compensated by the density of photoionized EL2 ($n=p+EL2^{+}$). As we showed in Chapter III, since the ionized EL2 are immobile, carrier transport results in a long-lived field between the excess electrons and photoionized EL2. As we have already seen, this long lived modulated electron density produces a constant component to the non-rotated diffraction efficiency.

As the fluence is decreased in figures 8.6a-d, the long-lived feature becomes increasingly important in the diffraction efficiency. This result is expected, given the light absorption and carrier generation properties of our semi-insulating GaAs crystal (discussed in Chapter II). As the fluence is decreased, saturation of the EL2 absorption decreases, so that light absorption at the EL2 sites produces proportionally higher

densities of electrons and ionized EL2, and a proportionally lower density of holes. In addition, the importance of instantaneous two-photon absorption, which produces equal densities of electrons and holes, decreases.

Another important difference between the data of figure 8.6d and the data taken at the higher fluences (figures 8.6a-c) is that the former data set exhibits no observable transient photorefractive diffraction efficiency. The absence of this feature is not surprising, and can be understood in the following way. As we noted, instantaneous two-photon absorption is insignificant at the incident fluence of $50\mu J/cm^2$, so that the photorefractive nonlinearity that is observed at this fluence is due to free carriers that are generated via linear absorption at the EL2 sites. As we noted in Chapter II, linear absorption at the EL2 sites results in free electrons with an excess energy of roughly 0.5eV. Using the simple carrier cooling formula given in Chapter II, we estimate that carriers with this excess energy cool in a time of roughly 2.5ps. However, using the EL2CB carrier generation equation with the equation for the dielectric relaxation time, we estimate a formation time of roughly 4.8ps for the space-charge field that is responsible from producing the rotated diffraction efficiency shown in figure 8.6d. Thus, for the experimental conditions relevant to figure 8.6d, the carriers cool in about one-half the time required to form the space-charge field, so that there is no hot carrier enhancement to the space-charge field.

A general comparison between the non-rotated and rotated diffraction efficiency results shows that the long-lived component of the rotated diffraction efficiency is much more prominent in these results than the constant component of the non-rotated

diffraction efficiency is in the non-rotated results. This follows from a fundamental difference between the free-carrier and photorefractive nonlinearities that can be understood as follows. Since the non-rotated diffraction efficiency is proportional to the square of the free-carrier population, diffraction efficiencies that are due to small carrier densities, such as the excess electron population that is responsible for the long-lived component, are not easily observed. In contrast, the rotated diffraction efficiencies, which we have shown arise from the photorefractive nonlinearity, are proportional to the square of the space-charge field magnitude. The space-charge field magnitude is proportional to the integrated charge separation, so that observable diffraction efficiencies can be generated when small carrier densities are present, so long as an appreciable charge separation is produced.

8.3.3 Time Resolution of the Formation of the Photorefractive Nonlinearities in semi-insulating GaAs

As we have noted throughout this thesis, the primary goal of our study is to time-resolve the formation of the picosecond photorefractive nonlinearities in semi-insulating GaAs and undoped CdTe. While CdTe is an important photorefractive material, our emphasis throughout this thesis has been on semi-insulating GaAs. It is therefore fitting, as we consider the temporal dynamics of the photorefractive nonlinearity in semi-insulating GaAs, to separately consider how our results detail the formation of the picosecond photorefractive nonlinearities.

In the CdTe results, we saw that we could not time-resolve the formation of the

Dember photorefractive nonlinearity. As a result, the onset of the rotated diffraction efficiency was manifest in a cumulative rise that was at roughly half of its peak value at a probe delay of 0ps. In viewing the rotated diffraction efficiency results for GaAs in figures 8.6a-c, we see roughly the same behavior. As in undoped CdTe, the instantaneous rise of the photorefractive nonlinearity at these fluences results from two factors. First, for these experimental conditions, the photogenerated carrier densities are high enough so that the field formation time is shorter than the duration of our probe pulses. In addition, especially for the experimental conditions relevant to figures 8.6a and b, a significant portion of the free carrier density is produced as a result of instantaneous two-photon absorption. As we have seen, instantaneous two-photon absorption results in free carriers with an excess energy of roughly 1eV. As we noted in Chapters V and VI, for our experimental conditions, this results in enhanced carrier mobilities and a faster field formation time. Thus, as in undoped CdTe, we do not resolve the rise of the photorefractive nonlinearity for the middle and high fluences that are used in our experiments.

At the lowest fluences used in our experiments, we see the diffraction efficiency reach one-half of its maximum value at a probe delay that is greater than 0ps. This result, which is an indication that the rise of the field is not instantaneous with respect to the duration of the probe pulses, is not surprising given the low carrier density and the absence of hot carrier effects. Nevertheless, we find that at this fluence, the rise time of the photorefractive nonlinearity is comparable to but less than the duration of our probe pulses, so that our resolution is at best incomplete. To illustrate this, we can use the data

of figure 8.6d to estimate the observed rise time of the photorefractive nonlinearity. Here we note that the rise of the diffraction efficiency follows the convolution of the probe pulse intensity with the rise of the square of the induced index change. As a result, the rise time of the diffraction efficiency is approximately equal to the sum of the FWHM duration of the probe pulses and one half the formation time of the photorefractive nonlinearity. Using the ~5ps rise time that is observed for the diffraction efficiency with the probe pulse duration of 3-5ps, we estimate a rise time of ~1ps for the photorefractive nonlinearity. This is in the range of values that is expected. For these experimental conditions, we find a dielectric relaxation time that is roughly equal to the electronic diffusion time of 5ps. Together, these suggest a field formation time of 2.5ps, which is approximately equal to the photorefractive rise time given above.

Unfortunately, at a similar fluence and a grating spacing of 3.8μm, we find a result that is only slightly different. Shown in figure 8.7 for an incident fluence of 47μJ/cm^2, we observe a rise time for the diffraction efficiency of roughly 7ps. Using this, with the method described in the previous paragraph and the duration of the probe pulses, we estimate a rise time for the photorefractive nonlinearity of 4-8ps. Since this rise time is comparable to the duration of our probe pulses, the rise of the photorefractive nonlinearity is again only partially resolved. The rise time of 4-8ps that is observed is also in the range of values that is expected. This follows from the fact that, since the increase in grating spacing increases the electronic diffusion time by a factor of 4, the field formation time is approximately equal to the dielectric relaxation time of ~5ps.

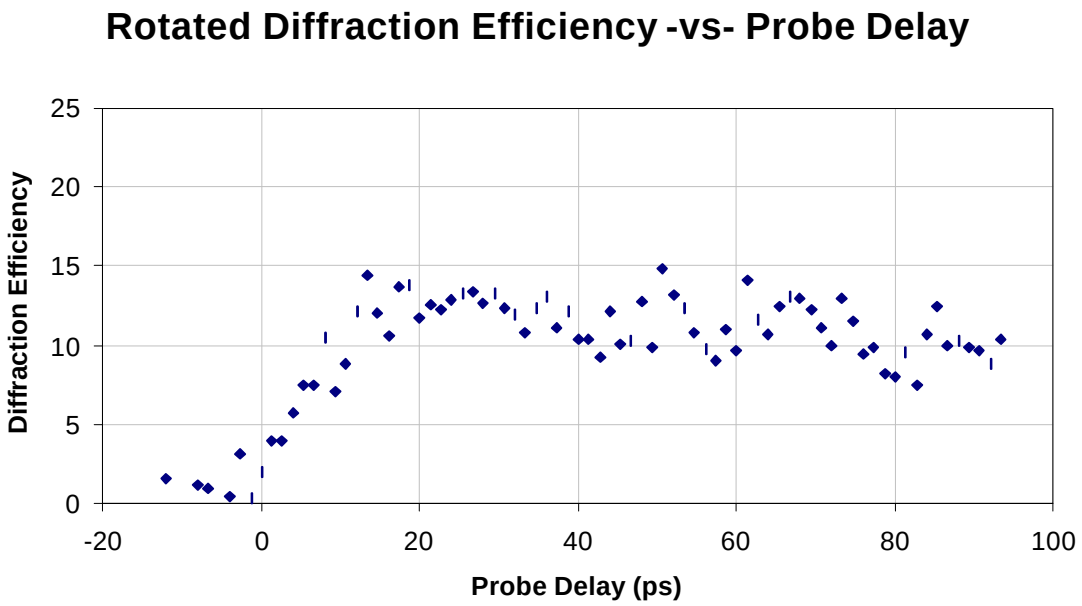

Figure8.7 – Rotated diffraction efficiency versus probe delay for a fluence of 0.047mJ/cm^2, and a grating spacing of 3.8μm. We estimate an observed rise time of 4-8ps for the photorefractive nonlinearity that is comparable to the duration of our probe pulses.

8.3.4 Fluence Dependencies of the Decaying and Long-Lived Diffraction Efficiencies

Having thoroughly discussed the temporal dynamics of the decaying and long-lived diffraction efficiencies, we now consider the fluence dependence of these features. Here we show that the fluence dependencies of the decaying and long-lived features are consistent with diffraction from photorefractive gratings.

As in previous discussions of this type, we begin by considering the expected fluence dependence of the decaying and long-lived diffraction efficiencies. We have already seen in section 8.2.2 that the presence of linear absorption, instantaneous two-photon absorption, and EL2 absorption saturation complicates the fluence dependence of the photogenerated free-carrier density in semi-insulating GaAs. As a result, the Dember and electron-ionized EL2 photorefractive nonlinearities might be expected to have

complicated fluence dependencies. However, as we noted in Chapter III, the drift limited space-charge field magnitude increases sub-linearly with carrier density at carrier densities near to the transition point between the diffusion and drift limits, and then is independent of carrier density at high carrier densities. Since our experiments are performed near to or above the transition point (the critical carrier density), we therefore expect the fluence dependence of the Dember and electron-ionized EL2 photorefractive nonlinearities to take relatively simple forms. While we expect both diffraction efficiencies to be fluence independent at high fluences, we expect both diffraction efficiencies to increase at a rate that is less than F^2 at low fluences. This latter dependence follows from the fact that, at low fluences, the dominant carrier generation mechanism is single-photon absorption at the EL2 sites.

The fluence dependence of the decaying and long-lived diffraction efficiencies are shown in figure 8.8. Also shown in figure 8.8 is a reference line depicting a fluence-squared (F^2) dependence. In the figure, the data taken at a constant probe delay of 130ps highlight the long-lived diffraction efficiency. The data taken at a constant probe delay of 20ps do not consider the transient feature, but take into account both the decaying and long-lived features. Especially at higher fluences, we expect this diffraction efficiency to be due mainly to the Dember photorefractive nonlinearity. As can be seen from the figure, at low fluences both diffraction efficiencies increase at a rate that is less than F^2, which is the behavior that is expected for diffraction from drift-limited photorefractive gratings. As the fluence is increased, we see the decaying diffraction efficiency slowly increase in the fluence range between 0.1mJ/cm^2 and 2.2mJ/cm^2. This behavior, which is slightly

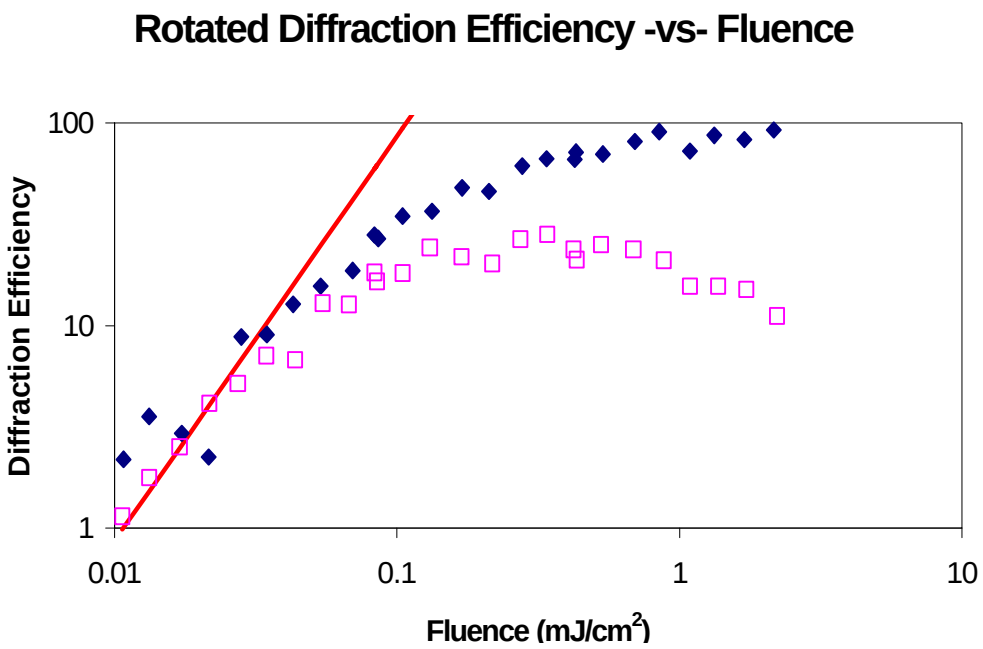

Figure8.8 – Diffraction efficiency versus fluence for the decaying and long-lived diffraction efficiencies. The components exhibit fluence dependencies that are expected for drift-limited photorefractive gratings.

different than that which is expected, can be attributed to hot carrier effects. Over the same fluence range, we see the long-lived diffraction efficiency reach a constant value and then decrease. We can understand this behavior by considering the long-lived electron-ionized EL2 field magnitude in the presence of EL2 saturation. Using the balance between the electron drift and diffusion current densities to determine the field magnitude, and considering up to the n=2 component of the electron density, we find a field magnitude of:

$$E_{sc1} \approx \frac{2\pi k_B T}{\lambda_g e}\frac{n_1}{n_0}\left(1-\frac{n_2}{n_0}\right), \qquad (8.2)$$

which reduces to E_D (equation 3.6) when a small modulation ratio is considered ($n_2 \to 0$). Thus, the presence of the n=2 excess electron density results in a smaller n=1 charge

separation and space-charge field. The high fluence decrease in the long-lived diffraction efficiency can be understood by noting that the n=2 component of the long-lived carrier density, which arises as a result of EL2 absorption saturation, is prevalent at high fluences. Thus, the decaying and long-lived diffraction efficiencies exhibit the fluence dependencies expected for drift-limited photorefractive gratings.

8.4 Modeling

In this section we discuss the modeling of our semi-insulating GaAs experimental results. We model our semi-insulating GaAs results in the way discussed in Chapter VI, using the small signal diffraction efficiency and the beam propagation equation. The parameters used in our model are summarized in table 8.1. See Chapters II and III for a description of these parameters.

Parameter	Value	Reference
ε_r	12.9	K. S. Champlin et al., 1967
n_b	3.47	D. T. F. Marple, 1964
μ_e	5000 (cm^2/V-s)	M. B. Klein, 1984
μ_h	265 (cm^2/V-s)	This work
σ_e	1.7×10^{-16} (cm^2)	This work
σ_h	1.3×10^{-16} (cm^2)	This work
β	19 (cm/GW)	M. D. Dvorak et al., 1994
N-N^+	1.2×10^{16}(cm^{-3})	M. B. Klein, 1984
N^+	1.4×10^{15} (cm^{-3})	M. B. Klein, 1984

Table 8.1 – Parameters used in modeling our semi-insulating GaAs experimental results.

Figures 8.9a and b show the decay of the free-carrier grating at grating periods of 1.7μm and 3.8μm. Also shown in the figure are fits to the data that are generated using

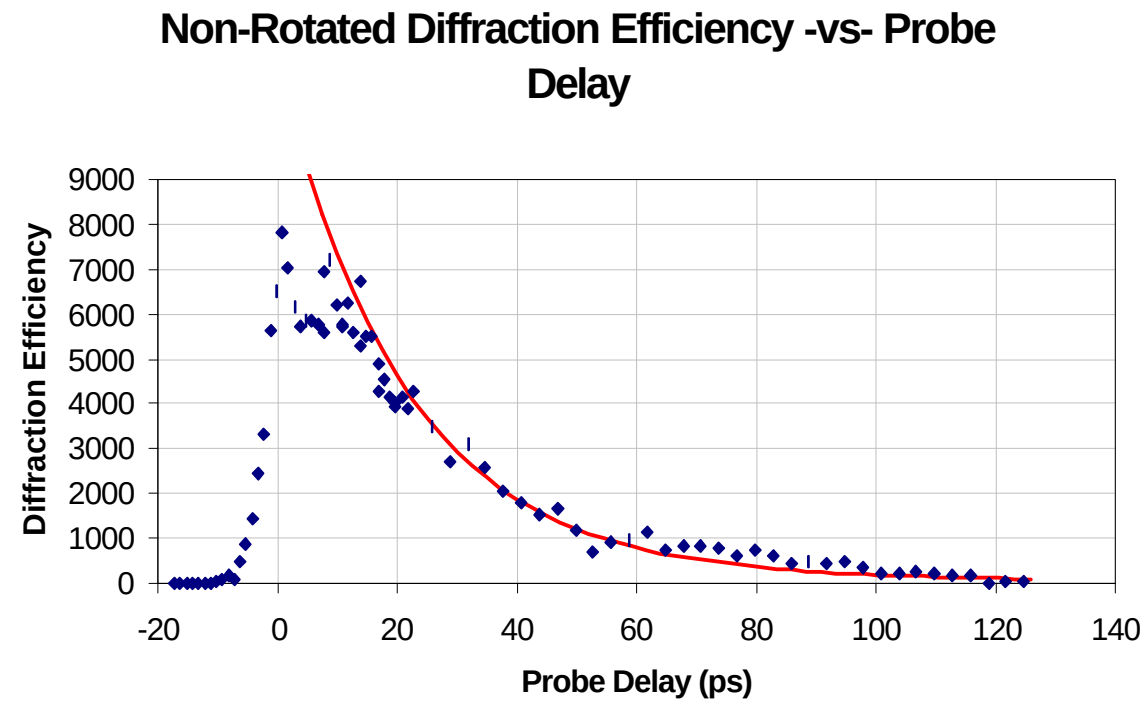

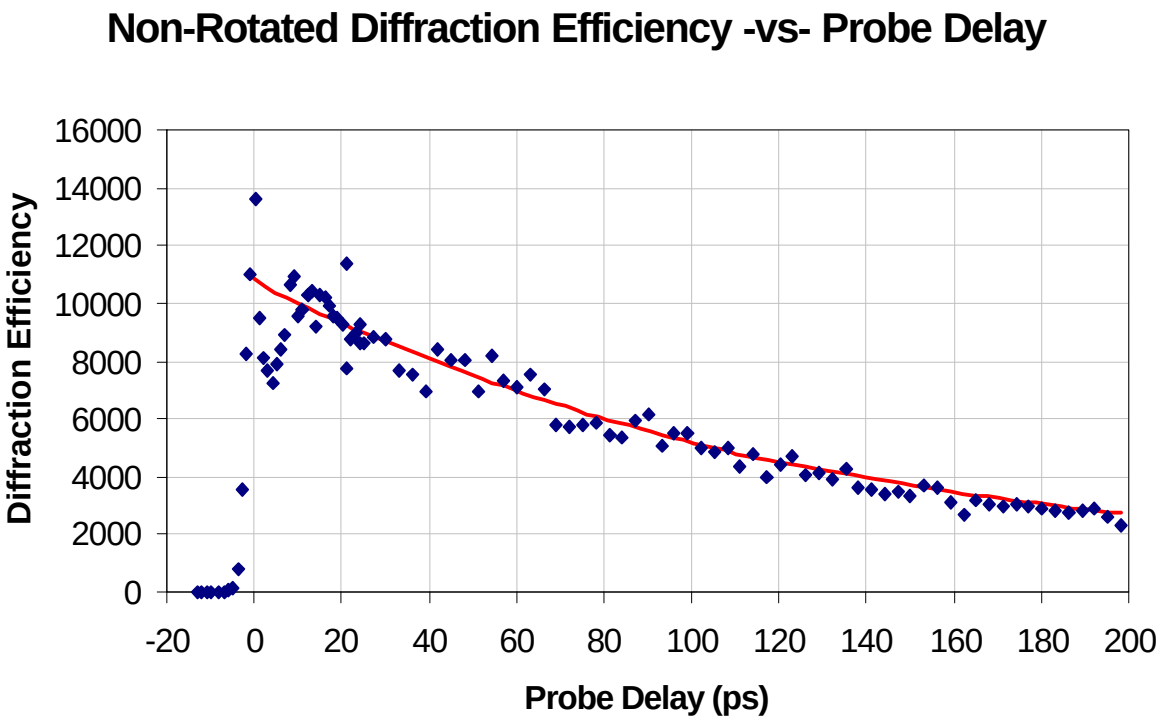

Figure 8.9a and b – Numerical modeling of our non-rotated diffraction efficiency versus probe delay results. At both grating periods, the predictions fit the data well.

the equations derived in Chapter III. In generating these predictions, we have used the measured value for the hole mobility, squared the output from these equations, and then fit the result to the magnitude of the diffraction efficiency. As in CdTe, though we show the results from our model in the high modulation limit, in both limits the model describes the same result: exponential decay of the free carrier populations via ambipolar diffusion, with the time constant given by the ambipolar diffusion time for the grating period. As can be seen from the plots, our model fit the data very well, indicating that our model accurately accounts for the dynamics of the n=1 modulated free carrier population.

The dynamics of the photorefractive diffraction efficiency are shown in figure 8.10a and b for a grating period of 3.8μm, along with fits from our model in the high modulation limit. In the case of figure 8.10b, we have simply re-plotted the data of figure 8.7 with the prediction from our model in the high modulation limit. In generating these fits, we have followed a slightly different procedure than in the CdTe results. Whereas we previously determined the time-dependent space-charge field magnitude from the average carrier density, in these results we use the beam propagation equation to divide the crystal into slices over which the beam intensity decreases by 20%. For each crystal slice we determine the average carrier density, and from each set of carrier densities, a time dependent space-charge field. We square the field magnitude for each slice and then weight this using the square of the thickness of the crystal slice. The sum of these weighted field magnitudes is then fit to the experimental results. As we discussed in Chapter VI, this procedure is followed because the carrier dynamics can vary significantly over the length of our semi-insulating GaAs

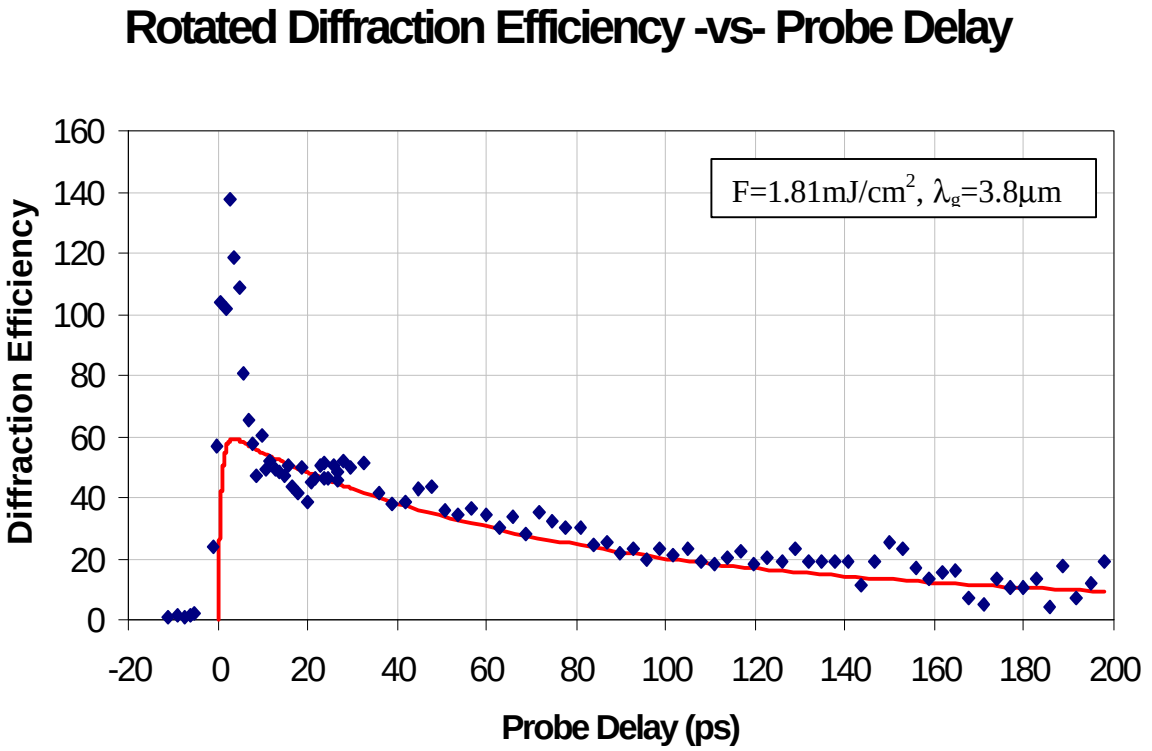

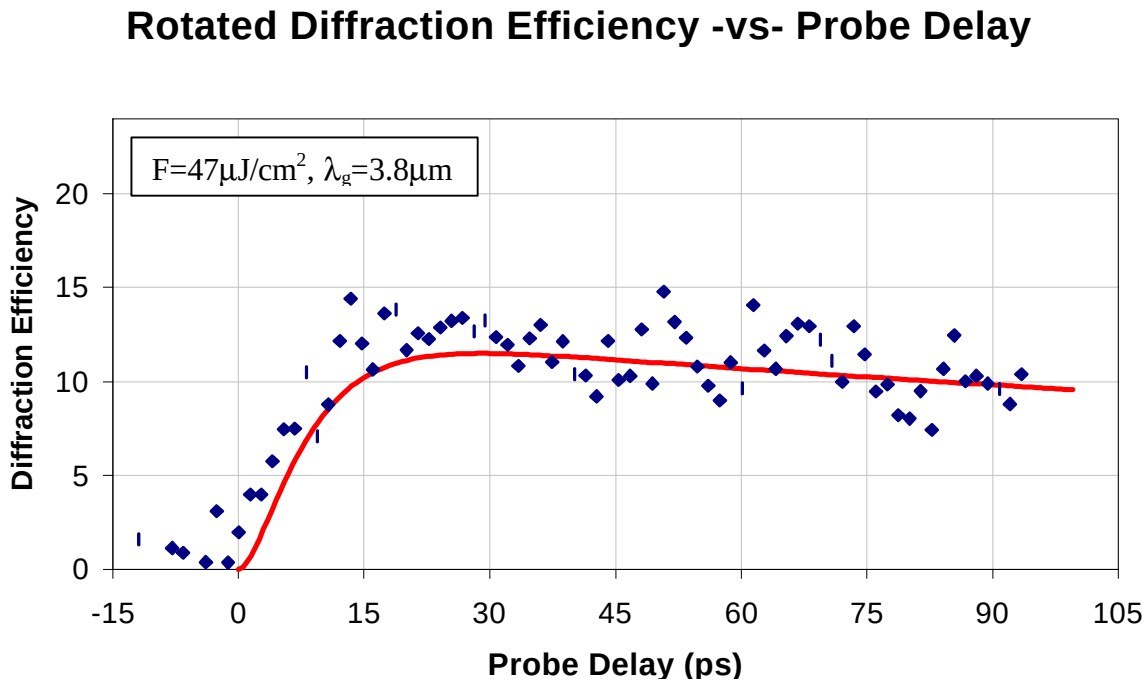

Figure8.10a and b – Comparison of the predictions of our model (solid lines) with our rotated diffraction efficiency results for a range of fluences and a grating period of 3.8μm. See the text for description.

crystal for our experimental conditions.

As in the CdTe results, there is disagreement between our model and the experimental results for probe delays less than about 10ps. This disagreement is not surprising, since we have shown that the transient feature in our data arises from hot carrier effects, and our model considers only free carriers at the lattice temperature. At probe delays greater than 10ps, we see good agreement between our model and the experimental results. The decay constant of 113ps that is associated with the decaying feature in figure 8.10a is shorter than the 137ps decay constant that is observed for the free-carrier grating and similar experimental conditions (see figure 8.9b). This behavior, which arises because higher-order carrier harmonics contribute to the decay of the n=1 space-charge field, is expected. For an explanation of this effect, see the discussion in section 6.4. In figure 8.10b, we see the diffraction efficiency arise more quickly than the prediction of our model. This can be understood by noting that the diffraction efficiency follows the convolution of the probe pulses with the rise of the photorefractive grating. Since we have already shown that the rise time of the photorefractive grating is comparable to the duration of the probe pulses, we expect the diffraction efficiency to rise more quickly than our prediction of the space-charge field.

Results for the rotated diffraction efficiency and the 1.7μm grating period are shown in figures 8.11a-d. While the predictions of our model are fit to the experimental results at delays of roughly 20ps in figures 8.11a and b, they are fit to the maximum diffraction efficiency in figures 8.11c and d. In the latter two figures, this follows from the fact that at the lowest fluences, the photogenerated carrier densities are relatively small

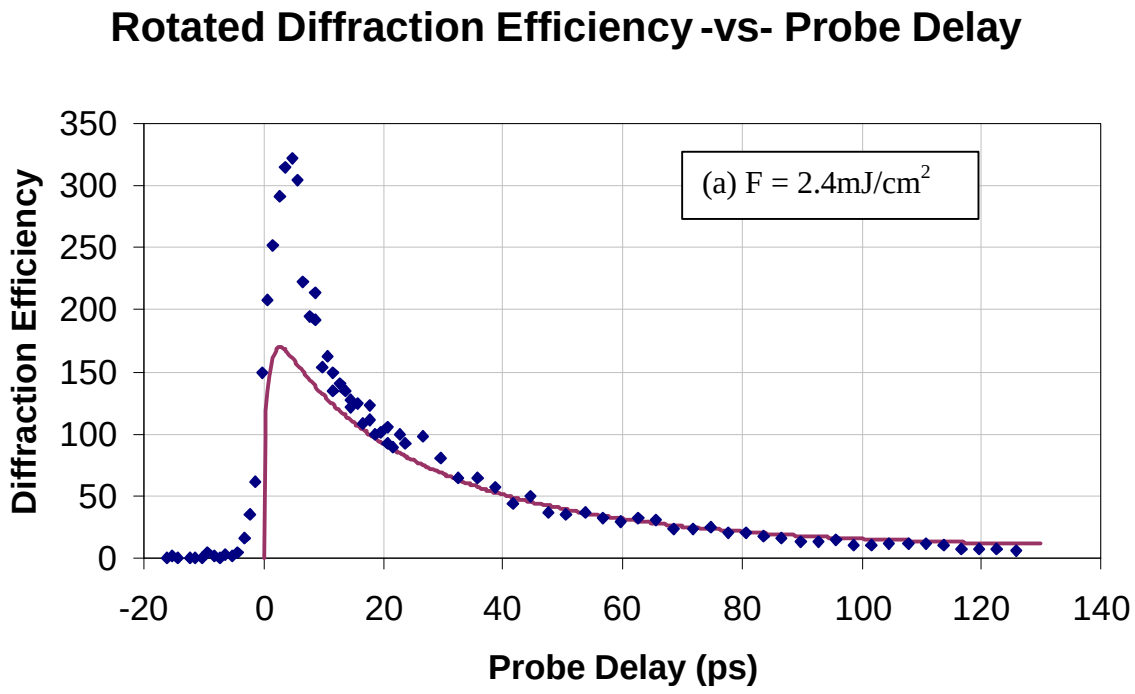
Rotated Diffraction Efficiency -vs- Probe Delay
(a) F = 2.4mJ/cm2
Diffraction Efficiency
Probe Delay (ps)
350
300
250
200
150
100
50
0
-20
0
20
40
60
80
100
120
140

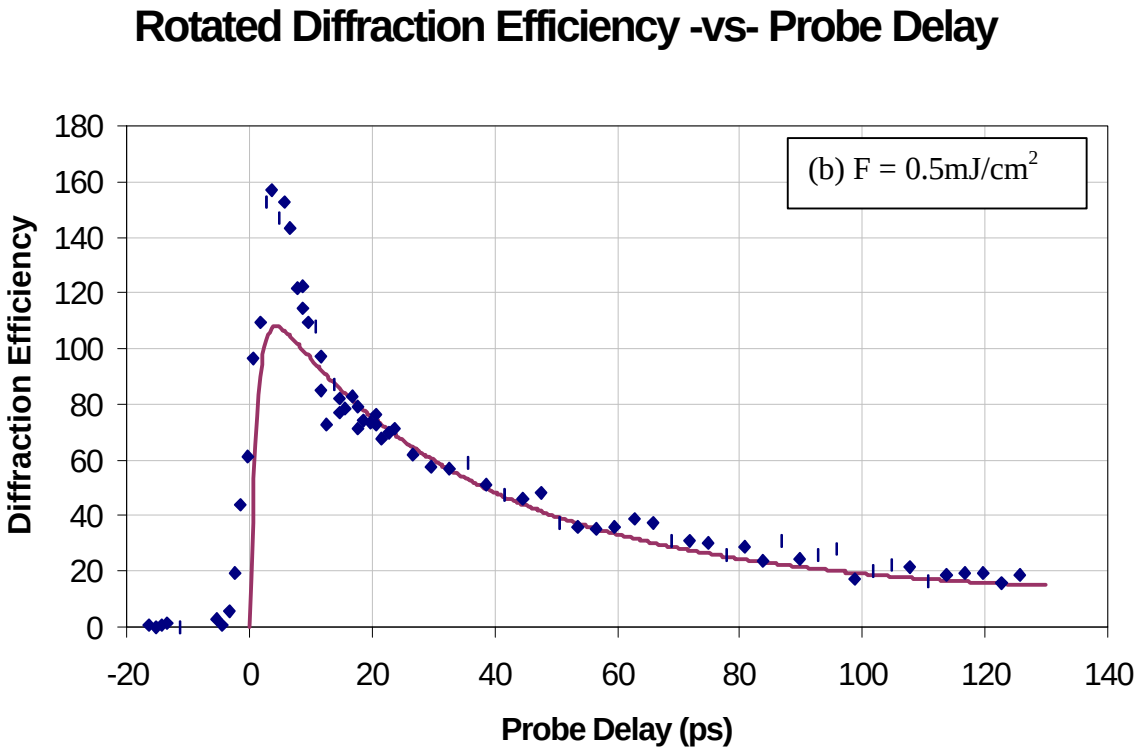
Rotated Diffraction Efficiency -vs- Probe Delay
(b) F = 0.5mJ/cm2
Diffraction Efficiency
Probe Delay (ps)
180
160
140
120
100
80
60
40
20
0
-20
0
20
40
60
80
100
120
140

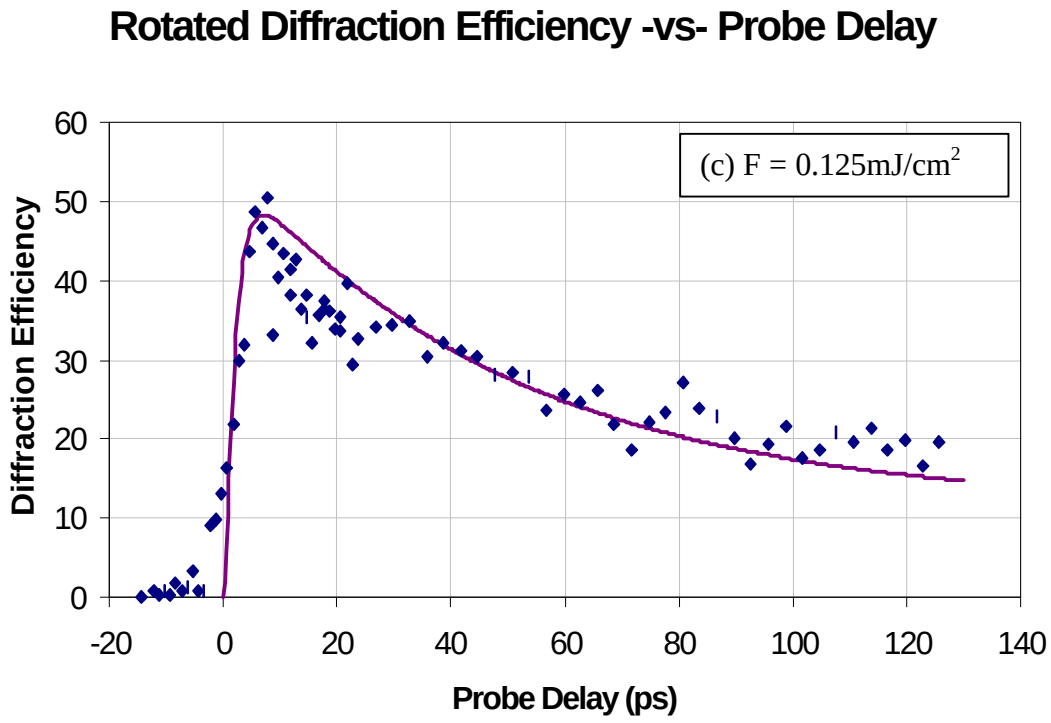

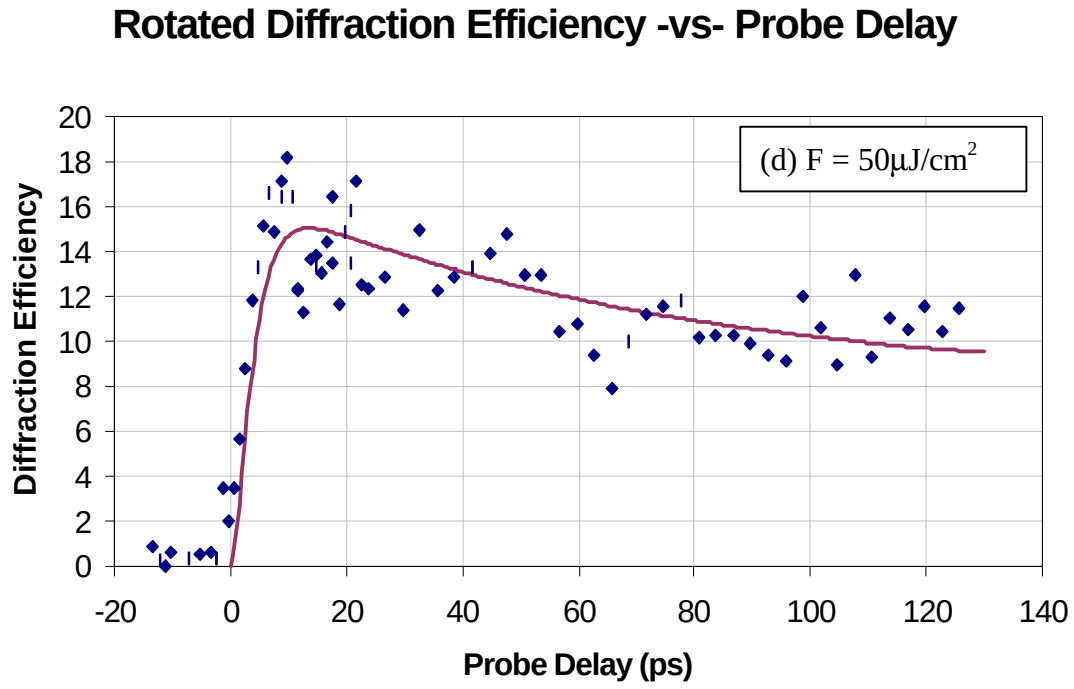

Figures 8.11a-d – Comparison of the predictions of our model (solid lines) with our rotated diffraction efficiency results for a range of fluences and a grating period of 1.7µm. See the text for description.

and are created with an excess energy of only ~0.5eV. As a result, the carrier cooling time is equal to or less than the field formation time, so that we do not observe a significant enhancement to the diffraction efficiency due to hot carrier effects. As can be seen from the figures, the overall agreement between the experimental results and the predictions of our model are good. Thus, we conclude that for a wide range of experimental conditions, our numerical model accurately predicts the dynamics of the carrier densities and space-charge fields, as well as the relative magnitudes of the Dember and excess-electron-ionized EL2 photorefractive nonlinearities.

8.5 Summary

The experimental results that are presented in this chapter provide a unique picture of the picosecond dynamics of the carrier densities and space-charge fields that generated in semi-insulating GaAs as a result of excitation with our 960nm optical pulses. Our results for the non-rotated component of the diffraction efficiency illustrate two separate free-carrier nonlinearities whose temporal and fluence dependencies are consistent with the light absorption and carrier generation properties of our crystal. We observe a decaying free-carrier nonlinearity that arises from the electron and hole populations generated by instantaneous two-photon absorption and EL2 absorption, as well as a long-lived free carrier nonlinearity that arises from the excess electron population that is generated as a result of single-photon absorption at the EL2 sites.

By exhibiting the expected temporal, fluence, and crystal-orientation dependencies, our results for the rotated component of the diffraction efficiency provide the most

complete and unambiguous illustration of the picosecond photorefractive response of semi-insulating GaAs to date. Our results illustrate two separate components of the photorefractive response that are consistent with the free-carrier results, and the light absorption and carrier generation properties of our crystal. The first of these, a decaying diffraction efficiency that is shown to arise from a Dember photorefractive nonlinearity, is unique to picosecond photorefractive experiments. The second component, a long-lived diffraction efficiency, is shown to arise from a photorefractive nonlinearity that arises from the space-charge field that is generated between the excess photogenerated electrons, and the ionized EL2. As we noted in this chapter, carrier recombination transforms this photorefractive nonlinearity into the photorefractive nonlinearity that is observed in experiments with CW laser beams. Though not considered in detail, our results also show a third, transient component that is consistent with a photorefractive nonlinearity that is produced by hot carrier effects. The magnitude, rise and decay of this component were considered in greater detail in Chapter VII.

Our numerical model, which is applied to both the non-rotated and rotated components of the diffraction efficiency, produces predictions that are in good agreement with our experimental results over a wide range of conditions. More specifically, using constants that have been measured for our crystal, our model accurately predicts the dynamics of the free carrier populations and space-charge fields, as well as the relative magnitudes of the Dember and excess electron-ionized EL2 photorefractive nonlinearities, for a range of fluences and grating periods.

Unfortunately, while our results provide a detailed picture of the picosecond

photorefractive response of semi-insulating GaAs, they fail to illustrate the fundamental formation of this nonlinearity. At best, we only partially-resolve the drift-limited rise of the photorefractive nonlinearity at the lowest fluences, and at the longest grating period.

CHAPTER IX

DISSERTATION SUMMARY

9.1. Purpose

The results presented in this dissertation constitute an important step forward in the field of photorefractive nonlinear optics. In this, the final chapter of this dissertation, we summarize these results and place them into context with the body of scientific research in this area. We conclude with possible directions for future research.

9.2 Subject Area Review and Research Summary

The photorefractive effect has been studied extensively in a wide variety of materials, and for a wide variety of applications, over the past thirty years. A very large fraction of these studies have been conducted with CW and nanosecond-pulsed laser beams, where the photorefractive nonlinearity arises from a space-charge field that results from the steady-state balance between the photogeneration, transport, and recombination processes that occur in the material during illumination. In performing studies of this type, many researchers have reported “rise times” for the photorefractive nonlinearity. However these “rise times”, which in all cases are the time required for the optically-

induced index change to reach steady-state, cannot be considered the fundamental formation time for this optical nonlinearity.

Some of the most important photorefractive studies that have been conducted have involved semiconducting materials. Semiconductors are an important class of photorefractive materials because their carrier transport properties make them optimum for both speed and sensitivity. Moreover, the use of semiconductors as nonlinear optical materials offers the potential for a variety of new and technologically-fruitful applications, such as the integration of high-speed electronic and optical processing devices on a single semiconductor chip.

Though comparatively few in number, photorefractive studies conducted with picosecond optical pulses are some of the most relevant. These studies are in direct contrast with those conducted with CW and nanosecond-pulsed laser beams in that the photorefractive nonlinearities arise from free carriers that are generated in times comparable to, or less than, the time required for carrier transport to form the field. For this reason, these studies, which probe the *transient* space-charge fields that are generated in the material, are well suited to provide information about the fundamental processes that produce this optical nonlinearity. While studies of this type are of clear relevance for the fundamental physics that they detail, in the case of semiconductors, where the majority of the picosecond photorefractive studies have been conducted, such information is also relevant to the design of both electronic and optical devices.

Up to the date of this research, the picosecond photorefractive experiments that have been conducted have shared the same shortcoming that was described above for the

CW/nanosecond photorefractive experiments: they have not provided a direct picture of the fundamental processes that produce the photorefractive nonlinearity. For this reason, in this dissertation, we have sought to time-resolve the picosecond dynamics of the photorefractive nonlinearities that are produced in two zincblende semiconductors, semi-insulating GaAs and undoped CdTe. While semi-insulating GaAs has been chosen because it is an important photorefractive material in its own right, it has been used in high speed electronic applications, and offers a lattice match to near infra-red diode laser and LED materials. Furthermore, since semi-insulating GaAs has been well characterized though a wealth of studies, our experimental results can be compared with theory that is based on material parameters that are readily available in the literature. Similarly, while CdTe has been chosen because it is a highly-touted photorefractive material, it also offers a lattice-match to the important infra-red detection material, $Hg_xCd_{1-x}Te$. In addition, since undoped CdTe has no optically-active midgap species or traps, use of this material allows direct study of the Dember space-charge field and photorefractive nonlinearity.

In order to measure the picosecond photorefractive nonlinearities that are produced in zincblende semiconductors, we have had to overcome some important experimental challenges. As we showed in Chapters II and III, while the overall magnitude of the picosecond photorefractive effects that are produced in these materials are small, they coexist with other absorptive and refractive optical nonlinearities that are of comparable or larger magnitude. In Chapter IV we reviewed what has been, prior to the research described in this dissertation, the most widely used method for measuring

picosecond photorefractive effects in semiconductors. Called the two-beam coupling measurement method, this measurement technique allows the picosecond photorefractive nonlinearities to be separated from the other competing nonlinearities that are generated in these materials. However, one important shortcoming of the two-beam coupling measurement technique is that it requires the photorefractive nonlinearities to be generated and probed with the same optical pulses. As a result, the experimental data that are produced do not provide a direct, unambiguous picture of the evolution of the photorefractive nonlinearity at arbitrary times in its formation and decay. This shortcoming led us to seek a new transient-grating measurement technique where the photorefractive nonlinearities are written and probed independently.

Our measurements were made with a novel transient-grating measurement technique that was presented in Chapter V, called the Photorefractive Polarization-Rotation Transient-Grating (PPRTG) measurement technique. The PPRTG measurement technique utilizes a forward-probing geometry to allow 3-5ps temporal resolution over millimeter crystal interaction lengths, photorefractive polarization rotation to allow the photorefractive nonlinearities to be separated from the other competing nonlinearities, and a probe beam of a second color for increased sensitivity.

Our experimental results for undoped CdTe, which were presented in Chapter VII, detailed the Dember space-charge field, which is unique to picosecond photorefractive experiments. These results, which detail the crystal-orientation, temporal, and fluence dependencies of the photorefractive diffraction efficiency, provide the most comprehensive and unambiguous evidence of the Dember photorefractive

nonlinearity given to date. We emphasize that our results for this photorefractive nonlinearity supersede the results of recent photorefractive studies (A. L. Smirl et al., 1988, G. C. Valley, 1989, M. S. Petrovic et al., 1991, W. A. Schroeder et al., 1991), where the Dember photorefractive response has been assumed in order to account for the magnitude of the nonlinear coupling between beams. Our photorefractive results were presented with similar results that detail the evolution of the photogenerated free carrier populations. In providing a simultaneous picture of the evolving free-carrier populations as well as the evolving space-charge field (that forces the carrier populations to evolve together), our experimental results provide an extensive picture of carrier transport on picosecond time scales.

Our results for semi-insulating GaAs provide a clear and detailed picture of the picosecond photorefractive response of this material, which is the most comprehensive given to date. As in undoped CdTe, our results exhibit a large Dember photorefractive nonlinearity. However, in addition, we observe a long-lived photorefractive nonlinearity that arises as a result of the EL2 midgap species and the excess photogenerated electrons. The excess electron population is destroyed through carrier recombination, and this produces the space-charge field and photorefractive nonlinearity that are observed with CW and nanosecond-pulses laser beams. On the whole, our semi-insulating GaAs results provide a rich picture of the picosecond carrier transport processes that take place in this material.

In both undoped CdTe and semi-insulating GaAs, we observed an ultrafast enhancement to the photorefractive response that is consistent with space-charge field

formation via hot carrier transport. This result, which is clearly unique to picosecond photorefractive experiments, marks the first direct observation of hot carrier photorefraction. Though we have not given a detailed discussion of hot carrier photorefraction, we have given qualitative arguments to show that hot carrier effects are expected for our experimental conditions, and that the formation time, magnitude and decay time associated with this diffraction efficiency are consistent with expectations. In undoped CdTe, where the hot carrier enhancement to the space-charge field is the largest, we observe an order-of-magnitude increase in the photorefractive diffraction efficiency.

In both undoped CdTe and semi-insulating GaAs, we fail to time-resolve the rise of the photorefractive nonlinearities. This is due to the presence of hot carrier effects, which cause the field to form more quickly than the measurement limits of the PPRTG technique. The minimum resolvable time for our technique is 3ps-5ps, and photorefractive nonlinearities are measurable with our technique that are generated at carrier densities where the field formation time is less than this limit.

We have coupled our experimental work with the development of a numerical model that predicts the diffraction efficiencies that we observe with our PPRTG measurement technique (described in Chapters III and VI). While our work is based on a model that was previously formulated to describe picosecond photorefractive beam coupling experiments, it is novel in that it describes the diffraction efficiency associated with the photorefractive nonlinearity, and that it considers the picosecond carrier and field dynamics that result when the induced gratings are generated with a large (unity) optical intensity modulation. We have shown that the following consideration is

important in that it requires the carrier populations and space-charge field to be represented by Fourier series truncated after the n=5 component. This is in contrast to other models in which the same Fourier series are truncated after the n=1 or n=2 components. We find excellent agreement between the predictions of our model and our experimental results, for both materials and a wide variety of experimental conditions. Moreover, in comparing the results of our model with our experimental results, we see some unique features that are characteristic of the photorefractive nonlinearity. Most notably, in the decay of the Dember photorefractive nonlinearities, we observe the interplay between the fundamental Fourier component of the space-charge field, and the higher order components of the carrier densities and space-charge field.

9.3 Directions For Future Research

As with all investigations of this type, many unanswered questions remain. In this section, we discuss some future research that could address these questions.

As we noted in the previous section and in Chapters VII and VIII, we failed to time-resolve the rise of the photorefractive nonlinearities in GaAs and CdTe in this study. In order to be able to time resolve the formation of these nonlinearities, there are at least two changes that must be made to our laser system and experimental technique. The simplest way to change our experimental technique for these purposes is to incorporate more sensitive detection equipment. With this change, we could measure the rise of the photorefractive nonlinearities in the diffusion limit of carrier dynamics. Since the rise and decay of the photorefractive nonlinearities are dependent on the electron and hole mobilities in this limit, measurements of this type have the potential for yielding

fundamental information about the electron-hole transport properties of the material. For materials such as undoped CdTe, where the photorefractive response is due only to the Dember space-charge field (decays on nanosecond time scales), greater detection sensitivity can be gained by using phase sensitive detection methods (lock-in amplifiers) and higher repetition rate laser systems. However, for semi-insulating GaAs, where the presence of the long-lived photorefractive nonlinearity forces us to operate at low repetition rates, other detection methods must be sought.

We can change our measurement technique to attain greater temporal accuracy by reducing the duration of the probe pulses. This can be done by generating the probe pulses from a second laser, or by shortening the duration of the 960nm pump pulses. Unfortunately, both of these alternatives result in additional experimental complexity, especially since we need probe pulses shorter than ~100fs duration to resolve the rise of the photorefractive nonlinearity at the middle and high excitation fluences used in our experiments.

As we have noted, the photorefractive effect can easily be used for a variety of spectroscopic applications. Towards this end, with the existing measurement technique, or with the changes described above, there are numerous studies that could be performed. For example, our laser system and measurement technique could be used to study the photorefractive properties of semiconducting materials such as GaN. This material has been targeted for use in the manufacture of blue-green laser diodes and LEDs, and the material's midgap defect structure – which is highlighted by its photorefractive response -

dictates its suitability for applications such as these. Other materials that could be studied are II-VI materials such as ZnSe, which are also of interest for LED applications.

Finally, with the datasets that have been generated in our experiments, further modeling and analyses could be done to investigate the properties of each material that are related to hot carrier transport and carrier cooling. This would be especially useful in undoped CdTe, since very little work has been done in this area. To carry out analyses such as these, it is necessary to develop a model similar to that discussed in Chapter III, which describes the formation of the space-charge field due to hot carrier transport. However, since our experiments were conducted with a unity intensity modulation, such a model must necessarily include the effects of heat transport along with those of charge transport. Work has been done to derive equations to describe these effects, and these equations have been numerically solved using methods similar to those used in computational fluid dynamics studies. However, in order to model our results with best computational efficiency, these equations must be “parameterized” in the Fourier series form that is given in Appendix C.

APPENDIX A

POLARIZATION ROTATION IN THE (111) CUT CdTe CRYSTAL

A.1 Purpose

In this appendix, we discuss the polarization rotation properties of the photorefractive grating that follow when the photorefractive gratings are generated in our (111) cut undoped CdTe crystal. In particular, we show that while a the photorefractive grating produces a diffracted beam with a 90° polarization rotation when the space-charge field is oriented along the $(1\bar{1}0)$ axis, no polarization rotation results when the space-charge field is placed along the $(11\bar{2})$ axis.

A.2 Space-Charge Field Parallel to the $(1\bar{1}0)$ Crystallographic Axis

When the space-charge field is generated as in figure A.1, parallel to the $(1\bar{1}0)$ crystallographic axis, it can be written:

$$\overrightarrow{E_{sc}} = \frac{E_{sc}}{\sqrt{2}}(\hat{x} - \hat{y}). \qquad \text{(A.1)}$$

As in Chapter V, we find the new principal axes for the material by diagonalizing the index ellipsoid matrix, which takes the form:

$$\begin{bmatrix} x & y & z \end{bmatrix} \begin{bmatrix} \frac{1}{n_b^2} & 0 & -\frac{r_{41}E_{sc}}{\sqrt{2}} \\ 0 & \frac{1}{n_b^2} & \frac{r_{41}E_{sc}}{\sqrt{2}} \\ -\frac{r_{41}E_{sc}}{\sqrt{2}} & \frac{r_{41}E_{sc}}{\sqrt{2}} & \frac{1}{n_b^2} \end{bmatrix} \begin{bmatrix} x \\ y \\ z \end{bmatrix} = 1, \qquad \text{(A.2)}$$

This procedure produces the following principal axes and index changes:

$$x' = (1,1,0), \qquad \Delta n_{x'} = 0, \qquad \text{(A.3)}$$

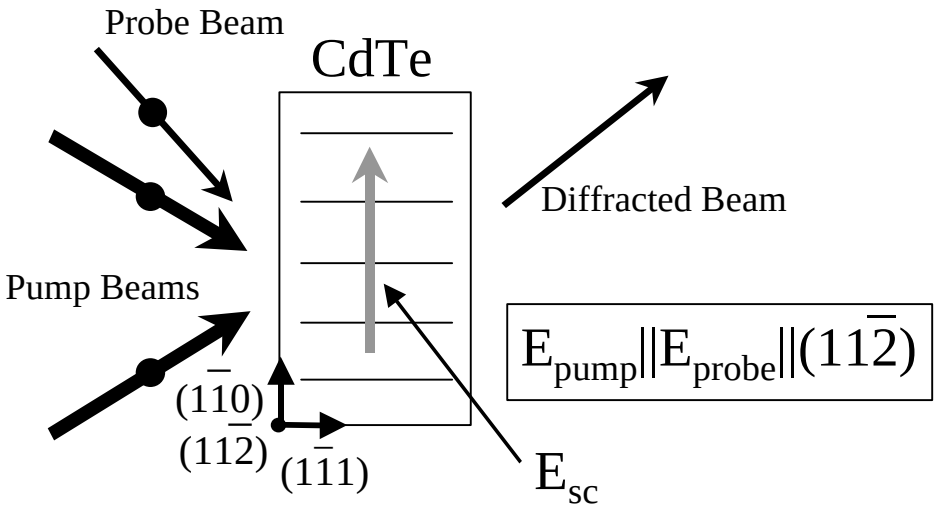

Figure A.1 – Orientation of the optical beams and CdTe crystal used in our experiments. As shown in the text, the photorefractive grating produces a diffracted beam with a polarization rotation of exactly 90° for this arrangement of the crystal and beams.

$$y' = \frac{1}{\sqrt{2}}(1\text{–},1,\sqrt{2}) \qquad \Delta n_{y'} = -\frac{1}{2} n_b^3 r_{41} E_{sc}, \qquad \text{(A.4)}$$

and

$$z' = \frac{1}{\sqrt{2}}(-1,1,\sqrt{2}) \qquad \Delta n_{z'} = \frac{1}{2} n_b^3 r_{41} E_{sc}, \qquad \text{(A.5)}$$

To find the orientation of the probe beam with respect to each of these axes, we take the inner product of the probe electric field, which is polarized along the $(11\bar{2})$ direction, with each of the directions defined by equations (A.3) – (A.5). This procedure shows that the probe electric field has a projection along the x' axis, though there is no index change along this direction. It also shows that the probe electric field has equal projections along the *y'* and *z'* axes. Since the projections along these axes are equal, and since the index

changes along these directions are equal but opposite, the photorefractive grating will produce a diffracted beam with a polarization rotation of exactly 90° when the crystal and beam orientation of figure A.1 is used.

A.3 Space-Charge Field Parallel to the $(11\bar{2})$ Crystallographic Axis

Referring again to figure A.1, when we rotate the crystal by 90° about the $(1\bar{1}1)$ crystallographic axis, we find a different result. Under these circumstances, the space-charge field is aligned along the $(11\bar{2})$ axis, so that it takes the form:

$$\overrightarrow{E_{sc}} = \frac{E_{sc}}{\sqrt{6}}\left(\hat{x} + \hat{y} - 2\hat{z}\right). \qquad \text{(A.6)}$$

Under these circumstances, the index ellipsoid matrix takes the form:

$$\begin{bmatrix} x & y & z \end{bmatrix} \begin{bmatrix} \frac{1}{n_b^2} & -\frac{2}{\sqrt{6}} r_{41} E_{sc} & \frac{1}{\sqrt{6}} r_{41} E_{sc} \\ -\frac{2}{\sqrt{6}} r_{41} E_{sc} & \frac{1}{n_b^2} & \frac{1}{\sqrt{6}} r_{41} E_{sc} \\ \frac{1}{\sqrt{6}} r_{41} E_{sc} & \frac{1}{\sqrt{6}} r_{41} E_{sc} & \frac{1}{n_b^2} \end{bmatrix} \begin{bmatrix} x \\ y \\ z \end{bmatrix} = 1, \qquad \text{(A.7)}$$

Diagonalization of this matrix produces the following set of principal axes and index changes:

$$x' = \frac{1}{\sqrt{2}}(-1,1,0), \quad \Delta n_{x'} = -0.408 n_b^3 r_{41} E_{sc} \qquad \text{(A.8)}$$

$$y' = \frac{1}{4.754}(-1.37,-1.37,1), \quad \Delta n_{y'} = 0.558 n_b^3 r_{41} E_{sc} \qquad \text{(A.9)}$$

and

$$z' = \frac{1}{1.274}(0.37,0.37,1), \quad \Delta n_{z'} = -0.15 n_b^3 r_{41} E_{sc} \quad \text{(A.10)}$$

As in the previous analyses, the polarization properties of the diffracted field are determined by finding the projection of the probe electric field along the principal axes defined by equations (A.8) – (A.10). When the space-charge field is oriented along the $(11\bar{2})$ axis, the probe electric field is aligned along the $(1\bar{1}0)$ axis. In taking the inner product between the probe electric field and the principal axes defined above, we find that the probe electric field has no projection along either axis. Thus, for this orientation of the probe electric field and CdTe crystal, the electric field that is diffracted from the photorefractive grating has no polarization rotation. This is the result that is observed experimentally in section 7.3.

APPENDIX B

FORTRAN COMPUTER CODES

B.1 Purpose

In this appendix, we give a source listing for the fortran computer codes used in modeling our experiments. In section B.2, we list "beamprop.for" and "cdte5.for" which were used in modeling our CdTe results. In section B.2, we list "carrgen.for" and "gaas5.for" which were used to model our semi-insulating GaAs results.

B.2 CdTe Computer Codes – "beamprop.for" and "cdte5.for"

Beamprop.for

```
C     Last change:  TS    4 May 99    2:48 pm
C
C     Beam propagation and carrier generation in undoped CdTe for two optical beams of
equal intensity.
C     linear absorption is neglected.
C
C
      program main

      REAL*8 e,bmav
      REAL*8 bm0, bm, length, nav, zprop
      REAL*8 dz, hnu, bet
      REAL*8 zct, nsl, dt
c---------------------------------------------------------------------
c     Declaration of constants.  e is the electronic charge, hnu is the photon energy in eV
c     length is the crystal length in cm.  bet is the two photon absorption coefficienct
(cm/W).
c     bm0 is the incident intensity (both beams combined), dt is the pulse length in seconds.
c     dz is the propagation slice thickness in cm, zct is the number of slices comrising the
crystal.
c     nsl is the electron density generated in a single dz crystal slice.

      e=1.602e-19
      hnu=1.3
      length=1.0e-1
      bet=17e-9
      bm0=2.4e9
      dt=1e-12
```

```
      dz=1.0e-4
      refl=0.695
c-------------------------------------------------------------------------
c     Initialize constants, open the output file
c
      open(unit=56,file='bmp1out.dat')
      zprop=0
      zct=1
      bm=bm0*refl
      nav=0

c-------------------------------------------------------------------------
c     Loop to iterate through the beam propagation equation for the crystal thickness
c     bm is the changing beam intensity, zprop is the total distance traveled. nav is used
c     to determine the average carrier density
c
      do while (zprop.lt.length)
      nsl=((bet*bm*bm*dt)/(2*hnu*e))
      nav=nav+nsl
      zct=zct+1
      bm=bm-(3.0/2.0)*bet*bm*bm*dz
      bmav=bmav+bm
      zprop=zprop+dz
10    format (F11.5, ES21.11E3, ES21.5E3)
      write (56,10) zprop, bm, nsl
      end do
      bmav=bmav/zct
      nav=nav/zct
      WRITE(6, *) bmav, nav
      end program main
```

CdTe5.for

```
C     Electron Transport and Space-charge field formation over an optically-induced
C     grating in undoped CdTe.  The electron and hole densities,
C     and space-charge field are modeled by Fourier series truncated
C     after the n=5 component.  The equations are solved iteratively in the loop
C     below.
C
C
C
      program main
```

```
      REAL*8 eps0,epsrel,e,mu,kbt,kg,dt
      REAL*8 n0,n1,n2,n3,n4, n5, esc1,esc2
      REAL*8 esc3, esc4, esc5, mup, lg
      REAL*8 p1, p2, p3, p4, p5, nt
      INTEGER wiq, wi
c-----------------------------------------------------------------------
c     Declaration of constants.  eps0 and epsrel are the free space and
c     relative permittivities.  e is the electronic charge and mu (e) and (p) are the
c     electron and hole drift mobilities in cm2/V-s.  kbt is Boltzmann's constant
c     times temp=300K.  kg is the grating wave vector, and dt is the time
c     step.
c
      eps0=8.854e-14
      epsrel=10.4
      e=1.602e-19
      mu=1010
      mup=93
      kbt=4.143e-21
      tr=1e-9
      lg=1.7e-4
      kg=(6.28)/lg
      dt=5e-17
c-----------------------------------------------------------------------
c     Initialize the Fourier components of the carrier densities and the
c     space-charge field. Open output file. wiq and wi are counters that control the output.
c
      n0=1e17
      n1=1.33e17
      n2=0.33e17
      n3=0e0
      n4=0e0
      n5=0e0
      p0=n0
      p1=n1
      p2=n2
      p3=0e0
      p4=0e0
      p5=0e0
      esc1=0e0
      esc2=0e0
      esc3=0e0
      esc4=0e0
      esc5=0e0
```

```
      open(unit=56,file='enp172out.dat')
      wiq=10000
      wi=10000
      t=0
      nt=0
10     format (F11.5, ES36.20E3, ES21.5E3)
      write (56,10) nt, esc1, n1
c-----------------------------------------------------------------------
c      Loop to iterate through equations for n1-n5, p1-p5 and esc1-esc5
c
      do while (t.lt.200e-12)
      nt=t/(1.0e-12)
      n0=n0-(n0*dt/tr)
      n1=n1-((mu*kbt*kg*kg*n1*dt)/e)-(n1*dt/tr)
      n1=n1+(mu*kg*dt/2)*(2*n0*esc1+n1*esc2-n2*esc1-n3*esc2+n2*esc3)
      n1=n1+(mu*kg*dt/2)*(n3*esc4-n4*esc3+n4*esc5-n5*esc4)
      n2=n2-((4*mu*kbt*kg*kg*n2*dt)/e)-(n2*dt/tr)
      n2=n2+mu*kg*dt*(2*n0*esc2+n1*esc1-n3*esc1+n1*esc3)
      n2=n2+mu*kg*dt*(n2*esc4-n4*esc2-n5*esc3+n3*esc5)
      n3=n3-((9*mu*kbt*kg*kg*n3*dt)/e)-(n3*dt/tr)
      n3=n3+mu*kg*dt*(3*n0*esc3+(3/2)*n1*esc2+(3/2)*n2*esc1)
      n3=n3+mu*kg*dt*(3/2)*(n1*esc4-n4*esc1+n2*esc5-n5*esc2)
      n4=n4-((16*mu*kbt*kg*kg*n4*dt)/e)-(n4*dt/tr)
      n4=n4+2*mu*kg*dt*(2*n0*esc4+n1*esc3+n2*esc2+n3*esc1)
      n4=n4+2*mu*kg*dt*(n1*esc5-n5*esc1)
      n5=n5-((25*mu*kbt*kg*kg*n5*dt)/e)-(n5*dt/tr)
      n5=n5+(5/2)*mu*kg*dt*(2*n0*esc5+n2*esc3+n3*esc2+n1*esc4+n4*esc1)
c-----------------------------------------------------------------------
      p0=p0-(p0*dt/tr)
      p1=p1-((mup*kbt*kg*kg*p1*dt)/e)-(p1*dt/tr)
      p1=p1-(mup*kg*dt/2)*(2*p0*esc1+p1*esc2-p2*esc1-p3*esc2+p2*esc3)
      p1=p1-(mup*kg*dt/2)*(p3*esc4-p4*esc3+p4*esc5-p5*esc4)
      p2=p2-((4*mup*kbt*kg*kg*p2*dt)/e)-(p2*dt/tr)
      p2=p2-(mup*kg*dt)*(2*p0*esc2+p1*esc3+p2*esc4-p3*esc1)
      p2=p2-(mup*kg*dt)*(p3*esc5-p4*esc2-p5*esc3+p1*esc1)
      p3=p3-((9*mup*kbt*kg*kg*p3*dt)/e)-(p3*dt/tr)
      p3=p3-mup*kg*dt*(3*p0*esc3+(3/2)*p1*esc2+(3/2)*p1*esc4)
      p3=p3-mup*kg*dt*(3/2)*(p2*esc1+p2*esc5-p4*esc1-p5*esc2)
      p4=p4-((16*mup*kbt*kg*kg*p4*dt)/e)-(p4*dt/tr)
      p4=p4-2*mup*kg*dt*(2*p0*esc4+p1*esc3+p1*esc5+p2*esc2)
      p4=p4-2*mup*kg*dt*(p3*esc1-p5*esc1)
      p5=p5-((25*mup*kbt*kg*kg*p5*dt)/e)-(p5*dt/tr)
      p5=p5-(5/2)*mup*kg*dt*(2*p0*esc5+p1*esc4+p2*esc3+p3*esc2+p4*esc1)
```

```
c-------------------------------------------------------------------------------
      esc1=(e/(eps0*epsrel*kg))*(p1-n1)
      esc2=(e/(2*eps0*epsrel*kg))*(p2-n2)
      esc3=(e/(3*eps0*epsrel*kg))*(p3-n3)
      esc4=(e/(4*eps0*epsrel*kg))*(p4-n4)
      esc5=(e/(5*eps0*epsrel*kg))*(p5-n5)
      if (nt.gt.0) then
      if (wi.eq.wiq) then
      write (56,10) nt, esc1, n1
      WRITE(6,*) nt, esc1
      wi=0
      end if
      wi=wi+1
      end if

      t=t+dt


      end do
      end program main
```

B.3 GaAs Computer Codes – “carrgen.for” and “gaas5.for”

Carrgen.for

```
      C     Beam propagation and carrier generation in semi-insulating GaAs for two
beams of equal intensity
      C     which form a modulated intensity profile.  Code calculates the n=0, 1 and 2
Fourier components
      C     of the carrier and EL2 densities assuming EL2 absorption and two-photon
absorption.  Concurrently,
      C     the optical intensity is depleted according to the beam propagation equation.
      C
      C
      C
            program main

            REAL*8 e,tdc,tac,n0,n1,n2,se,sh,f0,ii0
            REAL*8 hnu,bet,nsat,fsat,tmax,ict2,ict3,zct
            REAL*8 dt,p0,p1,p2,tr0,tr1,tr2,iif,fi,ict1
            REAL*8 alph,dz,fwml,tlng,lct

      c-------------------------------------------------------------------------
```

```
      c     Declaration of constants.  hnu is the photon energy in eV.  bet is the crystal
orientation-
      c     dependent two-photon absorption coefficient.  dt is the pulse duration in
seconds, se and sh
      c     are the electron and hole el2 absorption cross sections in cm2.  refl is the
front surface
      c     reflection coefficient, fi and f0 are the incident fluences before and after
reflection
      c     (at the peak of the modulation).  dz is the crystal slice thickness, the ii
variables are used to
      c     decrement the beam intensity by 20% as the beam propagates through the
crystal, and to determine
      c     representative intensity for the crystal slice.  alph is the constant linear
absorption coefficient
      c     determined from the electron and hole cross sections. fsat is the EL2
saturation fluence, nsat is
      c     the saturation density of ionized el2.
      c
            hnu=1.3e0
            bet=19e-9
            dt=1e-12
            se=1.68e-16
            sh=0.76*se
            refl=0.695
            fi=2.4e-3
            dz=1.0e-4
            f0=fi*refl
            ii0=fi/dt
            iif=0.8e8
            ict1=0.0e0
            ict2=00.0e0
            ict3=ii0
            alph=se*(1.2e16)+sh*(1.4e15)
            fsat=(e*hnu)/(se+sh)
            nsat=(se*1.34e16)/(se+sh)
            tlng=0.317
            lct=0

      c-------------------------------------------------------------------------
      c
            open(unit=56,file='CG2out.dat')

      10    format (F11.5, ES21.5E3, ES21.5E3, ES21.5E3)
```

```
      11    format (F11.5, ES21.5E3, ES21.5E3, ES21.5E3, F11.5)
      c-----------------------------------------------------------------------
      c     Loop to deplete beam and generate carriers.
      c     first decrements the intensity by 20% and determines the representative
intensity
      c     for the slice, then calculates the thickness of the slice in cm.  Following this,
      c     uses the intensity and fluence to calcualte the n=0, 1 and 2 carrier and el2
densities.
      c
            do WHILE (ii0.gt.iif)
            ict1=ict3*0.8
            ict2=(ict3-ict1)/2.0d0
            ii0=ict1+ict2
            zct=0
            do while (ict3.gt.ict1.and.lct.lt.tlng)
            zct=zct+1
            lct=lct+dz
            ict3=ict3-(alph*ict3*dz)-(3.0/2.0)*(bet*ict3*ict3*dz)
            end do
            fwml=dz*zct
            f0=ii0*dt
            tmax=nsat+(1.4e15-nsat)*EXP(-(f0)/fsat)
            tac=(tmax-1.4e15)/2
            tdc=tac+1.4e15
            n0=(se*f0/(hnu*e))*(1.34e16-tdc-tac/2)
            n0=n0+(3.0e0*bet/(4.0e0*hnu*e))*ii0*f0
            p0=(sh*f0/(hnu*e))*(tdc+tac/2.0e0)
            p0=p0+(3.0e0*bet/(4.0e0*hnu*e))*ii0*f0
            tr0=n0+1.4e15-p0
            n1=(se*f0/(hnu*e))*(1.34e16-tdc-tac)
            n1=n1+(bet/(hnu*e))*ii0*f0
            p1=(sh*f0/(hnu*e))*(tdc+tac)
            p1=p1+(bet/(hnu*e))*ii0*f0
            tr1=n1-p1
            n2=(se*f0/(hnu*e))*(-tac/2.0e0)
            n2=n2+(bet/(4.0e0*hnu*e))*ii0*f0
            p2=(sh*f0/(hnu*e))*(tac/2.0e0)
            p2=p2+(bet/(4.0e0*hnu*e))*ii0*f0
            tr2=n2-p2
            WRITE(6,*) n0, n1, n2
            WRITE(6,*) p0, p1, p2
            WRITE(6,*) tr0, tr1, tr2
            write (56,11) f0, n0, n1, n2, fwml
```

```
            write (56,10) f0, p0, p1, p2
            write (56,10) f0, tr0, tr1, tr2
            ict3=ict1
            end do
      end program main
```

GaAs5.for

```
      C     Electron Transport and Space-charge field formation over an optically-
induced
      C     grating in undoped GaAs.  The electron and hole densities,
      C     and space-charge field are modeled by Fourier series truncated
      C     after the n=5 component.  The equations are solved iteratively in the loop
      C     below.
      C
      C
      C
            program main

            REAL*8 eps0,epsrel,e,mu,kbt,kg,dt
            REAL*8 n0,n1,n2,n3,n4, n5, esc1,esc2
            REAL*8 esc3, esc4, esc5, mup, lg
            REAL*8 p1,p2,p3,p4,p5,nt,el0,el1,el2
            REAL*8 wiq, wi
      c-----------------------------------------------------------------------
      c     Declaration of constants.  eps0 and epsrel are the free space and
      c     relative permittivities.  e is the electronic charge and mu (e) and (p) are the
      c     electron and hole drift mobilities in cm2/V-s.  kbt is Boltzmann's constant
      c     times temp=300K.  kg and lg are the grating wave vector and period, and dt
is the time
      c     step. tr is the carrier recombination time.
      c
            eps0=8.854d-14
            epsrel=13.03
            e=1.602d-19
            mu=5000
            mup=265
            kbt=4.143d-21
            tr=2d-9
            lg=1.7d-4
            kg=(6.28)/lg
            dt=5.000d-17
      c-----------------------------------------------------------------------
```

```
c     Initialize the Fourier components of the carrier and EL2 densities and the
c     space-charge field.
c
      n0=1.1017e15
      n1=1.2237e15
      n2=1.2199e14
      n3=0d0
      n4=0d0
      n5=0d0
      p0=4.8264e14
      p1=6.2178e14
      p2=1.3914e14
      p3=0d0
      p4=0d0
      p5=0d0
      el0=n0+1.4e15-p0
      el1=n1-p1
      el2=n2-p2
      esc1=0d0
      esc2=0d0
      esc3=0d0
      esc4=0d0
      esc5=0d0
      open(unit=56,file='eg17m12o.dat')
      wiq=0.5000e4
      wi=0.5000e4
      t=0
      nt=0
10     format (F11.5, ES36.20E3, ES21.5E3)
      write (56,10) nt, esc1, n1
c-----------------------------------------------------------------------
c Loop to iterate through equations for n1-n5, p1-p5 and esc1-esc5
c
      do while (t.lt.130e-12)
      nt=t/(1.0e-12)
      n0=n0-(n0*dt/tr)
      n1=n1-((mu*kbt*kg*kg*n1*dt)/e)-(n1*dt/tr)
      n1=n1+(mu*kg*dt/2)*(2*n0*esc1+n1*esc2-n2*esc1-n3*esc2+n2*esc3)
      n1=n1+(mu*kg*dt/2)*(n3*esc4-n4*esc3+n4*esc5-n5*esc4)
      n2=n2-((4*mu*kbt*kg*kg*n2*dt)/e)-(n2*dt/tr)
      n2=n2+mu*kg*dt*(2*n0*esc2+n1*esc1-n3*esc1+n1*esc3)
      n2=n2+mu*kg*dt*(n2*esc4-n4*esc2-n5*esc3+n3*esc5)
      n3=n3-((9*mu*kbt*kg*kg*n3*dt)/e)-(n3*dt/tr)
```

```
      n3=n3+mu*kg*dt*(3*n0*esc3+(3/2)*n1*esc2+(3/2)*n2*esc1)
      n3=n3+mu*kg*dt*(3/2)*(n1*esc4-n4*esc1+n2*esc5-n5*esc2)
      n4=n4-((16*mu*kbt*kg*kg*n4*dt)/e)-(n4*dt/tr)
      n4=n4+2*mu*kg*dt*(2*n0*esc4+n1*esc3+n2*esc2+n3*esc1)
      n4=n4+2*mu*kg*dt*(n1*esc5-n5*esc1)
      n5=n5-((25*mu*kbt*kg*kg*n5*dt)/e)-(n5*dt/tr)
      n5=n5+(5/2)*mu*kg*dt*(2*n0*esc5+n2*esc3+n3*esc2+n1*esc4+n4*esc1)
c-----------------------------------------------------------------------------
      p0=p0-(p0*dt/tr)
      p1=p1-((mup*kbt*kg*kg*p1*dt)/e)-(p1*dt/tr)
      p1=p1-(mup*kg*dt/2)*(2*p0*esc1+p1*esc2-p2*esc1-p3*esc2+p2*esc3)
      p1=p1-(mup*kg*dt/2)*(p3*esc4-p4*esc3+p4*esc5-p5*esc4)
      p2=p2-((4*mup*kbt*kg*kg*p2*dt)/e)-(p2*dt/tr)
      p2=p2-(mup*kg*dt)*(2*p0*esc2+p1*esc3+p2*esc4-p3*esc1)
      p2=p2-(mup*kg*dt)*(p3*esc5-p4*esc2-p5*esc3+p1*esc1)
      p3=p3-((9*mup*kbt*kg*kg*p3*dt)/e)-(p3*dt/tr)
      p3=p3-mup*kg*dt*(3*p0*esc3+(3/2)*p1*esc2+(3/2)*p1*esc4)
      p3=p3-mup*kg*dt*(3/2)*(p2*esc1+p2*esc5-p4*esc1-p5*esc2)
      p4=p4-((16*mup*kbt*kg*kg*p4*dt)/e)-(p4*dt/tr)
      p4=p4-2*mup*kg*dt*(2*p0*esc4+p1*esc3+p1*esc5+p2*esc2)
      p4=p4-2*mup*kg*dt*(p3*esc1-p5*esc1)
      p5=p5-((25*mup*kbt*kg*kg*p5*dt)/e)-(p5*dt/tr)
      p5=p5-(5/2)*mup*kg*dt*(2*p0*esc5+p1*esc4+p2*esc3+p3*esc2+p4*esc1)
c-----------------------------------------------------------------------------
      esc1=(e/(eps0*epsrel*kg))*(p1+el1-n1)
      esc2=(e/(2*eps0*epsrel*kg))*(p2+el2-n2)
      esc3=(e/(3*eps0*epsrel*kg))*(p3-n3)
      esc4=(e/(4*eps0*epsrel*kg))*(p4-n4)
      esc5=(e/(5*eps0*epsrel*kg))*(p5-n5)
      if (nt.gt.0) then
      if (wi.eq.wiq) then
      write (56,10) nt, esc1, n1
      WRITE(6,*) nt,esc1
      wi=0
      end if
      wi=wi+1
      end if

      t=t+dt


      end do
end program main
```

APPENDIX C

TRANSIENT CARRIER TRANSPORT AND SPACE-CHARGE FIELD EQUATIONS

C.1 Purpose

In Chapter III we discussed carrier transport and space-charge field formation under transient conditions, and in the low and high modulation limits. In our discussions on the low modulation limit, we cited equations that describe these processes. With our starting point the fundamental equations for transient space-charge field formation, in this appendix, we produce the equations cited in Chapter III for the low modulation limit.

C.2 Fundamental Equations – General Method of Solution

Even after recombination is neglected, equations (3.9) – (3.14) are difficult to solve. In general, this is due to the time dependence of the optical intensity (I), and the fact that the equations for the free carrier densities are coupled through the space-charge field (E_{sc}). As a result, it is necessary to make additional simplifying assumptions to solve these equations. In the following paragraphs, we discuss these assumptions and their validity for our experimental conditions.

In order to eliminate equation (3.11), and the carrier generation terms in equations (3.9) and (3.10), we can assume that carrier generation occurs instantaneously compared to field formation. In place of these terms, we assume the presence of t=0 concentrations of ionized EL2, free electrons, and holes ($N^+(0)$, $n(0)$ and $p(0)$). While this assumption simplifies the solution of equations (3.9) – (3.14), it is not completely valid for our experimental conditions. Since photoexcitation with our 1.0ps FWHM optical pulses produces average free electron densities as large as $1x10^{16}$ cm^{-3} in our semi-insulating GaAs crystal, the space-charge field forms in times of ~100fs at the largest excitation

intensities in our experiments. Thus, under these conditions, field formation can occur nearly simultaneously with carrier generation. After assuming that carrier generation occurs instantaneously, equations (3.9) – (3.14) reduce to:

$$\frac{\partial n}{\partial t} = \frac{1}{e}\nabla \cdot j_e \quad , \tag{C.1}$$

$$\frac{\partial p}{\partial t} = -\frac{1}{e}\nabla \cdot j_p \quad , \tag{C.2}$$

$$j_e = \mu_e k_B T \nabla n + e\mu_e E_{sc} n \ , \tag{C.3}$$

$$j_p = -\mu_p k_B T \nabla p + e\mu_p E_{sc} p \quad , \tag{C.4}$$

and

$$\nabla \cdot E_{sc} = \frac{e}{\varepsilon}\left(p + N^+ - n - A^-\right) \ . \tag{C.5}$$

By assuming a solution for the carrier densities and space-charge field, we can further simplify equations (C.1) – (C.5). In assuming a functional form for the carrier densities and space-charge fields, we refer to the arrangement of the crystal and optical beams shown in figure 3.1, which is the basis for our experiments. Since we probe the n=1 Fourier components of the induced optical nonlinearities, it is convenient to express the ionized EL2 density, free carrier densities, and space-charge fields in the general form of a Fourier series in the grating period:

$$n(x,t) = n_0 + \sum_{m=1}^{\infty} n_i(t)\cos\left(m2\pi x / \Lambda_g\right), \tag{C.6}$$

$$p(x,t) = p_0 + \sum_{m=1}^{\infty} p_i(t)\cos\left(m2\pi x / \Lambda_g\right), \tag{C.7}$$

$$N^{+}(x) = \sum_{m=0}^{\infty} N^{+}{}_{i} \cos\left(m2\pi x / \lambda_{g} \right), \qquad \text{(C.8)}$$

and

$$E_{sc}(x,t) = \sum_{m=1}^{\infty} E_{sci}(t) \cos\left(m2\pi x / \lambda_{g} \right), \qquad \text{(C.9)}$$

Here we have assumed that the time dependence of the free carrier densities and space-charge field are contained in the magnitudes of the different Fourier components, with the zero order components independent of time. In addition, since recombination has been neglected the EL2 concentration is independent of time, and since there is no applied electric field, there is no zero order component of the space-charge field.

When equations (C.6) – (C.9) are substituted into equations (C.1) – (C.5), the following problem arises. We find that the equations for the fundamental Fourier components of the carrier densities and space-charge field are coupled to like equations for the higher order components, and the general result is that the set of equations is not analytically soluble. In order to proceed, we assume that the free carrier densities are generated with a small modulation ratio (see equation (3.3), m<<1). Under these conditions, the higher order components of the carrier densities and space-charge fields can be neglected, so that the fundamental Fourier components of the carrier densities and space-charge fields are dependent only on the zero order and fundamental components of these quantities. As a result, equations (C.6) – (C.9) reduce to:

$$n(x,t) = n_0 + n_1(t) \cos\left(2\pi x / \lambda_{g} \right), \qquad \text{(C.10)}$$

$$p(x,t) = p_0 + p_1(t)\cos\left(2\pi x / \Lambda_g\right), \qquad \text{(C.11)}$$

$$N^+(x) = N^{+'} + N_1^+ \cos\left(2\pi x / \Lambda_g\right), \qquad \text{(C.12)}$$

$$E_{sc}(x,t) = E_{sc1}(t)\cos\left(2\pi x / \Lambda_g\right). \qquad \text{(C.13)}$$

Here N^+' is equal to the sum of the dark density of ionized EL2, plus the density generated by photoexcitation (N^+'=N_D^++$N^+(0)$).

C.3 Electrons and Ionized EL2

In considering the ideal case where the space-charge field is formed by electrons and holes, we assume that photoexcitation produces only equal population densities of electrons and ionized EL2. More specifically, we assume that p=0 at all times, and that the density of neutral EL2 is large enough so that photoexcitation produces no saturation of the EL2CB transition. Under these circumstances, we must solve only the following equations:

$$\frac{\partial n}{\partial t} = \frac{1}{e}\nabla \cdot j_e, \qquad \text{(C.1)}$$

$$j_e = \mu_e k_B T \nabla n + e\mu_e E_{sc} n, \qquad \text{(C.3)}$$

and

$$\nabla \cdot E_{sc} = \frac{e}{\varepsilon}\left(N^+ - n - A^-\right), \qquad \text{(C.14)}$$

with the electrons, ionized El2 and space-charge field following the form given by equations (C.10), (C.12) and (C.13).

Generally, the above equations are solved by first eliminating variables to produce a differential equation for the time dependent modulated free carrier density $n_1(t)$. This equation is then solved, and $n_1(t)$ is used in equation (C.14) to determine the time dependent space-charge field ($E_{sc1}(t)$). The differential equation for the modulated carrier density is formed from the differential equation for n(t) (equation (C.1)) using the electron current density (equation (C.3)) and the functional form for $n(x,t)$ (equation (3.24)). The space-charge field is eliminated from the resulting equation by using the functional forms for the electron density (equation (C.10)), the ionized EL2 density (equation (C.12)) and the space-charge field (equation (C.13)) in Gauss' Law (equation (C.14)). The acceptor density (A^-) is eliminated by using the relationship between the dark density of ionized EL2 and the acceptor population ($N_D^+ = A^-$), and the relationship between the total dc population density of ionized EL2 and the dark density of ionized EL2 ($N^+{}' = N_D^+ + N^+(0)$).

The procedure outlined in the previous paragraph yields the following differential equation for $n_1(t)$:

$$\frac{\partial n_1(t)}{\partial t} = -n_1\left[\Gamma_{die} + \Gamma_{Dn}\right] + \Gamma_{die} N_1^+ \ . \qquad \text{(C.15)}$$

Here the constants Γ_{die} and Γ_{Dn} are the inverse of the dielectric relaxation time ($\tau_{die} = \varepsilon / n_0 e \mu_e$) and diffusion time ($\tau_{Dn} = l_g^2 e/(2\pi)^2 \mu_e k_B T$), respectively. While the dielectric relaxation time has been previously described, the diffusion time is the time required for electrons to

diffuse across the grating period. Solution of this equation yields the time dependent carrier density:

$$n_1(t) = n_1(0)\left(\frac{\Gamma_{die} + \Gamma_{Dn} e^{-(\Gamma_{die}+\Gamma_{Dn})t}}{\Gamma_{die} + \Gamma_{Dn}}\right). \qquad \text{(C.16)}$$

This leads to the equation for the transient space-charge field:

$$E_{sctr} = \frac{-imE_D}{1 + E_D / E_q'}\left(1 - e^{-(\Gamma_{die}+\Gamma_{Dn})t}\right), \qquad \text{(C.17)}$$

which is similar to the steady-state space-charge field (equation (3.4)) in form, and that it shows that the space-charge field is 90° out of phase with the incident irradiance pattern.. As in the case of the steady-state space-charge field, E_D is the diffusion field:

$$E_D = \frac{2\pi k_B T}{\Lambda_g e}. \qquad \text{(3.6)}$$

The field E_q' is given by the equation:

$$E_q' = \frac{e\Lambda_g N_1^+}{2\pi\varepsilon}, \qquad \text{(C.18)}$$

and is so named because it is clearly similar to the limiting field, E_q, that was introduced in the discussion of the steady-state space-charge field. In these equations, we have used the relationship between the zero order free electron density, and the fundamental component of the ionized EL2 density ($n_0 = N_1^+/m$). It is these equations that are used in the discussions of section 3.3.2.

C.4 Electrons and Holes

When the field arises from equal populations of electrons and holes, equation (C.5) reduces to:

$$\nabla \cdot E_{sc} = \frac{e}{\varepsilon}(p - n) \quad . \qquad \text{(C.19)}$$

Together, equations (C.1) – (C.4) and (C.19) completely describe the carrier and field dynamics. In solving these equations we proceed as before, by assuming that the Fourier series for the carrier densities can be truncated after the n=1 component (equations (C.10), (C.11)) and field (equation (C.13)). As before, the carrier densities and space-charge field are used in equations (C.1) – (C.4) to produce equations for ¶n_1/¶t *and* ¶p_1/¶t:

$$\frac{\partial n_1}{\partial t} = -\Gamma_{die}(p_1 - n_1) - \Gamma_{Dn} n_1, \qquad \text{(C.20)}$$

and

$$\frac{\partial p_1}{\partial t} = \Gamma_{dip}(p_1 - n_1) - \Gamma_{Dp} p_1. \qquad \text{(C.21)}$$

Here Γ_{dip} and Γ_{Dp} are defined in an analogous way to Γ_{die} and Γ_{Dn}, as the inverse of the hole dielectric relaxation time ($\tau_{dip} = \varepsilon/p_0 e\mu_p$), and the inverse of the hole diffusion time ($\tau_{Dp} = \Lambda_g^2 e/(2\pi)^2 \mu_p k_B T$). In order to de-couple these equations, we differentiate with respect to time, and use the relationship between ¶n_1/¶t and p_1, and ¶p_1/¶t and n_1 (given by equations (3.40) and (3.41) to eliminate variables. The result is two second-order equations for n_1 and p_1:

$$\frac{\partial^2 n_1}{\partial t^2} = -\left(\Gamma_{die} + \Gamma_{Dn} + \Gamma_{dip} + \Gamma_{Dp}\right)\frac{\partial n_1}{\partial t} - \left(\Gamma_{Dn}\Gamma_{Dp} + \Gamma_{dip}\Gamma_{Dn} + \Gamma_{die}\Gamma_{Dp}\right) n_1,$$

and

$$\frac{\partial^2 p_1}{\partial t^2} = -\left(\Gamma_{dip} + \Gamma_{Dp} + \Gamma_{die} + \Gamma_{Dn}\right)\frac{\partial p_1}{\partial t} - \left(\Gamma_{Dn}\Gamma_{Dp} + \Gamma_{dip}\Gamma_{Dn} + \Gamma_{die}\Gamma_{Dp}\right)p_1,$$

which can be recognized as equations for overdamped simple harmonic oscillators. These equations can be solved to yield the general form for the time dependent carrier densities and space-charge field:

$$n_1(t) = n_1(0)\left[e^{-\frac{w_0^2 t}{2g}}\left(1 - \frac{\Gamma_{Dn}}{2g}\right) + \frac{\Gamma_{Dn}}{2g}e^{-(2g - w_0^2/2g)t}\right], \qquad \text{(C.22)}$$

$$p_1(t) = p_1(0)\left[e^{-\frac{w_0^2 t}{2g}}\left(1 - \frac{\Gamma_{Dp}}{2g}\right) + \frac{\Gamma_{Dp}}{2g}e^{-(2g - w_0^2/2g)t}\right], \qquad \text{(C.23)}$$

and

$$E_{sc1} = \frac{e l_g n_1(0)}{2pe}\left[\frac{\Gamma_{Dn} - \Gamma_{Dp}}{2g}\right]\left(e^{-\frac{w_0^2}{2g}} - e^{-\left(2g - w_0^2/2g\right)t}\right). \qquad \text{(C.24)}$$

Here $2g = (G_{die} + G_{dip} + G_{Dn} + G_{Dp})$, and $w_0^2 = G_{die}G_{Dp} + G_{dip}G_{Dn} + G_{Dp}G_{Dn}$. Also, since $g^2 >> w_0^2$, we have made the approximation: $(g^2 - w_0^2)^{1/2} \approx g - w_0^2/2g$. Equations (C.22) – (C.24) are those that are used in the discussion of section 3.3.3.

BIBLIOGRAPHY

Alfano, R., Ed., *The Supercontinuum Laser Source*, Springer-Verlag, New York, NY, 1989.

Amodei, J. J., Appl. Phys. Lett., **18**, pg.22, 1971.

Ashkin, A., Boyd, G. D., Dziedzic, J. M., Smith, R. G., Bollman, A. A., Levenstein, J. J., and Nassau, K., Appl. Phys. Lett., **9**, pg.72, 1966.

Auston, D. H., McAfee, S., Shank, C. V., Ippen, E. P., and Teschke, O., Sol. State Elect., **12**, pg.147, 1978.

Becker, P. C., Fragnito, H. L., Brito-Cruz, C. H., Fork, R. L., Cunningham, J. E., Henry, J. E., and Shank, C. V., Phys. Rev. Lett., **61**, pg.1647, 1988.

Bepko, S. J., Phys. Rev. B, **12**, pg.669, 1975.

Blakemore, J. S., Journ. Appl. Phys., **53**, pg.R123, 1982.

Boggess, T. F., Smirl, A. L., Moss, S. C., Boyd, I. W., Van Stryland, E. W., IEEE Journ. Quant. Elect., **21**, pg.488, 1985.

Bohnert, K., Kalt, H., Smirl. A. L., Norwood, D. P., Boggess, T. F., and D'Haenens, I. J., Phys. Rev. Lett., **60**, pg.37, 1988.

Butcher, P. N. and Cotter, D., *Dynamical Optical Nonlinearities in Semiconductors*, Chapter 8 of *The Elements of Nonlinear Optics*, Cambridge University Press, New York, NY, 1990.

Bylsma, R. B., Bridenbaugh, P. M., Olson, D. H., and Glass, A. M., Appl. Phys. Lett., **51**, pg.889, 1987.

Champlin, K., S., Erlandson, R. J., Glover, G. H., Hauge, P. S., and Lu, T., Appl. Phys. Lett., **11**, pg.348, 1967.

Chen, F. S., La Macchia, J. T. and Fraser, D. B., Appl. Phys. Lett., **13**, pg.223, 1968.

Chen, F. S., Journ. Appl. Phys., **40**, pg.3389, 1969.

Cudney, R. S., Pierce, R. M., Bacher, G. D., and Feinberg, J., Journ. Opt. Soc. Am. B, **8**, pg.1326, 1991.

Cui, A. G., Ph. D. Thesis, Univ. of North Texas, 1992.

DeSalvo, R., Sheik-Bahae, M., Said, A. A., Hagan, D. J., and Van Stryland, E. W., Opt. Lett., **18**, pg.194, 1993.

Ducharme, S., Scott, J. C., Twieg, R. J., and Moerner, W. E., Phys. Rev. Lett., **66**, pg.1846, 1991.

Dvorak, M. D., Schroeder, W. A., Andersen, D. R., Smirl, A. L., and Wherrett, B. S., IEEE Journ. Quant. Elect., **30**, pg.256, 1994.

Eastman, Lester F., Phys. Today, pg.77, Oct. 1986.

Eckhardt, G, IEEE Journ. Quant. Elect., **2**, pg.1, 1966.

Eichler, H. J., Günther, P., and Pohl, D. W., *Laser Induced Dynamic Gratings*, Springer-Verlag, New York, NY, 1986.

Elsaesser, T., Shah, J., Rota, L., and Lugli, P., Phys. Rev. Lett., **66**, pg.1757, 1991.

Feinberg, J., Heiman, D., Tanguay, A. R., and Hellwarth, R. W., Journ. Appl. Phys., **51**, pg.1297, 1980.

Feinberg, J., and Bacher, G. D., Appl. Phys. Lett., **48**, pg.570, 1986.

Flytzanis, C., Phys. Rev. Lett., **23**, pg.1336, 1969.

Flytzanis, C., Phys. Lett., **31A**, pg.273, 1970.

Franz, V. W., Naturoforch, **13a**, pg.94, 1958.

Gires, F., C. R. Acad. Sci. Ser. B, **266**, pg.596, 1968.

Glass, A. M., Von Der Linde, D., and Negran, T. J., Appl. Phys. Lett., **25**, pg.233, 1974.

Glass, A. M., Johnson, A. M., Olson, D. H., Simpson, W. and Ballman, A. A., Appl. Phys. Lett., **44**, pg.948, 1984.

Glass, A. M., and Strait, J., *The Photorefractive Effect in Semiconductors*, Chapter 8 of *Photorefractive Materials and Their Applications* I, Günther, P. and. Huignard, J. P, Eds., Topics in Applied Physics, Vol. 61, Springer-Verlag, New York, NY, 1988.

Günther, P., and Micheron, F., Ferroelectrics, **18**, pg.27, 1978.

Huignard, J. P., Herriau, J. P., Rivet, G. and Günther, P., Opt. Lett., **5**, pg.102, 1980.

Huignard, J. P. and Marrakchi, A., Opt. Lett., **6**, pg.622, 1981.

Ja, Y. H., Appl. Phys. B, **36**, pg.21, 1985.

Jain, R. K., and Klein, M. B., *Degenerate Four-Wave Mixing in Semiconductors*, Chapter 10 of *Optical Phase Conjugation*, Fisher, R. A., Ed., Academic Press, New York, NY, 1983.

Kaminow, I. P., *An Introduction to Electrooptic Devices*, Academic Press, New York, NY, 1974.

Kash, J., Phys. Rev. B, **40**, pg.3455, 1989.

Keldysh, L. V., Sov. Phys. JETP, **7**, pg.788, 1958.

Kittel, C., and Kroemer, H., *Thermal Physics*, W. H. Freeman & Co., New York, NY, 1980.

Klein, M. B., Opt. Lett., **9**, pg.350, 1984.

Klein, P. B., Furneaux, J. E., and Henry, R. L., Phys. Rev. B, **29**, pg.1947, 1984.

Kogelnik, H., Bell Syst. Tech. Journ., **48**, pg.2909, 1969.

Krätzig, E. and Orlowski, R., Appl. Phys., **15**, pg.133, 1978.

Krätzig, E., Welz, F., Orlowski, R., Doorman, V., and Rosenkranz, M., Sol. State Comm., **34**, pg.817, 1980.

Kukhtarev, N. V., Markov, V. B., Odulov, S. G. and Vinetskii, V. L., Ferroelectrics, **22**, pg.940, 1979.

Kurz, H., Krätzig, E., Keune, W., Engelmann E., Gonser, U., Dischler, B., and Räuber, D., Appl. Phys. **12**, pg.355, 1977.

Landolt-Börnstein, *Numerical Data and Functional Relationships in Science and Technology*, New Series, Group III, Vol.17, Semiconductors, *Physics of Group III Elements and III-V Compounds*, Springer-Verlag, New York, NY, 1982.

Landolt-Börnstein, *Numerical Data and Functional Relationships in Science and Technology*, New Series, Group III, Vol.17b, *Physics of II-VI and I-VII Compound Semimagnetic Semiconductors*, Springer-Verlag, New York, NY, 1982.

Lee, H. J., and Look, D. C., Journ. Appl. Phys., **54**, pg.4446, 1982.

Levenson, M. D., and Kano, S. S., *Introduction to Nonlinear Laser Spectroscopy*, Academic Press, New York, NY, 1988.

Li, T., Phys. Today, pg.24, May, 1985.

Liu, D. T. H., and Cheng, L-J., Journ. Opt. Soc. Am. B, **6**, pg.1554, 1989.

Marple, D. T. F., Journ. Appl. Phys., **35**, pg.1241, 1964.

Martin, G. M., and Makram-Ebeid, S., *The Midgap Donor Level EL2 in GaAs*, Chapter IV of *Deep Centers in Semiconductors*, Pantelides, S. T., Ed., Gordon and Breach Scientific Publishers, 1986.

Miller, A., Miller, D. A. B., and Smith, S. D., Adv. Phys., **30**, pr.697, 1981.

Miller. D. A. B., Chemla, D. S., Damen, T. C., Wood, T. H., Burrus, C. A., Gossard, A. C., and Wiegmann, W., IEEE Journ. Quantum Electron. **21**, pg.1462, 1985.

Mircea, A., Mitonneau, A., Martin, G. M., and Pons, D., Appl. Phys., **11**, pg.153, 1976.

Motisuke, P., Arguello, Leite, R. C. C., Sol. State Comm., **16**, pg.763, 1975.

Namba, S., Journ, Opt. Soc. Am., **51**, pg.148, 1961.

Nather, H., and Quagliano, L. G., *Proceedings of the 17th International Conference on Physics of Semiconductors*, pg.1293, Springer, New York, NY, 1985.

Odulov, S. G., Sal'kova, E. N., Sukhoverkhova, L. G., Krolevets, N. S., Pekar, G. S., and Sheinkman, V., Vischashkola Kiev, **9**, pg.87, 1978.

Partovi, A., Kost, A. and Garmire, E., Appl. Phys. Lett., **56**, pg.1089, 1990.

Pauliat, G. and Roosen, G., J. Opt. Soc. Am. B, **7**, pg.2259, 1990.

Petrovic, M. S., Suchocki, A., Powell, R. C., Valley, G. C., and Cantwell, G. J., Journ. Appl. Phys., **66**, pg.1359, 1989.

Petrovic, M. S., Suchocki, A., Powell, R. C., Cantwell, G. J., and Aldridge, J., Phys. Rev. B, **43**, pg.2228, 1991.

Portella, M. T., Bigot, J.-Y., Schoenlein, R. W., Cunningham, J. E., and Shank, C. V., Appl. Phys. Lett., **60**, pg.2123, 1992.

Rajbenbach, H., Deboulbe, A., and Huignard, J. P., Opt. Lett., **14**, pg.1275, 1989.

Rossi, F., Haas, S., and Kuhn, T., Phys. Rev. Lett., **72**, pg.152, 1994.

Rother, W., Meyer, H., and Kaiser, W., Naturforsch. Teil A, **25**, pg.1136, 1970.

Said, A. A., Shiek-Bahae, M., Hagan, D. J., Wei, T. H., Wang, J., Young, J., and Van Stryland, E. W., Journ. Opt. Soc. Am. B, **9**, pg.405, 1992.

Schroeder, W. A., Stark, T. S., Smirl, A. L., and Valley, G. C., Opt. Comm., **84**, pg.369, 1991.

Schroeder, W. A., Stark, T. S., Dawson, M. D., Boggess, T. F., and Smirl, A., L., Opt. Lett., **16**, pg.159, 1991.

Schroeder, W. A., Stark, T. S., and Smirl, A. L., Opt. Lett., **16**, pg.989, 1991.

Schroeder, W. A., Dvorak, M. D., Andersen, D. R., and Smirl, A. L., paper MSS1 in *Technical Digest of the 1992 Annual Meeting of the Optical Society of America*, Albuquerque, NM, 1992.

Seeger, K., *Semiconductor Physics*, An Introduction, 3rd Ed., Springer-Verlag, New York, NY, 1985

Shah, J., Phys. Rev. B, **9**, pg.562, 1974.

Shah, J., *Ultrafast Spectroscopy of Semiconductors and Semiconductor Nanostructures*, Springer-Verlag, New York, NY, 1996.

Shank, C. V., Fork, R. L., Leheny, R. F., and Shah, J., Phys. Rev. Lett., **42**, pg.112, 1979.

Sheik-Bahae, M., Said, A. A., and Van Stryland, E. W., Opt. Lett., **14**, pg.955, 1989.

Sheik-Bahae, M., Hutchings, D. C., Hagan, D. J., and Van Stryland, E. W., IEEE Journ. Quant. Elect., **27**, pg.1296, 1991.

Shih, C. C., and Yariv, A., J. Phys. C: Sol. State Phys., **15**, pg.825, 1982.

Silence, S. M., Burland, D. M., and Moerner, W. E., *Photorefractive Polymers*, Chapter 5 of *Photorefractive Effects and Materials*, Nolte, D. D., Ed., Kluwer Academic Publishers, Boston, MA, 1995.

Smirl, A. L., Valley, G. C., Bohnert, K. M., and Boggess, T. F., IEEE Journ. Quant. Elect. **24**, pg.289, 1988.

Smirl, A. L., Dubard, J., Cui, A. G., Boggess, T. F., and Valley, G. C., Opt. Lett., **14**, pg.242, 1989.

Smirl, A. L., Dawson, M. D., Schroeder, W. A., Stark, T. S., Boggess, T. F., and Valley, G. C., pg.324 in *Ultrafast Phenomena VII*, Harris, C. B., Ippen, E. P., Mourou, G. A., and Zewail, A. H., Springer-Verlag, New York, NY, 1990.

Spindler & Hoyer Optics Catalog, Spindler & Hoyer, Inc., Millford, MA, 1999.

Stark, T. S., Dawson, M. D., and Smirl, A. L., Opt. Comm., **68**, pg.361, 1988.

Sutter, K., and Günther, P., J. Opt. Soc. Am. B, **7**, pg.2274, 1990.

Takeda, K., Matsumoto, N., Taguchi, A., Taki, H., Ohta, E., and Sakata, M., Phys. Rev. B, **32**, pg.1101, 1985.

Trebino, R., and Siegman, A. E., Opt. Comm., **56**, pg.297, 1985.

Valley, G. C., Smirl, A. L., Klein, M. B., Bohnert, K. and Boggess, T. F., Opt. Lett., **11**, pg.647, 1986.

Valley, G. C., Klein, M. B., Mullen, R. A., Rytz, D. and Wechsler, B., Ann. Rev. Mater. Sci., **18**, pg.165, 1988.

Valley, G. C. and Smirl, A. L., IEEE Journ. Quant. Elect., **24**, pg.304, 1988.

Valley, G. C., and Lam, J. F., *Theory of Photorefractive Effects in Electrooptic Crystals*, Chapter 3 of *Photorefractive Materials and Their Applications I*, Günther, P. and Huignard, J. P., eds., Topics in Applied Physics, Vol.61, Springer-Verlag, New York, NY, 1988.

Valley, G. C., Boggess, T. F., Dubard, J., and Smirl, A. L., Journ. Appl. Phys., **66**, pg.2407, 1989.

Valley, G. C., Dubard, J., Smirl, A. L., and Glass, A. M., Opt. Lett., **14**, pg.961, 1989.

Von Lehmann, A., and Ballantyne, J. M., Journ. Appl. Phys., **58**, pg.958, 1985.

Vinetskii, V. L., Zaporozhets, T. E., Kukhtarev, N. V., Matviichuk, A. S., Odulov, S. G., and Soskin, M. S., JETP Lett., **25**, pg.404, 1976.

Walsh, K., Hall, T. J., Burge, R. E., Opt. Lett., **12**, pg.1026, 1987.

Walukiewicz, W., Pawlowicz, L., Lagowski, J., and Gatos, H. C., *Characterization of Semi-insulating GaAs, in Semi-insulating III-V Materials*, Makram-Ebeid, S., and Tuck, B., Eds., Shiva, Nantwitch, UK, 1982.

Wang, C. S., *The Stimulated Raman Process*, pg.447 of, Quantum Electronics, Vol. 1, Part A, Rabin, H., and Tang, C. L., Eds., 1985.

Wherrett, B. S., and Higgins, N. A., Proc. R. Soc. Lond., **379**, pg.67, 1982.

White, J. O. and Yariv, A., Appl. Phys. Lett., **37**, pg.5, 1985

Yariv, *Optical Electronics*, 3rd Ed., Holt, Reinhart and Winston, New York, NY, 1985.

Yariv, A., *Quantum Electronics*, 3rd Ed., Wiley & Sons, New York, NY, 1989.

Yeh, P., Journ. Opt. Soc. Am. B, **4**, pg.1382, 1987.

Yeh, Pochi, *Introduction to Photorefractive Nonlinear Optics*, J. Wiley and Sons, New York NY, 1993.

Zanio, K., *Semiconductors and Semimetals*, Vol. 13, *Cadmium Telluride*, Academic Press, New York, NY, 1978.